# Size dependent reactivity of metal nanoparticles and alloys supported on HOPG, probed by the H-D exchange and the NH3 decomposition reactions

**Fiordaliso, Elisabetta Maria; Chorkendorff, Ib**

*Publication date:*
2012

*Document Version*
Publisher's PDF, also known as Version of record

# Size dependent reactivity of metal nanoparticles and alloys supported on HOPG, probed by the H-D exchange and the $NH_3$ decomposition reactions

Elisabetta Maria Fiordaliso

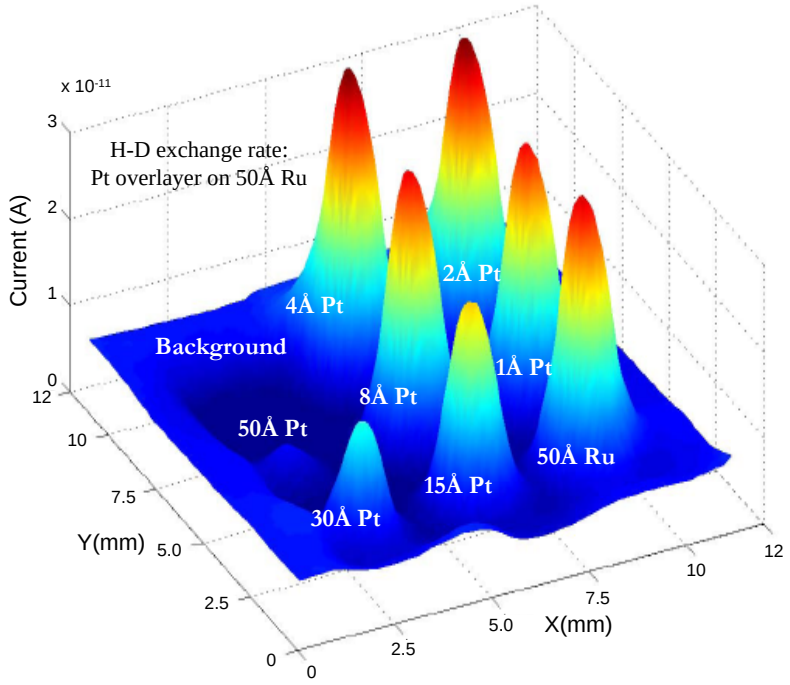


Center for Individual Nanoparticle Functionality - CINF
Technical University of Denmark - DTU

# Contents

# Preface and Acknowledgements

This thesis is submitted in partial fulfillment of the requirements for obtaining the Ph.D. degree from the Technical University of Denmark (DTU). It summarizes results obtained at the Center for Individual Nanoparticle Functionality (CINF), Department of Physics, DTU, under the supervision of Prof. Ib Chorkendorff, in the period 2008-2011. Within this period I have been in maternity leave for a year, from February 2009 to February 2010. CINF is funded by The Danish National Research Foundation which is acknowledged for their support.

I would like to thank my supervisor for offering me the possibility of starting an interesting PhD project in a excellent center of research. He is also acknowledged for his kind and inspiring guidance through the PhD period, for his support and his helpfulness, for taking the time to listen and for addressing me to the right direction when a problem needed to be solved. Søren Dahl is also acknowledged for the great support. Although he has never been officially my supervisor, he has always been available for discussions and I have appreciated his advices and his valuable teaching. Jane Nielsen has also been an important figure for me through out the PhD project, helping me out from many frustrating situations. Therefore I would like to thank her for this.

I would like to thank Martin Johansson, which has been my co-supervisor for the first year and a half of my PhD, for sharing with me his knowledge about the experimental setup and surface science, and for helping me in getting good results, which have been published in international journals.

Special thanks go to Sebastian Kuld and Christian Conradsen, which have been working with me in the last year of my PhD, sharing with me joy and pain related to the experimental setup.

I would also like to thank Dan Shacham and Peter Christensen for fixing all the parts of the setup that broke down during the PhD, Ole Mogensen for solving the many computer related problems and Anders Poulsen for his help in electronics issues.

I would like to thank all the other PhD students and post docs, especially the ones that I have shared the office with, for the great time in the lab and during our challenges. I am certainly going to miss the positive and exciting working environment that I have experienced at CINF.

I would also to thank my family, Tobias Johansson and the little Elias, that have been taking care of me and supporting me in this project, and my parents, that have found the courage to let me go far away in order to fulfil my dreams.

Finally, I would like to thank everybody at the Physics department for the nice chats and for appreciating my cakes.

Elisabetta Maria Fiordaliso
Kgs. Lyngby, January 2012

# Abstract

This thesis presents the results obtained from experiments performed in an Ultra High Vacuum (UHV) apparatus, named *Parallel Screening*, consisting of a preparation chamber combined to a High Pressure Cell (HPC) for testing catalytic activity at 1 bar. Two catalytic reactions have been carried out on different transition metals and metal alloys supported on sputtered Highly Ordered Pyrolytic Graphite (HOPG). The first is the H-D exchange reaction, used as probe reaction for $H_2$ dissociation, which is relevant for Proton Exchange Membrane (PEM) fuel cells. Experiments have been performed on Pt, Ru, and Rh nanoparticles and on Pt/Ru alloys in the pure $H_2/D_2$ mixture and also in the presence of 10 ppm CO, since this is a poison for the anode of the PEM fuel cells, where the $H_2$ dissociation takes place. It is found that the activity for Ru and Rh is strongly dependent on the particle size, with the larger particles being more active, whereas the activity for Pt does not show any dependence on size. The apparent energy of desorption shows a dramatic increase with decreasing particle diameter for Ru and Rh, whereas it is only weakly dependent on particle diameter for Pt. It is suggested that the strong variation for Ru and Rh is due to the formation of compressed hydrogen adlayers on the terraces of the larger particles. In the case of the Pt/Ru alloys, it is found that the activity exceeds the values measured on the individual metals and have a maximum on alloys with surface composition ratio of Pt:Ru equal to 1:1. In the presence of CO the exchange rate decreases significantly, for all the metals. Alloying Pt with Ru improves significantly the resistance towards CO poisoning with respect to pure Pt and the resistance is found to increase with increasing amount of Ru in the alloys. The results from the exchange reaction on the nanoparticles and on alloys have been summarized in two scientific articles which have been recently published [1, 2].
The exchange reaction is carried out on supported catalysts. The effect of the interaction between metals and support on the catalytic activity has been investigated in the case of Pt and Ru deposited on HOPG, which were annealed to high temperatures in the UHV chamber. It is found that upon annealing the amount of carbon present in the films increases up to 95%, as derived by surface analysis, indicating the formation of a carbon layer on the metal films. The exchange rate decreases dramatically with increasing carbon content in the films for both metals, indicating a decrease in the ability of the films to adsorb hydrogen. It is also shown that performing $He^+$ sputtering enables the removal of the carbon layer and regenerates

the Pt catalysts. The results from this investigation have been summarized in a scientific article which has been submitted to the Journal of Physical Chemistry.
The second reaction investigated in this thesis is the $NH_3$ decomposition reaction, relevant for hydrogen storage and production in a $CO_x$ free environment, which has been performed on Ru, Ir, Rh and Pt thin films, on Ru nanoparticles and on Ir/Ru alloys. Preliminary results indicated that Ru is the most active among the selected metals, but no definitive conclusions can be drawn on the effect of the particle diameter on the decomposition rate. In the case of the Ru/Ir alloys, it is found that the activity exceeds the values measured on the individual metals and have a maximum on alloys containing roughly 10% Ir on the surface.

# Dansk Resumé

Denne afhandling sammenfatter resultaterne opnået ved en *Parallel Screening* opstilling, som består af et ultra højt vakuum (UHV) kammer til forberedelse af prøver kombineret med en højtrykscelle (HPC) til test af katalytisk aktivitet ved 1 bar. To katalytiske reaktioner er blevet undersøgt på forskellige overgangsmetaller og metallegeringer på sputtered Highly Ordered Pyrolytic Graphite (HOPG). Den første er H-D udvekslingsreaktionen, der er relevant for Proton Exchange Membrane (PEM) brændselsceller. Reaktionen er blevet udført på Pt, Ru og Rh nanopartikler og på Pt/Ru legeringer. Forsøgene blev også udført med 10 ppm CO føjet til $H_2/D_2$ blandingen, som er en gift for anoden af PEM brndselsceller, hvor $H_2$ splitningen forløber under drift. Det blev fundet at den målte aktivitet, af Ru og Rh er stærkt afhængig af partikelstørrelsen, og at de større partikler bliver mere aktive, mens aktiviteten for Pt ikke viser nogen afhængighed af størrelsen. Den tilsyneladende desorptionsenergi viser en dramatisk stigning med faldende partikeldiameter for Ru og Rh, mens der kun er en svag afhængig af partikeldiameteren for Pt. Det foreslås, at den stærke variation for Ru og Rh skyldes dannelsen af komprimerede brint adlayers på terrasserne af de større partikler. For Pt/Ru legeringer, blev det fundet, at aktiviteten overstiger værdierne målt på rene metaller og har et maksimum for legeringer med overfladesammensætningen af Pt:Ru svarende til forholdet 1:1. I tilstedeværelse af CO er det fundet, at raten falder markant, for alle metaller. Det blev også fundet, at legeringer med Pt og Ru markant mindsker CO forgiftningen i forhold til rent Pt og at effekten falder med større mængde af Ru i bulk-legeringer. Resultaterne fra udvekslingsreaktionen på nanopartiklerne og på legeringerne er opsummeret i to videnskabelige artikler som for nyligt er blevet publiceret [1, 2].
Udvekslingsreaktionen er udført på understøttede katalysatorer. Endelig er samspillet mellem metal og support undersøgt i tilfældet hvor Pt og Ru deponeres på HOPG, der er opvarmet til høje temperaturer i UHV kammeret. Indflydelsen af metal-support samspillet på den katalytiske aktivitet af Pt filmene er probed med H-D udvekslingsreaktionen. Det er fundet, at opvarmning af tyndfilmene til høje temperature øger mængden af kulstof i filmene op til 95%, hvilket blev bestemt ved overfladeanalyse. Dette indikerer dannelsen af et lag kulstof oven på metal filmen. Udvekslingsraten falder drastisk med stigende kulstof indhold i filmen for begge metaller, hvilket indikerer et fald i brint adsorption på filmen. Det blev også vist hvordan man ved at udføre $He^+$ sputtering, som gør det muligt at fjerne kulstof lag og regenerere Pt katalysatoreren. De ovenstående resultater er opsummeret i en

videnskabelig artikel, som er indsendt til Journal of Physical Chemistry.
Den anden reaktion, som blev undersøgt i denne afhandling er $NH_3$ dekomponering. Denne reaktion er relevant for lagring og produktion af brint som ikke indeholder spormængder af $CO_x$. Reaktionen blev undersøgt på Ru, Ir, Rh og Pt tyndfilm, Ru nanopartikler og på Ir/Ru legeringer. De foreløbige resultater viser, at Ru er den mest aktive af de testede katalysatorer, men det kunne ikke endelig konkluderes om, der er en effekt af partikeldiameteren på dekomponeringshastigheden. Modsat dette blev det fundet at for Ru/Ir legeringer stiger aktiviteten ved legeringen i forhold til de rene metaller. Den maksimale aktivitet blev observeret for en legering med ca. 10% Ir i legeringens overflade.

# 1 Introduction

## 1.1 Hydrogen as energy carrier

This thesis focuses on investigating the relation between particle size and reactivity of some selected transition metals, such as Pt, Ru and Rh, as well as on finding the optimum surface composition of binary alloys, such as Pt/Ru and Ir/Ru, for two catalytic processes: the H-D exchange and the $NH_3$ decomposition reactions, described in Eq. 1.1 and 1.2, respectively.

$$H_2 + D_2 \Leftrightarrow 2HD \tag{1.1}$$

$$2NH_3 \Leftrightarrow N_2 + 3H_2 \tag{1.2}$$

The first reaction is used as probe reaction for the $H_2$ dissociation, while the latter describes one possible strategy for $H_2$ storage and production. The two reactions are relevant in the field of sustainable and renewable energy, with the aim of finding alternatives to fossil fuels. Presently, 81% of the energy produced by our society is based on fossil fuels [3]. Cars, trains and airplanes are fueled almost exclusively by gasoline and diesel, while power plants use coal, oil and natural gas. The combustion of these fuels produces harmful byproducts, such as $CO_x$ and $NO_x$ species along with unburned hydrocarbons, which are responsible for air pollution and global warming. Since fossil fuels are also a limited resource, clean and sustainable alternatives to such fuels are therefore needed.
Currently, there are different ways to generate electricity without using fossil fuels, such as nuclear power, reforming of biomass, hydroelectric dams, solar cells, wind turbines and fuel cells. The results presented in this thesis are relevant for fuel cell applications, where hydrogen is used as an energy carrier.
The two primary advantages of fuel cells are their high efficiency, which is 40-60% [4], and the non-polluting byproduct, consisting of water. Several kind of fuel cells are available with different properties [5]. Among them, best suited for mobile applications are the Proton Exchange Membrane (PEM) fuel cells, which operate

at moderate temperatures ($\sim$ 80°C). In this kind of fuel cell, $H_2$ is dissociated at the anode catalyst, which typically consists of Pt nanoparticles on a carbon support. Hydrogen is oxidized into protons, which diffuse through the membrane to the cathode, while the electrons reach the cathode passing through an external circuit, generating electricity. At the cathode the protons react with oxygen from air and recombine with the electrons, producing water and heat. A illustration of a PEM fuel cell is shown in Fig. 1.1 [6].

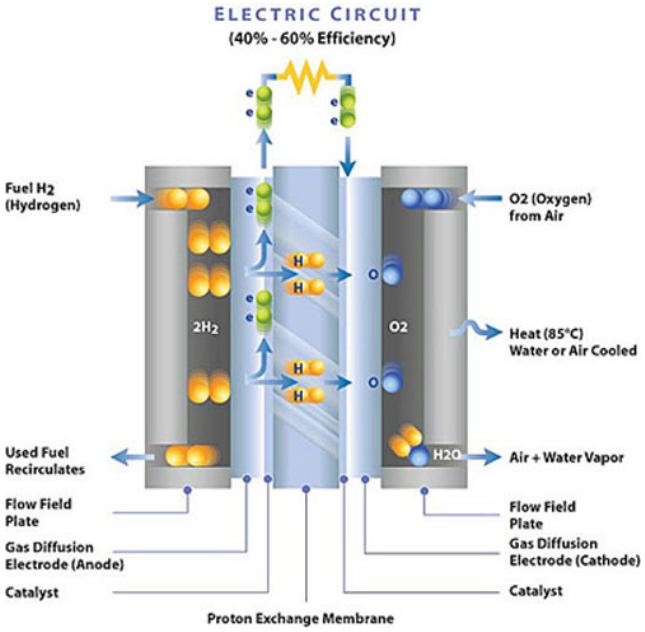


Figure 1.1: An illustration of a PEM fuel cell [6].

Hydrogen is commonly produced by steam reforming of natural gas, especially steam methane reforming, resulting in a rest concentration of CO in hydrogen of at least 10 ppm. The $H_2$ dissociation is poisoned by such low CO concentrations [7], which corresponds to a full monolayer of adsorbed CO on a polycrystalline Pt surface, at temperatures relevant for PEM fuel cells [8]. The present interest in improving the activity of the anode catalyst in fuel cells has resulted in several fundamental studies of hydrogen dissociation on transition metals with different structures and on alloys [9–14]. Moreover, the $H_2$ dissociation in the presence of CO has also been widely investigated under Ultra High Vacuum (UHV) conditions [15–18] and at realistic hydrogen pressures on thin metal films [19–21].
In this thesis the influence of particle size on the H-D exchange reaction, described by Eq. 1.1, and therefore on the $H_2$ dissociation, is investigated in the case of Ru, Rh and Pt particles, at 1 bar hydrogen pressure. Experiments are also carried out in the presence of 10 ppm CO added to the $H_2/D_2$ mixture, in order to investigate whether the resistance to CO poisoning may be improved by selecting a certain particle diameter. Experiments have been also carried out on Pt/Ru alloys, which

are reported to be very CO-tolerant anode catalysts in low-temperature fuel cells [22–29]. Different ratios between the two metals have been tested, in the pure $H_2/D_2$ mixture and in the presence of 10 ppm CO, in order to find for which Pt/Ru composition the highest resistance towards CO poisoning is obtained.
Although hydrogen is an excellent energy carrier, its storage is challenging. Hydrogen has a high gravimetric energy density, around 33 kWh/kg, compared to other fuels [30]. For applications such as space rockets, where mass is important, hydrogen has been utilized as a fuel for many years. However, for transportation use, the volumetric density plays an important role. The volumetric density of hydrogen gas is significantly lower compared to fossil fuels, therefore it requires a larger tank for being stored. For instance, at room temperature and atmospheric pressure 1 kg hydrogen occupies a volume of around 12 $m^3$ [30]. The lack of satisfactory hydrogen storage means represent the main impediment to the widespread use of hydrogen as a fuel for transportation applications.
Conventionally, hydrogen is stored in high pressure gas tanks at 200-300 bars, which lead to several safety issues. Hydrogen can also be liquified, but this requires a cryogenic storage with a significant use of energy, since the boiling temperature of hydrogen is -253°C. Alternatively, metal hydrides and amides can be used for hydrogen storage, since they can store more hydrogen per volume than liquid or compressed hydrogen do. Moreover, the hydrogen absorption and desorption rates can be controlled by adjusting temperature or pressure [31]. However, they have a very low gravimetric hydrogen density, making them very heavy and unsuitable for transportation uses [32]. Automobiles need light, compact and safe energy storage devices. In average, a car burns about 24 kg of petrol in a combustion engine for driving a distance of 400 km. It is reported that an electric car with a fuel cell needs 4 kg hydrogen to drive the same range [33]. The volume that is needed to store 4 Kg of hydrogen in the form of gas, liquid and in hydrates is shown in Fig. 1.2, where the dimensions are related to the size of a car [33].

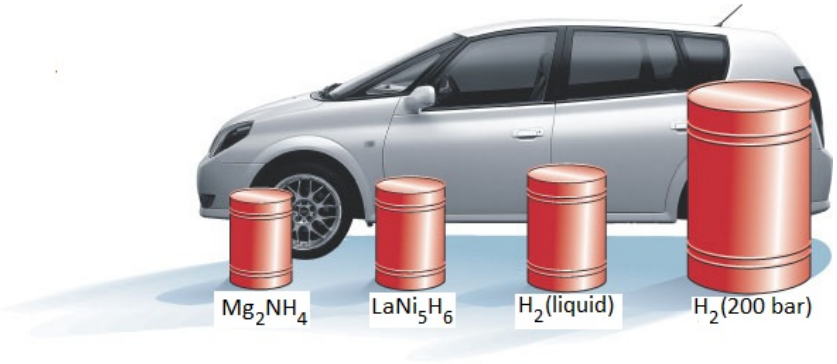


Figure 1.2: Volume of 4 kg of hydrogen compacted in different ways, with size relative to the size of a car [33].

A more attractive alternative for hydrogen storage is ammonia, $NH_3$, which has many desirable characteristics. First of all, it has a large weight fraction of hydrogen, which constitutes 17.65% of its mass, looking appealing for use as a potential hydrogen carrier for onboard storage. Secondly, it is a commonly used industrial and agricultural chemical, which is produced in million of tons per year and can be handled and transported safely. Moreover, it can be liquefied under mild conditions and can be stored in simple, inexpensive pressure vessels. In addition, an ammonia-based solid-state hydrogen storage solution has been found by the company called *Amminex*[†], which has developed a pellet where ammonia is incorporated in magnesium chloride as $Mg(NH_3)_6Cl_2$. A small pellet can contain the equivalent of 75 liters of ammonia gas and the kinetics of the $NH_3$ adsorption and desorption are reversible and fast [34, 35]. The pellets of $Mg(NH_3)_6Cl_2$ are shown in Fig. 1.3.

Figure 1.3: Pellets of $Mg(NH_3)_6Cl_2$ [35].

The pellets are currently used on diesel cars to reduce the emission of NO and $NO_2$ through the Selective Catalytic Reduction (SCR), where the $NO_x$ gases react with $NH_3$ producing nitrogen and water. In order to use ammonia as a hydrogen source, the molecule needs to be catalytically cracked over a catalyst. The $NH_3$ decomposition reaction is described by Eq. 1.2. This is a clean process producing $H_2$ along with $N_2$, which can be released to the atmosphere without significant environmental impact, since it is a non-toxic and non-greenhouse gas. The reaction does not involve any CO, therefore the produced $H_2$ can be used in a fuel cell. For applications in a PEM fuel cell, the $H_2$ needs to be purified by any rest concentration of ammonia, since the membrane gets poisoned by levels as low as 1 ppm [36]. However, other kind of fuel cells can be used, such as alkaline fuel cells, able to tolerate low amounts of $NH_3$ [37].
The dissociation reaction is endothermic and the rate depends on temperature, pressure and used catalysts. Many catalysts have been tested [38–43] and among them, Ru is found to be the most active metal [38, 40, 44–47]. In this thesis the $NH_3$ decomposition reaction is carried out on films of Ru, Ir, Rh and Pt and the results

[†]http://www.amminex.net/

are compared to the trend reported in literature. The reaction is also carried out on Ru nanoparticles, aiming at investigating whether the particle size has an effect on the decomposition rate. Moreover Ir/Ru alloys are also tested to see whether alloying Ru with other metals enhances its activity.

## 1.2 The role of the support in heterogenous catalysis

The H-D exchange and the $NH_3$ decomposition reactions are carried out on supported catalysts, as most of the reactions in heterogeneous catalysis. In a PEM fuel cell, for instance, different diffusion-type carbon electrodes are used to support the Pt catalyst, as reviewed in [48]. The $NH_3$ decomposition reaction is carried out on catalysts supported on oxides and also on carbon based materials, as reviewed in [49]. Supports are generally used in order to enhance the dispersion and the surface area of the catalysts, with the aim of improving their performance. However, in some cases it is found that they suppress the catalyst's activity for a specific reaction. For instance, for metals supported on $TiO_2$ which are annealed to high temperatures, it is reported that the $H_2$ and CO chemisorption is drastically reduced, as a consequence of the so called *Strong Metal-Support Interaction* (SMSI) [50–56].
The experiments described in this thesis are carried out on metals supported on Highly Ordered Pyrolytic Graphite (HOPG) and it is interesting to investigate whether an interaction between metals and support occurs when the catalysts are annealed to high temperatures in the UHV chamber. The effect of the metal-support interaction on the catalytic activity of Pt and Ru films is probed by the H-D exchange reaction and different surface sensitive techniques are used to investigate the surface of the metals before and after annealing.

## 1.3 Outline

The thesis is divided into six chapters, the first being this introduction. In chapter two, the experimental setup is introduced, along with the surface techniques available and the principles of the high pressure experiments. In chapter three, the H-D exchange reaction and its kinetics is described. Moreover, the results from the Ru, Pt and Rh nanoparticles and the Pt/Ru alloys are presented. In chapter four, the interaction between metals and support is investigated in the case of Pt and Ru films deposited on HOPG. In chapter five, the $NH_3$ decomposition reaction and its kinetics is described. Moreover, the results obtained from the Ru, Ir, Rh and Pt films, the Ru nanoparticles and the Ir/Ru alloys are presented. A conclusion for each part is given at the end of the corresponding section or chapter, while general conclusions and an outlook are presented in chapter six.

# 2 Experimental setup

## 2.1 The *Parallel screening* apparatus

The experiments described in this thesis are performed in a *Parallel Screening* apparatus, which consists of an Ultra High Vacuum (UHV) chamber for sample preparation and characterization combined with a High Pressure Cell (HPC) for studies of catalytic reactions. A schematic drawing of the apparatus is shown in Fig. 2.1.

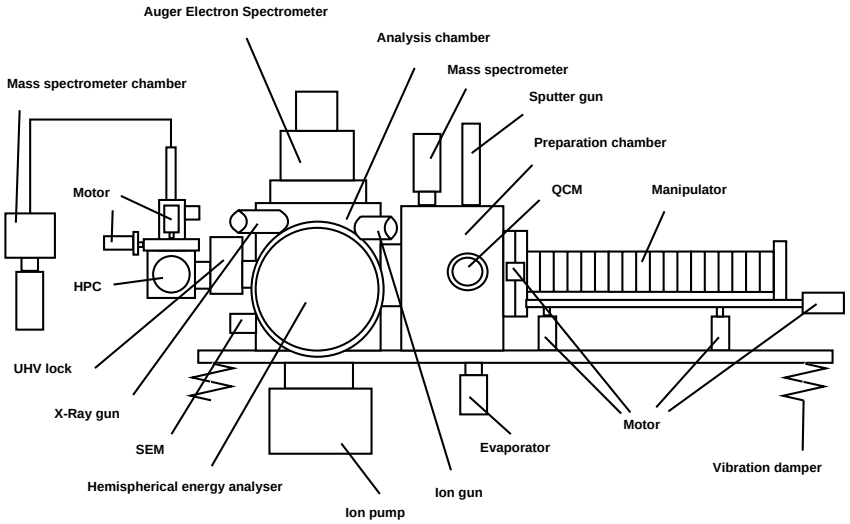


Figure 2.1: Schematic drawing of the *Parallel Screening* apparatus.

The UHV is maintained by a 550 L/s turbo molecular pump, a 220 L/s ion pump and a titanium sublimation pump, providing a base pressure of $1.0 \cdot 10^{-10}$ Torr. The chamber is equipped with an electron beam evaporator for sample preparation and a quadrupole mass spectrometer for leak testing and monitoring residual gases in the chamber. It is also equipped with an electron gun for characterizing the catalysts by Auger Electron Spectroscopy (AES), an X-ray source for X-ray Photoelectron

Spectroscopy (XPS) and an ion gun for Ion Scattering Spectroscopy (ISS). A Hemispherical Energy Analyzer (HSA) is used to detect photoelectrons and ions, while a Cylindrical Mirror Analyzer (CMA) is used for the AES electrons. A second ion gun is mounted on the chamber and used for sputtering purposes. The activity of the catalysts is tested in the HPC by a gas sampling device, consisting of a scanning sniffer probe combined with a second quadrupole mass spectrometer, allowing the surface of a sample to be mapped. The main chamber can be isolated from the HPC by a UHV lock. The catalysts are deposited on a support which is mounted on a manipulator arm, able to rotate and move the sample in x, y and z-directions through the whole apparatus. The x, y and z movement of the manipulator is controlled by stepper motors, which in turn are controlled from a LabVIEW program. The repeatability of a movement is estimated to be better than 0.01 mm in all directions. Further details can be found in [57, 58].
The setup enables to prepare, characterize and test the activity of multiple catalysts in a combinatorial approach, as illustrated in Fig. 2.2. A pattern of circular metal films is deposited on a substrate by evaporation through a mask in the UHV chamber. Each film is individually characterized in UHV by AES, XPS and ISS. Eventually the samples are transferred to the HPC, for screening the catalytic activity of each film individually. After screening, the samples are transferred back into the UHV chamber and characterized again, detecting adsorbed impurities or changes in surface compositions.

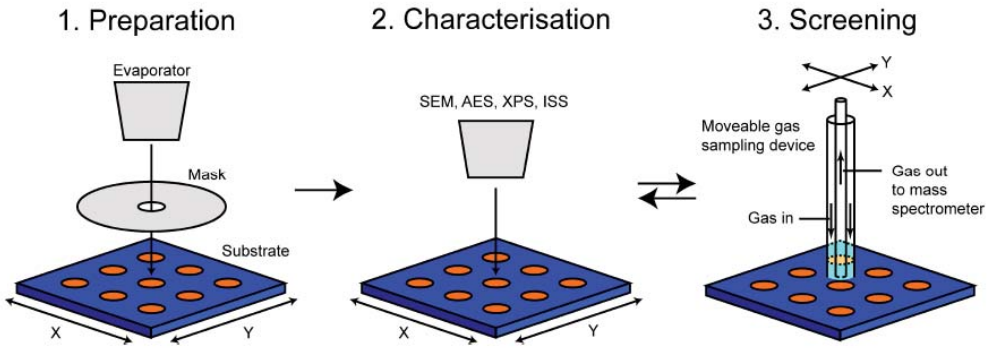


Figure 2.2: A pattern of films is deposited on a substrate. Each film is individually characterized in UHV and the activity is tested in the HPC [59].

## 2.2 The substrate

A $10 \times 10$ mm Highly Ordered Pyrolytic Graphite (HOPG) is used as support for the catalysts, which consists of graphene sheets ordered parallel to the surface. By cleaving the graphite, a smooth surface can be obtained. This support is conduc-

tive, making it ideal for the surface characterization techniques provided by the experimental setup. Furthermore, since carbon is used as support for the platinum catalyst in the PEM fuel cell [48], the results shown in this thesis are relevant for this application.
The HOPG is glued onto a graphite disc by a carbon glue, called Graphi-bond 669. The disc is mounted on two tungsten wires, which are used for heating the substrate and the supported catalysts. The temperature is measured by a thermocouple glued to the side of the HOPG. The maximum temperature reached in UHV is 800°C, while it is approximately 550°C when the HOPG is exposed to 1 bar of gas in the HPC. An image of the sample taken from a window of the HPC is shown in Fig. 2.3, while the gas sampling device is positioned close to the surface of the HOPG.

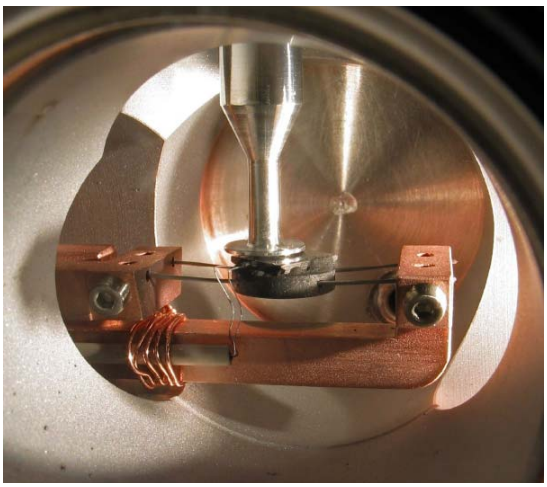

Figure 2.3: The sample inside the high pressure cell.

It is important that the HOPG is mounted parallel to the x-y plane of the gas sampling device. For reliable measurements the height of the sniffer probe must not change by more than a few hundreds of a millimeter, as it moves across the surface of the HOPG. When the substrate needs to be replaced, a tool is placed around the head of the manipulator, which consists in an arm holding an aluminium disc over the surface of the HOPG, resembling the bottom of the gas sampling device. The surface of the aluminium disc is in the correct x-y plane and the position of the sample can be tweaked until it becomes parallel to the aluminium disc. However, even with the mounting tool, it is not possible to achieve a high precision. Fortunately, rotating the manipulator arm can correct a deviation along the y-axis. Moreover the sniffer probe can be tilted by a few degrees in the x-z plane, correcting any small deviation along the x-axis. A schematic drawing of the sample holder and the tool used to align the HOPG to the gas sampling device is shown in Fig. 2.4.

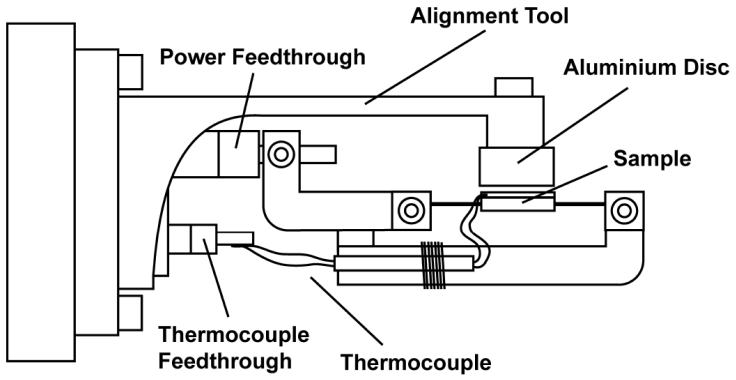


Figure 2.4: A schematic drawing representing how the support is mounted on the holder, showing also the tool used to align the HOGP in the x-y plane.

Between two series of experiments, the substrate is cleaned by 1 keV $Ar^+$ sputtering. The sputtering time needed to remove a series of 50 Å thick films from the HOPG substrate is around 15 hours. After sputtering AES or ISS is used to confirm that the films are removed and the HOPG is annealed at 800°C for 30 minutes to desorb any remaining Ar. A Scanning Electron Microscope (SEM) image acquired from the sputtered HOPG in another experimental apparatus is shown in Fig. 2.5. It can be seen that the sputtered HOPG is a highly defected substrate. However, the presence of defect sites on the support is reported to prevent particle sintering [60, 61] and surface characterization is still possible.

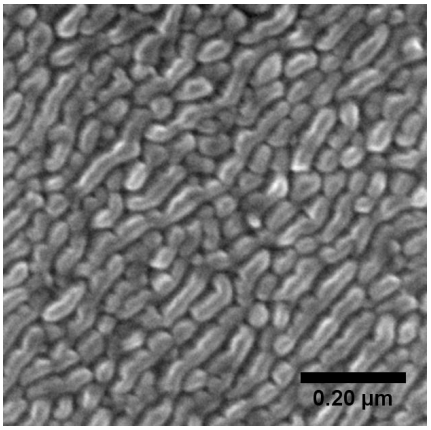


Figure 2.5: A SEM image of the sputtered HOPG [1].

## 2.3 The evaporator

The catalysts are produced by Electron Beam Physical Vapor Deposition (EBPVD), with typical deposition rates of 5 - 10 Å/min. An image of the evaporator is shown in Fig. 2.6. It consists of four pockets containing different metal rods. The deposition rate from each pocket can be measured, independently, with four flux plates, placed above the metal rods. When the ions of the evaporated metal vapor hit the plates create a current of up to 1000 nA. Since the metals are properly degassed, this current is a measure of the deposition rate from each pocket. The rates are calibrated using a Quarts Crystal Microbalance (QCM), where the change in mass per area of the crystal is related to the change in its vibration frequency, according to the Sauerbrey equation [62]. The densities and acoustic impedances for each metal are taken into account in order to calibrate the correct deposition rate. The actual deposition time is controlled by blocking the metal vapour with a shutter, consisting of a metallic plate. The flux current depends on both the geometry of the rod and the material. Since the geometry changes slowly over time as the material is consumed, all the rates are always recalibrated before a pattern of films is deposited. A review on how to evaporate metals, including suitable crucible materials, can be found in [63].

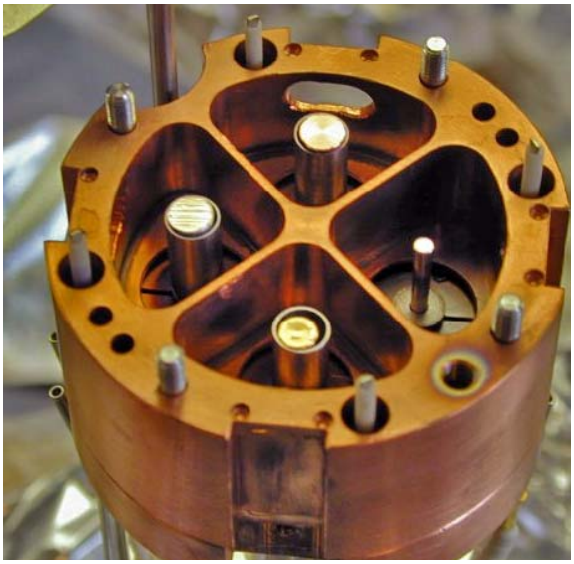

Figure 2.6: The evaporator with the top lid removed, exposing the four pockets.

A pattern of films is created on the HOPG by placing a mask in between the evaporator and the substrate. The mask consists of a pierced metal plate with holes of 3 mm, 2 mm and 1 mm in diameter and it is mounted on the QCM, as illustrated in Fig. 2.7 and 2.8. The linear motion of the QCM allows the QCM or any of the three mask to be placed in front of the evaporator. Well defined patterns of films are created by moving the sample using a LabVIEW program, able to use predefined positions during metal deposition. The same set of positions is then used later

for characterization of the catalysts in the UHV chamber and when screening for catalytic activity in the HPC. Usually a square pattern of nine ($3 \times 3$) position is used, in order to maximize the number of different catalysts that can be tested. For 1 mm diameter films deposited on a $10 \times 10$ mm HOPG, the distance between the centers of the films is 3 mm. In this pattern only eight films are deposited, while the last position available is left clean from metal, as shown in 2.8, and used as a background measurement.
The catalysts tested in the experiments described in this thesis are single metals or alloys, such as overlayers or bulk alloys. When a metal is chosen to be tested, typically a different amount of it is deposited in a predefined pattern, in order to have a variety of catalysts to test. In this case, only one pocket is used and the rate is calibrated before deposition. When few metals need to be tested, typically the same amount of each metal is deposited in a pattern, for a fair comparison of the catalytic activity. In this case one pocket at the time is used, with one deposition rate for each metal. In the case of an overlayer, a pattern of films consisting of the same metal is deposited first and a different amount of another metal is deposited on top of each film afterwards. In this way a number of overlayers with different compositions is tested. Also in this case one pocket at the time is used, with one deposition rate for each metal. Finally, when a bulk alloy is created, two pockets are used at the same time, resulting in a co-deposition of two metals. By calibrating a range of rates for the two metals, it is possible to deposit the same amount of metal in each position of the predefined pattern, but varying the ratio between the two metals.

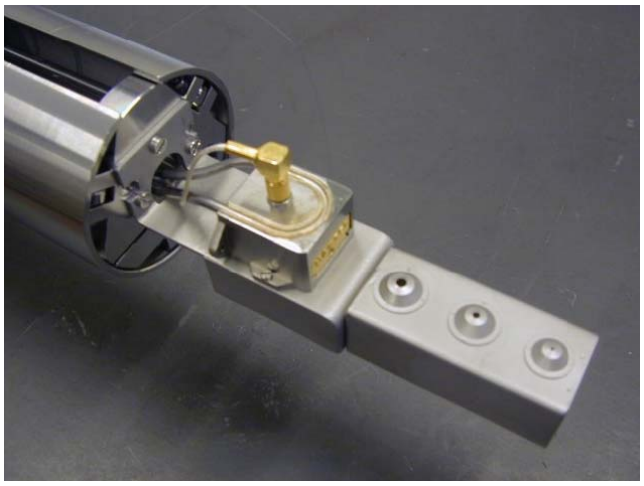

Figure 2.7: The QCM and the three masks, consisting of holes in a steel plate. The masks in the picture are 3 mm, 2 mm and 1 mm.

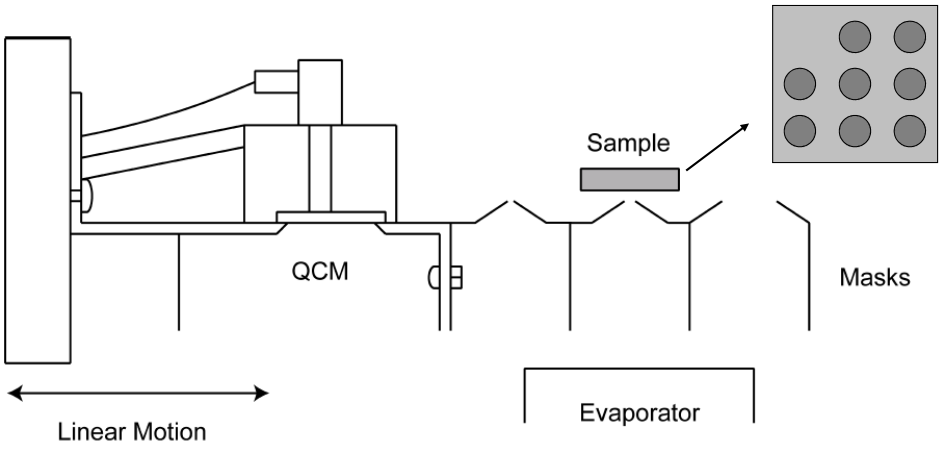


Figure 2.8: The masks mounted on the QCM.

## 2.4 Surface analysis techniques

The UHV chamber is equipped with three surface sensitive analysis techniques to characterize the supported catalytic films. Characterization is always performed at the sample temperature of 150°C, in order to keep the surface of the catalysts clean from contaminants, such as CO.

### 2.4.1 Auger electron spectroscopy

AES is performed by focusing a 3 KeV electron beam on the sample. The incoming electrons cause the atoms of the sample to emit electrons from a deep-lying core level. This configuration is highly excited and it will therefore undergo a relaxation process. With a high probability, the energy released during this process is transferred to other electrons which are emitted and detected by the CMA. By measuring the kinetic energy of the emitted electrons, named AES electrons, it is possible to gain knowledge of the elements on the sample's surface, since this energy is characteristic of each element.
In the setup the AES is combined to Scanning Electron Microscopy (SEM), which uses secondary electrons for locating and imaging a 1 mm diameter film on the substrate, as shown in 2.9(a), in the case of a 50 Å Rh film.
The resolution of the SEM is above 1000 nm, which is not good enough to provide information on the structure of the metal films. This is why the SEM image of the sputtered HOPG shown in Fig. 2.5 is acquired in another experimental setup, which is able to achieve a resolution down to few nm. The poor resolution of the SEM on the *Parallel screening* apparatus is probably due to two main factors. The first is the position of the SEM electron detector, which is located below the surface of the sample. Therefore, since a line-of-sight to the surface of the sample is missing, this

reduces the amount of secondary electrons reaching the detector. The latter is that the 550 L/s turbo pump is not vibrationally isolated from the rest of the chamber, which could also affect the the electron detection. However, SEM greatly serves the purpose of visually locate a film on the substrate and select an area within the film to acquire a AES spectrum. The green rectangle in Fig. 2.9(a) represent, for instance, an area selected within the Rh film and the corresponding AES spectrum is shown in Fig. 2.9(b). In addition, SEM is often used to identify the position of the edges of the HOPG for alinement purposes.

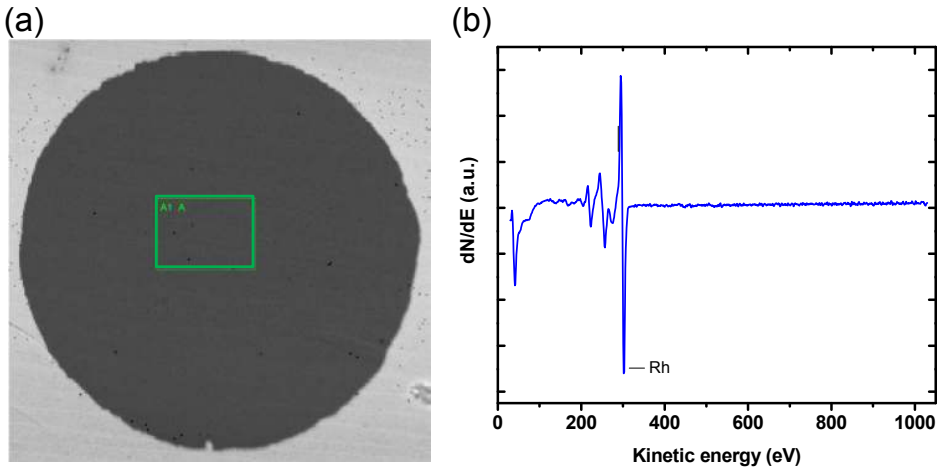


Figure 2.9: (a) SEM image of a 50 Å Rh film of 1 mm diamter. An area is selected for AES analysis. (b) AES spectrum of the selected area of the 50 Å Rh film.

### 2.4.2 Ion scattering spectroscopy

ISS is performed focusing a 1keV $He^+$ ions on the sample. When the ions hit the surface they experience a collision with the surface atoms and are elastically backscattered. By analyzing the ions energy loss in the collisions by the HSA, it is possible to calculate the mass of the target atoms, according to Eq. 2.1, which implies conservation of energy and momentum:

$$m_t = m_i \frac{2\sqrt{E_a E_0} cos\theta + E_a + E_0}{E_0 - E_a} \tag{2.1}$$

$m_t$ and $m_i$ are the masses of the target and the ion atom, respectively. $E_0$ and $E_a$ are the energies of the ions before and after scattering, respectively. $\theta$ is the angle between the analyzer and the ion gun, which is 50° in the *Parallel screening* apparatus.

ISS is very useful, since it is possible to focus the ion beam and raster it over on an area of 1 $mm^2$ in order to cover and analyze each film individually, as in the case of the AES technique. The damage to the sample's surface caused by sputtering is be

kept low by using a low ion flux. Typically only light elements are removed by the $He^+$ beam. This actually allows to use ISS as a soft sputtering technique and light contaminants, such as carbon, can be removed from the surface of a metal.
With ISS it is generally difficult to distinguis two elements with similar mass and quantify the surface composition, since the peaks that they generate would overlap. The alloys tested in this thesis, such as Pt/Ru and Ir/Ru, fortunately contain metals which have a quite different mass, resulting in separated ISS peaks, as shown for the case of a Pt/Ru alloy in Fig. 2.10.

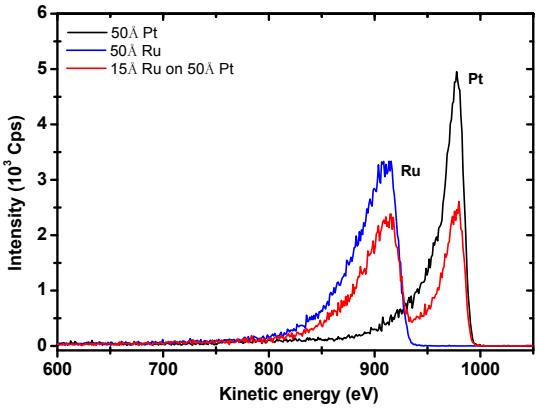


Figure 2.10: ISS spectra from a 50 Å Ru, Pt film and a 15 Å Ru overlayer on a Pt film.

It can be noticed that the same amount of deposited metal for Ru and Pt generates ISS peaks with different heights, which is due to the difference in the cross section of the two metals [64]. In order to get the correct surface composition of each film, all the signals are normalized to the signals generated by the pure metals according to the formula:

$$x_a = 100\% \frac{\frac{I_a}{I_A}}{\frac{I_a}{I_A} + \frac{I_b}{I_B}} \tag{2.2}$$

where $x_a$ is the surface concentration of element $a$, $I_a$ and $I_b$ are the signals of element $a$ and $b$ in the alloy and $I_A$ and $I_B$ are the signals of the pure metals. This formula is also used to calculate the surface composition of the Ir/Ru alloys.

### 2.4.3 X-ray photoelectron spectroscopy

XPS is performed on the catalysts using 1253.6 eV photons coming from a $Mg_{K_\alpha}$ anode. The incoming X-rays are absorbed by the target atoms and electrons are emitted, named photoelectrons, and detected by the HSA. The technique is based

on the photoelectric effect [65] and the kinetic energy of the detected photoelectrons is:

$$E_k = h\nu - E_b - \phi \tag{2.3}$$

where $E_b$ is the binding energy and $E_k$ is the kinetic energy of the photoelectrons, $h\nu$ is the photon energy and $\phi$ is the work function of the analyzer. As the radiation is monochromatic, the energy distribution of the electrons will display fairly discrete peaks, corresponding to the energy levels of a specific element. Auger electrons are also emitted upon relaxation, generating lines in the XPS spectra.
The entire HOPG is irradiated with X-rays. In order to reduce the area of the sample analyzed and the spread in the electron energy, the settings of the lens system and the variable slit mechanism mounted on the entrance of the HSA need to be optimized. At the beginning of the PhD project, XPS spectra from a single film could not be acquired, since the smallest sampling area achieved was around 3 mm for a 1 mm diameter film [59]. Following changes in the lens system, the resolution have significantly improved, as shown in Fig. 2.11. The signal coming from a Ru film is measured while moving the sample in a plane perpendicular to the analyzer entrance slit, in steps of 0.1 mm. The ideal result would be a rectangular function of width 1 mm, but the actual result is a bell shape function, with a nearly flat area at the center. This means that the resolution is larger than 0.1 mm in both directions and the film appears to have a larger diameter than 1 mm. According to the width of the flat region, the resolution achieved is around 0.8 mm, which allows to analyze the films individually. The overlap between the sampling area and the film while moving the sample in one of the two directions is shown by a schematic drawing in Fig. 2.11.
The XPS spectra are typically acquired at the position giving the maximum signal. However, a significant signal of carbon from the substrate surrounding the film is detected, which is likely due to the combination of the large resolution and a sensitivity function having tails outside the area covered by the metal film. As a consequence, quantification of the surface composition with this technique is less reliable compared to AES and ISS.
In addition, when acquired a XPS spectrum, photoelectrons emitted with low kinetic energy are deviated due to a strong magnetic field generated by the presence of the AES electron gun placed very close to the XPS gun. According to the energy of the element deposited on the substrate, the signal can be optimized around that energy window, but the rest of the spectrum results in a much lower intensity. As an example, in Fig. 2.12 a XPS spectrum from a 50 Å Ru film is reported, showing that electrons with energies higher than 500 eV are highly deviated and not reaching the analyzer. The insert shows a XPS spectrum acquired from a Ru single crystal in another experimental apparatus, which is not equipped with an AES gun.
However XPS is very useful for detecting impurities on the surface of the catalysts, such as sulfur, with greater accuracy compared to AES or ISS. In AES the sulfur peak overlaps with one of the Ru lines, for instance, and in ISS the peaks are broad and,

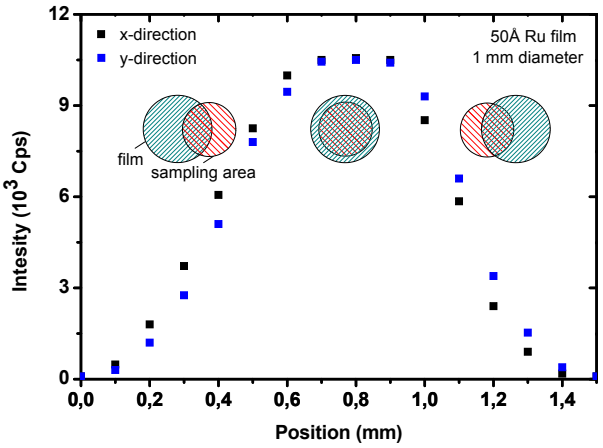


Figure 2.11: XPS signal from a 50 Å Ru film as a function of the sample position, in a x-y plane perpendicular to the HSA. The drawings represent the overlap between the sampling area and the film while moving the sample in one of the two directions.

as mention in the previous section, it is difficult to distinguish between neighbors elements in the periodic table.

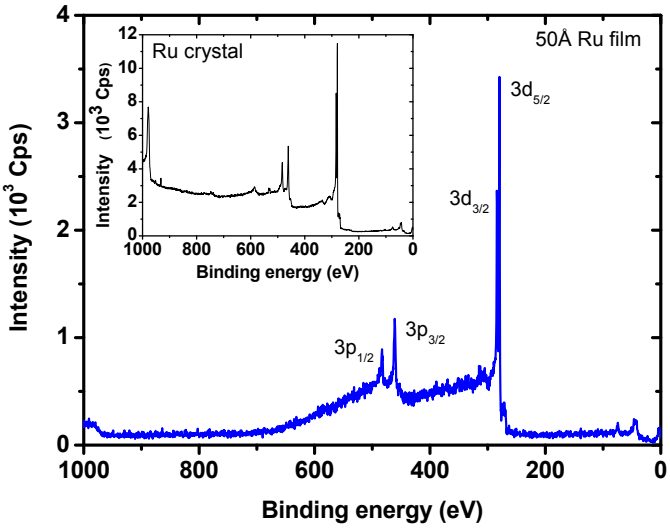


Figure 2.12: XPS spectrum acquired from a 50 Å Ru film at the *Parallel screening* apparatus. The insert shows a XPS spectrum acquired from a Ru single crystal at another experimental apparatus.

### 2.4.4 Surface sensitivity

The most surface sensitive technique among the ones available at the experimental setup is ISS, able to provide information on the outer layer of a catalyst, due to the high neutralization probability of the $He^+$ ions. In order to estimate the surface sensitivity of the AES and XPS techniques, the mean free path of the AES electrons and the photoelectrons in a solid as a function of energy needs to be considered. This is shown in Fig. 2.13 [66]. The kinetic energy of the AES electrons emitted by the metals analyzed in this thesis is quite low (64 eV for Pt and 273 for Ru, for instance), meaning that the sampling depth for this technique is in the range of $0.5 - 0.8$ nm, corresponding to the first layers of the films. The kinetic energy of the photoelectron emitted by the same metals is much higher than the AES electrons (1182 eV for Pt and 974 for Ru, for instance), meaning that the sampling depth for this technique is 1.2 nm or higher. The large sampling depth of XPS, added to the large resolution and to the effect of the magnetic field on the XPS spectra, make this technique the least used to characterize the catalysts during the experiments.

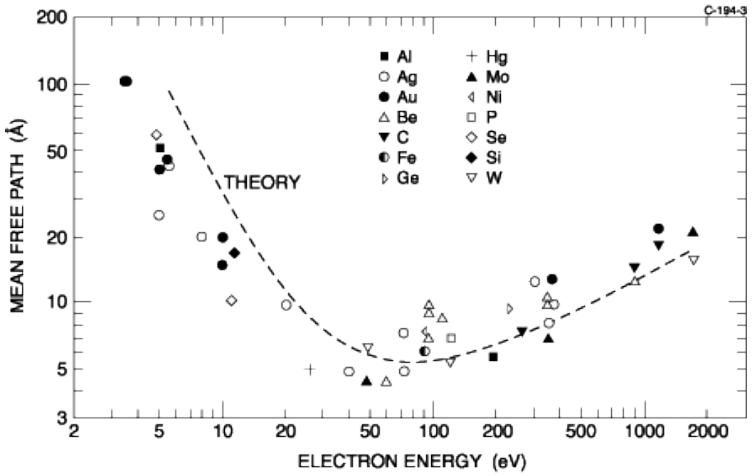


Figure 2.13: The mean free path of the electrons in a solid [66].

## 2.5 The high pressure experiments

### 2.5.1 The high pressure cell and the gas system

The catalytic screening takes place in the HPC, which is equipped with two windows to facilitate the transfer of the sample and the alignment of the sniffer. The windows are designed for vacuum and they are not able to withstand pressures beyond 1 bar. When the sample is standing in the UHV chamber, the HPC can be isolated by a UHV lock. During experiments, the HPC is sealed by pressing a copper gasket

against a stainless steel knife edge on the head of the manipulator arm, which holds the sample. The seal limits the pressure rise in the UHV chamber to approximately $1 \cdot 10^{-9}$ mbar when the sample is exposed to 1 bar of gas in the HPC. The HPC is also equipped with a bellow, allowing the sniffer probe to be moved in three dimensions. Another bellow allows the capillary to be moved up and down inside the sniffer probe. The x, y and z movement of the sniffer probe is controlled by stepper motors, which in turn are controlled from a LabVIEW program. The repeatability of a movement is estimated to be better than 0.01 mm in all directions.
Inside the HPC the sample can be exposed to a pure gas or a mixture of more gases. The mixture is controlled by flow controllers, capable of dosing up to 100 mln/min of a specific gas. The pressure is controlled by a pressure controller placed downstream of the HPC.
An important point when performing experiments at high pressures is the cleanliness of the gasses used. The surface area of the 1 mm diameter metal films is 0.8 $mm^2$ and it is exposed to a flow of 100 mln/min of gas at 1 bar for up to few days. Therefore, any impurities in the gas can adsorbs on the metal films and deactivate them.
Extremely clean Hydrogen (99.999999%) and Deuterium (99.8%) are used for the H-D exchange reaction and they are purified further by passing over a reduced $Cu/ZnO/Al_2O_3$ catalysts (Haldor Topse LK-821/MK-121) kept at room temperature. At room temperature hydrogen does not adsorb on copper whereas impurities such as CO, water and hydrocarbons do, resulting in a purified gas stream. The copper catalysts are reduced in a flow of 20 mln/min hydrogen at 240°C for 4 hours before being used.
Experiments are also carried out with CO added to the $H_2/D_2$ mixture. A mixture of 1000 ppm CO (99%) in hydrogen (99.999%) is used and the gas is passed over active carbon but otherwise not further purified.
A mixture of 5000 pmm $NH_3$ (99.999999%) in He (99.99%) is used for the $NH_3$ decomposition reaction and the gas is not further purified since the low amount of $NH_3$ would otherwise be adsorbed on the used catalysts.

### 2.5.2 The gas sampling device

The sniffer probe is designed to measure the catalytic activity of the supported films individually, while it is moved across the surface of the HOPG. The working principle of the sniffer is illustrated in Fig. 2.14(a). The sniffer consists of two concentric tubes, one inside the other. The outer tube works as gas inlet to the HPC, while the inner tube is a quarts capillary with a leak, sampling gas into a mass spectrometer. At the end of the outer tube a nozzle is screwed, which has a T-shaped cross section profile and is made from pure aluminum (99.999%). The inner diameter of the gas inlet tube is 2 mm, which represent the lateral resolution of the the gas sampling device. According to this, the metal films are deposited in a pattern with a distance of 3 mm between two neighbor positions. The quarts capillary is 1.3 mm diameter and its bottom is melted in order to create a micrometer sized

leak. The size of the leak has been designed so that a pressure of 1 bar in the HPC produces a pressure of approximately $10^{-6}$ mbar inside the mass spectrometer. Computational Fluid Dynamic (CFD) calculations of the sniffer are presented in Fig. 2.14(b) in the case of the H-D exchange reaction, showing the gas velocity, the production of HD and the consumption of $D_2$ beneath the sniffer [19]. The flow used in the calculations is 100 mln/min of 1% $D_2$ in $H_2$, at a pressure of 1 bar. The surface temperature is 100°C, the temperature of the sniffer is 72.5°C, the diameter of the film is 1 mm and the height of the sniffer over the surface is 0.20 mm. This working distance produces a ring of high velocity gas (> 2 m/s), between the gas inlet tube and the substrate. The ring of high velocity gas acts as a diffusion barrier, preventing reaction products produced outside the ring from entering the volume inside the ring. Hence, the composition of the sampled gas originates from the film directly below the sniffer and no contribution from other films are measured. The height of the sniffer above the sample is determined by gently touching the four corners of the sample with the sniffer. The contact is detected by measuring electrical contact between the sample and the sniffer probe, which is grounded through the chamber.

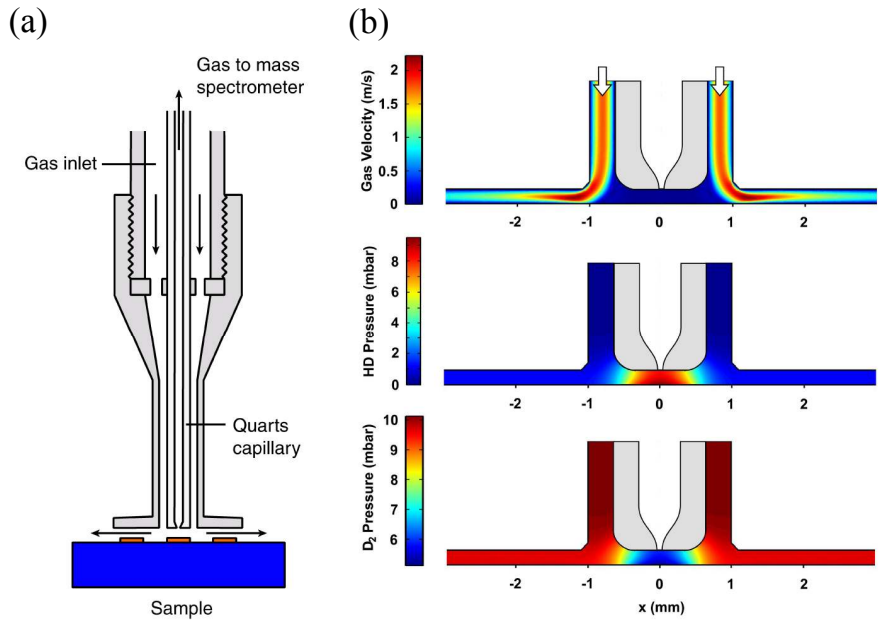


Figure 2.14: (a) The sniffer probe used for screening the catalytic activities of the films, consisting of two concentric tubes. (b) Computational Fluid Dynamic (CFD) calculations showing the production of HD, the consumption of $D_2$ beneath the sniffer and the high gas velocity creating the diffusion barrier [19].

### 2.5.3 Gas analysis

A quadrupole mass spectrometer is used to analyze the gas sampled by the capillary inside the sniffer probe. The principle of the mass detection is based on ionizing a molecule and measure its mass to charge ratio. A molecule can also be double ionized or to break into fragments, therefore a wide range of signals have to be monitored in order to identify the different compounds in a gas mixture.
The progress of the H-D exchange reactions is monitored by measuring the signals of 2 Atomic Mass Unit (AMU) for $H_2$, 3 AMU for HD and 4 AMU for $D_2$. However, hydrogen gives a significant contribution to the signal measured at 3 AMU, which is attributed to the formation of $H_3^+$ [19]. By decreasing the emission current of the mass spectrometer from 1.000 mA to 0.070 mA, which is the lowest setting of the mass spectrometer, the contribution to the 3 AMU signal from hydrogen is reduced to 0.1% of the 2 AMU signal.
When performing the $NH_3$ decomposition reaction, the signals of 17, 16, 15 and 14 are monitored for $NH_3$, while the signals of 2 and 28 AMU are monitored for $H_2$ and $N_2$, respectively. However, the gas used for this reaction is a mixture of 5000 pmm of $NH_3$ in He, the latter giving a signal at 4 AMU and also at 2 AMU. The signal at 2 AMU is believed to generate by $He^{++}$. Since the level of the background signal for 2 AMU is high enough to mask the $H_2$ signal during experiments, only the $N_2$ signal gives a reliable measurement of the products of the reaction. This problem could be solved by using a different gas mixture, as $NH_3$ in Ar for instance, in future experiments.

### 2.5.4 Cleaning the HPC

When exposing the sample to gas in the HPC during experiments at high temperature deactivation of the catalytic metal films is often observed. Characterization of the films after experiments reveals that the metals are generally contaminated by sulfur. Sulfur is present in the air, therefore when venting the HPC or a gas line sulfur contaminants adsorb on the walls of the HPC and of the gas inlet system. The standard procedure to remove the sulfur is baking the entire HPC and the gas inlet system at 150°C for 48 hours in a flow of 100 mln/min $H_2$. At this temperature the sulfur desorbs and reacts with the hydrogen forming hydrogen sulfide, which is carried out of the HPC with the $H_2$ flow. This procedure is enough to remove sulfur before performing the H-D exchange reaction, which is carried out at temperatures up to 200°C.
The $NH_3$ decomposition reaction takes place at temperatures above 450°C. At these temperatures the sniffer probe is significantly heated up during experiments and impurities contained in the gas sampling device are believed to segregate to its surface and desorb. As a consequence, a catalyst deactivates due to the adsorption of these impurities on its surface. Before performing the $NH_3$ decomposition reaction the standard cleaning procedure is followed while the sample is locked in the HPC and the sniffer is placed 0.2 mm above the surface of the sample, which is heated to

550°C. This is the maximum temperature which can be reached, corresponding to the maximum current that the feedthroughs can stand. In addition the nozzle and steel tube of the sniffer probe are heated by a heating band up to 200°C and two focus halogen lamps (power up to 150 W) are placed in front of the two windows of the HPC, focusing on the sniffer probe. The aim is to heat up the gas sampling device to a temperature which is significantly higher than the one reached during experiments, in order to desorb as many impurities as possible before performing the reaction. A schematic of the extended cleaning procedure is shown in Fig. 2.15(a), while an image of the HPC with the lamps on is shown in Fig. 2.15(b). Fig. 2.15(c) is an image taken from the front window of the HPC, showing that the lamps are focusing on the sniffer probe.

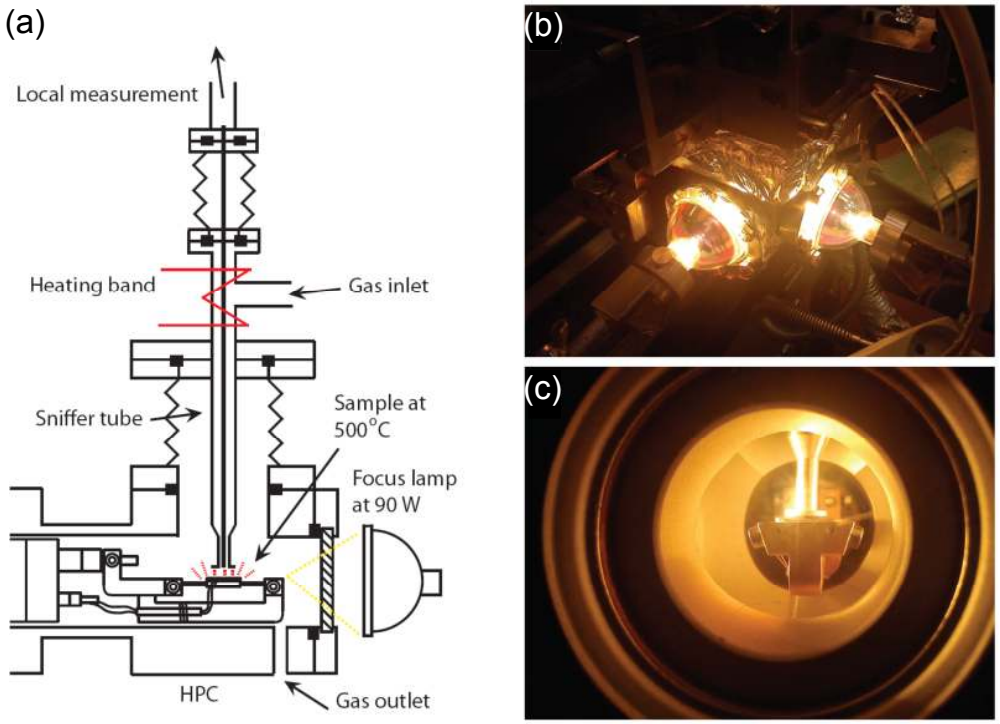


Figure 2.15: Schematic drawing of the sniffer probe during the cleaning procedure. (a). Image of the HPC with a focus lamp placed at each window (b). An image taken from one of the windows (c).

Before the cleaning procedure a 50 Å Ru film is deposited on the HOPG. XPS and ISS spectra acquired on the metal film after the procedure reveal the presence of sulfur, as expected, but also lead, which is also believed to originate from the sniffer tube. A narrow energy window of the XPS spectrum acquired on the contaminated Ru film is shown in Fig. 2.16. After this procedure the sample is sputtered and new

films are deposited. When the $NH_3$ decomposition reaction is performed at temperatures up to 500°C catalyst deactivation is no longer observed. This procedure is repeated each time the HPC is vented.

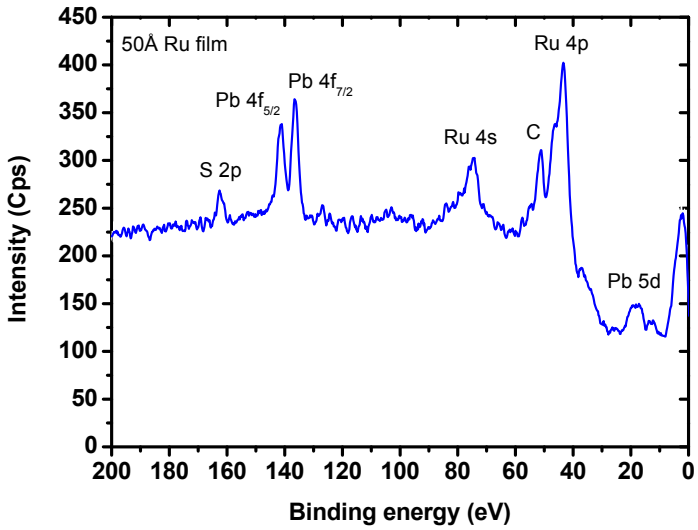


Figure 2.16: XPS signal from a 50 Å Ru film after the cleaning procedure of the HPC, in a narrow energy window.

# 3 The H-D exchange reaction

The dissociation of hydrogen on solid surfaces is an initial step in many important surface reactions [67]. Hydrogen dissociation can be conveniently studied by monitoring the hydrogen-deuterium exchange reaction:

$$H_2 + D_2 \Leftrightarrow 2HD \tag{3.1}$$

As described in the introduction, the interest in this thesis is towards PEM fuel cells, where the dissociation occurs on Pt/C catalyst at the anode of the device. It is universally accepted that the overall Hydrogen Oxidation Reaction (HOR) reaction takes place in two steps, involving three elementary reactions. In the first step, $H_2$ is dissociated and H adsorbed. This is achieved either by the Tafel reaction:

$$2H_2 \rightarrow 2H^* \tag{3.2}$$

or by the Heyrovsky reaction:

$$H_2 \rightarrow H^* + H^+ + e^-. \tag{3.3}$$

The adsorbed H is then discharged, following the Volmer route:

$$H^* \rightarrow H^+ + e^- + ^* \tag{3.4}$$

Despite intensive research efforts it is still under debate which of the two pathways, Tafel-Volmer or Heyrovsky-Volmer, dominates under different conditions even on Pt [68]. The Volmer reaction is generally considered fast [26], therefore the first step is believed to be the rate determining step [69].
The experiments described in this thesis are carried out at 1 bar pressure using a mixture of 1% of $D_2$ in $H_2$, in order to make the adsorbed overlayer resemble a pure H overlayer. Moreover, experiments in the presence of 10 ppm of CO added to the mixture are also permormed, since CO is poison for the anode catalyst of a PEM

fuel cell [7, 8].
The H-D exchange reaction is carried out in a much simpler environment compared to a real PEM fuel cell, since the experiments described in this thesis are performed with no Nafion membrane, water or overpotentials which are present in a working PEM fuel cell. In this simplified system the relation between particle size and hydrogen dissociation of some selected transition metals, such as Pt, Ru and Rh is investigated, in order to see how the particle size affects the reaction rate. Moreover, experiments in the presence of CO are carried out to find out whether the resistance to CO poisoning may be improved by selecting a certain particle diameter.
Experiments are also performed on binary alloys, such as Pt/Ru, which are reported to be very CO-tolerant anode catalysts in low-temperature fuel cells [22–29]. Alloys with a different Pt/Ru ratio are studied in order to find whether an optimal composition exists for the reaction and for which the highest resistance towards CO poisoning is measured.
The origin of the increased CO tolerance and activity for CO electrooxidation of Pt/Ru alloy catalysts as compared to monometallic Pt catalysts is still under debate. Ruthenium improves the CO tolerance of platinum due to two phenomena. The first is the ligand effect, where surface segregation of platinum to the surface of the alloy creates a platinum overlayer on top of a ruthenium rich second layer, weakening the binding energy of CO compared to pure platinum [70, 71]. The second is the bi-functional effect, in which ruthenium promotes oxidation of CO by reducing the overpotential needed for dissociating [72, 73]. In these thesis only the ligand effect is considered, due to the fact that experiments are performed in a simplified system compared to a PEM fuel cell.

## 3.1 A model for the H-D reaction

The kinetics of the H-D exchange reaction is described by a simple model which has been developed for studies of other catalytic systems and is explain in greater detail in [19]. Experiments are performed under equilibrium conditions and in the model it is assumed that the equilibrium dissociative sticking probability, $S$, is the same for $H_2$, HD or $D_2$. It is also assumed that $S$ does not depend on the relative amount of H to D on the surface, but only on the total coverage. Since the experiments are made with only 1% $D_2$, the total coverage is assumed to equal that corresponding to 1 bar of pure $H_2$, which is close to one under the conditions of the experiments [19, 20, 74–79]. In order to extract $S$ from the partial pressures of HD and $D_2$ measured over the surfaces of the metals, the gas composition as a function of $S$, is obtained from numerical calculations of the local gas velocity, temperature, and partial pressures inside the gas sampling device. The results from these calculations are presented in Fig. 3.1, where the partial pressure of $H_2$, HD and $D_2$ are plotted as function of $S$.
In the low conversion region, the calculated partial pressure of HD, $p_{HD}$, is proportional to the desorption rate of HD, which is proportional to $S$, as shown in Fig. 3.1.

At higher conversion, $p_{HD}$ gets limited by equilibrium of the H-D exchange reaction and $S$ is more accurately determined from the depletion in the minority reactant $D_2$. The partial pressure of $D_2$, $p_{D_2}$, is used to calculate $S$, if the lowering in relative to the $D_2$ pressure over the HOPG surface (the partial pressure in the gas fed to the HPC) is more than 8%, otherwise $p_{HD}$ is used to determine $S$. In the latter case, the calibration factor for the HD signal is obtained from a measurement where $p_{D_2}$ is also used to obtain $S$. The lower detection limit for the HD pressure is determined by the sensitivity limit of the mass spectrometer, which is only 0.1 mbar in this case, due to the background of $H_3^+$ formed in the ion source, as mentioned in section 2.5.3. From Fig. 3.1 it can be seen that 0.1 mbar HD corresponds to $S = 5 \cdot 10^{-6}$, while the maximum value which can be measured reliably is $S = 3 \cdot 10^{-2}$. The signals for $H_2$ and $D_2$ are calibrated using the signals measured over the HOPG, where the gas composition is the same as in the gas fed to the HPC. The relative uncertainty in the measured $p_{H_2}$ and $p_{D_2}$ is approximately 1%. The dominating source of error, when determining the calibration factor for HD, is the uncertainty in the position of the capillary and the nozzle relative to the sample surface. This gives an uncertainty in the absolute value for $p_{HD}$ of $\pm 10\%$ [19].

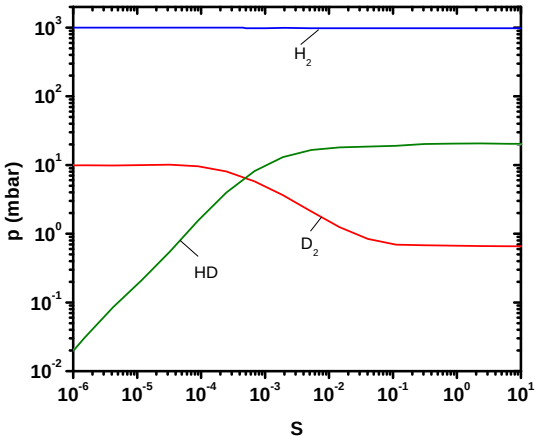


Figure 3.1: The calculated partial pressures of $H_2$, HD and $D_2$ at the capillary leak as a function of the sticking probability, $S$, at 200°C [19].

Once the sticking probability is known, the rate constant for $H_2$ desorption, $k_{des}$, can be obtained from $S$ since at equilibrium the adsorption rate, $r_{ads}$, is equal to de desorption rate, $r_{des}$:

$$r_{ads} = r_{des} \Leftrightarrow FS = k_{des}\theta_H^2 \approx k_{des} \tag{3.5}$$

where $F$ is the molecular flux of hydrogen and $\theta_H$ is the equilibrium coverage of hydrogen, which is assumed to be very close to one. The apparent energy for desorption is then obtained from the desorption rate as a function of temperature.

## 3.2 Results from Pt, Ru and Rh nanoparticles*

### 3.2.1 Particle preparation and characterization

Pt, Ru and Rh films of 1 mm diameter are deposited on a sputtered HOPG substrate. The films have an average metal thickness from 0.2 to 30 Å, as illustrate in the schematic drawing shown in Fig. 3.2. An area of the HOPG is left free from metal for background measurements.

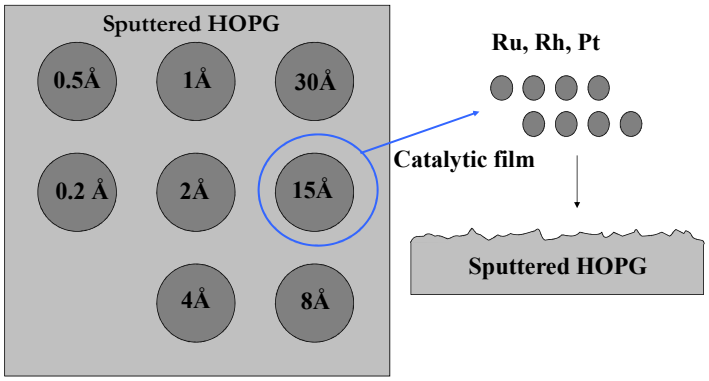


Figure 3.2: A schematic drawing of the sample after deposition: the circular metal films (dark gray) are the films of Ru, Rh and Pt deposited on the sputtered HOPG substrate (light gray). The average thickness is indicated on each film.

In order to obtain information on the structure of the films, the sample is transferred in air to an apparatus equipped with a Scanning Tunneling Microscope (STM). STM is performed at room temperature in constant current mode, using a W tip. Further details on the techniques used and on the programs used for image analysis can be found in [61]. STM images acquired on Pt and Ru films are shown in Fig. 3.3. Rather than forming a continuous film, each metal film consists of nanoparticles decorating the rough structure of the HOPG surface, even at a deposition thickness of 30 Å. Fig. 3.3(a) and (b) show STM images acquired on 2 Å and 8 Å Pt films, respectively, whereas (c) and (d) show images acquired on 2 Å and 8 Å Ru films. The particles appear round in the STM and indicate insignificant sintering below 200°C. This is in agreement with previous results on the morphology of Ru nanoparticles deposited on HOPG, obtained with STM and TEM techniques, where it was found that Ru nanoparticles with diameter below 6 nm are round and they start to exhibit hexagonal symmetry only above this diameter [61, 80].
By size distribution analysis of the STM images it is possible to establish a relationship between the particle diameter and the film thickness. The results for Pt and Ru nanoparticles are reported in Fig. 3.4.

*The content of this section is taken from Ref. [1].

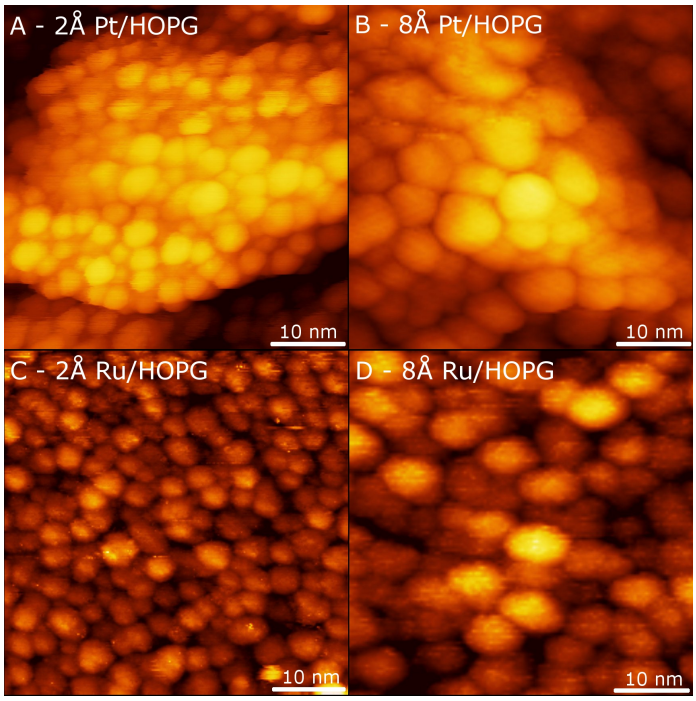


Figure 3.3: STM images of Pt nanoparticles corresponding to 2 Å (a) and 8 Å Pt films (b). STM images of Ru nanoparticles corresponding to 2 Å (c) and 8 Å Ru films (d).

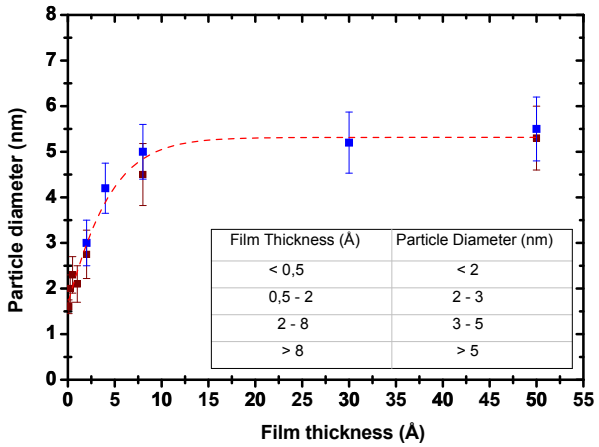


Figure 3.4: The particle diameter as a function of the film thickness for Pt and Ru. The dots are the average values for the diameter of Pt (blue dots) and Ru nanoparticles (brown dots). The error bar is the standard deviation. The table shows the relation between the film thickness and nanoparticle size.

Each point represents the average diameter of the nanoparticles corresponding to a certain film thickness. The error bar is the standard deviation and the red curve is a sigmoidal fit to the data and is supplied as a guide to the eye. It is found that the Ru and the Pt films of the same thickness are made of nanoparticles with similar sizes and that the particle diameter varies between 2 and 5 nm. Therefore this is the range of particle diameter investigated in these experiments. It could be surprising that for a 30 Å film 5 nm diameter particles are formed. However the films are not flat and continuous and particles taller than the nominal film thickness can form.
The particle size is determined by two main factors. The first is the thickness of the deposited film, i.e. the density of particles, and the second is the presence of the substrate defect sites, which are created by $Ar^+$ sputtering and are randomly distributed on the HOPG, preventing particle diffusion and aggregation. This is shown in studies on size-selected clusters deposited on graphite [60, 61].
The Rh metal films have not been characterized by STM, but based on what determines the particle size, it is reasonable to assume that the diameter of the Rh nanoparticles falls in the same range as for Ru and Pt, within the error bar.

### 3.2.2 Metal surface area

The active surface area of the catalytic films formed by EBPVD depends on the film thickness. The relative surface area, $A_r$, for the metal film $i$, is equal to the ratio between the active surface area and the total planar surface area, which is the same for all the films, since they are they are deposited in a circular area of 1 mm diameter. $A_r$ can be calculated as:

$$A_r = N_i \cdot A_n = \frac{t_i}{V_n} A_n \tag{3.6}$$

where $N_i$ is the number of particles per area in the film $i$, equal to the ratio between the thickness of the metal film, $t_i$, and the average volume $V_n$ of the nanoparticles in the film. $A_n$ is the surface area of the nanoparticles. Assuming semi spherical nanoparticles of radius $r_i$, which is estimated by STM analysis (see Fig. 3.4), both $V_n$ and $A_n$ can be calculated from $r_i$, which results in the relative surface area, $A_r$, as a function of film thickness plotted in Fig. 3.5.
In this model the relative area of the thickest film is overestimated, since more than one monolayer of nanoparticles are formed. By looking at the STM images in Fig. 3.3, it is not trivial to find a good way to describe the arrangement of the particles on the substrate, which is needed in order to get a reasonable value for the relative area of the thickest film. However, assuming that the nanoparticles have a simple honeycomb-like arrangement, the roughness factor of the thickest film can be estimated to be around 2, represented by the black dots in Fig. 3.5.
Other kind of measurements, such as Temperature Programmed Desorption (TPD) measurements, would give more reliable indications of the active surface area. Unfortunately at the moment the mass spectrometer mounted in the UHV chamber,

is not sensitive enough for these kind of measurements. However, there is already a plan to improve this, by mounting a long copper tip with an overture of 1 mm on the mass spectrometer in order to be able to measure a signal from a single film.

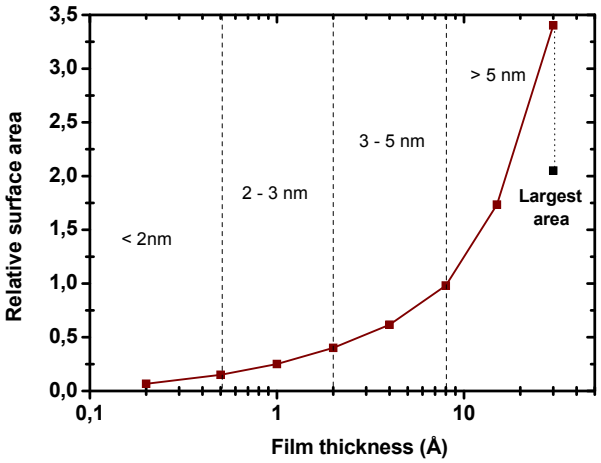


Figure 3.5: The relative surface area of the metal films as a function of film thickness. The black dot represents an estimate of the largest area obtainable when more than one layer of close packed nanoparticles are formed, which holds for the thickest film. The diameter in nm of the nanoparticles is also indicated in the figure.

### 3.2.3 Measured gas composition

Fig. 3.6 shows the measured partial pressure of HD, $p_{HD}$, for the Ru, Rh and Pt films in the temperature range $40 - 200$°C, as a function of the film thickness. The nanoparticle size derived by STM analysis is indicated in each plot. The measurements are carried out for decreasing temperatures with start at 200°C and the first measurement is repeated at the end of the series. Fig. 3.6(a-c) show $p_{HD}$ in the pure $H_2/D_2$ mixture and it is found that Ru and Rh nanoparticles are very active for the H-D exchange reaction. $p_{HD}$ is weakly dependent on temperature for those two metals and increases with film thickness. Pt nanoparticles show lower activity and a strong temperature dependence. These results are in agreement with a former investigation on 50 Å thick transition metal films [20]. It was found that Ru is the most active metal for the H-D exchange reaction, immediately followed by Rh, whereas Pt is less active, roughly half of the activity for Ru and Rh at 200°C.
The addition of 10 ppm CO inhibits the reaction significantly, also at 200°C, as shown in Fig. 3.6(d) and (e). Moreover the temperature dependence of $p_{HD}$ becomes stronger in the presence of CO. For Pt films with thickness up to 30 Å, $p_{HD}$ in the presence of CO is below the detection limit. The H-D exchange reaction on 50 Å Pt films in the presence of 10 ppm CO was previously investigated and it was shown that Pt is very sensitive to CO and that $p_{HD}$ for 50 Å Pt films decreases roughly of a factor of 20 at 200°C relative to the value in pure $H_2/D_2$ mixture [21].

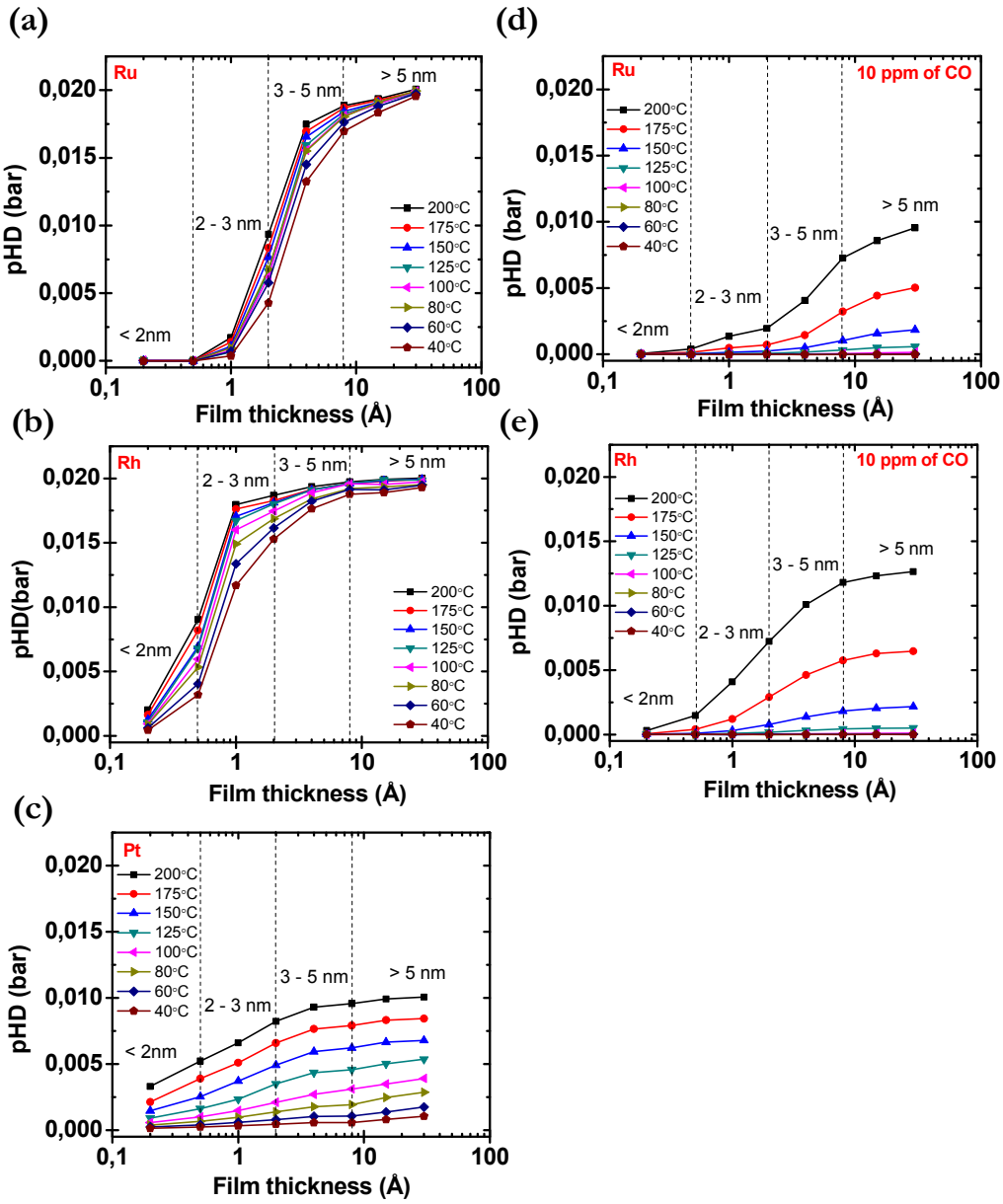


Figure 3.6: Measured values for $p_{HD}$ of Ru, Rh and Pt nanoparticles in the temperature range $40 - 200$°C as a function of the film thickness. The diameter in nm of the nanoparticles is also indicated in the figure. Panels (a-c) show $p_{HD}$ obtained in experiments in pure $H_2/D_2$ mixture, whereas (d) and (e) show $p_{HD}$ when 10 ppm CO is added to the gas mixture.

### 3.2.4 The sticking probability

The equilibrium dissociative sticking probability for $H_2$, $S$, on the surface of the different metals is determined from the results in Fig. 3.6 using the correlation in Fig. 3.1 and dividing by the relative surface area shown in Fig. 3.5. The results are shown in Fig. 3.7(a-c).

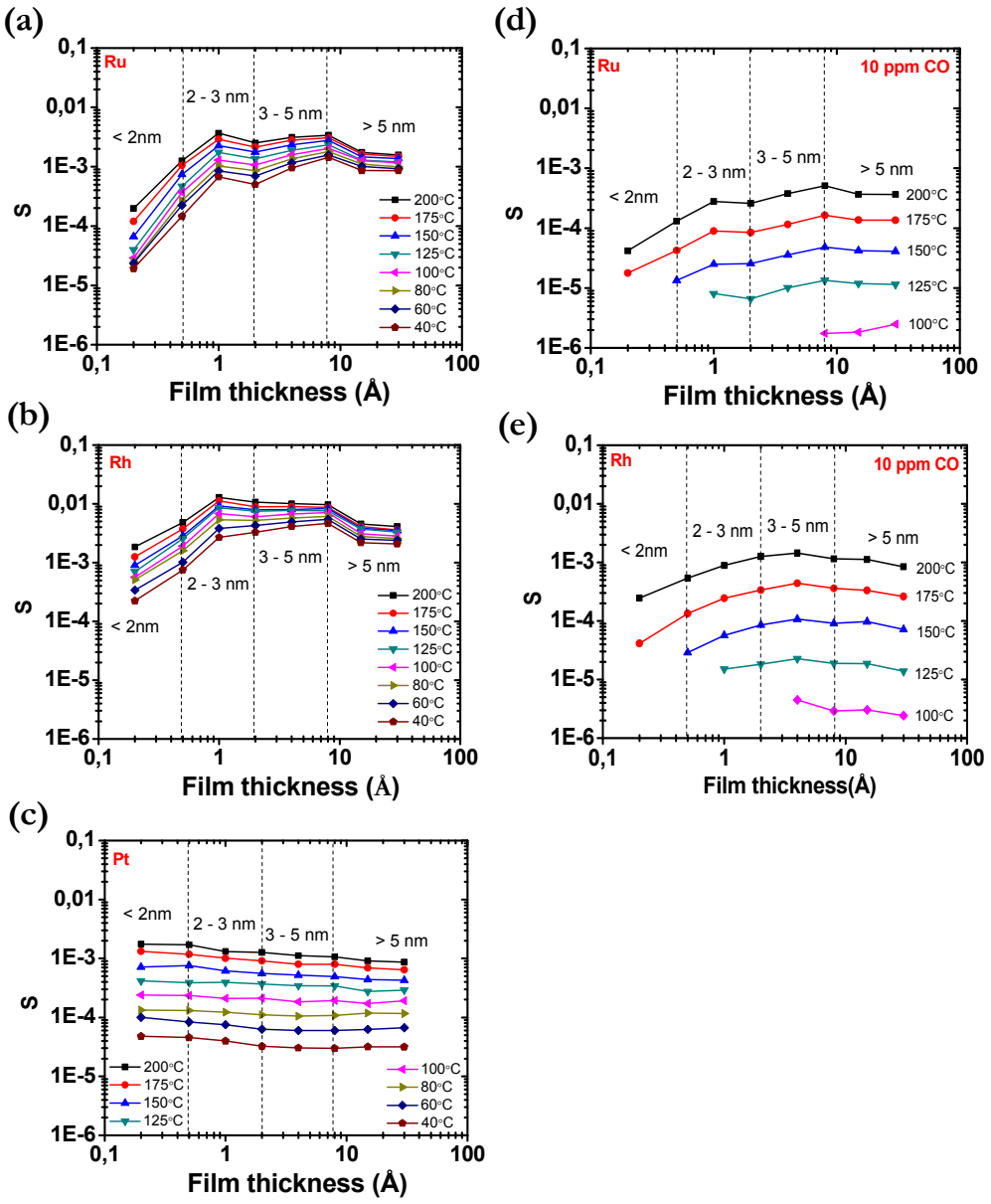


Figure 3.7: $S$ for hydrogen at 1 bar for Ru, Rh and Pt nanoparticles in the range 40 – 200°C as a function of the film thickness. The diameter in nm of the nanoparticles is also indicated. (a-c) show $S$ in pure $H_2/D_2$ mixture. (d) and (e) show $S$ when 10 ppm CO is added to the gas mixture.

The oscillatory behavior of some of the results is an artefact that mainly stems from the uncertainty in determining the relative surface area of the nanoparticle films. It is therefore only the overall trends of the results that is considered here. It is found that $S$ in the pure $H_2/D_2$ mixture for Ru and Rh is weakly dependent on temperature and decrease for nanoparticle diameters below 3 nm. For the Pt nanoparticles $S$ does not change significantly with the nanoparticle diameter and shows lower values compared to Ru and Rh nanoparticles. Moreover, $S$ for the Pt nanoparticles shows a strong temperature dependence and increases significantly with increasing temperature.
In the presence of 10 ppm CO, $S$ can only be determined above 100°C in the case of Ru and Rh nanoparticles, as shown in Fig. 3.7(d) and (e). Moreover, $S$ does not change significantly with nanoparticle diameter for Ru and Rh in the presence of CO. For Pt films with thickness up to 30 Å, $S$ in the presence of CO cannot be determined because the HD signal is below the detection limit. A previous investigation showed that $S$ in the presence of CO can only be measured above 200°C for a 50 Å Pt film, giving a value which is roughly a factor of 30 lower compared to the value obtained in the pure $H_2/D_2$ mixture [21]. The high sensitivity to CO has been explained by the fact that the difference in binding energy for hydrogen and CO is particularly large for Pt [21].

### 3.2.5 Desorption energies for $H_2$

As described in Eq. 3.5, the $H_2$ desorption rate constant, $k_{des}$, can be determined from $S$ under the assumptions of hydrogen coverage close to one. The apparent desorption energy for $H_2$ at the equilibrium coverage, $E_{app}$, can therefore be obtained from the data in Fig. 3.7. Arrhenius plots of the desorption rate, $r_{H_2}$, for Ru, Rh and Pt nanoparticles, calculated from Eq. 3.5 are shown in Fig. 3.8(a), (b) and (c). Generally the data show a linear behavior in the plots, even though small deviations are observed for nanoparticles smaller than 2 nm in diameter, due to a low signal. $E_{app}$ for Ru, Rh and Pt nanoparticles as a function of the film thickness is shown in Fig. 3.9. $E_{app}$ show a dramatic decrease with the nanoparticle diameter in the case of Ru and Rh nanoparticles: for 5 nm particles $E_{app}$ is roughly $3-4$ times lower than for 2 nm particles. A different result is obtained in the case of the Pt nanoparticles, for which $E_{app}$ is found to decrease slightly with particle diameter. Moreover the values measured for the Pt nanoparticles are higher compared to those for Ru and Rh.

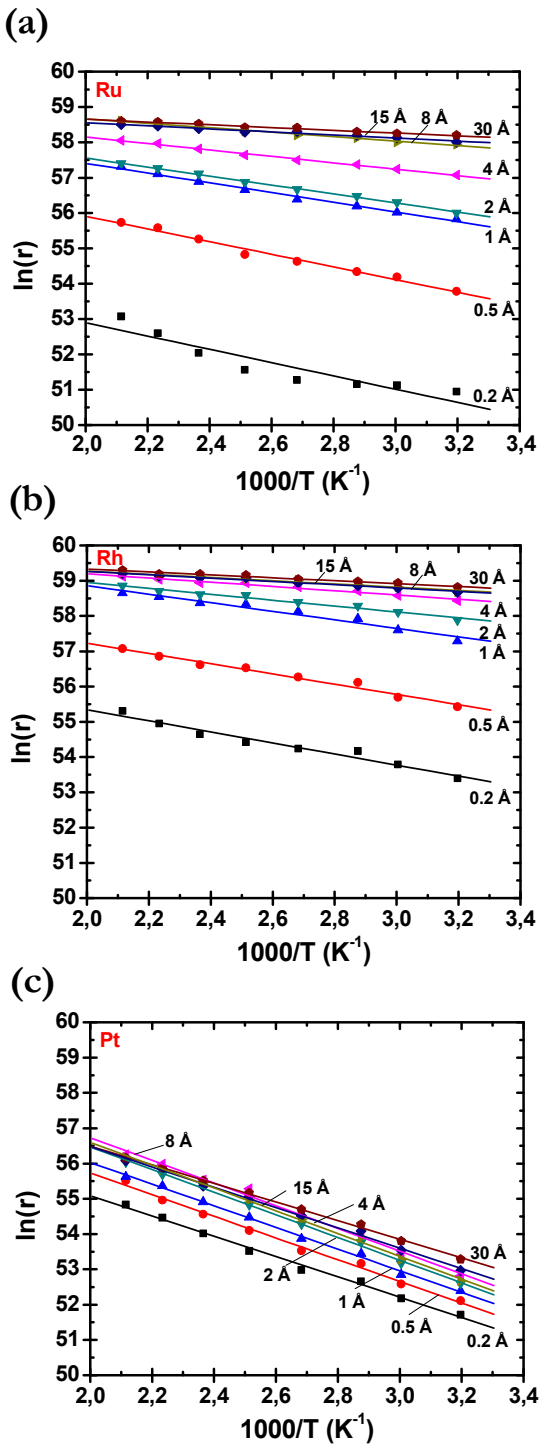


Figure 3.8: Arrhenius plots of the equilibrium hydrogen desorption rate on for Ru (a), Rh (b) and Pt (c) nanoparticles.

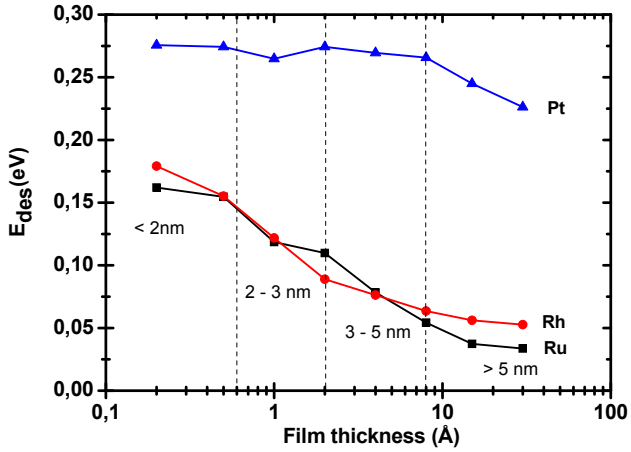


Figure 3.9: The apparent desorption energy for Ru, Rh and Pt nanoparticles as a function of the film thickness. The diameter in nm of the nanoparticles is also indicated in the figure.

### 3.2.6 Discussion

For all the metals, there is an increase in $p_{HD}$, and thus in the rate of the H-D exchange as a function of the film thickness, as shown in Fig. 3.6. The increase in the rate is due to a combination of two effects: an increase of the active surface area, as shown in Fig. 3.5, and a change in reactivity with nanoparticle diameter, which is significant for Ru and Rh. This is evident when the sticking probability per metal area, $S$, is calculated from the measured $p_{HD}$, as shown in Fig. 3.7. Thus $S$ obtained in the experiments with the pure $H_2/D_2$ mixture decreases for nanoparticle diameters below 3 nm for Ru and Rh. The temperature dependence of the rate varies strongly with particle diameter, which manifests itself as an apparent desorption energy at equilibrium, $E_{app}$, which decreases nearly to zero over the range of particle diameters studied, as shown in Fig. 3.9.
For all the nanoparticle diameters investigated, Ru and Rh show higher $H_2$ equilibrium exchange rates than Pt at 1 bar pressure. This is similar to the observations made for 50 Å metal films, where it was found that Ru and Rh give much higher values for $S$ than Pt, despite the fact that the heat of adsorption for H on Ru and Rh is much higher than for Pt at low coverage [20]. So far, the unexpectedly high activity of these two metals has been attributed to the presence of special adsorption states with low heat of adsorption that are populated at the high hydrogen coverage at equilibrium [20]. One possibility is that such adsorption states are located at steps, defects, corners or edges on the nanoparticle surfaces. The ratio of the undercoordinated sites to terrace sites on equilibrium shaped nanoparticles increases as the nanoparticles get smaller and, for some reactions, these sites give reaction rates which are orders of magnitude higher than on terraces [81, 82]. In such cases, the

reaction rate is expected to increase with decreasing particle size, which, however, is the opposite effect of what is observed here.
The formation of a compressed hydrogen adlayer, where the heat of adsorption is lowered with coverage as a consequence of H-H repulsion, could be the reason for the strong change in the exchange rate and in the apparent desorption energy with particle diameter for Ru and Rh, due to quantization of the hydrogen binding energy. The principle of a compressed adlayer is illustrated in the following simplified model, where it is assumed that the heat of adsorption on a single facet of a nanoparticle, $\Delta H_{ads}$, can be expressed as:

$$\Delta H_{ads} = \Delta H_{ads,0} + \theta_H \xi = \Delta H_{ads,0} + \frac{n}{N_s}\xi \tag{3.7}$$

where $\theta_H$ is the coverage of hydrogen, $n$ is the number of hydrogen atoms adsorbed on the surface and $N_s$ the number of available sites on the facet. $\Delta H_{ads,0}$ is the low coverage limit of $\Delta H_{ads}$ and must be a negative number if any adsorption should occur. For simplicity it is assumed a linear coverage dependence which is naturally not valid at low coverage, where there will be little or no repulsion, but that is not the case in our experiments, since the hydrogen coverage is close to one. The Gibbs free energy of adsorption, $\Delta G_{ads}$, is given by

$$\Delta G_{ads} = \Delta H_{ads} - T\Delta S_{ads} \tag{3.8}$$

where $\Delta S_{ads}$ is the change in entropy by adsorption. The equilibrium is characterized by $\Delta G_{ads} = 0$ and since $\Delta S_{ads}$ is always negative due to the loss of entropy when going from the gas phase to the more localized adsorption, $\Delta H_{ads}$ will have to be negative at equilibrium. The change in $\Delta H_{ads}$ when one adsorbed atom is added into the facet is $\xi/N_s$. This number will be small for large $N_s$ and appear continuous, however, for small values of $\Delta H_{ads}$, i.e. small terraces, there will be a gap in $\Delta H_{ads}$ of at most $\xi/N_s$ when $\Delta G_{ads} = 0$, as illustrated in Fig. 3.10. For instance, adding a hydrogen atom to a terrace with 25 sites for which $\xi = 100$ kJ/mole will give a gap of 4 kJ/mole. In this simple illustration it is neglected that the adsorption sites close to edges and corners may have a different heat of adsorption than the sites on the terraces and that the heat of adsorption may change with particle size.
In the following it is shown how this may result in an apparent desorption energy close to zero, as measured in Fig. 3.9. Normally the desorption energy is associated with the numerical value of the adsorption enthalpy i.e. $E_{des} = -\Delta H_{ads}$ when there is no barrier for adsorption, which is the quantity measured in a temperature programmed desorption (TPD) experiment. But TPD is not an equilibrium measurement as the exchange experiments described in this thesis. At equilibrium $-\Delta H_{ads}$ has to be significant and equal to $T\Delta S_{ads}$. The net rate of adsorption at equilibrium is:

$$r = 0 = r_{ads} - r_{des}. \tag{3.9}$$

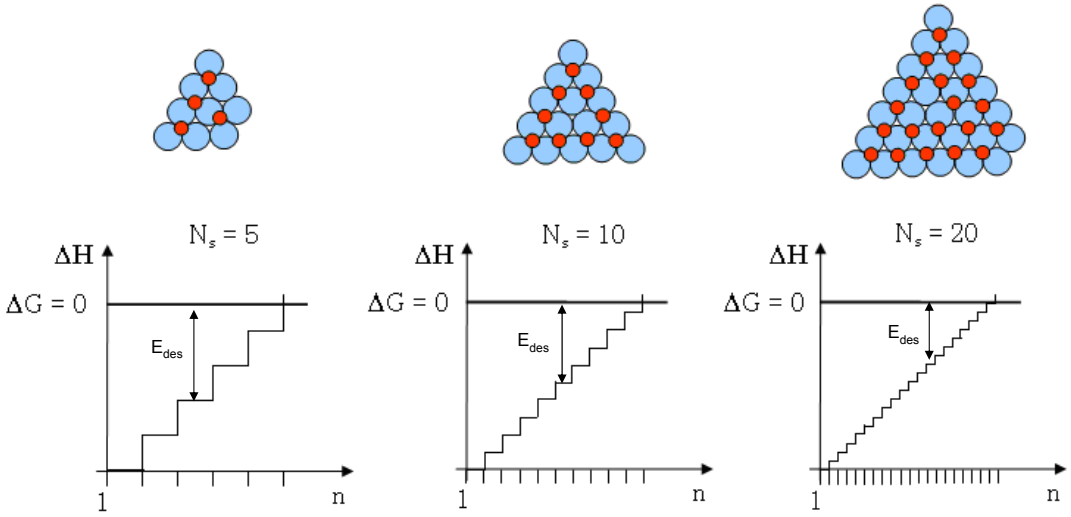


Figure 3.10: The principles of a quantized adsorption energy in a compressed adlayer. The upper panels show a schematic picture of a facet at maximum coverage. The lower panels show schematic energy diagrams for adsorbed H as a function of the number of adsorbed H, $n$, for various number of available sites, $N_s$. The hydrogen bond to the surface must be strong enough to keep below the $\Delta G_{ads} = 0$ line. The diagrams show how at maximum coverage small facets will lead to an increasingly larger apparent desorption energy the smaller the facet gets.

In the mean field approximation the desorption rate is described as:

$$r_{des}(\theta_H) = A(\theta_H, T) e^{-\frac{E_{des}(\theta_H)}{RT}} \theta_H \theta_D \tag{3.10}$$

and this is the rate measured in the exchange experiments. In the following analysis it is assumed for simplicity that the hydrogen and deuterium behave in the same way, that the total coverage is close to one and the ratio is given by the gas composition, i.e. the coverages show little or no temperature dependence for the interval studied here. The definition of the apparent activation energy, $E_{des}^{app}$, for a desorption reaction with desorption rate, $r_{des}$, is given by:

$$E_{des}^{app} \equiv RT^2 \frac{dln(r_{des})}{dT}. \tag{3.11}$$

If it is assumed that the pre-exponential factor is only very weakly dependent on temperature and coverage, i.e. $A(\theta_H, T) \approx A$, the apparent desorption energy, $E_{des}^{app}$, from a compressed hydrogen adlayer is given by:

$$E_{des}^{app}(\theta_H) = RT^2 \frac{dln(r_{des}(\theta_H))}{dT} = RT^2 \frac{d(-\frac{E_{des}(\theta_H)}{RT})}{dT}$$
$$= -T\frac{dE_{des}(\theta_H)}{dT} + E_{des}(\theta_H). \quad (3.12)$$

In the case of exchange reaction at the equilibrium conditions, the hydrogen coverage will be the one for which the free energy of adsorbed hydrogen, $G_{H_{ads}}(\theta_H^{eq})$, is equal to the free energy of gas phase hydrogen, $G_{H_2}(g)$:

$$G_{H_{ads}}(\theta_H^{eq}) - G_{H_2}(g) = (H_{H_{ads}} - TS_{H_{ads}}) - (H_{H_2(g)} - TS_{H_2(g)})$$
$$= \Delta H_{H_{ads}}(\theta_H^{eq}) - T\Delta S_{H_{ads}} = \Delta G_{ads}(\theta_H^{eq}) = 0. \quad (3.13)$$

Since $E_{des}$ is equal to $-\Delta H_{H_{ads}}$ when there is no barrier for adsorption it follows:

$$0 = \Delta G_{ads}(\theta_H^{eq}) = \Delta H_{H_{ads}}(\theta_H^{eq}) - T\Delta S_{H_{ads}} = -E_{des}(\theta_H^{eq}) - T\Delta S_{H_{ads}}. \quad (3.14)$$

So if the adsorption energy can be tuned continuously, due to compression of the hydrogen adlayer, the last two terms in Eq. 3.14 will be exactly equal. Hence if it is assumed that the entropy only changes slowly with temperature it follows that:

$$E_{des}(\theta_H^{eq}) = -T\Delta S_{H_{ads}} \rightarrow \frac{dE_{des}(\theta_H^{eq})}{dT} = -\Delta S_{H_{ads}} - T\frac{\Delta S_{H_{ads}}}{dT} \cong -\Delta S_{H_{ads}}. \quad (3.15)$$

The apparent desorption energy can therefore by written as:

$$E_{des}^{app}(\theta_H^{eq}) = -T\frac{dE_{des}(\theta_H^{eq})}{dt} + E_{des}(\theta_H^{eq}) = T\Delta S_{H_{ads}} + E_{des}(\theta_H^{eq}) \quad (3.16)$$

according to the equilibrium conditions in Eq. 3.14 and 3.15.
However if $E_{des}(\theta_H^{eq}) = -\Delta H_{ads}$ is a step function as illustrated in Fig. 3.10, it may not be able to match the continuous function $TS_{H_2}$ but be slightly larger, resulting in an apparent desorption energy. This will naturally be most evident when the steps in $\Delta H_{H_{ads}}$ are large, i.e. for small terraces. For the largest Ru and Rh nanoparticles the majority of the terraces are large enough to allow free tuning of the adsorption energy by compression of the adlayer, so that $E_{des}(\theta_H^{eq}) = TS_{H_2}$. For the smallest nanoparticles this is not possible for most of the terraces, which means that the apparent desorption energy will be higher than zero.
The catalysts produced in the experiments contain a range of nanoparticle sizes with different facets and $E_{app}$ is a measure of an ensemble average. If there is no barrier for adsorption for Ru and Rh, this explains why $E_{app}$ increases as the particles (and thus the terraces) become smaller. The formation of a compressed adlayer would also explain why the measured $E_{app}$ is so much lower than the heat of adsorption

for H on clean Ru and Rh, which is about 100 kJ/mole $H_2$ [20].
The argument of a compressed adlayer formation on large terraces has been used previously in TPD experiments of isotopic exchange of CO on Pt and Ru single crystals and nanoparticles as the explanation for a faster exchange rate observed on the single crystal surface compared to the surface of the nanoparticles, due to size effects [83, 84].
In the case of Pt, a much slower exchange rate as a function of nanoparticle diameter and a larger but nearly constant apparent activation energy for desorption with respect to Ru and Rh are measured, as shown in Fig. 3.6(c) and 3.9. The small variation in rate with particle diameter indicates that the surface structure for Pt is not very important for $H_2$ dissociation and desorption, or possibly that the local surface structure and defect density in these experiments is similar for all particle diameters. The high values measured for the apparent desorption energy could find an explanation in the hydrogen adsorption being slightly activated on the terraces of Pt nanoparticles in the range of size investigated, while not activated on undercoordinated sites. This is consistent with the observed increase in the hydrogen splitting rate with increasing temperature, as shown in Fig. 3.6(c). Adsorption of $H_2$ is activated on Cu [85] and Ni [86–89] and there are also indications of activation energies on the terraces of Pt single crystals and Pt alloys [90–92]. Moreover, if steps and defects are relevant sites in the $H_2$ dissociation on Pt nanoparticles, the HD exchange rate on small particles may be enhanced by the presence of these sites, which will annihilate the compressed adlayer effect observed for Ru and Rh nanoparticles. The existence of a barrier on the terraces of Pt nanoparticles would also be one of the reasons for the high sensitivity of Pt towards CO poisoning, beside the large difference in binding energy between hydrogen and CO on Pt [21], since it binds to step sites more strongly than to terraces [93]. The value for $E_{app}$ for the largest Pt particle diameters agrees well with the value of 0.21 eV reported for 50 Å thick deposited films on graphite. This value was found to be in good agreement with values for the heat of adsorption measured at high coverage on Pt(111) under vacuum conditions [19].
When 10 ppm of CO is added to the $H_2/D_2$ mixture, $p_{HD}$ drops for all the metals, as shown in Fig. 3.6(d) and (e), indicating a lower HD exchange rate. As a consequence, $S$ is inhibited significantly for all the metals, even at 200°C, as shown in Fig. 3.7(d) and (e). Even if there is a slight decrease in $S$ for particle diameters below 3 nm in those cases where $S$ is measurable, there is no evidence of special nanoparticle diameters that are more resistent to CO poisoning than others.

### 3.2.7 Summary and conclusions for this part

The equilibrium hydrogen exchange rate between adsorbed and gas phase hydrogen is investigated as a function of the nanoparticle diameter for Pt, Ru and Rh supported on a sputtered HOPG substrate by measuring the rate of the H-D exchange reaction at a hydrogen pressure of 1 bar, in the temperature range $40 - 200$°C. It is found that Ru and Rh nanoparticles show higher ability than Pt in dissociating $H_2$

at 1 bar. The partial pressure of HD increases with the nanoparticle diameter for all the metals, as a consequence of a combination of a change in active surface area and in reactivity. In the case of Ru and Rh nanoparticles the equilibrium sticking probability per surface area, $S$, decreases for nanoparticle diameter below 3 nm, indicating that the $H_2$ dissociation is size sensitive at very small diameters and that it is faster on larger surfaces. The apparent energy of desorption, $E_{app}$, shows an increase for nanoparticle diameters below 5 nm. This is explained by the formation of a compressed hydrogen adlayer on Ru and Rh nanoparticles, where the heat of adsorption is lowered with coverage as a consequence of H-H repulsion. For Pt nanoparticles $S$ does not change significantly with the nanoparticle diameter, indicating that the $H_2$ dissociation is not size sensitive. The higher values of $E_{app}$ for Pt with respect to Ru and Rh are attributed to a possible activation energy for hydrogen dissociation on the terraces of the Pt nanoparticles at high coverage, which is consistent with the observed increase in the hydrogen splitting rate with increasing temperature.
Experiments are also carried out in the presence of 10 ppm CO. Pt is found to be very sensitive to CO poisoning and the hydrogen splitting rate in the presence of CO on Pt nanoparticles are below detection limit. In the case of Ru and Rh nanoparticles, CO decreases the splitting rate significantly, also at 200°C. There is no evidence for Ru and Rh of special nanoparticle diameters that improve the resistance to CO poisoning.

## 3.3 Results from Pt/Ru alloys*

### 3.3.1 Particle preparation

Three Pt/Ru systems are prepared by EBPVD and deposited on a sputtered HOPG substrate, consisting of Pt overlayers on Ru films, Ru overlayers on Pt films and Pt/Ru bulk alloys, with different Pt/Ru ratio. The Pt/Ru bulk alloys are prepared by co-evaporation of Pt and Ru with different deposition rates, in order to have eight films of a total thickness of 50 Å, but with a different Pt-Ru bulk composition, as illustrated in Fig. 3.11(a). The Pt overlayers on Ru films are prepared by depositing first eight 50 Å thick Ru films and then on top of each film an amount of Pt which varies between 1 and 30 Å, as illustrated in Fig. 3.11(b). In a similar way, the Ru overlayers on Pt films are prepared. For the overlayers the total thickness of each film therefore varies between 50 and 80 Å. For the three Pt/Ru systems, two of the eight films always consist of 50 Å of pure Ru and pure Pt, respectively, and an area of the HOPG far from any metal is used as background during measurements. According to the STM analysis described in section 3.2.1, it is expected that the films consist of nanoparticles with a diameter of around 5 nm.

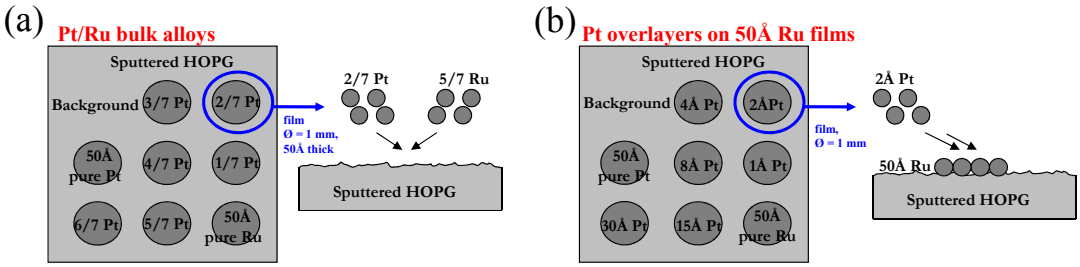


Figure 3.11: A schematic drawing of the Pt/Ru bulk alloys (a) and of the Pt overlayers on Ru films (b) after deposition: the circular metal films (dark gray) are deposited on the sputtered HOPG substrate (light gray). The film composition is indicated on each film.

### 3.3.2 Measured gas composition and sticking probability

Fig. 3.12(a), (b) and (c) shows the measured partial pressure of HD, $p_{HD}$, plotted as a function of film composition for the Pt overlayers on Ru films, the Ru overlayers on Pt films and the Pt/Ru bulk alloys, respectively, in the temperature range $40 - 200°C$, in pure $H_2/D_2$ mixture. The measurements are carried out for decreasing temperatures with start at 200°C and the first measurement is repeated at the end of the series. Fig. 3.12(d) shows a 3-D map for $p_{HD}$ acquired at 200°C on the Pt overlayers on Ru films by scanning the sniffer over the whole $10 \times 10$ mm sample for several hours. Fig. 3.12(e) represents a profile of one of the films. Notice that the

*The content of this section is taken from Ref. [2].

width of the curve is larger than 1 mm, due to the gas diffusing out from the sniffer probe.

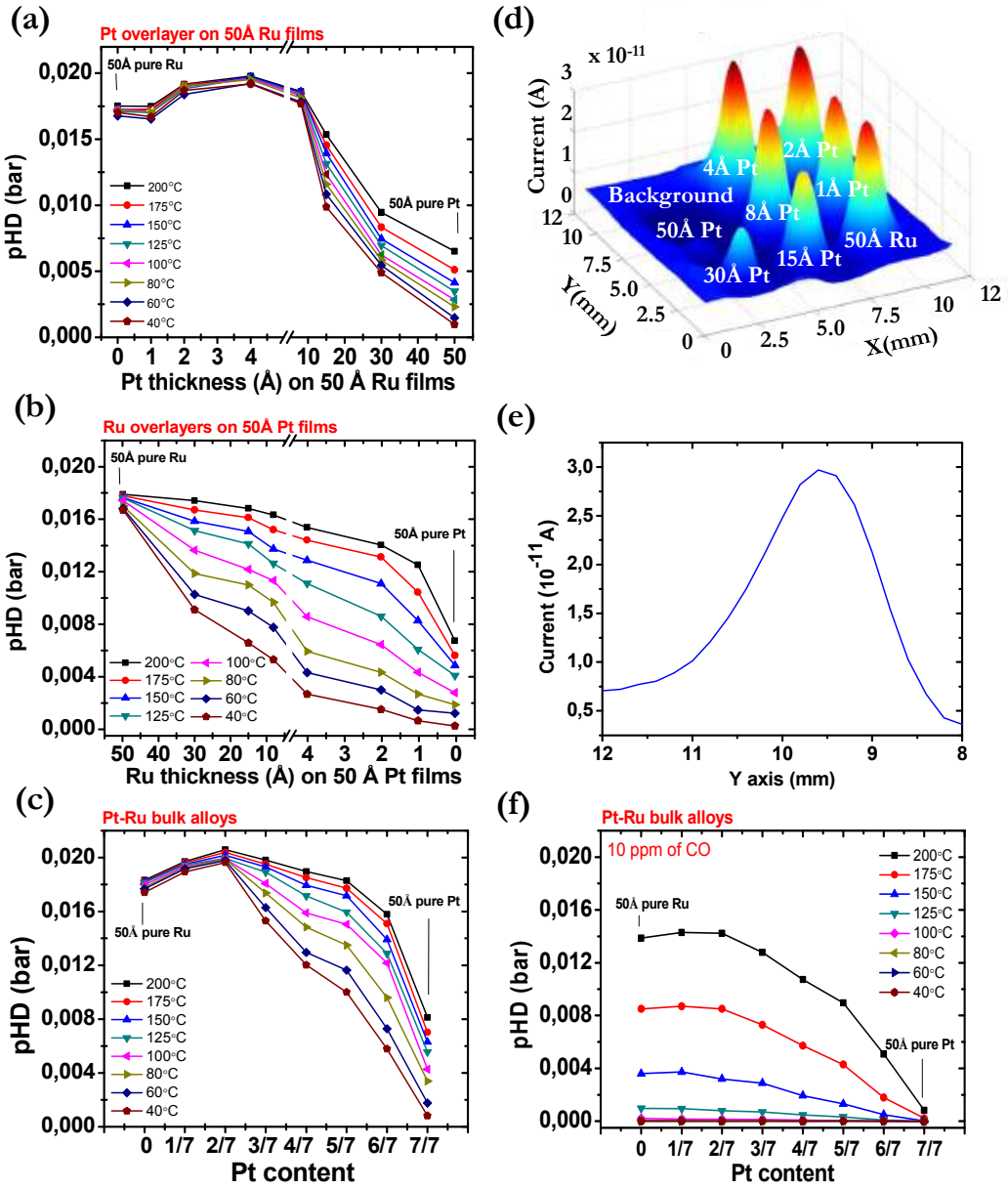


Figure 3.12: Measured values for $p_{HD}$ as a function of film composition for the Pt overlayers on Ru films (a), of the Ru overlayers on Pt films (b) and of the Pt/Ru bulk alloys (c), in the temperature range $40 - 200$°C, in pure $H_2/D_2$ mixture. (d) 3-D map for $p_{HD}$ acquired at 200°C on the Pt overlayers on Ru films. (e) A profile of one of the films is shown. (f) Measured values for $p_{HD}$ as a function of film composition when 10 ppm CO is added to the gas mixture in the case of Pt/Ru bulk alloys.

The equilibrium dissociative sticking probability, $S$, is determined from the data in Fig. 3.12, using the correlation in Fig. 3.1. The results are shown in Fig. 3.13(a), (b), and (c) for the Pt overlayers on Ru films, the Ru overlayers on Pt films and the Pt/Ru bulk alloys, respectively.

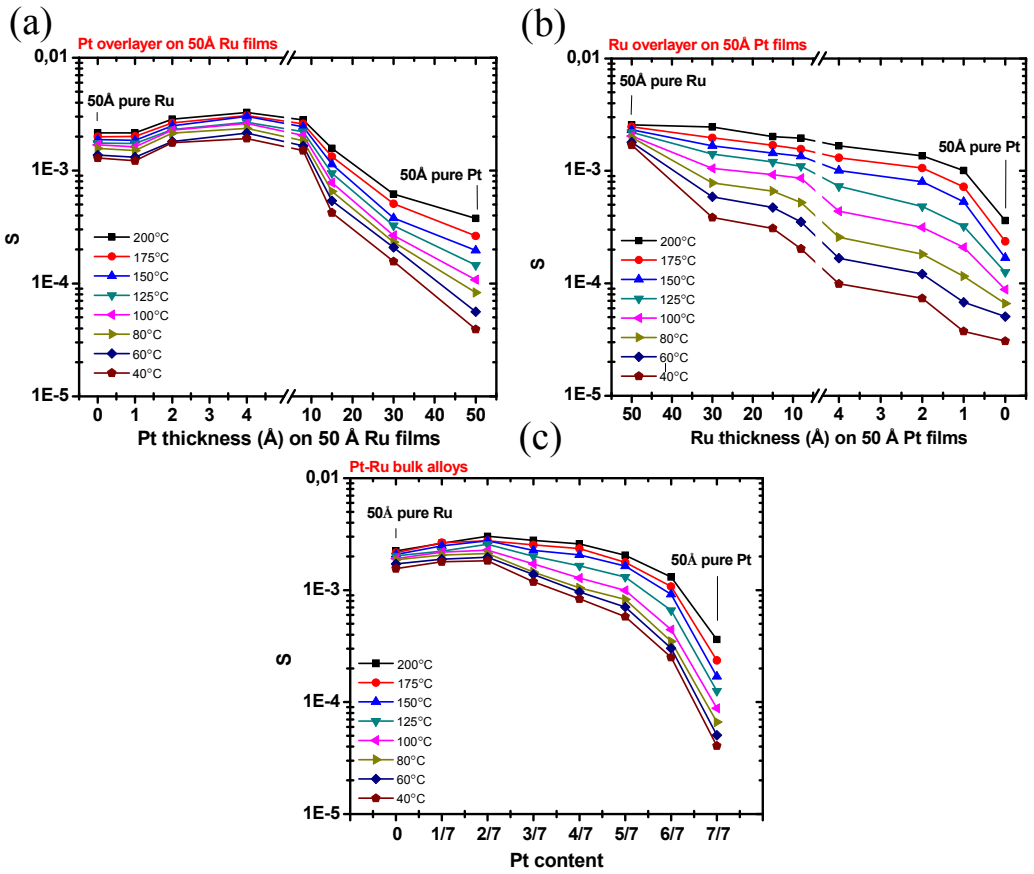


Figure 3.13: The equilibrium sticking probability for hydrogen at 1 bar, $S$, as a function of film composition for the Pt overlayers on Ru films (a), the Ru overlayers on Pt films (b) and the Pt/Ru bulk alloys (c), in the temperature range $40 - 200$°C.

It is found that pure Ru films are very active for the H-D exchange reaction and $p_{HD}$ is weakly dependent on temperature. Pure Pt films show lower activity and a stronger temperature dependence, which is in agreement with the results reported in the previous section. Moreover, an exchange rate and an equilibrium sticking probability which exceed the ones measured on pure Ru films are measured when less than 10 Å of Pt are deposited on 50 Å Ru films, with a maximum corresponding to 4 Å of Pt, as shown in Fig. 3.12(a) and 3.13(a). A maximum of $p_{HD}$ and $S$ on the Pt/Ru bulk alloys is also measured, corresponding to a bulk composition of 2/7 Pt and 5/7 Ru, as shown in Fig. 3.12(d) and 3.13(c). For the Ru overlayers on Pt films $p_{HD}$ and $S$ increase with increasing Ru overlayer thickness on Pt films, as shown

in Fig. 3.12(c) and 3.13(b). For this system a stronger temperature dependence is observed for all the films, with the exception of pure Ru films.
When 10 ppm of CO are added to the $H_2/D_2$ mixture the H-D exchange rate is inhibited significantly, also at 200°C, and the temperature dependence in $p_{HD}$ becomes stronger, as shown in Fig. 3.12(f) for the Pt/Ru bulk alloys. The exchange rate in the presence of CO is found to increase with increasing amount of Ru in the bulk-alloys and at 200°C has a weak maximum corresponding to a bulk composition of 2/7 Pt and 5/7 Ru.

### 3.3.3 Desorption energies for $H_2$

As described in Eq. 3.5, the $H_2$ desorption rate constant, $k_{des}$, can be determined from $S$ under the assumptions of hydrogen coverage close to one made in the kinetic model for the H-D exchange reaction. The apparent desorption energy for $H_2$ at the equilibrium coverage, $E_{app}$, can therefore be obtained from the data in Fig. 3.13. Arrhenius plots of the desorption rate, $r_{H_2}$, for the Pt overlayers on Ru films, of the Ru overlayers on Pt films and of the Pt/Ru bulk alloys are shown in Fig. 3.14(a), (b) and (c), respectively. Straight lines are obtained from a least squares fits of the logarithm of the desorption rate. Fig. 3.15(a), (b) and (c) shows $E_{app}$ as a function of the composition for the different films. $E_{app}$ show a dramatic decrease with increasing Ru content for all the Pt/Ru systems, showing values which are 4 times lower when going from a pure Ru film to a pure Pt film.

### 3.3.4 Surface composition analysis

ISS is performed on the Pt/Ru systems in order to gain information on the surface composition. Fig. 3.16 shows ISS spectra for 1keV $He^+$ ions scattered from the Pt/Ru surfaces after metal deposition and after the H-D exchange reactions in the HPC. The spectra are acquired at 150°C and show no peaks at low energy, indicating that the surfaces are clean from any contaminations. Fig. 3.16 only shows the high energy region of the ISS spectra, which contains the Ru peak at 910 eV and the Pt peak at 977 eV. The 50 Å pure Ru and pure Pt films have a different peak height due to the difference in the cross section of two metals, resulting in a higher peak for Pt with respect to Ru for the same amount of deposited metal, as explained in section 2.4.2.
Fig. 3.16(a-c) shows the ISS spectra acquired from all the films after metal deposition. The corresponding surface concentrations, which are derived according to Eq. 2.2, are shown in Fig. 3.17 (a-c). 3.16(d-f) shows the ISS spectra acquired from all the films after the H-D exchange reaction and Fig. 3.17 (d-f) the corresponding the surface concentrations.
It is found that Ru and Pt are both present on the surface of the bulk alloys and the overlayer structures, also at the thickest overlayers, namely the 30 Å of Pt deposited on 50 Å Ru films and the 30 Å of Ru on 50 Å Pt films. Fig. 3.17(d) and (e) shows that for the Pt overlayers on Ru films and the bulk alloys there is an enrichment

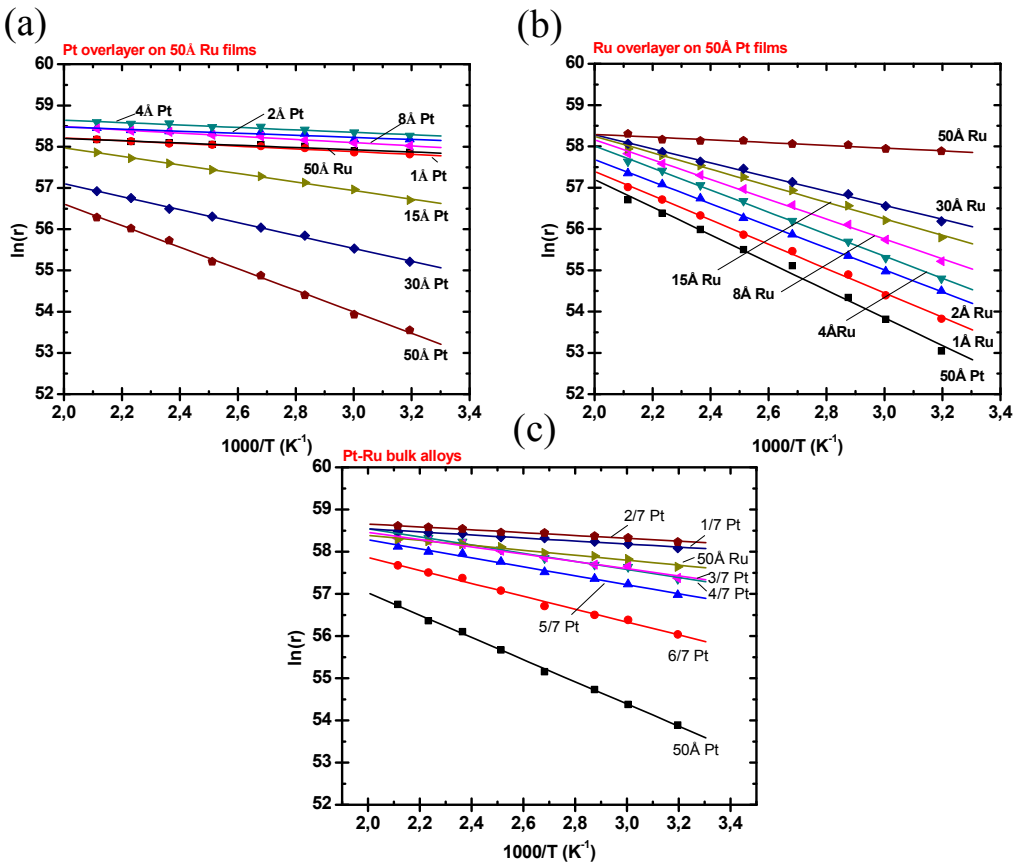


Figure 3.14: Arrhenius plots of the equilibrium hydrogen desorption rate for the Pt overlayers on Ru films (a), the Ru overlayers on Pt films (b) and the Pt/Ru bulk alloys (c).

of Pt on the surface after experiments in the HPC, due to Pt surface segregation. A much stronger Pt segregation is observed for the Ru overlayers on Pt films, for which Pt dominates the surface of the catalysts after experiments, as seen when comparing Fig. 3.17(c) and (f).

### 3.3.5 Discussion

Ru and Pt films show a different ability to dissociate $H_2$, with Ru being more active, as shown in Fig. 3.12. This is in agreement with the results presented in the previous section, where a possible explanation related to the formation of a compressed hydrogen adlayer is presented. When screening over a range of different Pt/Ru compositions it is found that for some ratio of the two metals, the exchange rate and the equilibrium sticking probability exceed the values measured on pure Ru, as seen in Fig. 3.12 and 3.13. This happens when less than 10 Å of Pt are deposited on 50 Å Ru films, with a maximum corresponding to 4 Å of Pt, and when in the bulk

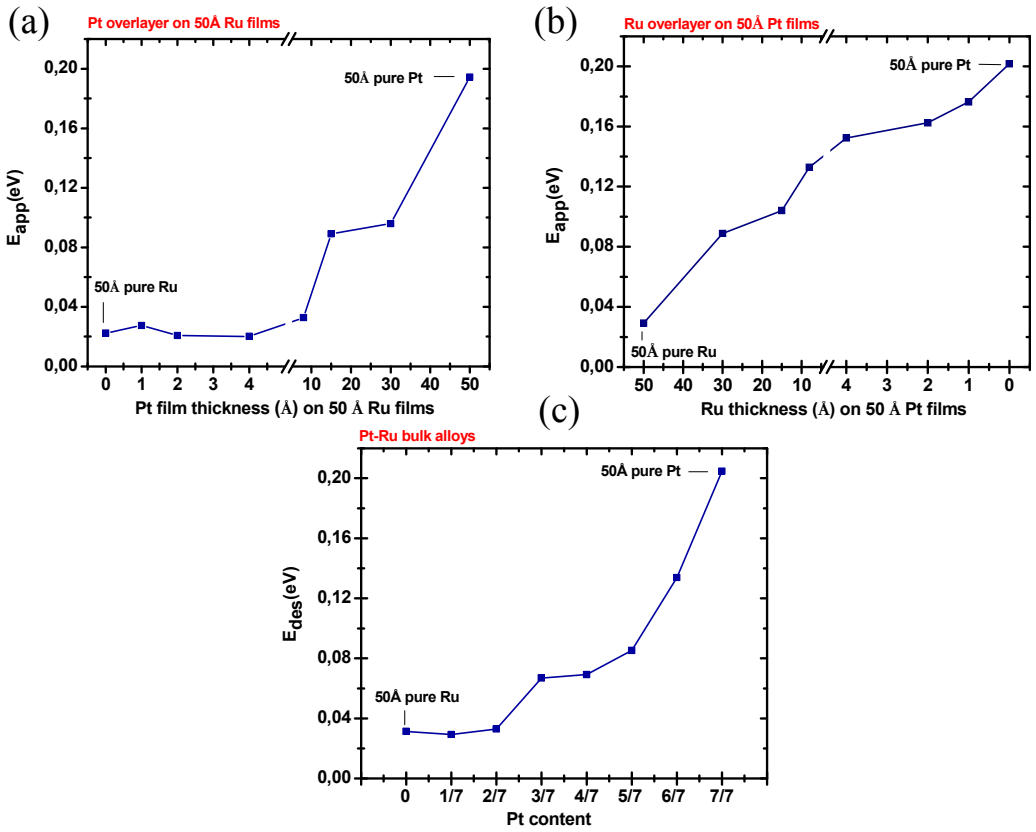


Figure 3.15: The desorption energy, $E_{app}$, as a function of the film composition for the Pt overlayers on Ru films (a), of the Ru overlayers on Pt films (b) and of the Pt/Ru bulk alloys (c). $E_{app}$ shows a dramatic increase with increasing amount of Pt in the overlayers and bulk alloys.

alloys the two metals have a ratio of 2/7 Pt and 5/7 Ru. From the ISS spectra in Fig. 3.16, it can be seen that both metals are present on the catalyst surfaces, also at the thickest overlayers, indicating that the two metals form a surface alloy already at 200°C. From Fig. 3.17 it is found that the most active catalysts for hydrogen dissociation/desorption have a surface composition corresponding to a Pt:Ru ratio equal to 1 : 1. According to literature, catalysts with a Pt/Ru ratio equal to 1 : 1 also give the highest activity for CO oxidation [64, 94, 95] and methanol oxidation [96–98].

The explanation for the high activity of the Pt/Ru catalysts with respect to the individual metals is understood in terms of the *d*-band theory, according to which the modification of the chemical properties of the alloys, which include strain and ligand effects, are due to the changes in the *d*-band center of the surface alloy [99–

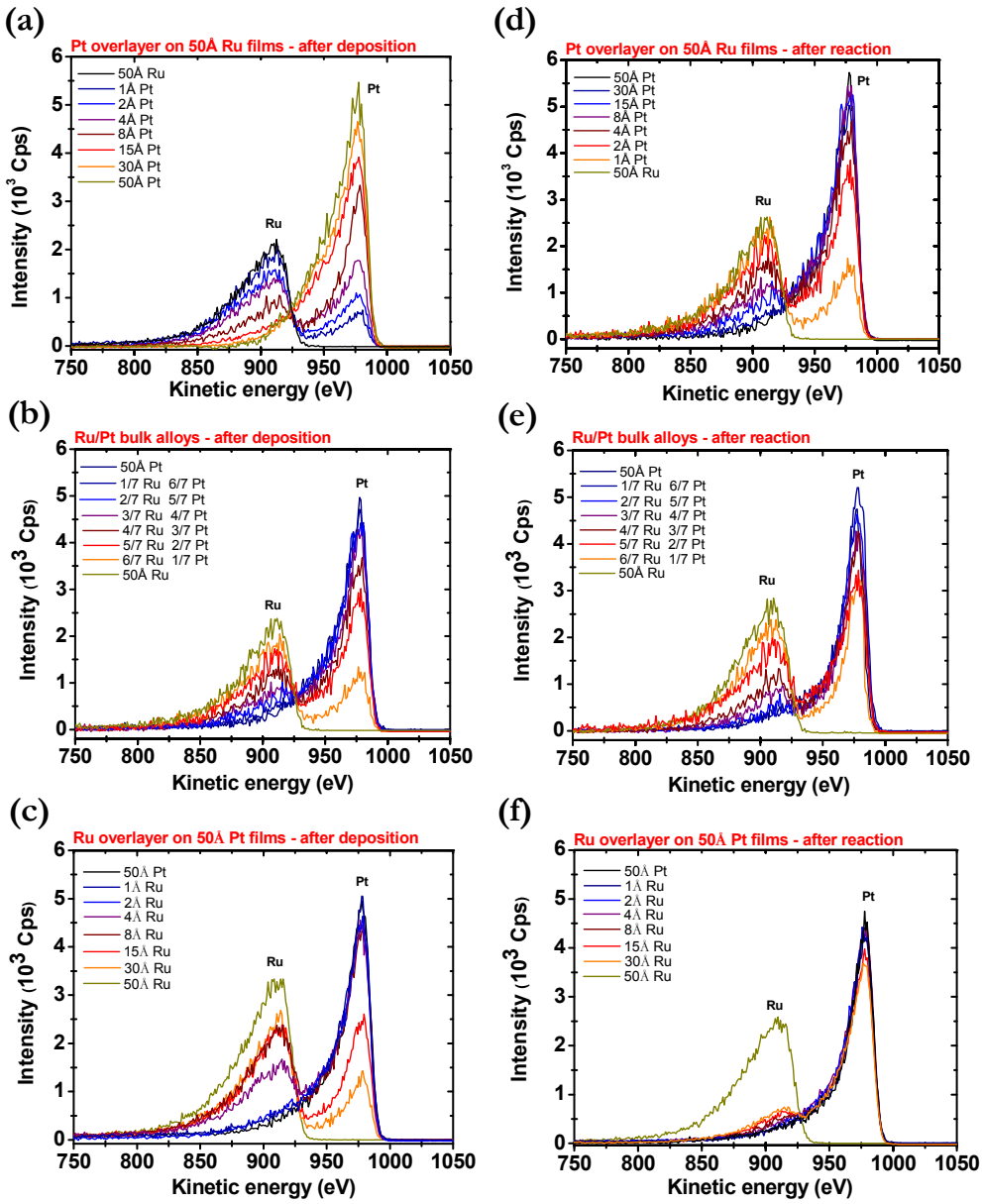


Figure 3.16: ISS spectra for 1 keV $He^+$ ions scattered from the Pt overlayers on Ru films, the Ru overlayers on Pt films and the Pt/Ru bulk alloys after deposition (a-c) and after H-D exchange reaction (d-f).

102]. Compressive strain and ligand effects destabilize the Ru-H bond since the larger Pt atoms compress the neighbouring Ru surface atoms and bring a lower hydrogen binding energy on the surface alloys compared to the pure metals. Indeed,

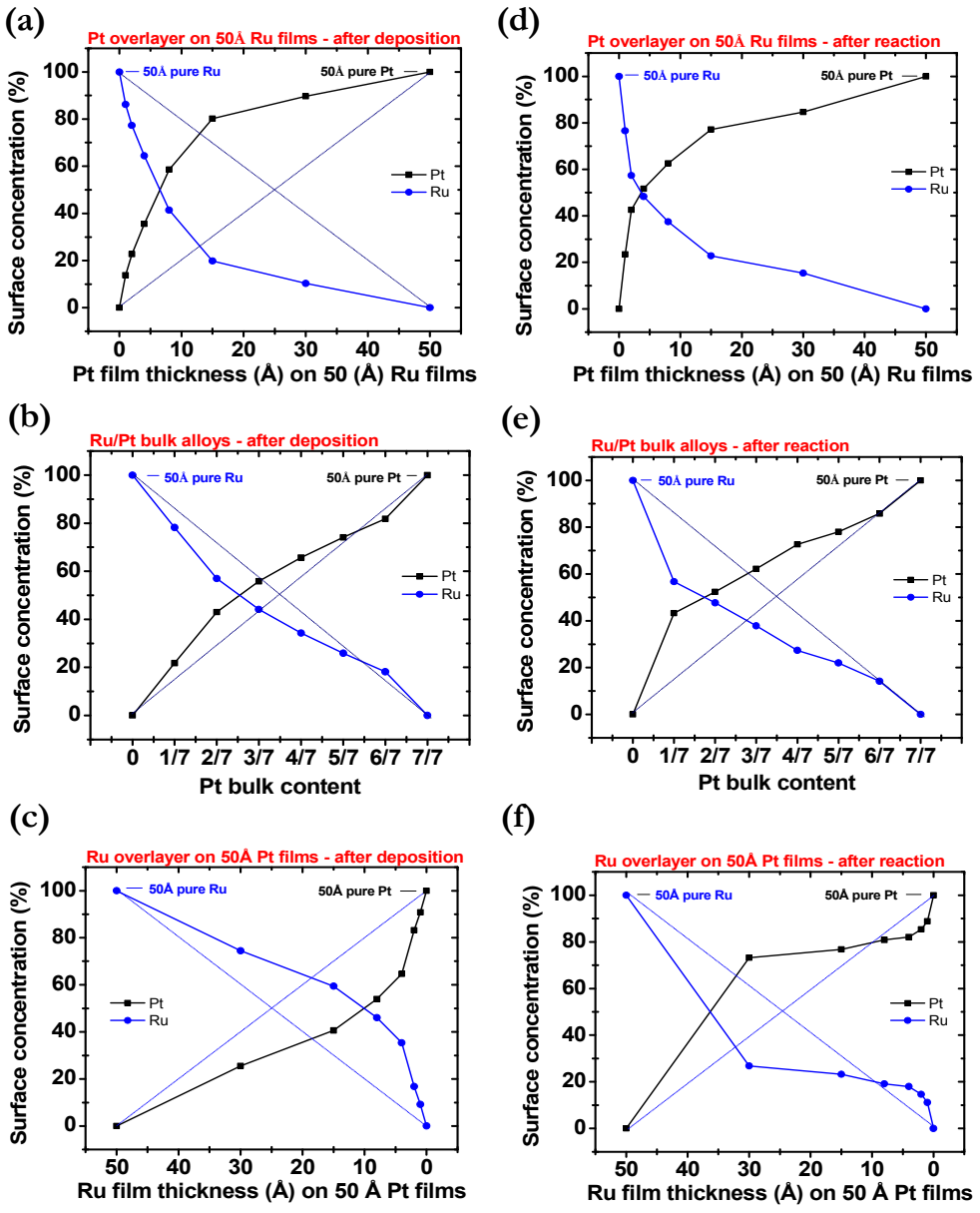


Figure 3.17: Surface concentrations corresponding to the ISS spectra from the Pt overlayers on Ru films, the Ru overlayers on Pt films and the Pt/Ru bulk alloys after deposition (a-c) and after H-D exchange reaction (d-f).

when the dissociative adsorption energy for hydrogen is plotted as a function of the *d*-band center, a downshift is predicted for the Pt/Ru alloys with respect to the pure metals [71, 101, 102]. Moreover, experimental works on Pt/Ru alloys also show

a downshift in temperature of the hydrogen (or deuterium) desorption peak with respect to the pure metals in TPD experiments. At saturation coverage it is shown that desorption starts already at the beginning of the temperature ramp [103, 104]. The faster equilibrium hydrogen exchange rate that it is measured compared to the pure metals on the Pt/Ru alloys which have a 1 : 1 ratio (see Fig. 3.12) is then in agreement with these theoretical predictions and experimental works.
When 10 ppm of CO are added to the $H_2/D_2$ mixture the H-D exchange rate on Pt decreases significantly, also at 200°C, as shown in Fig. 3.12(f) in the case of the Pt/Ru bulk alloys. However, a higher tolerance towards CO poisoning of the Pt/Ru alloys compared to pure Pt is measured, which increases with increasing amount of Ru in the bulk-alloys. As shown in Fig. 3.12(f) the exchange rate maintains a high value on the alloys which have a low content of Pt, with a weak maximum corresponding to 2/7 Pt in the alloy.
Since the exchange reaction is carried out at 1 bar pressure with the addition of 10 ppm CO in the $H_2/D_2$ mixture and the overpotentials present in a PEM fuel cell are absent in the experiments, it is not possible to measure any bi-functional effect. Therefore strain and ligand effects with a consequent downshift of the *d*-band center are most likely responsible for the higher CO tolerance that are measured in the experiments, which cause a reduction of the Pt-CO bond strength. This result is confirmed by a number of theoretical [70, 71, 105, 106] and experimental works [72, 107–109].
The difference in activity between Ru and Pt gives an apparent desorption energy, $E_{des}$, which is much lower for Ru than for Pt, as shown in Fig. 3.15. It is found that $E_{des}$ decreases dramatically with increasing Ru content in the three Pt/Ru systems, as it is seen in Fig. 3.15(a-c). Geometrical ensemble effects and the presence of mixed adsorption/desorption sites are found to be responsible for this behavior [102]. On close packed metal surfaces hydrogen is found to adsorb on the three fold sites of the surface [110–113], which can be either monometallic or mixed sites on the Pt/Ru alloys. It is shown that desorption proceeds via recombination of two neighbor adatoms and involve five surface atoms, which have up to 20 different compositions [103, 114]. This variety of compositions results in a desorption energy which vary almost continuously between the two cases of all Pt sites, which give the highest desorption energy, and all Ru sites, which give the lowest values, as shown in Fig. 3.15.
From the ISS spectra and the surface composition analysis shown in Fig. 3.16 and 3.17 it can also be seen how the surface composition of the catalysts changes after the H-D exchange reaction, with respect to what it was after deposition. It is found that Pt has a strong tendency to segregate to the surface of the catalysts, when comparing the ISS spectra or the surface composition, before and after experiments. Since the catalysts are not annealed before experiments (the sample is kept at 150°C after deposition), the segregation occurs in the high pressure cell and it can either be due to the increase in temperature from 150°C to 200°C during measurements or it could be induced by the presence of 1 bar of hydrogen. The segregation of Pt to the surface is predicted by a number of theoretical works on bimetallic alloys [115–118]

and other experimental studies show that there is a barrier for Pt diffusion into the bulk of a Ru substrate and Pt losses on the surface are negligible [103, 119].
In the case of Ru overlayers on Pt films it is found that the hydrogen exchange rate and the sticking probability increase with increasing deposited amount of Ru, as shown in Fig.3.12(b) and 3.13 (b), respectively. From the ISS spectra in Fig. 3.16(c) and (f) and the corresponding surface concentrations shown in Fig. 3.17 (c) and (f) it can be seen that the Pt segregation results in a composition of more than 70% Pt on the surfaces of the catalysts, also at the thickest Ru overlayers on Pt films. According to these results, it seems that much more Ru is needed than the amount deposited on the Pt films in order to get the observed improvement in the activity as in the other two Pt/Ru systems, since the surfaces do not reach the optimal composition of Ru:Pt equal to 1 : 1, but they are dominated by Pt. The abundance of Pt on the surface of the catalysts in this Pt/Ru system also gives a spread in temperature in the exchange rate and sticking probability which is typical of the Pt films, as shown in Fig.3.12(b) and 3.13 (b), respectively.

### 3.3.6 Summary and conclusions for this part

The equilibrium hydrogen exchange rate between adsorbed and gas phase hydrogen at 1 bar is measured on three different Pt/Ru systems: Pt overlayers on Ru films, Ru overlayers on Pt films and Pt/Ru bulk alloys. The hydrogen exchange rate is measured in the temperature range $40 - 200$°C at 1 bar, by utilization of the H-D exchange reaction. It is found that for Ru the exchange rate, $r$, and the equilibrium dissociative sticking probability, $S$, are higher than for Pt and have a maximum for a composition of 2/7 Pt in the bulk-alloys. The Pt overlayers on Ru films give similar results for $r$ and $S$, and maximum activity is found when 4 Å of Pt are deposited on 50 Å Ru films. ISS spectra show that both Ru and Pt are on the surface, which indicates the formation of a surface alloy already at 200°C. It is also found that the maximum activity is given by the alloys with surface composition of Pt:Ru equal to 1 : 1 ratio. When 10 ppm CO are added to the $H_2/D_2$ mixture it is found that the hydrogen exchange rate decreases significantly on Pt, but alloying Pt with Ru improves significantly the resistance towards CO poisoning. The resistance increases with increasing amount of Ru in the bulk-alloys, with a weak maximum corresponding to 2/7 Pt in the alloy. The faster hydrogen exchange rate with respect to the pure metals and the higher CO tolerance of the alloys is attributed to strain and ligand effects, caused by the compression of the surface due to the presence of the larger Pt atoms in the neighbouring Ru atoms. Finally an apparent energy of desorption at equilibrium which decrease with increasing amount of Ru in the three different Pt/ Ru systems is measured and this is attributed to geometrical ensemble effects and mixed adsorption/desorption sites.

# 4 Metal-support interaction

The experiments presented in this thesis are performed on supported catalysts. In heterogeneous catalysis, reactions are often carried out on supported catalysts, which are dispersed on the substrate in order to obtain and maintain a large surface area, where the catalytic reactions take place. Supports are generally metal oxides or different forms of carbon, able to provide a stable high surface area. The efficiency of the catalysts is often also dependent on the interaction between the metals and the support, which can affect significantly the performance of the catalysts. In the last decades the case of the group VIII-X metals supported on reducible oxides has been intensively studied. For these metals it is found that $H_2$ and CO chemisorption is drastically decreased after reduction at high temperature [50–55], whereas methanation of CO or $CO_2$ and $H_2$ is significantly increased [56]. It is shown that the modification of the catalytic activity is related to an encapsulation of the deposited metal by a reduced thin oxide layer migrating from the support during annealing, which causes the strong decrease on the metals ability to adsorb $H_2$ and CO [120–126]. STM images of encapsulated platinum clusters can be found in [127]. This effect has been named *Strong metal-support interaction* (SMSI) and was first observed for Pt supported on a $TiO_2$ substrate [50]. The encapsulated metals are said to enter the SMSI state. It is shown that re-oxidation and reduction cycles, steam treatments at different conditions and sputtering can reverse the SMSI state, leading to a full recovery of the metallic states of the catalysts and of their catalytic properties [128–130].

In this chapter the interaction between 50 Å Pt and Ru films and the HOPG support is investigated, when the metals are annealed in UHV to high temperatures, as in the case of metals supported on $TiO_2$. The hydrogen exchange rate of the Pt and the Ru films is measured before and after annealing in order to see whether there is any change in the ability of the two metals to adsorb hydrogen. Experiments are performed on metals deposited on sputtered and unsputtered HOPG and the results are compared. AES, ISS and XPS are used to monitor the surface of the metals upon annealing. Moreover, the effect of the ISS used as a soft sputtering technique on the annealed Pt film is described. Finally, the analogies between the results obtained for the metals supported on HOPG and the SMSI phenomenon are discussed.

## 4.1 Results from 50 Å Pt films deposited on sputtered HOPG

### 4.1.1 Sample preparation and surface composition analysis

A pattern of 50 Å Pt film is deposited on sputtered HOPG. ISS with 1 keV $He^+$ ions is performed at 150°C on the films to investigate the composition of the outer layer after deposition. The films are eventually annealed in UHV at temperatures up to 700°C and they are cool down to 150°C before performing ISS. The ISS spectra from one of the film are shown in Fig. 4.1 and the wide energy range is reported.

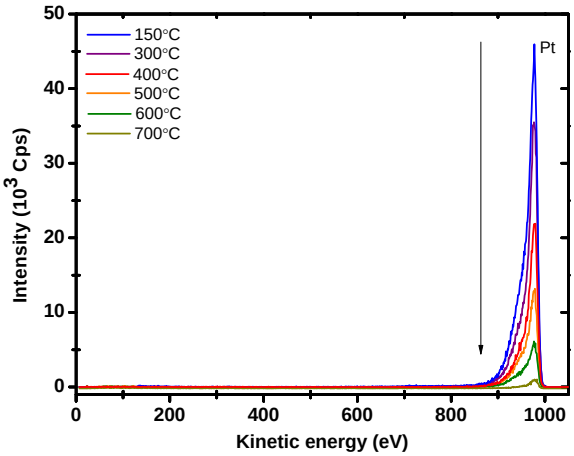


Figure 4.1: ISS spectra for 1 keV $He^+$ ions scattered from a 50 Å Pt film deposited on sputtered HOPG after annealing to temperatures up to 700°C.

The Pt generates a peak located at 977 eV, whereas for C it is not possible to measure any signal in this energy range. This is in agreement with results of a previous work, where it was shown that a graphitic carbon signal is detectable only at primary energies of 3.5 keV or higher [131]. Here it is found that with increasing temperature the Pt signal drops significantly and no other peaks are appearing. Since the Pt is not simply disappearing, the interpretation is that carbon, likely in a graphitic form, is segregating to the surface of the Pt films upon annealing. This is also similar to the observations made in a work on a carbon doped Re sample, where it was found that by increasing the temperature a full layer of graphitic carbon was formed and the Re ISS signal dropped to the noise level [131].
AES is also performed on the 50 Å Pt films, since with this technique the Pt and the C signals are both detectable. AES spectra with 3 keV electrons are acquired from the films at 150°C after metal deposition and after annealing in UHV to temperatures up to 700°C. The AES spectra are acquired in a wide energy range but since no contaminations are observed, only narrow energy windows are shown in Fig. 4.2 (a-g), where the main Pt and C AES lines are located at 64 eV and 272 eV, respectively.

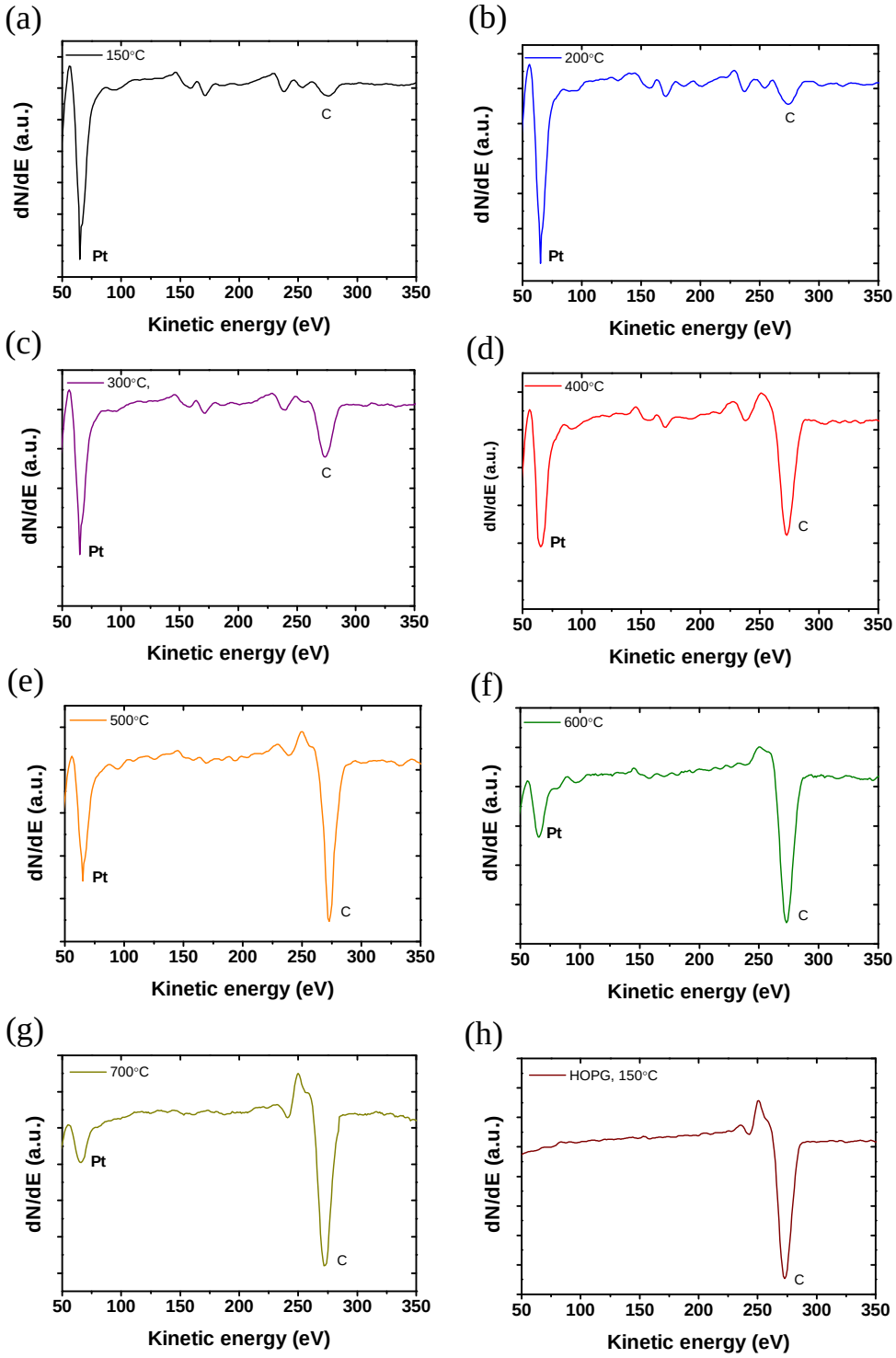


Figure 4.2: (a-g) AES spectra for 3 keV electrons of a 50 Å Pt film deposited on sputtered HOPG, after annealing to temperatures up to 700°C. (h) AES spectrum of the HOPG.

The low kinetic energy of these auger electrons indicates that the sampling depth for this technique is $\sim 0.5$ nm for Pt and $\sim 0.7$ nm for C, according to Fig. 2.13, corresponding roughly to the first few layers of the Pt film. For comparison, an AES spectrum of the HOPG at 150°C far from the metal films is shown in Fig. 4.2(h), in a narrow energy window around the C peak. It can be seen that with increasing annealing temperature the Pt signal decreases and the C signal increases significantly, confirming that the surface of the Pt films get covered by C upon annealing.
Finally, XPS with 1253.6 eV photons coming from a $Mg_{K_a}$ anode is also used to characterize the 50 Å Pt films deposited on sputtered HOPG. Fig. 4.3 shows the XPS spectra acquired at 150°C after annealing the films in UHV to 400°C, 600°C and 700°C. A narrow range of energy from 100 eV to 0 eV, where the Pt $4f_{7/2}$ and Pt $4f_{5/2}$ peaks are located at 74 eV and 71 eV, respectively, is reported. The insert of Fig. 4.3 shows a narrow energy window around the C peak, located at 284 eV. For comparison, a spectra of the HOPG far from the metal films is also shown. The kinetic energy of the emitted photoelectrons for Pt and C is higher compared to the Auger electrons, meaning that XPS has a larger sampling depth than AES, of $\sim 1.8$ nm for Pt and $\sim 1.6$ nm for C, according to Fig. 2.13. It is found that with increasing temperature the Pt signal decreases and the C signal increases.

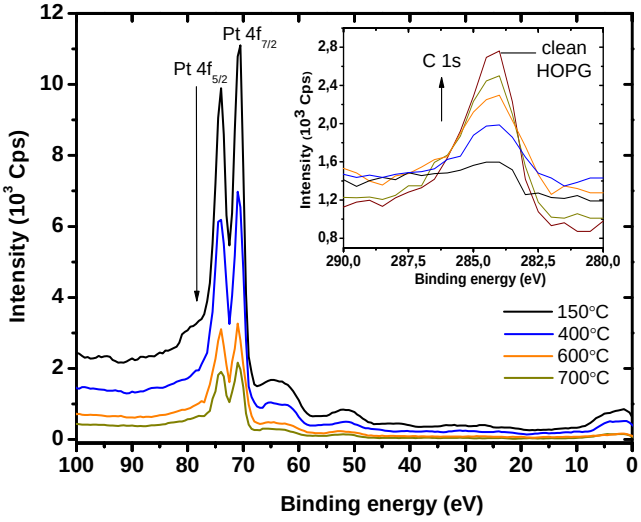


Figure 4.3: XPS spectra of a 50 Å Pt film deposited on sputtered HOPG, after annealing to temperatures up to 700°C. The insert shows the C signal.

The changes in the C and Pt signals as a function of the temperature are reported in Fig. 4.4(a) and (b), respectively, which show a dramatic increase of C upon annealing. In Fig. 4.4(b) the decrease of the Pt signal as a function of the temperature measured by ISS is also plotted, where the initial value for the Pt signal is norma-

lized to the initial value given by AES, which is reasonable due to the high surface sensitivity for Pt of both ISS and AES techniques, resulting in a similar trend in the drop of the Pt signal.
With XPS a larger C signal is measured compared to AES. This is due to the large sampling depth of XPS combined to a large sampling area, which causes a signal from the carbon underneath the Pt film (the support) and from the Pt free areas of the HOPG (the surrounding areas) to reach the analyzer, as explained in section 2.4. According to that, the XPS signals are not considered for further analysis in this investigation.

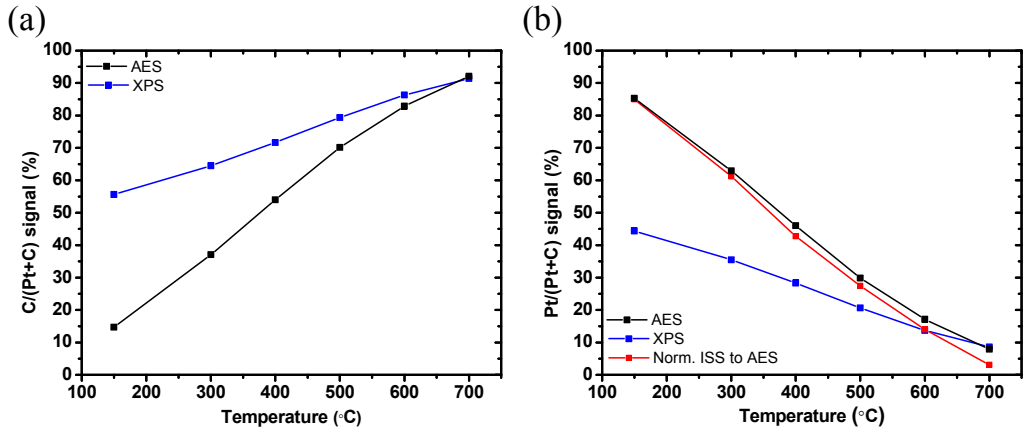


Figure 4.4: (a) C/(Pt+C) signal as a function of annealing temperature, as derived by AES amd XPS analysis. (b) Pt/(Pt+C) signal as a function of annealing temperature, as derived by AES, XPS and ISS analysis, where the initial Pt signal given by ISS is normalized to the initial signal given by AES.

### 4.1.2 H-D exchange rate

Fig. 4.5 shows the results of the H-D exchange reaction measured on the 50 Å Pt films deposited on sputtered HOPG after annealing to temperatures up to 700°C. $p_{HD}$ is plotted as a function of the reaction temperature, in the range $40 - 200$°C. It is found that $p_{HD}$ increases as a function of temperature and decreases dramatically with annealing temperature, due to the increase of the carbon content in the Pt films upon annealing, as shown in Fig. 4.5(b), which poisons the surface of the catalyst.
In Fig. 4.6 $p_{HD}$ measured at 200°C is plotted as a function of the Pt signal, given by ISS, after annealing the 50 Å Pt films to temperatures up to 700°C, which are indicated in the plot. A linear decrease of $p_{HD}$ is observed with decreasing Pt signal, indicating that the hydrogen exchange reaction on Pt is not structure sensitive. This result is in agreement to the results obtained from the $H_2$ dissociation on Pt nanoparticles, reported in section 3.2.6.

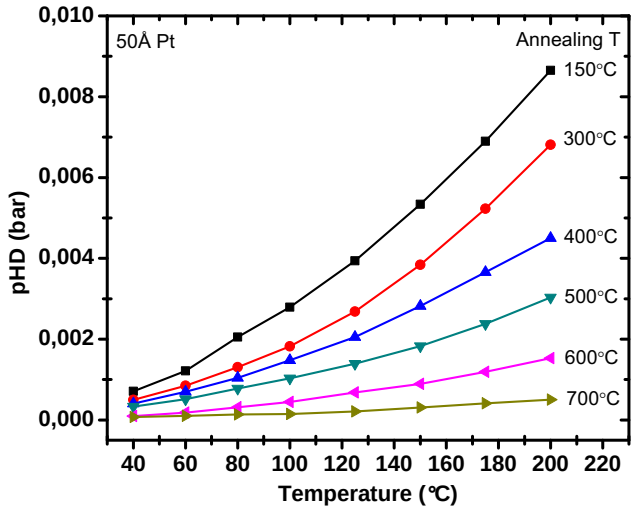


Figure 4.5: Measured values for $p_{HD}$ as a function of the reaction temperature for the Pt films deposited on sputtered HOPG. The annealing temperatures are indicated for each curve.

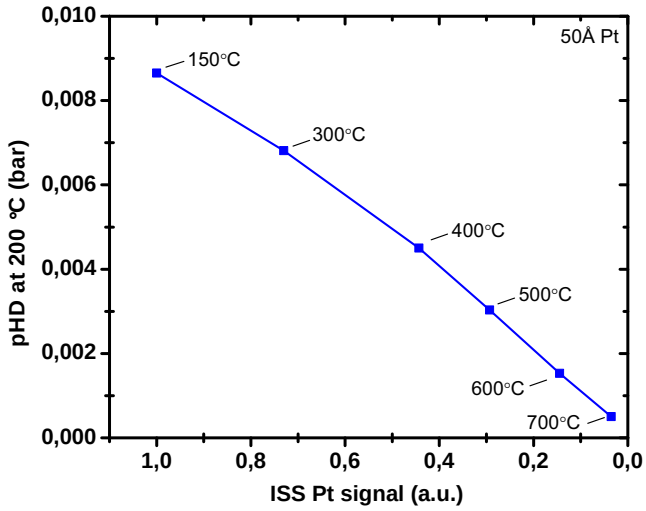


Figure 4.6: Measured values for $p_{HD}$ at 200°C for the Pt films deposited on sputtered HOPG, as a function of the Pt signal, given by ISS. The annealing temperatures are indicated next to the data points.

## 4.2 Results from 50 Å Ru films deposited on sputtered HOPG

Similar experiments are performed on 50 Å Ru films deposited on sputtered HOPG, since Ru is very active for the exchange reaction. AES spectra with 3 keV electrons are acquired on the films at 150°C after deposition. Afterwards, the films are annealed in UHV to temperatures up to 700°C and the temperature is decreased to 150°C before performing AES. Fig. 4.7(a) and (b) shows AES spectra of 50 Å films acquired after deposition and after annealing to 700°C, in a narrow energy window around the Ru AES lines. Since the main AES line for Ru is located at 273 eV and overlaps with the C line, located at 272 eV, quantification of the surface composition is difficult with this technique. However a dramatic decrease in the amplitude of the secondary lines for Ru after the films are annealed to 700°C is observed, indicating that largest contribution to the main peak in Fig. 4.7(b) is given by C.

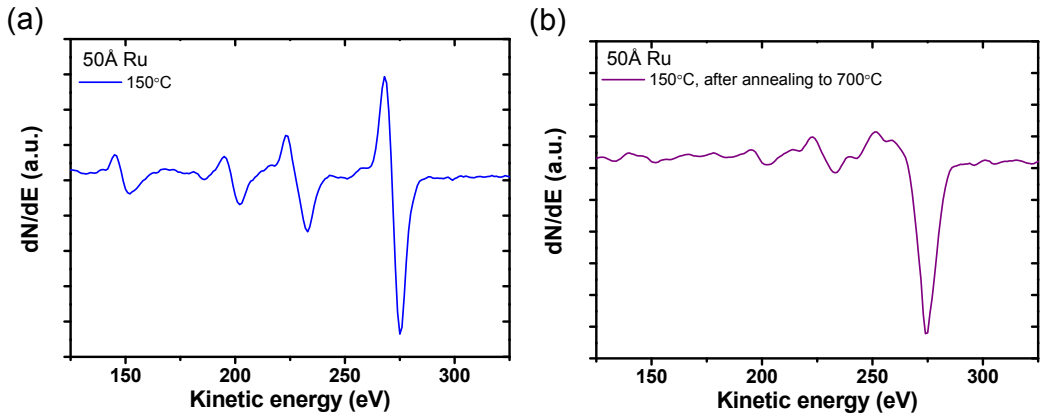


Figure 4.7: AES spectra for 3keV electrons of a 50 Å Ru film deposited on sputtered HOPG acquired after deposition (a) and after annealing to 700°C (b).

ISS is also performed on the 50 Å Ru films at 150°C, with 1 keV $He^+$ ions, after annealing the films up to 700°C. ISS spectra are shown in Fig. 4.8(a) in a narrow energy window around the Ru peak, which is located at 934 eV. It is found that with increasing temperature the Ru signal decreases down to around 5% of the initial value, as in case of the Pt films, indicating that the Ru films also get covered by C upon annealing. Finally the H-D exchange experiment is carried out on the Ru films, after deposition and after annealing to 700°C. The results are shown in Fig. 4.8(b), where $p_{HD}$ is plotted as a function of the reaction temperature, in the range $40 - 200$°C. It is found that $p_{HD}$ decreases significantly when the Ru films are annealed to 700°C, due to the carbon poisoning the surface of the Ru films, as for the Pt films.

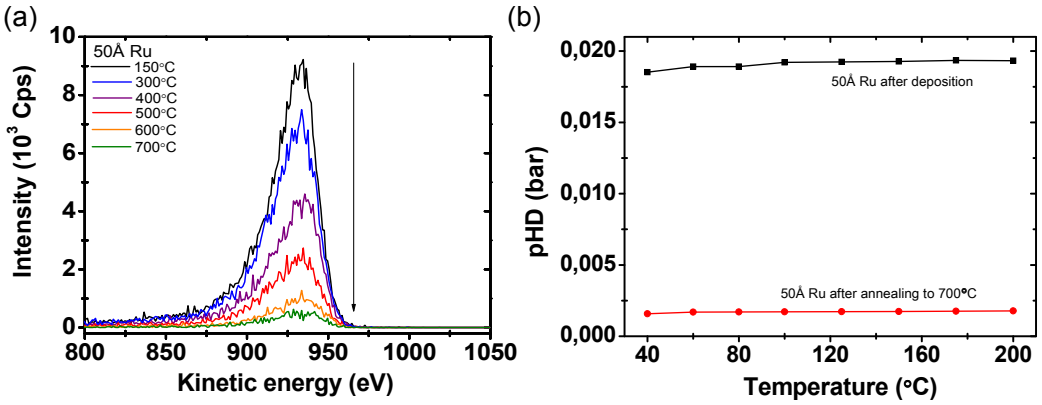


Figure 4.8: (a) ISS spectra at 150°C for 1 keV $He^+$ ions scattered from the 50 Å Ru film at different annealing temperatures. (b) Measured values for $p_{HD}$ as a function of the reaction temperature for the Ru films after deposition and after annealing to 700°C.

## 4.3 Results from 50 Å Pt and Ru films deposited on fresh HOPG

The $Ar^+$ sputtered HOPG is a highly defective substrate, as shown in Fig. 2.5, which could contain loose carbon and strongly fragmented graphite sheets. In order to investigate if the sputtering process is responsible for the carbon poisoning upon annealing, 50 Å Ru and Pt films are deposited on a fresh cleaved HOPG.
First, the H-D exchange rate is measured on the films after deposition and the results are reported in Fig. 4.9(a), where they are compared to the values measured on the films deposited on sputtered HOPG. It is found that the values for $p_{HD}$ on the films deposited on unsputtered HOPG are lower than the ones measured on sputtered HOPG at any temperature, for both metals. The loss in activity is believed to be a consequence of a decrease of the nanoparticles surface area within the films, caused by sintering effects due to a poorer adhesion to the substrate, which has a low density of nucleation sites when it is not sputtered. The effect of the substrate conditions on the particle size formation has been shown in previous works on Ru and Ag particles deposited on carbon substrates [60, 61]. Moreover the decrease in activity is larger for Pt than for Ru, which is likely due to Ru being more reactive and having a higher melting point with respect to Pt, making the Pt nanoparticles more inclined to sintering on a unsputtered substrate.
Eventually, the films are annealed in UHV to 700°C. Fig. 4.9(b) shows an AES spectrum for 3 keV electrons of the Pt films, in a narrow energy window around the Pt and the C peaks. The insert shows the AES spectrum acquired after deposition. It is found that the C signal on the Pt films after annealing is around 90% and is comparable to the value found on the films deposited on sputtered HOPG, shown in Fig. 4.4. Depositing the metals on unsputtered HOPG therefore does not prevent that the metals upon annealing get covered by C. However, in this case a contribution

to the loss in the Pt signal could also be given by a further particle sintering upon annealing.

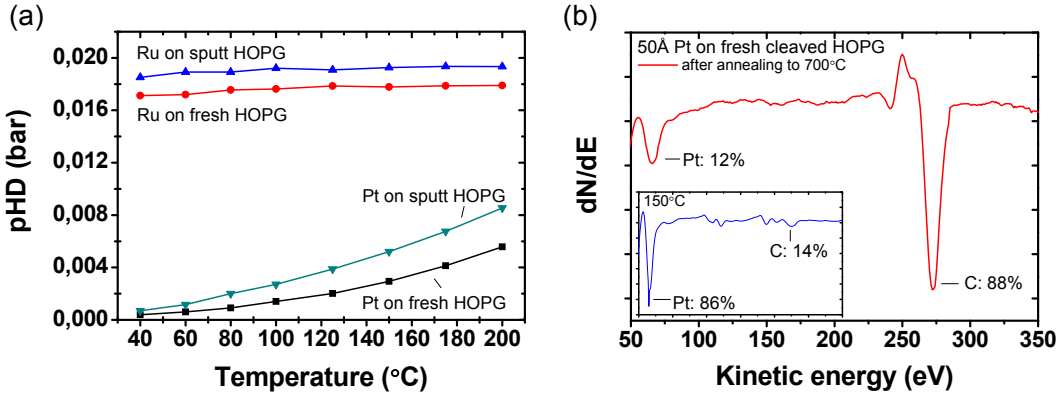


Figure 4.9: (a) Measured values for pHD as a function of the reaction temperature for the Pt and Ru films after deposition on a fresh cleaved HOPG, compared to the values measured on sputtered HOPG. (b) AES spectra for 3 keV electrons of a 50 Å Pt film deposited on a fresh cleaved HOPG after annealing to 700°C. The insert is a AES spectrum of the Pt films, as deposited.

## 4.4 Effect of the $He^+$ sputtering on the annealed Pt films

The ISS Pt signal of the Pt film deposited on sputtered HOPG after annealing to 700°C drops to less than 5% of its initial value, as shown in Fig. 4.4. The 1 keV $He^+$ ion beam is used as soft sputter beam, which is focused on the Pt film. The current through the sample is around 20 nA and the beam is rastered on an area of 1 $mm^2$, to cover the whole Pt film. The temperature of the sample is 150°C. Under these conditions an ISS spectrum is acquired every 5 minutes for 1 h and the results are reported in Fig. 4.10(a). It is found that the Pt signal increases with sputtering time and it reaches around 95% of its initial value after around 45 minutes of sputtering, leveling out after this time, as shown in Fig. 4.10(b).
Eventually the catalytic activity of the Pt films is tested and the measured partial pressure of HD, $p_{HD}$, is plotted in Fig. 4.11, as a function of the reaction temperature, in the range $40 - 200$°C. In the figure, $p_{HD}$ is compared to the values measured on the Pt film after deposition and it is found that the activity of the Pt films after sputtering is roughly 95% of what it was after deposition, which is consistent with the ISS results.

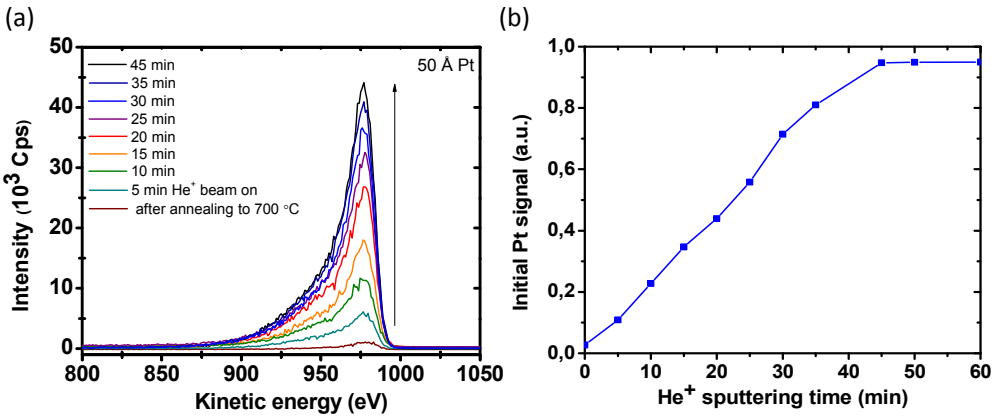


Figure 4.10: (a) ISS spectra at 150°C for 1keV $He^+$ ions scattered from a 50 Å Pt film which was annealed to 700°C, acquired within 45 minutes. (b) Pt signal as a function of the sputtering time.

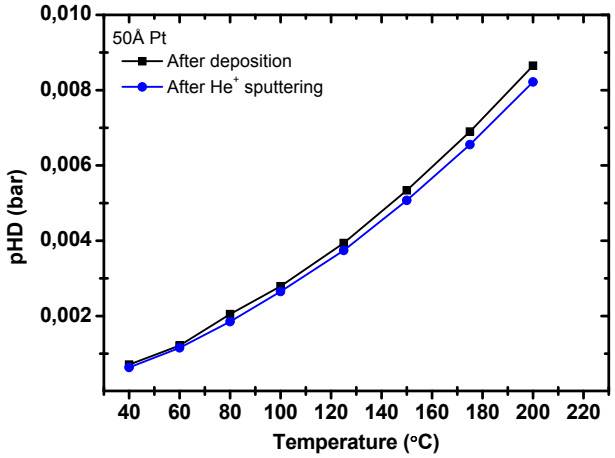


Figure 4.11: Measured values for $p_{HD}$ as a function of the reaction temperature for the 50 Å Pt film after deposition and after 60 minutes $He^+$ sputtering.

## 4.5 Discussion

In the previous sections it is shown that annealing to high temperature Pt and Ru films supported on HOPG in UHV, causes a dramatic decrease of their catalytic activity. The ISS spectra show that the metals' signal decrease to roughly 5% of their initial values upon annealing and the AES spectra reveal a significant increase of the carbon signal. It could be argued that the decrease in the exchange rate and in the ISS signals are due to losses in the surface area caused by particle sintering

upon annealing. If this was the case, it would not be possible to regenerate the catalyst and obtain ISS signals comparable to the initial values. Full recovery of the catalysts can be achieved by performing $He^+$ sputtering, as shown for Pt supported on sputtered HOPG. Therefore the suppression of the catalytic performance of the metals is likely caused by carbon covering the surface of the metals upon annealing, which inhibits the ability of the metals to adsorb hydrogen, and it is a reversible effect. These results are similar to the ones reported in the case of the metals supported on reducible oxides, which are annealed to high temperature. For these metals it is shown that the modification of their activity is caused by a reduced thin oxide layer migrating from the support onto the metals during annealing, causing the suppression of their ability to adsorb $H_2$ and CO [120–126]. For the same metals it is also shown that this effect can be reversed by few treatments, included sputtering, leading to a full recovery of their metallic states and of their catalytic performances [128–130]. This phenomenon is traditionally called Strong metal-support interaction (SMSI) [50]. In the light of the analogies between the two systems, the term SMSI can also be used to describe the case of the metals supported on HOPG, which are annealed to high temperature. However, it is important to keep in mind that this term refers to the migration of a layer from the support to the top of the metals upon annealing, rather than to vertical interactions between the metals and the support, which the term SMSI originally indicated [50].
In the following the thickness of the carbon layer covering the Pt films upon annealing is quantified. In order to do that, the number of carbon layers that are removed while sputtering the Pt films with the 1 KeV $He^+$ beam, is calculated. The sputtering rate per hour, $S_r$, is given by:

$$S_r = \frac{J}{M} Y_\theta \tag{4.1}$$

where $J$ is the beam current density on the sample, given by:

$$J = \frac{I}{A} = \frac{0.02\mu A}{0.01 cm^2} = 12.5 \cdot 10^{12} \frac{q}{s \cdot cm^2} \tag{4.2}$$

$M$ is the density of graphene per monolayer, equal to $2.05 \cdot 10^{15}$ atoms/($cm^2 \cdot$ ML). $Y_\theta$ is the angular sputter yield, equal to $Y \cdot cos(\theta)^{-1}$ [132, 133] where $\theta$ is the angle between the $He^+$ beam and the sample, which is 50° in these experiments. A sputter yield of 0.07 [134] results in $Y_\theta = 0.1$.
According to these values, $S_r$ is 1.7 ML/h, indicating that upon annealing the Pt films get covered by between one and two carbon layers in the sputtering hour. $S_r$ is only an indicative number, which is strongly dependent on the values used while calculating it, especially since $Y$ and its angular dependence are not exactly defined. However, a sputtering rate of 1.7 ML/h is a reasonable number.
Another way to estimate the thickness of the carbon layer is to use the AES signals from Pt and C to calculate the damping in the Pt signal due to the formation of the C overlayer. The probability to escape from the sample of electrons which are

emitted from a depth of $z$, can be calculated as:

$$\frac{P_{Pt}(z)}{P_C(z)} = \frac{S_{Pt}}{S_C} \frac{\int_a^\infty N_{Pt}(z) \cdot e^{-\frac{z}{\lambda_{Pt}}} dz}{\int_0^a N_C(z) \cdot e^{-\frac{z}{\lambda_C}} dz} \tag{4.3}$$

where $P_x$, $S_x$ and $N_x$ are the AES signal of the element $X$, its AES sensitivity and its density, $a$ is the thickness of the carbon layer to estimate and $\lambda_x$ is the mean path for the emitted electron. Eq. 4.3 can be simplified by considering the film homogeneous and using the same density for Pt and C. Moreover the mean path can also be approximated to be the same for Pt and C, roughly equal to 0.5 nm. With these assumptions it follows:

$$\frac{P_{Pt}(z)}{P_C(z)} = A \frac{\int_a^\infty e^{-\frac{z}{\lambda_{Pt}}} dz}{\int_0^a e^{-\frac{z}{\lambda_C}} dz} = A \frac{e^{-\frac{a}{\lambda}}}{1 - e^{-\frac{a}{\lambda}}} = \frac{A}{e^{\frac{a}{\lambda}} - 1} \tag{4.4}$$

where $A$ is the ratio of the AES sensitivity for Pt and C and $\lambda$ is the inelastic mean path, which it is assumed to be the same for both elements. When solving Eq. 4.4 for $a$ and using the AES signals as a function of the temperature, it results that the thickness of the carbon layer increases with temperature and reaches roughly 0.54 nm after annealing to 700°C, as shown in Fig. 4.12.

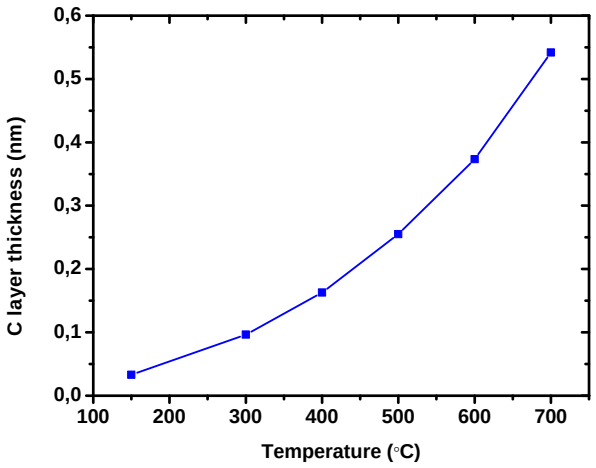


Figure 4.12: The thickness of the C layer which covers the surface of the Pt films upon annealing to high temperature in UHV, as calculated according to Eq. 4.4.

Since the C-C distance between graphene layers is 0.33 nm, it follows that with this calculation the Pt films get covered by almost two carbon layers, which is in agreement with the result provided by the calculation of sputtering rate. However,

since the sputtered HOPG surface is highly defected, with a roughness factor around 2, as discussed in section 3.2.2, it is reasonable that the actual amount of carbon covering the Pt films is roughly just a single monolayer.

## 4.6 Summary and conclusions for this part

The metal-support interaction is investigated in the case of Pt and Ru films supported on HOPG, which are annealed to high temperatures in UHV. It is found that the surface of the metal films get covered by carbon upon annealing, causing a suppression of the catalytic performance of both metals. It is also shown, in the case of the Pt films supported on sputtered HOPG, that the effect is reversible and the catalytic performance is restored by performing $He^+$ sputtering, which is able to remove the carbon layer from the surface of the metal. An attempt to estimate the thickness of the carbon layer forming on the metal films upon annealing is presented, by calculating the sputtering rate and the damping of the AES Pt signal through the carbon layer as a function of the annealing temperature. Due to the roughness of the HOPG surface, it is reasonable that the actual amount of carbon covering the Pt films is roughly a single monolayer. Since the results obtained are similar to the observations made for the metals supported on reducible oxides, the term SMSI can also be used to describe the case of metals supported on HOPG, which are annealed to high temperature in UHV.

# 5 The $NH_3$ decomposition reaction

In this chapter the results obtained from the dissociation of $NH_3$ on different catalytic systems are reported. The $NH_3$ decomposition reaction is investigated since $NH_3$ represents a possibility for $H_2$ storage. $NH_3$ has a large weight fraction of hydrogen, which constitutes 17.65% of its mass, representing a valid alternative to liquid and compressed hydrogen, as discussed in the introduction of this thesis. $NH_3$ needs to be catalytically cracked in order to produce hydrogen and the decomposition reaction is described by the reaction:

$$2NH_3 \Leftrightarrow N_2 + 3H_2 \tag{5.1}$$

This is a clean process producing $H_2$ along with $N_2$, which can be released to the atmosphere without significant environmental impact. For PEM fuel cell applications, the produced hydrogen needs to be purified by any rest concentration of $NH_3$, since the membrane gets poisoned by levels as low as than 1 ppm [36]. However, other kind of fuel cells can be used, such as alkaline fuel cells, able to tolerate low amounts of $NH_3$ [37].
The $NH_3$ decomposition has been investigated both experimentally and theoretically over a wide range of supported catalysts, single crystals and alloys of transition metals [38–43]. The general trend from the literature is illustrated in Fig. 5.1, which show the $NH_3$ conversion calculated from microkinetic modeling over a range of single crystals as a function of the nitrogen binding energy at 850K [135]. The same figure also shows the Turn Over Frequencies (TOF) measured on different catalysts [136]. The calculations leads to a volcano curve for the decomposition reaction displayed by the dashed green line and it is found that Ru is the best catalyst for the reaction. This is also supported by a number of other works mentioned earlier in this thesis [38, 40, 44–47]. However Ru is an expensive material and a limited source, therefore researchers are making an effort in order to find cheaper alternatives to it. The experiments presented in this chapter are carried out on 50 Å films of Ru, Pt, Rh, Ir and the results are compared to the trend reported in literature. Ru nanoparticles with different diameters are also tested, in order to see whether the particle

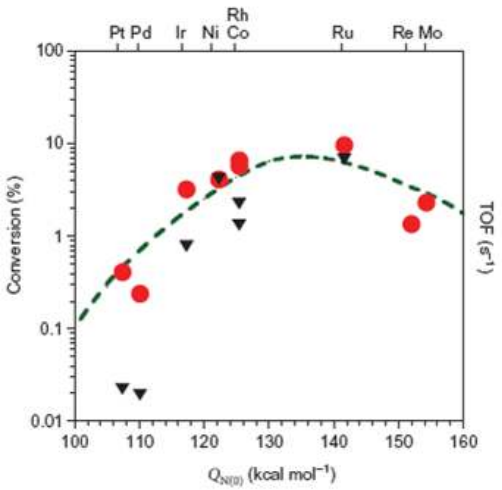


Figure 5.1: The $NH_3$ conversion calculated from microkinetic modeling (circles, left axis), and experimentally found turn over frequencies of supported catalysts (triangles, right axis) plotted for a range of single crystals [135].

size has an effect on the reaction rate. Since alloying two metals of the two sides of a volcano curve often brings to alloys which exceed the activity of the individual metals [83, 137–139], Ir/Ru alloys are chosen to be tested for the $NH_3$ decomposition reaction. For the same reason, measurements are conducted also on Ni/Fe alloys, which could represent a cheaper alternative to Ru based alloys.
It is important to mention that in this chapter only prelimiray results are presented, since many difficulties have been encountered during experiments, due to the complexity when running this reaction compared to the H-D exchange reaction. The progress of the reaction is monitored by measuring the signals of 17, 16, 15 and 14 for $NH_3$, and of 2 and 28 AMU for $H_2$ and $N_2$, respectively. The gas mixture consists of 5000 ppm $NH_3$/He and the He gives a signal at 4 AMU and also at 2 AMU, which is attributed to the presence of $He^{++}$, as mentioned in section 2.5.3. The first difficulty lies in the fact that the level of the background signal for 2 AMU is high enough to mask the evolution of the $H_2$ signal when performing the reaction, therefore only the evolution of the $N_2$ signal is considered a reliable measurement of the decomposition rate. In general, the signals measured are low compared to the values measured during the exchange reaction, which is much faster than the $NH_3$ decomposition reaction. For the least active catalysts the signal is just above the noise level. On the other hand, when a measurement is performed on an active metal as Ru spillover effects are observed. Therefore some time has been spent in order to understand whether the activity of the different films influence each other and how to measure a reasonable background signal. Another difficulty is related to the fact that the reaction is carried out at temperatures up to 500°C, pushing the feedthroughs of the manipulator arm to work at the maximum power. In order to help heating the HPC when filled with 1 bar of $NH_3$/He, two 150 W lamps are

placed at the two windows of the HPC during experiments. Moreover, at these temperatures, the catalysts get poisoned by carbon, which might effect significantly the activity of the metals. Unfortunately the AES/SEM system stopped working during these experiments and it was not longer possible to acquire any AES spectra. The catalysts are therefore characterized only by ISS and XPS before and after carrying out the reaction. Finally, since the sniffer probe gets significantly heated up during experiments, in the first measurements the supported catalysts were severely contaminated by sulfur and lead, which are believed to originate from the walls of the sniffer probe, as explained more in detail in section 2.5.4. However, an efficient cleaning procedure has been developed, using focus lamps on the sniffer probe in order to desorb as many impurities as possible before running the reaction, as explained in section 2.5.4.

## 5.1 Thermodynamics and kinetics

The equilibrium constant between the forward and backward reaction as a function of the temperature is given by:

$$K_{eq}(T) = e^{-\frac{\Delta G^0}{RT}} = \frac{(p_{H_2})^{3/2}(p_{N_2})^{1/2}}{p_{NH_3}} \tag{5.2}$$

where $\Delta G^0$ is the change in Gibbs free energy of the reaction, $R$ is the gas constant and $T$ is the temperature. $p_{NH_3}$, $p_{H_2}$ and $p_{N_2}$ are the partial pressure of $NH_3$, $H_2$ and $N_2$, respectively, which are temperature dependent. The change in Gibbs free energy is defined as:

$$\Delta G^0 = \Delta H^0 - \Delta S^0 T \tag{5.3}$$

where $\Delta H^0$ is the change in enthalpy of the reaction and $\Delta S^0$ is the change in entropy. At room temperature the Gibbs free energy change for the $NH_3$ decomposition reaction is 16.4 kJ/mol and the change in enthalpy is 45.9 kJ/mol [140].
The partial pressure of $p_{NH_3}$ can be expressed with respect to the partial pressure of nitrogen as:

$$p_{NH_3} = p^0_{NH_3} - 2p_{N_2} \tag{5.4}$$

where $p^0_{NH_3}$ is the initial partial pressure of $NH_3$. Using Eq. 5.2, 5.4 and the following scaling relation:

$$p_{H_2} = 3p_{N_2}, \tag{5.5}$$

the equilibrium constant $K_{eq}(T)$ can be expressed only in terms of $p_{N_2}$, $p_{H_2}$ or $p_{NH_3}$. By solving the resulting equations numerically, the equilibrium partial pressures can be plotted as a function of the temperature, as shown in Fig. 5.2. For an initial pressure of 5 mbar $NH_3$ in 1 bar of He, it is found that full conversion is reached for temperatures above 100°C.

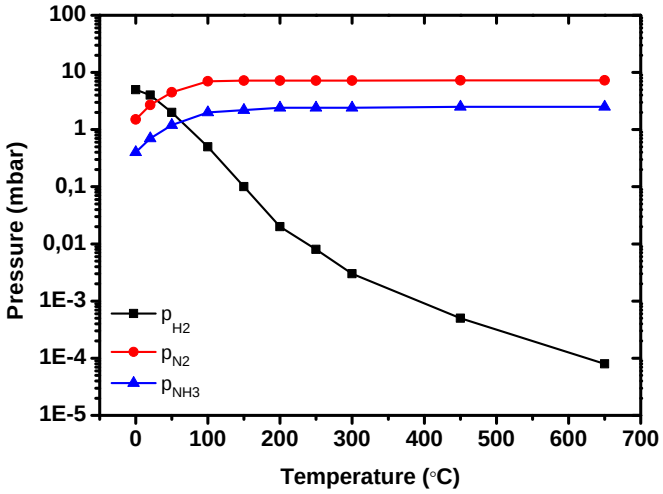


Figure 5.2: The equilibrium partial pressures of $NH_3$, $H_2$ and $N_2$ as a function of temperature for the $NH_3$ decomposition reaction.

In the microkinetic model for the $NH_3$ decomposition reaction a Langmuir-Hinshelwood path consisting of the following elementary reaction steps is followed [141]:

$$NH_3 + * \overset{K_1}{\leftrightarrows} NH_3^* \tag{R1}$$

$$NH_3^* + * \overset{K_2}{\leftrightarrows} NH_2^* + H^* \tag{R2}$$

$$NH_2^* + * \overset{K_3}{\leftrightarrows} NH^* + H^* \tag{R3}$$

$$NH^* + * \overset{K_4}{\leftrightarrows} N^* + H^* \tag{R4}$$

$$N^* \overset{K_5}{\leftrightarrows} N_2 + 2^* \tag{R5}$$

$$H^* \overset{K_6}{\leftrightarrows} H_2 + 2^* \tag{R6}$$

where $^*$ denotes a free site on the surface and $X^*$ denotes a species adsorbed on a site. The recombination and desorption of atomic nitrogen on the surface, i.e. R5, is identified as the rate limiting step of the overall reaction [142]. The overall reaction rate, $r$, can be therefore expressed as:

$$r = 2k_5^+\theta_N^2 - 2k_5^-\theta_*^2 p_{N_2} = 2k_5^+\left(\theta_N^2 - \frac{1}{K_5}p_{N_2}\theta_*^2\right) \tag{5.6}$$

where $K_5 = k^+/k^-$ describes the relation between the forward and backwards rate constants. $\theta_*$ denotes the coverage of free sites on the surface and $\theta_N$ is the coverage of atomic nitrogen adsorbed on a surface site.

The equilibrium rate constants of the elementary steps can be expressed in terms of the surface coverage of the individual species as follows:

$$K_1 = \frac{\theta_{NH_3}}{\theta_* p_{NH_3}} \quad \Leftrightarrow \quad \theta_{NH_3} = K_1 p_{NH_3} \theta_* \tag{5.7a}$$

$$K_2 = \frac{\theta_{NH_2}\theta_H}{\theta_* \theta_{NH_3}} \quad \Leftrightarrow \quad \theta_{NH_2} = \frac{K_2 \theta_{NH_3} \theta_*}{\theta_H} \tag{5.7b}$$

$$K_3 = \frac{\theta_{NH}\theta_H}{\theta_* \theta_{NH_2}} \quad \Leftrightarrow \quad \theta_{NH} = \frac{K_3 \theta_{NH_2} \theta_*}{\theta_H} \tag{5.7c}$$

$$K_4 = \frac{\theta_N \theta_H}{\theta_* \theta_{NH}} \quad \Leftrightarrow \quad \theta_N = \frac{K_4 \theta_{NH} \theta_*}{\theta_H} \tag{5.7d}$$

$$K_6 = \frac{p_{H_2}\theta_*^2}{\theta_H^2} \quad \Leftrightarrow \quad \theta_H = \sqrt{\frac{p_{H_2}}{K_6}}\theta_* \tag{5.7e}$$

By combining these equations it follows that the coverage of free sites, $\theta_*$ can be expressed in terms of the partial pressures of $NH_3$, $N_2$ and $H_2$ and the surface coverage of atomic nitrogen, $\theta_N$:

$$\theta_*^2 = \frac{{p_{H_2}}^3}{K_1^2 K_2^2 K_3^2 K_4^2 K_6^3 p_{NH_3}^2} \theta_N^2 \tag{5.8}$$

The physical requirement of conservation of sites on the surface gives:

$$\theta_* + \theta_{NH_3} + \theta_{NH_2} + \theta_{NH} + \theta_N + \theta_H = 1 \tag{5.9}$$

The number of surface sites occupied by a nitrogen atom can now be expressed in terms of partial pressures and equilibrium constants as:

$$\theta_N = \left(1 + \frac{p_{H_2}^{3/2}}{K_2 K_3 K_4 K_6^{3/2}} + \frac{p_{H_2}}{K_3 K_4 K_6} + \frac{p_{H_2}^{1/2}}{K_4 K_6^{1/2}} + \frac{p_{H_2}^{3/2}}{K_1 K_2 K_3 K_4 K_6^{3/2} p_{NH_3}} + \frac{p_{H_2}^2}{K_1 K_2 K_3 K_4 K_6^2 p_{NH_3}}\right)^{-1} \tag{5.10}$$

The overall reaction rate described in Eq. 5.6 can now be written as:

$$r = 2{k_5}^+ \theta_N^2 \left(1 - \frac{p_{N_2} p_{H_2}^3}{K_5 K_1^2 K_2^2 K_3^3 K_4^2 K_6^3 p_{NH_3}^2}\right) = 2{k_5}^+ \theta_N^2 (1 - \beta) \tag{5.11}$$

where the term $\beta$ describes the approach to thermodynamic equilibrium. Since the experiments are performed at conditions far from equilibrium, this means that the rate can be simplified to:

$$r = 2{k_5}^+ \theta_N^2, \tag{5.12}$$

where $\theta_N$ is given by Eq. 5.10. The decomposition rate depends on the partial pressure of $NH_3$ and also of hydrogen, which inhibits the decomposition reaction by driving the equilibrium of the elementary reactions $R2 - R5$ towards the left. It would have been interesting to perform the reaction in an initial high partial pressure of hydrogen, but due to time limitations this was not done.

## 5.2 Results

### 5.2.1 Background measurements

When evaporating a pattern of metal films on the HOPG one of the positions is left free from metal for background measurements, since the activity of a metal is measured relative to the background signal. However, it is observed that the $N_2$ signal over a metal free area of the support depends on the location of this area on the HOPG. Therefore an extended background analysis is conducted by carrying out the $NH_3$ decomposition reaction on a clean $Ar^+$ sputtered HOPG substrate. The background signal for $N_2$ is measured as a function of the temperature over a $3 \times 3$ position pattern and the result is shown in Fig. 5.3(a). It is found that the background signal changes with the position on the HOPG and increases with increasing temperature. A map of the $N_2$ signal is shown in Fig. 5.3(b), acquired by scanning the sniffer over the whole HOPG for several hours. The black square indicates the edges of the HOPG and the black circles represent the nine positions of the pattern. It can be seen that the lowest signal is measured towards the center of the HOPG and the highest signal is measured towards the edges.

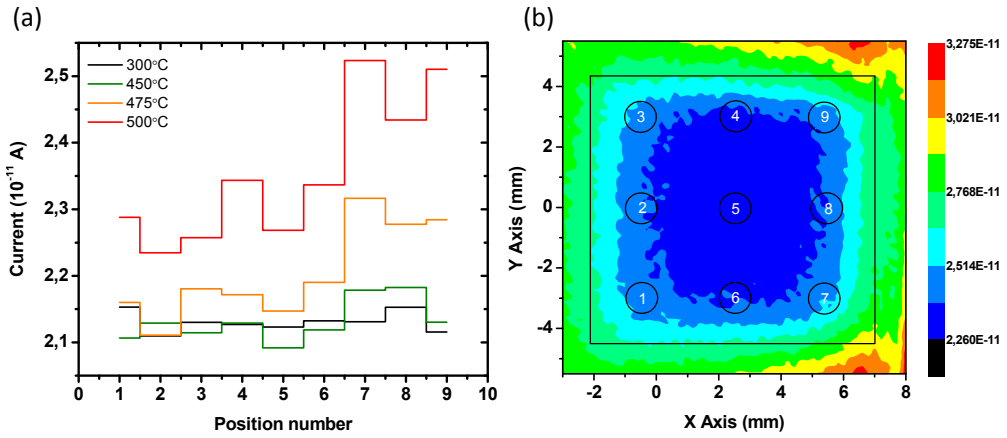


Figure 5.3: (a) $N_2$ measurement over a $3 \times 3$ position pattern on a sputtered HOPG substrate. The temperature is indicated in the legend. (b) The map of the $N_2$ signal measured at 475°C over the whole HOPG.

By looking at the HOPG through the windows of the HPC during the acquisition of the map it can be seen that the W-filaments used for heating the sample are

glowing red hot, which indicates a local temperature of the filaments above 700°C. The high background signal of $N_2$ is therefore due to the $NH_3$ decomposition on the W-filaments, which affects the background measurements at the edges of the HOPG.
For an active catalysts as Ru, the signal measured is roughly three times higher than the highest background signal. However, for less active metals, it is important to choose a location close to the center of the HOPG for background measurements or else their activity could be masked by the background signal. Moreover, it is also important to locate the background position close to the least active catalyst in the pattern, since also spillover effects are observed. In order to eliminate such effects the positions on the HOPG are revised and only five catalysts in a cross pattern are deposited, with a distance of 6 mm between two neighbor catalysts, as illustrated in Fig. 5.4. The background level for $N_2$ is then measured in between two films and the lowest signal is used as global background. Further details about background measurements and the spillover effect can be found in [143].

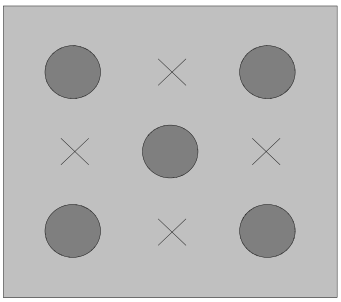

Figure 5.4: Schematic drawing of a cross pattern on the HOPG substrate.

### 5.2.2 $NH_3$ decomposition on metal Films

50 Å thick films of Ru, Ir, Pt and Rh are deposited on a sputtered HOPG substrate. The reason for choosing Ru and Ir is related to the high activity of these metals, which are eventually also tested in alloys, as mentioned earlier in this chapter. Pt and Rh are chosen since they are reported to be good catalysts for the $NH_3$ oxidation reaction [144, 145]. However, due to time limitation, it was unfortunately not possible to carry out this reaction and only the decomposition reaction is investigated on these metals.
After deposition the cleanliness of the surfaces is checked by XPS and ISS, and the sample is transferred to the HPC for testing the activity at 1 bar of $NH_3$/He in the temperature range $200 - 450$°C. The measurements are carried out for decreasing temperatures starting at 450°C. To check that the catalysts do not deactivate, the first measurement is always repeated at the end of the series. The activity is measured as a relative ion current of $N_2$ given by:

$$I_{rel} = \frac{I_{N_2} - I_{Bg}}{I_{He}} \tag{5.13}$$

where $I_{N_2}$ is the measured ion current for $N_2$, $I_{Bg}$ is the background signal and $I_{He}$ is the measured ion current for He. The results are reported in Fig. 5.5, where the relative signal of $N_2$, $I_{rel}$, is plotted as a function of the temperature. It is found that Ru is the most active catalyst among the tested metals and the activity decreases in the order: Ru>Ir>Rh>Pt. Although according to the volcano curve in Fig. 5.1, Rh is expected to be more active than Ir, the results obtained from these experiments are in agreement with the trend described in [45].
ISS spectra acquired before and after the reactions with the same settings are reported in Fig. 5.6. Only a narrow energy window around the peak generated by each metal is shown, since no other peaks are measured, indicating that no contaminants, such as sulfur, are present on the surface of the catalysts. It can be seen that after the reaction all the signals are lower compared to the ones measured after deposition. This could indicate that light species are adsorbed on the surface of the metals, such as hydrogen. However, XPS spectra reveal a decrease in the metals' signal and an increase in the carbon signal after the reaction compared to signals measured after deposition. As an example, the XPS spectra acquired before and after the reaction from a 50 Å Rh film are shown in Fig. 5.7, in the energy range $330 - 260$ eV containing the Rh and the carbon signals. This is likely due to the fact that the reaction is carried out at high temperature and no solution has been found to prevent carbon poisoning the metals which are deposited on HOPG.

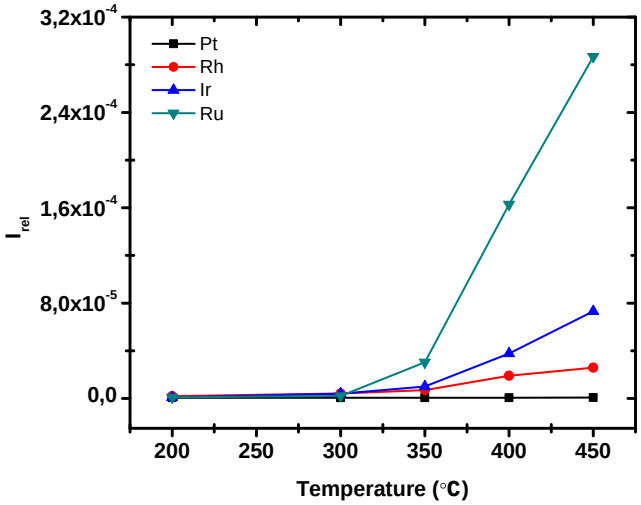


Figure 5.5: Measured $N_2$ signal as a function of the temperature 50 Å films of Ru, Ir, Pt and Rh.

### 5.2.3 $NH_3$ decomposition on Ru nanoparticles

Ru films of an average thickness from 0.5 to 50 Å are deposited on a sputtered HOPG substrate. According to the STM analysis described in section 3.2.1, the films consist

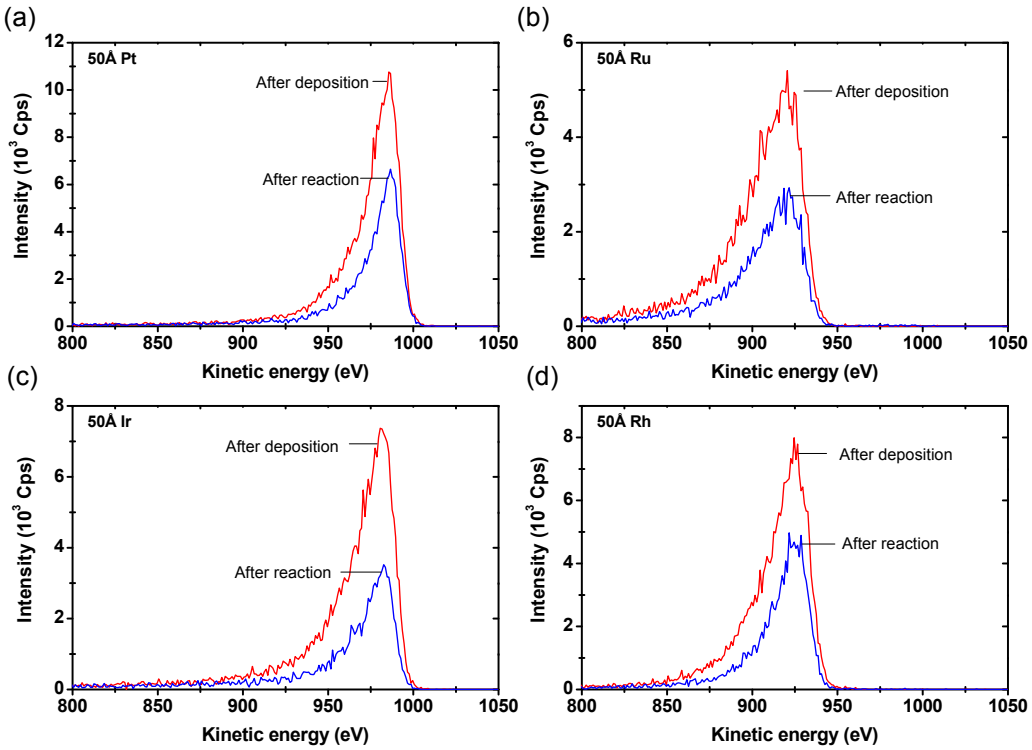


Figure 5.6: ISS spectra for 1 keV $He^+$ ions scattered from films of Pt (a), Ru (b), Ir (c) and Rh (d) before and after the $NH_3$ decomposition reaction.

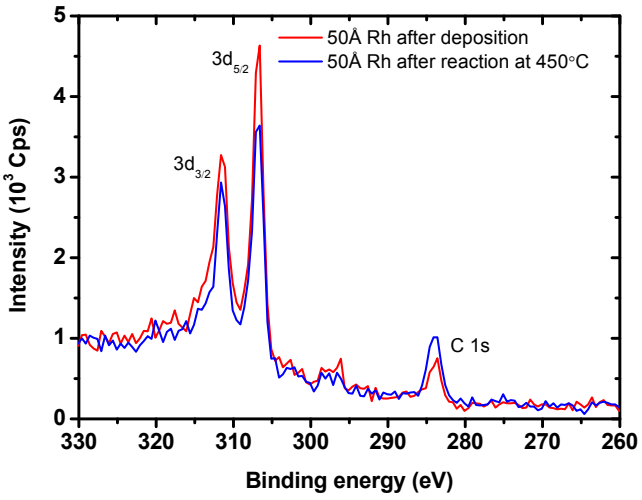


Figure 5.7: XPS spectra acquired from a 50 Å Rh film after deposition and after the $NH_3$ decomposition reaction.

of nanoparticles with diameter from 2 to 5 nm. The films are characterized by ISS and the sample is transferred to the HPC for testing the activity at 1 bar of $NH_3$/He in the temperature range $300 - 500°C$. Fig. 5.8 shows the relative signal of $N_2$, $I_{rel}$, which is normalized by the active surface area, as derived in section 3.2.2. The signal is plotted as a function of the film thickness and the particle diameter is also indicated in the plot. The measurements are carried out for decreasing temperatures starting at 500°C and the first measurement is repeated at the end of the series. A signal higher than the background level is measured only for films with thicknesses between 5 and 50 Å, corresponding to particles with diameter in the range 3 to 5 nm, as seen in Fig. 3.4. The decomposition rate is found to increase with increasing temperature, but it is hard to draw definitive conclusions on the effect of the particle size on the rate, since only a narrow particle range is investigated and no significant changes are observed in this range. Although the decrease of the decomposition rate for the particles which have a diameter smaller than 5 nm could indicate that the larger particles are more active than the smaller ones, the latter could be more affected by the carbon poisoning at high temperature. In order to clarify this point, experiments should be repeated on nanoparticles supported on a carbon free material. The maxima shown in Fig. 5.8 for the 8 Å films are most likely an artefact generated by the underestimation of the area used to correct the signal measured for this film.

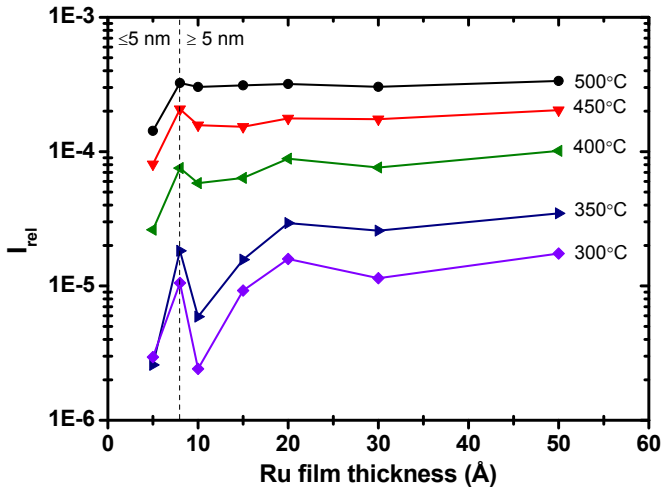


Figure 5.8: Measured $N_2$ signal as a function of the film thickness in the temperature range $300 - 500°C$. The particle diameter is also indicated.

### 5.2.4 $NH_3$ decomposition on Ir/Ru and Ni/Fe alloys

Ir overlayers on Ru films are deposited on a sputtered HOPG substrate, by preparing first a cross pattern of 50 Å thick Ru films and then depositing on top of each film an amount of Ir which varies between 0.5 and 10 Å. Thicker overlayers are not tested

for the reaction due to time limitations. Pure Ru and Ir films, 50 Å thick, are also deposited and tested for comparison.
Fig. 5.9 shows the relative signal of $N_2$, $I_{rel}$, as a function of the Ir film thickness. The reaction is carried out at 1 bar of $NH_3$/He in the temperature range $300 - 500°C$. The measurements are performed for decreasing temperatures starting at 500°C and the first measurement is repeated at the end of the series. It is found that the decomposition rate is higher for Ru than for Ir and that it increases with increasing temperature. Moreover a rate higher than for the pure Ru is measured for all the overlayers, with a maximum corresponding to 10 Å Ir on 50 Å Ru.
Arrhenius plots of the decomposition rate, $r$, for the Ir overlayers on Ru films are shown in Fig. 5.10(a). Straight lines are obtained from a least squares fits of the logarithm of the rate. Fig. 5.10(b) shows the apparent activation energy, $E_{act}$, as a function of the Ir film thickness. $E_{act}$ is higher for Ir than for Ru and decreases to a nearly constant level for all the overlayers, except for the 0.5 Å Ir, which gives a value for $E_{act}$ closer to the one derived for pure Ru.

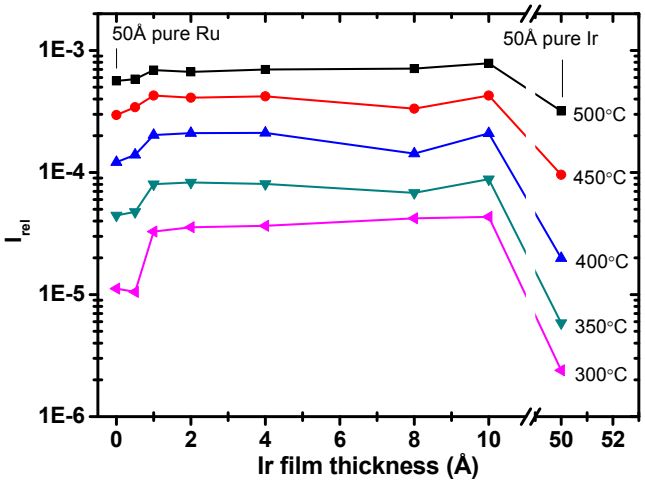


Figure 5.9: Measured $N_2$ signal as a function of film thickness for the Ir overlayers on Ru films, in the temperature range $300 - 500°C$.

ISS is performed on the overlayers in order to gain information on the surface composition. Fig. 5.11(a) and (b) shows ISS spectra for 1keV $He^+$ ions scattered from the Ir/Ru surfaces after metal deposition and after carrying out the $NH_3$ decomposition reaction in the HPC. Since no peaks are observed at low energy, only the high energy region of the ISS spectra, which contains the Ru peak at 930 eV and the Ir peak at 998 eV are shown. The surface concentrations, which are derived according to Eq. 2.2, are shown in Fig. 5.11(c) and (d). Again, the ISS signals after the reaction are lower compared to the ones measured after deposition. Although XPS spectra have not been acquired, the decrease is likely due to to carbon poisoning or also to the presence of hydrogen adsorbed on the catalysts' surface. Unfortunately

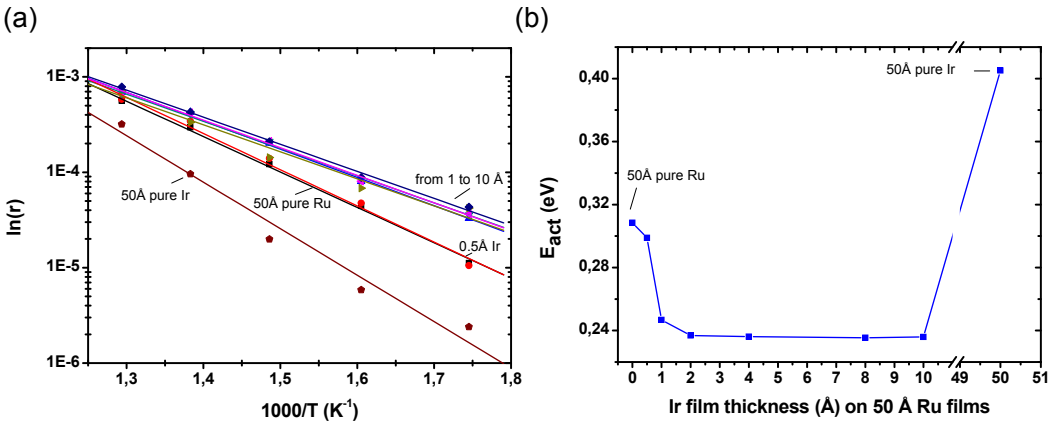


Figure 5.10: (a) Arrhenius plot of the decomposition rate for the Ir overlayers on Ru films. (b) Activation energies as a function of the Ir film thickness as derived from the Arrhenius plots.

none of the two elements can be measured with ISS, but the presence of heavier contaminants can be excluded.
It is found that Ru and Ir are both present on the surface of all the overlayers, indicating the formation of a surface alloy. When comparing the spectra obtained after deposition and after reaction a change in the surface concentration is observed, which is significant for the thickest overlayers. After deposition the Ir surface concentration is between 5% and 80%, whereas the final surface concentration is found to be between 5% and 10% for all the overlayers, indicating a tendency for Ru to segregate to the surface. According to DFT calculations performed on segregation energies of a solute in a host, Ir shows a moderate surface segregation in a Ru matrix [70]. However, the $NH_3$ decomposition reaction is carried out at high pressure of $NH_3$/He and temperatures up to 500°C, which could invalidate this tendency.
In literature there is no indications of experiments performed on Ir/Ru alloys for the $NH_3$ decomposition reaction. Since the two metals are placed at the two sides of the volcano curve shown in Fig. 5.1, it is likely that the enhancement of the overlayers activity compared to Ru is related to the modification of the chemical properties of the surface due to the alloy formation, leading to the changes in the *d*-band center of the surface alloy, as in the case of the Pt/Ru alloys. Ir/Ru alloys containing around 10% of Ir on the surface are found to give a higher decomposition rate compared to Ru and a lower apparent activation energies, likely indicating a lower nitrogen binding energy.
The $NH_3$ decomposition reaction is also carried out on 1 mm diameter films of Ni, Fe and on Ni/Fe overlayers with different ratio, prepared in a similar way as the Ir/Ru overlayers. Unfortunately no activity at all is measured for these metals at temperatures up to 500°C. A test is also carried out on 3 mm diameter films, with no success. ISS spectra are acquired from the pure metals before and after reaction and the results are reported in Fig. 5.12. The spectra show a narrow energy window

where the Fe and the Ni peaks are located at 840 and 857 eV, respectively. It can be seen that the ISS signals of the pure metals decreases significantly after the reaction.

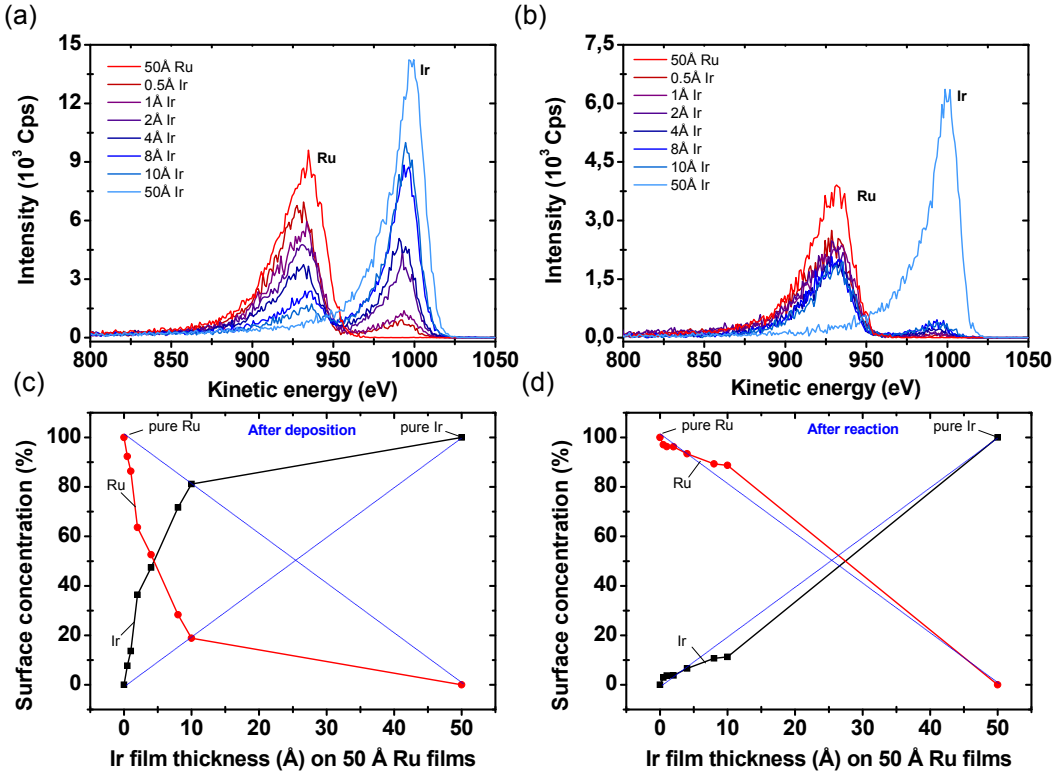


Figure 5.11: ISS spectra for 1 keV $He^+$ ions scattered from the Ir overlayers on Ru films, after deposition (a) and after the reaction (b). Surface concentrations corresponding to the ISS spectra after deposition (c) and after the reaction (d).

Also XPS spectra are acquired before and after the reaction and a spectra from a 50 Å Ni film is shown in Fig. 5.13. It can be seen that the Ni signal decreases while the carbon signal increases significantly, indicating that the catalyst is severely poisoned by carbon after the reaction. In literature several studies on Fe and Ni describe the carbon formation on such catalysts when carrying out reaction in the presence of gases containing carbon, as in the case of the steam reforming process [146–150]. The reason why it is not possible to measure a decomposition rate on Ni, Fe and on Ni/Fe overlayers is likely due to carbon poisoning of the catalysts in combination with a lower activity of these materials compared to Ru and Ir at temperatures up to 500°C.

## 5.3 Summary and conclusions for this part

The $NH_3$ decomposition reaction at 1 bar $NH_3$/He is measured on Ru, Ir, Rh and Pt films, on Ru nanoparticles and on Ir/Ru and Ni/Fe alloys in the temperature

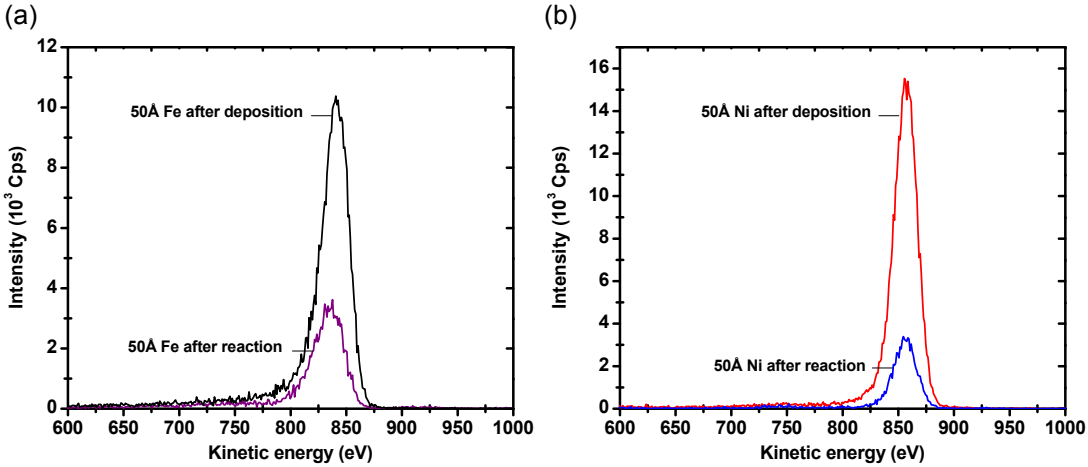


Figure 5.12: ISS spectra for 1 keV $He^+$ ions scattered from 50 Å films of Fe (a) and Ni (b) before and after the $NH_3$ decomposition reaction.

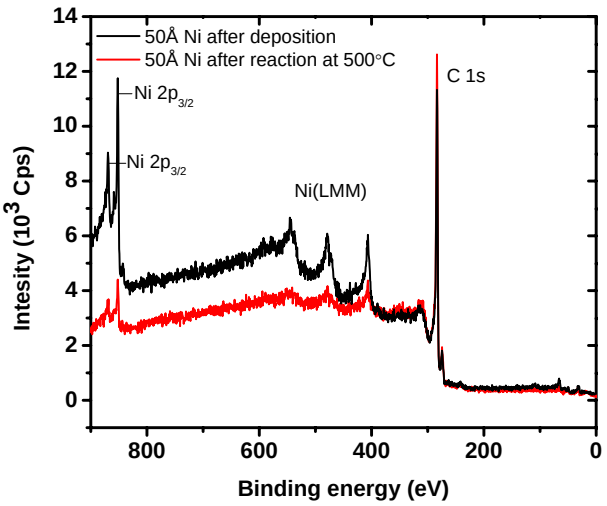


Figure 5.13: XPS spectra acquired from a 50 Å Ni film after deposition and after the $NH_3$ decomposition reaction.

range $300 - 500°C$. Despite many difficulties encountered in order to be able to carry out the reaction, some indicative results are obtained. In the case of the metal films, it is found that the $N_2$ signal, which is considered a reliable measurement of the decomposition rate, is highest for Ru and decreases in the order Ru>Ir>Rh>Pt. This result confirms the general trend observed in literature. The decomposition rate is also measured on Ir overlayers on Ru films, with the thickness of the overlayers varying from 0.5 to 30 Å. A decomposition rate higher than for Ru is measured for all the overlayers, with a maximum corresponding to 10 Å Ir on 50 Å Ru. ISS spectra show that both Ru and Pt are present on the surface, which indicates the

formation of a surface alloy. It is also found that the maximum activity is given by the alloys containing roughly 10% Ir on the surface. Experiments are also carried out on Ru nanoparticles and on Ni/Fe alloys, but unfortunately no conclusion can be drawn from the measurements, which are believed to be higly affected by carbon poisoning at high temperature.

# 6 General conclusions

Three main projects have been carried out during the PhD period and the most relevant experimental results have been described in this thesis. The focus of two of the projects was investigating the $H_2$ dissociation and the $NH_3$ decomposition reaction, respectively, on a range of supported metal films, nanoparticles and alloys, whereas the aim of the third was to understand how the support affects the catalytic activity of the metals.

The $H_2$ dissociation was probed by the H-D exchange reaction. It is found that the activity for Ru and Rh is strongly dependent on the particle size, with the larger particles being more active, whereas the activity for Pt does not show any dependence on size. It is suggested that the strong variation for Ru and Rh is due to the formation of compressed hydrogen adlayers on the terraces of the larger particles. In the case of the Pt/Ru alloys, it is found that the activity exceeds the values measured on the individual metals and has a maximum on alloys with surface composition of Pt:Ru equal to a 1:1 ratio. Experiments carried out in the presence of CO show no evidence of special nanoparticle diameters that improve the resistance to CO poisoning. However the CO resistance is improved by alloying Pt with Ru, with the alloys containing more Ru being more resistent.

The effect of the HOPG support on the H-D exchange rate for Pt and Ru has been investigated, after the metals have been annealed to high temperature in UHV. It is found that after annealing the metals get covered by $1-2$ layers of carbon and this decreases drastically their ability of adsorb hydrogen, with a consequent decrease in the exchange rate. It is also shown how to regenerate the catalysts performing $He^+$ sputtering.

Concerning the $NH_3$ decomposition reaction, it is found that Ru is the most active among the selected metals and that the catalytic activity decreases in the order Ru>Ir>Rh>Pt. Alloying Ru with Ir shows an enhancement of the activity and a maximum is found when 10% Ir is on the surface of the alloy. At the moment, no clear conclusion can be made on the effect of the particle size on the decomposition rate and it was not possible to measure any activity on the Ni/Fe alloys. The reason for that is believed to be the carbon poisoning the catalysts when measuring at high temperature.

Experiments have been performed in a UHV apparatus, consisting of a prepara-

tion chamber combined to a high pressure cell. The apparatus is named *Parallel Screening*, which has widely proven its ability to allow the screening of a pattern of catalysts both regarding the catalytic activity and the surface characterization. A series of catalysts was tested in a short period of time, typically a week. For many years preceding the beginning of this PhD, the experimental setup has been used and optimized for running the H-D exchange reaction on typically 1 mm diameter supported films. While ISS and AES/SEM were able to provide information on single films, for XPS modifications of the lens system of the hemispherical analyzer were needed in order to improve the resolution of this technique. This was fixed soon after the beginning of the PhD, allowing experiments on the exchange reaction and surface characterization to proceed smoothly. However, many difficulties have been encountered in order to be able to perform clean and reproducible experiments concerning the $NH_3$ decomposition reaction, due to the complexity of carrying out this reaction compared to the exchange reaction. The main difference is the reaction temperature that is much higher for the $NH_3$ decomposition reaction compared to the exchange reaction. Heating the system up to 500°C causes severe catalyst deactivation and leads to carbon poisoning. In order to get rid of contaminants, such as sulfur and lead, an efficient cleaning procedure has been developed. However, no solutions have been found to prevent the carbon poisoning when measuring at high temperature on metals supported on HOPG.

## 6.1 Outlook

More experiments on the $NH_3$ decomposition reaction are going to be conducted in the *Parallel Screening* apparatus to hopefully be able to answer some questions which have not found a clear answer yet. For instance, more accurate measurements on the Ru nanoparticles are needed to determine the effect of the size on the decomposition rate. Moreover it would be interesting to investigate a larger range of Ir overlayers on the Ru films and also cheaper alloys, such as Mo/Co and Ni/Fe. Since the biggest obstacle to perform good measurements seems to be the carbon poisoning the catalysts when working at high temperature, a decision to change the support has been taken. Among the different possibilities, $TiO_2$ has been chosen as new substrate. This choice is based on several aspects: $TiO_2$ provides a smooth surface which can be sputtered and annealed in the UHV chamber, it is a semiconductor which allow to perform surface analysis and it is compatible with the carbon glue which was used to fix the HOPG on the carbon disk. In general, $TiO_2$ is a very well studied material and a review on the surface science studies on this system can be found in [151]. Preliminary tests have already been carried out at the experimental setup, showing that it is possible to measure the decomposition rate on a Ru film deposited on $TiO_2$ and perform surface analysis, looking promising for future experiments. Although $TiO_2$ is a carbon free substrate, some tests have to be carried out in order to see whether any metal support interaction occurs when measuring the $NH_3$ decomposition rate at high temperature, which could also

affect the performance of the catalysts. Actually, in literature it is reported that the catalytic activity of Ru for the $NH_3$ decomposition reaction is support dependent [39, 152–154]. Surprisingly, the highest activity is measured on Ru deposited on carbon based materials, such as carbon nanotubes, also at 500°C [49]. Possible problems related to carbon poisoning are not mentioned. However, the experiments reported in literature are carried out at a higher pressure of $H_2$ compared to the ones described in this thesis, which could help cleaning the catalysts from carbon during the progress of the reaction.
At the moment, a gas mixture of 5000 ppm $NH_3$ in He is used during experiments, but a mixture of 5000 ppm $NH_3$ in Ar is going to be used in the future. This choice is based on the fact that Ar has a thermal conductivity which is roughly 10 times lower than He, which could help the process of heating the gas mixture during experiments. Moreover, this is expected to significantly reduce the background level of the signal measured at 2 AMU, which is attributed to $He^{++}$, and hopefully allow to use also the $H_2$ signal as a measurement for the decomposition rate.
Finally, the AES/SEM system has been replaced by a new mass spectrometer equipped with a long cupper tip having a cone shaped overture of 1 mm, which can be moved in the z-direction inside the UHV chamber. This mass spectrometer will be use to perform Temperature Programmed Desorption measurements in order to get information on the active surface area of the individual films, which at moments relies on the calculations described in section 3.2.2. Moreover, any changes after the reaction compared to after deposition could be monitored with these kind of measurements.

# Bibliography


[1] E.M. Fiordaliso, S. Murphy, R.M. Nielsen, S. Dahl, I. Chorkendorff, *Surf. Sci.* **606** (2012) 263.

[2] E.M. Fiordaliso, S. Dahl, I. Chorkendorff, *J. Phys. Chem. C* **115** (2011) 25351.

[3] BP Statistical review of world energy, 2011.

[4] B.L. Yi in: *Fuel CellPrinciple*, (Technology and Application, Chemical Industry Press, Beijing, 2003).

[5] J. Larminie, A. Dicks, in: *Fuel Cell Systems Explained,* $2^{nd}$ *Edition* (John Wiley & Sons, 2003).

[6] Ballard Power Systems, *http://www.ballard.com/about-ballard/fuel-cell-education-resources/how-a-fuel-cell-works.aspx*

[7] J.J. Baschuk, X. Li, *Int. J. Energy Res.* **25** (2001) 695.

[8] H. Igarashi, T. Fujino, M. Watanabe, *J. Electroanal. Chem.* **391** (1995) 119.

[9] S. Chen, B.D. Adams, A. Chen, *Electrochimica Acta* **56** (2010) 61.

[10] I. Pino, G.J. Kroes, M.C. van Hemert, *J. Chem. Phys.* **133** (2010) 184304.

[11] L. Wang, R.T. Yang, *J. Phys. Chem. C* **112** (2008) 12486.

[12] M. Yamauchi, H. Kobayashi, H. Kitagawa, *ChemPhysChem.* **10** (2009) 2566.

[13] H. Kobayashi, M. Yamauchi, H. Kitagawa, Y. Kubota, K. Kato, M. Takata, *J. Am. Chem. Soc.* **132** (2010) 5576.

[14] R. Campesi, F. Cuevas, E. Leroy, M. Hirscher, R. Gadiou, C. Vix-Guterl, M. Latroche, *Microp. Mesop. Mater.* **117** (2009) 511.

[15] T. Engel, G. Ertl, in: *The Chemical Physics of Solid Surfaces and Heterogeneous Catalysis*, Vol. 4, Fundamental Studies of Heterogeneous Catalysis (Elsevier, Amst. 1982), ISBN 0-444-41987-x.

[16] J.M. White, S. Akhter, *CRC Crit. Rev. Solid State Mater. Sci.* **14** (1988) 131.

[17] B. Riedmüller, D.C. Papageorgopoulos, B. Berenbak, R.A. van Santen, A.W. Kleyn, *Surf. Sci.* **515** (2002) 323.

[18] I.M. Ciobica, A.W. Kleyn, R.A. van Santen, *J. Phys. Chem. B* **107** (2003) 164.

[19] M. Johansson, O. Lytken, I. Chorkendorff, *Top. Catal.* **46** (2007) 175.

[20] M. Johansson, O. Lytken, I. Chorkendorff, *J. Chem. Phys.* **128** (2008) 034706.

[21] M. Johansson, O. Lytken, I. Chorkendorff, *Surf. Sci.* **602** (2008) 1863.

[22] M.P. Hogarth, G.A. Hards, *Platinum Metals Rev* **40** (1996) 150.

[23] T.R. Ralph, Platinum *Metals Rev.* **41** (1997) 102.

[24] F. Maillard, F. Gloaguen, F. Hahn, J.M. Lger, *Fuel Cells* **2** (2002) 143.

[25] F. Buatier de Mongeot, M. Scherer, B. Gleich, E. Kopatzki, R.J. Behm, *Surf. Sci.* **411** (1998) 249.

[26] M. Markovic, P.N. Ross, *Surf. Sci. Rep.* **45** (2002) 117.

[27] B.E. Conway, B.V. Tilak, *Electrochim. Acta* **47** (2002) 3571.

[28] H.A. Gasteiger, N.M. Markovic, P.N. Ross, *J. Phys. Chem.* **99** (1995) 8290.

[29] J. Greeley, M. Mavrikakis, *Nat. Mat.* **3** (2004) 810.

[30] *Basic research needs for the hydrogen economy*(Office of science, U.S. Department of energy, 2003).

[31] A. Züttel, *Mat. Today* **6** (2003) 24.

[32] H.H. Van Mal, K.H.J. Buschow, A.R. Miedema, *J. less-Comm. Met.* **35** (1974) 65.

[33] L. Schlapbach, A. Züttel, *Nature* **414** (2001) 353.

[34] Amminex, *http://www.amminex.net/technology/the-solid-formula.aspx*

[35] C.H. Christensen, R.Z. Sørensen, T. Johannessen, U.J. Quaade, K. Honkala, T.D. Elmøe, R. Køhlera, J.K. Nørskov, *J. Mat. Chem.* **15** (2005) 4106

[36] R. Halseid, P.J.S. Vie, R. Tunold, *J. Power Sources* **154** (2006) 343.

[37] J.R. Varcoe, R.C.T. Slade, *Fuel Cells* **5** (2005) 187.

[38] D.A. Goetsch, S.J. Schmit, *WO Patent* 0187770 (2001).

[39] S.F. Yin, Q.H. Zhang, B.Q. Xu, W.X. Zhu, C.F. Ng, C.T. Au, *J. Catal.* **224** (2004) 384.

[40] T.V. Choudhary, C. Svadinaragana, D.W. Goodman, *Catal. Lett.* **72** (2001) 197.

[41] J.G. Choi, M.K. Jung, S. Choi, T.K. Park, I.H. Kuk, J.H. Yoo, H.S. Park, H.S. Lee, D.H. Ahn, H.S. Chung, *Bull. Chem. Soc. Jpn.* **70** (1997) 993.

[42] J.G. Choi, J. Ha, J.W. Hong, *Appl. Catal. A: Gen.* **168** (1998) 47.

[43] C.H. Liang, W.Z. Li, Z.B. Wei, Q. Xin, C. Li, *Ind. Eng. Chem. Res.* **39** (2000) 3694.

[44] M.C.J. Bradford, P.E. Fanning, M.A. Vannice, *J. Catal.* **172** (1997) 479.

[45] G. Papapolymerou, V. Bontozoglou, *J. Mol. Catal. A: Chem.* **120** (1997) 165.

[46] S.J. Wang, S.F. Yin, L. Li, B.Q. Xu, C.F. Ng, C.T. Au, *Appl. Catal. B: Environ.* **52** (2004) 287.

[47] K. Hashimoto, N. Toukai, *J. Mol. Catal. A: Chem.* **161** (2000) 171.

[48] S. Litster, G. McLean, *Journal of Power Sources* **130** (2004) 61.

[49] S.F. Yin, B.Q. Xu, X.P. Zhou, C.T. Au, *Appl. Catal. A: General* **277** (2004) 1.

[50] S.J. Tauster, S.C. Fung, R.L.J. Garten, *Amer. Chem. Soc.* **100** (1978) 170.

[51] M.A. Vannice, L.C. Hasselbring, B.J. Sen, *Phys. Chem.* **89** (1985) 2972.

[52] B. Sen, M.A. Vannice, *J. Catal.* **9** (1991) 130.

[53] K. Chen, Y. Fan, Q. Yan, *J. Catal.* **167** (1997) 573.

[54] T. Koertz, W.J.J. Welters, R.A. van Santen, *J. Catal.* **134** (1992) 1.

[55] T. Ishihara, K. Harada, K. Egushi, H. Arai, *J. Catal.* **136** (1992) 161.

[56] G.L. Haller, D.E. Resasco, *Adv. Catal.* **36** (1989) 173.

[57] M. Johansson, J.H. Jørgensen, I. Chorkendorff, *Rev. Sci. Instrum.* **75** (2004) 2082.

[58] M. Johansson, T. Johannesen, J. Hoffman Jørgensen, I. Chorkendorff, *Appl. Surf. Sci.* **252** (2006) 3673.

[59] O. Ole Lytken in: *Dissociation of CO and Methane on Ni(14 13 13) and A Surface Science Approach to Parallel Screening*, Ph.D. Thesis, 2005).

[60] F. Claeyssens, S. Pratontep, C. Xirouchaki, R.E. Palmer, *Nanotechnology* **17** (2006) 805.

[61] R.M. Nielsen, S. Murphy, C. Strebel, M. Johansson, J.H. Nielsen, I. Chorkendorff, *Surf. Sci.* **603** (2009) 3420.

[62] G. Sauerbrey, *Z. Phys.* **155** (1959) 206.

[63] K.J. Ross, B. Sonntag, *Rev. Sci. Instrum.* **66** (1995) 4409.

[64] H.H. Brongersma, M. Draxler, M. de Ridder, P. Bauer, *Surf. Sci. Rep.* **62**, (2007), 63.

[65] A. Einstein, *Ann. Phys.* **17** (1905) 549.

[66] G.A. Somorjai, in: *Chemistry in Two Dimensions: Surfaces* (Cornell University Press, Ithaca, 1981).

[67] P.N. Rylander, in: *Catalytic Hydhogenation over Platinum Metals* (Academic, New York, 1967).

[68] E. Skúlason, V. Tripkovic, M.E. Björketun, S. Gudmundsdóttir, G. Karlberg, J. Rossmeisl, T. Bligaard, H. Jónsson, J.K. Nørskov, *J. Phys. Chem. C* **114** (2010) 18182.

[69] P. Costamagna, S. Srinivasan, *J. Power Sources* **102** (2001) 242.

[70] A.V. Ruban, H.L. Skriver, J.K. Nørskov, *Phys. Rev. B* **59** (1999) 15990.

[71] T. Bligaard, J.K. Nørskov, *Electrochimica Acta* **52** (2007) 5512.

[72] E. Christoffersen, P. Liu, A.V. Ruban, H.L. Skriver, J.K. Nørskov, *J. Cat.* **199** (2001) 123.

[73] C. Roth, A.J. Papworth, I. Hussain, R.J. Nichols, D.J. Schiffrin, *J. Electroanal Chem* **581** (2005) 79.

[74] H. Conrad, G. Ertl, E.E. Latta, *Surf. Sci.* **41** (1974) 435.

[75] R.J. Behm, K. Christmann, G. Ertl, *Surf. Sci.* **99** (1980) 320.

[76] K. Christmann, G. Ertl, T. Pignet, *Surf. Sci.* **54** (1976) 365.

[77] K.D. Rendulic, A. Winkler, *J. Chem. Phys.* **79** (1983) 5151.

[78] K. Christmann, O. Schober, G. Ertl, M. Neumann, *J. Chem.Phys.* **60** (1974) 4528.

[79] P.R. Norton, J.A. Davies, T.E. Jackman, *Surf. Sci.* **121** (1982) 103.

[80] R.M. Nielsen, S. Murphy, C. Strebel, M. Johansson, I. Chorkendorff, J.H. Nielsen, *J Nanopart Res.* **12** (2010) 1249.

[81] S. Dahl, A. Logadottir, R.C. Egeberg, J.H. Larsen, I. Chorkendorff, E. Trnqvist, J.K. Nørskov, *Phys. Rev. Lett.* **83** (1999) 1814.

[82] M.P. Andersson, F. Abild-Pedersen, I.N. Remediakis, T. Bligaard, G. Jones, J. Engbæk, O. Lytken, S. Horch, J.H. Nielsen, J. Sehested, J.R. Rostrup-Nielsen, J.K. Nørskov, I. Chorkendorff, *J. Catal.* **255** (2008) 6.

[83] M. Andersen, M. Johansson, I. Chorkendorff, *J. Phys. Chem. B* **109** (2005) 10285.

[84] S. Murphy, C. Strebel, S.B. Vendelbo, C. Conradsen, Y. Tison, K. Nielsen, L. Bech, R.M. Nielsen, M. Johansson, I. Chorkendorff, J.H. Nielsen, *Phys. Chem. Chem. Phys.* **13** (2011) 10333.

[85] P.B. Rasmussen, P.M. Holmblad, H. Christoffersen, P.A. Taylor, I. Chorkendorff, *Surf. Sci.* **287/288** (1993) 79.

[86] J.N. Russel Jr., S.M. Gates, J.T. Yates Jr., *J. Chem. Phys.* **85** (1986) 6792.

[87] J.T. Yates Jr., J.N. Russel Jr., I. Chorkendorff, S.M. Gates, in: *Springer Series in Surface Science* 8, eds. M. Grunze and H.J. Kreuzer (Springer-Verlag, Heidelberg, 1987).

[88] D.O. Hayward, A.O. Taylor, *Chem. Phys. Lett.* **124** (1986) 264.

[89] H. Karner, M. Luger, H.P. Steinrück, A. Winkler, K.D. Rendulic, *Surf. Sci. Lett.* **163** (1985) 641.

[90] I.M.N. Groot, A.W. Kleyn, L.B.F. Juurlink, *Angew. Chem. Int. Ed.* **50** (2011) 5174.

[91] A.C. Luntz, J.K. Brown, M.D. Williams, *J. Chem. Phys.* **93** (1990) 5240.

[92] P. Sanson, A. Nesbitt, B.A. Koel, A. Hodgson, *J. Chem. Phys.* **109** (1998) 3255.

[93] H.R. Siddiqui, X. Guo, I. Chorkendorff, J.T.Yates Jr., *Surf. Sci.* **191** (1987) *L*813.

[94] T. Iwasita, R. Dalbeck, E. Pastor, X. Xia, *Electrochim. Acta* **11/12** (1994) 1817.

[95] R. Ianniello, V.M. Schmidt, U. Stimming, J. Stumper, A. Wallau, *Electrochim. Acta* **39** (1994) 1863.

[96] S. Alayoglu, A.U. Nilekar, M. Mavrikakis, B. Eichhorn, *Nat. Mat.* **7** (2008) 333.

[97] H.A. Gasteiger, N. Markovic, P.N. Ross, E.J.J. Cairns, *Electrochem. Soc.* **141** (1994) 1795.

[98] L. Li, Y.J. Xing, *Phys. Chem. C* **111** (2007) 2803.

[99] B. Hammer, J.K. Nørskov, *Adv. Catal.* **45** (2000) 71.

[100] B. Hammer, J.K. Nørskov in: *Chemisorption and Reactivity on Supported Clusters and Thin Films*, R.L. Lambert, G. Pacchioni Eds., (Kluwer Academic Publishers, Dordrecht, 1997).

[101] J.R. Kitchin, J.K. Nørskov, M.A. Barteau, J.G. Chen, *Phys. Rev. Lett.* **93** (2004) 156801.

[102] A. Ruban, B. Hammer, P. Stoltze, H. L. Skriver, J.K. Nørskov, *J. Mol. Catal. A* **115** (1997) 421.

[103] R.J. Behm, *Z. Phys. Chem.* **223** (2009) 9.

[104] T. Diemant, T. Hager, H.E. Hoster, H. Rauscher, R.J. Behm, *Surf. Sci.* **541** (2003) 137.

[105] J.C. Davies, B.A. Hayden, D.J. Pegg, *Surf. Sci.* **467** (2000) 118.

[106] R.J. Behm, *Acta Physica Polonica A* **93** (1998) 259.

[107] M.T.M. Koper, T.E. Shubina, R.A. van Santen, *J. Phys. Chem. B* **106** (2002) 686.

[108] P. Liu, A. Logadottir, J.K. Nørskov, *Electrochim. Acta* **48** (2003) 3731.

[109] Q. Ge, S. Desai, M. Neurock, K. Kourtakis, *J. Phys. Chem. B* **105** (2001) 9533.

[110] Y. Ishikawa, M.S. Liao, C.R. Cabrera, *Surf. Sci.* **513** (2002) 98.

[111] T. Mitsui, M.K. Rose, E. Fomin, D.F. Ogletree, M. Salmeron, *Nature* **422** (2003) 705.

[112] M.F. Luo, G.R. Hu, M.H. Lee, *Surf. Sci.* **601** (2007) 1461.

[113] M. Tatarkhanov, F. Rose, E. Fomin, D. F. Ogletree, M. Salmeron, *Surf. Sci.* **602** (2008) 487.

[114] C. Pistonesi, E. Pronsato, A. Juan, *Appl. Surf. Sci.* **254** (2008) 5827.

[115] T. Diemant, H. Rauscher, R.J. Behm, *J. Phys. Chem. C* **112** (2008) 8321.

[116] A. Christensen, A.V. Ruban, P. Stoltze, K.W. Jacobsen, H.L. Skriver, J.K. Nørskov, *Phys. Rev. B* **56** (1997) 5822.

[117] A.V. Ruban, H.L. Skriver, J.K. Nørskov, *Phys. Rev. B* **59** (1999) 15990.

[118] Y. Ma, P.B. Balbuena, *Surf. Sci.* **602** (2008) 107.

[119] H.E. Hoster, A. Bergbreiter, P.M. Erne, T. Hager, H. Rauscherw, R. Behm, *J. Phys. Chem. Chem. Phys.* **10** (2008) 3812.

[120] H.R. Sadeghi, V.E. Henrich, *Appl. Surf. Sci.* **19** (1984) 330.

[121] M. Bowker, P. Stone, P. Morrall, R. Smith, R. Bennett, N. Perkins, R. Kvon, C. Pang, E. Fourre, M. Hall, *J. Catal.* **234** (2005) 172.

[122] M. Bowker, P. Stone, R. Bennett, N. Perkins, *Surf. Sci.* **497** (2002) 155.

[123] M. Bowker, E. Fourré, *Appl. Surf. Sci.* **254** (2008) 4225.

[124] M. Bowker, *Phys. Chem. Chem. Phys.* **9** (2007) 3514.

[125] Z.H. Qin, M. Lewandowski, Y.N. Sun, S. Shaikhutdinov, H.J. Freund, *J. Phys.: Condens. Matter* **21** (2009) 134019.

[126] Y. Zhou, J.M. Perket, J. Zhou, *J. Phys. Chem. C* **114** (2010) 11853.

[127] O. Dulub, W. Hebenstreit, U. Diebold, *Phys. Rev. Lett.* **84** (2000) 3646.

[128] J.B.F. Anderson, R. Burch, J.A. Cairns, *Appl. Catal.* **25** (1986) 173.

[129] S.J. Tauster, S.C. Fung, R.T.K. Baker, J.A. Horsley, *Science* **211** (1981) 1121.

[130] H.F. Sadeghi, V.E. Henrich, *J. Catal.* **87** (1981) 279.

[131] S.N., Mikhailov, R.J.M. Elfrink, J.-P. Jacobs, L.C.A. van den Oetelaar, P.J. Scanlon, H.H. Brongersma, *Nucl. Instrum. Methods Phys. Res.B* **93** (1994) 210.

[132] Q. Wei, K.D. Li, J. Lian, L. Wang, *J. Phys. D: Appl. Phys.* **41** (2008) 172002.

[133] P. Sigmund, *Phys. rev.* **184** (1969) 383.

[134] R. Behrisch, W. Eckstein, *Top. Appl. Phys.* **110** (2007) 33.

[135] D.A. Hansgen, D.G. Vlachos, J.G. Chen, *Nature Chem.* **2** (2010) 484.

[136] J.C. Ganley, F.S. Thomas, E.G. Seebauer, R.I. Masel, *Catal. Lett.* **96** (2004) 117.

[137] J.H. Sinfelt, in: *Bimetallic Catalysts: Discoveries, Concepts and Applications* (Wiley, New York, 1983).

[138] D. Lj. Stojíc, T.D. Grozdić, M.P.M. Kaninski, A.D. Maksić, N.D. Simić, *Int. J. Hydr. En.* **31** (2006) 841.

[139] V.R. Stamenkovic, B. Fowler, B.S. Mun, G. Wang, P.N. Ross, C.A. Lucas, N.M. Marković, *Science* **315** (2007) 493.

[140] I. Chorkendorff, J.W. Niemantsverdiet, in: *Concepts Of Modern Catalysis And Kinetics* (Wiley-VCH Verlag Gmbh and Co, 2007).

[141] A. Hellman, K. Honkala, I.N. Remediakis, Á. Logadóttir, A. Carlsson, S. Dahl, C.H. Christensen, J.K. Nørskov, *Surf. Sci.* **603** (2009) 1731.

[142] S. Dahl, J. Sehested, C.J.H. Jacobsen, E. Törnqvist, I. Chorkendorff., *J. Catal.* **192** (2000) 391.

[143] S. Kuld, Master thesis *A model study of ammonia reaction on thin films of transition metals and metal alloys*, 2011.

[144] R. Imbihl, A. Scheibe, Y.F. Zeng, S. Güther, R. Kraehnert, V.A. Kondratenko, M. Baerns, W.K. Offermans, A.P.J. Jansen, R.A. van Santen, *Phys. Chem. Chem. Phys.* **9** (2007) 3522.

[145] Z.M. Rdzawski, J.P. Stobrawa, J. Szynowski, *J. A. M. M. E* **24** (2007) 106.

[146] I. Alstrup, M.T. Tavares, *J. Catal.* **139** (1993) 513.

[147] H.J. Grabke, *Ber. Busenges. Phys. Chem.* **69** (1965) 409.

[148] I. Alstrup, M.T. Tavares, C.A. Bernardo, O. Sørensen, J.R. Rostrup-Nielsen, *Mat. Corr.* **49** (1998) 367.

[149] R.T.K. Baker, M.A. Barber, P.S. Harris, F.S. Feates, R.J. Waite, *J. Catal.* **26** (1972) 51.

[150] C. Park, M.A. Keane, *J. Col. Int. Sci.* **250** (2002) 37.

[151] U. Diebold, *Surf. Sci.* **48** (2003) 53.

[152] S.F. Yin, B.Q. Xu, C.F. Ng, C.T. Au, *Appl. Catal. B: Environ.* **48** (2004) 237.

[153] S.F. Yin, B.Q. Xu, S.J.Wang, C.F. Ng, C.T. Au, *Catal. Lett.* **96** (2004) 113.

[154] S.F. Yin, B.Q. Xu, W.X. Zhu, C.F. Ng, X.P. Zhou, C.T. Au, *Catal. Today* **9395** (2004) 27.

# List of papers

## Paper I:

**$H_2$ splitting on Pt/Ru alloys supported on sputtered HOPG**
E.M. Fiordaliso, S. Dahl, I. Chorkendorff
*J. Phys. Chem. C* **115** (2011) 2535125358

## Paper II:

**$H_2$ splitting on Pt, Ru and Rh nanoparticles supported on sputtered HOPG**
E.M. Fiordaliso, S. Murphy, R.M. Nielsen, S. Dahl, I. Chorkendorff
*Surf. Sci.* **606** (2012) 263272

## Paper III:

**Strong metal support interaction of Pt and Ru nanoparticles deposited on HOPG probed by the H-D exchange reaction**
E.M. Fiordaliso, S. Dahl, I. Chorkendorff
*Submitted to the Journal of Physical Chemistry* 2011

THE JOURNAL OF PHYSICAL CHEMISTRY C

ARTICLE

pubs.acs.org/JPCC

# $H_2$ Splitting on Pt/Ru Alloys Supported on Sputtered HOPG

Elisabetta. M. Fiordaliso,* Søren Dahl, and Ib Chorkendorff

Danish National Research Foundation's Center for Individual Nanoparticle Functionality (CINF) and Nano DTU, Department of Physics, Technical University of Denmark, DK-2800 Kgs. Lyngby, Denmark

**ABSTRACT:** The equilibrium hydrogen exchange rate between adsorbed and gas phase hydrogen at 1 bar is measured on three Pt/Ru systems: Pt overlayers on Ru films, Ru overlayers on Pt films, and Pt/Ru bulk alloys, with different Pt/Ru compositions. The catalysts are prepared by electron beam physical vapor deposition and supported on a sputtered HOPG substrate. The hydrogen exchange rate is measured in the temperature range 40−200 °C at 1 bar, by utilization of the H-D exchange reaction. We find that the exchange rate, *r*, and the dissociative sticking probability, *S*, as a function of surface concentration exceed the values measured on the individual metals and have a maximum for a composition of 2/7 Pt in the bulk alloys. The Pt overlayers on Ru films give similar results for *r* and *S*, and maximum activity is found when 4 Å of Pt are deposited on 50 Å Ru films. ISS spectra show that both Ru and Pt are on the surface, which indicates the formation of a surface alloy already at 200 °C. We also find that the maximum activity is given by the alloys with a surface composition of Pt/Ru equal to a 1:1 ratio. Experiments are also carried out in the presence of 10 ppm CO for the Pt−Ru bulk alloys. We find that alloying Pt with Ru improves significantly the resistance toward CO poisoning with respect to pure Pt, and the resistance increases with an increasing amount of Ru in the bulk alloys. The faster hydrogen exchange rate with respect to the pure metals and the higher CO tolerance of the alloys are attributed to strain and ligand effects, caused by the compression of the surface due to the presence of the larger Pt atoms in the neighboring Ru atoms. The apparent energy of desorption at equilibrium, $E_{app}$, for the three Pt−Ru systems is found to decrease with an increasing amount of Ru in the alloys, and it is attributed to geometrical ensemble effects.

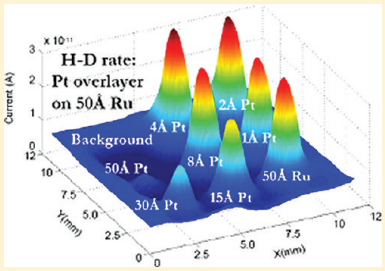


## 1. INTRODUCTION

Alloying metals provides a simple way to modify the electronic and geometrical properties of a surface, making it possible to optimize the activity of catalytic systems for a given reaction.[1,2] Many kinds of bimetallic surfaces have been studied intensively in the last decades, and often it has been shown that they exceed the activity of the individual metals.[3−6] Among all the bimetallic systems, the Pt/Ru alloys have found great interest for fuel cell applications. Currently, platinum supported on a carbon substrate is used to dissociate $H_2$ in proton exchange membrane (PEM) fuel cells. $H_2$ is usually produced together with CO by steam reforming of natural gas, and 10 ppm of CO in the $H_2$ stream are enough to poison a pure Pt catalyst surface.[7] Alloying Pt with other metals increases the CO-tolerance, and Pt/Ru alloys are found to be very CO-tolerant anode catalysts in low-temperature fuel cells,[8−15] becoming state of the art for direct methanol oxidation.[16−20] The origin of the increased CO tolerance and activity for CO electrooxidation of Pt/Ru alloy catalysts as compared to monometallic Pt catalysts is still under debate. Ruthenium may improve the CO tolerance of platinum due to two phenomena: (a) the ligand effect, where surface segregation of platinum to the surface of the alloy creates a compressed platinum overlayer on top of a ruthenium rich second layer, weakening the binding energy of CO compared to pure platinum,[21,22] and (b) the bifunctional effect, in which ruthenium promotes oxidation of CO by reducing the overpotential needed for dissociating water.[23,24]

In this work, we measure the hydrogen splitting rate and the $H_2$ apparent desorption energy at 1 bar hydrogen pressure for three Pt/Ru catalytic systems: Pt overlayers on Ru films, Ru overlayers on Pt films, and Pt/Ru bulk alloys, by screening over samples with different Pt/Ru compositions. Experiments are also carried out in the presence of 10 ppm CO in order to investigate for which Pt/Ru composition we get the highest resistance toward CO poisoning, i.e., the highest hydrogen exchange rate. Since we do not have the overpotentials present in a PEM fuel cell and no water as well, we will not see the bifunctional effect when we screen the different alloys for their catalytic activities in the presence of CO but only the ligand effect, which affects strongly the results of our experiments.

## 2. EXPERIMENTAL DETAILS

The experiments are performed in a parallel screening apparatus described in previous publications.[25,26] It combines an UHV chamber for sample preparation and surface analysis with a high pressure cell (HPC) for catalytic reactions. Circular metal films are produced by electron beam physical vapor deposition (EBPVD), with typical deposition rates of 5−10 Å/min. The evaporator can contain up to 4 different metals, which can be evaporated sequentially or at the same time. A 10 × 10 mm Ar sputtered highly ordered pyrolytic graphite (HOPG) is used as the substrate, which can accommodate up to 9 films of 1 mm diameter, as illustrated in Figure 1. Deposition takes place at room temperature, and the thickness of the films is determined

**Received:** August 19, 2011
**Revised:** November 18, 2011
**Published:** November 19, 2011

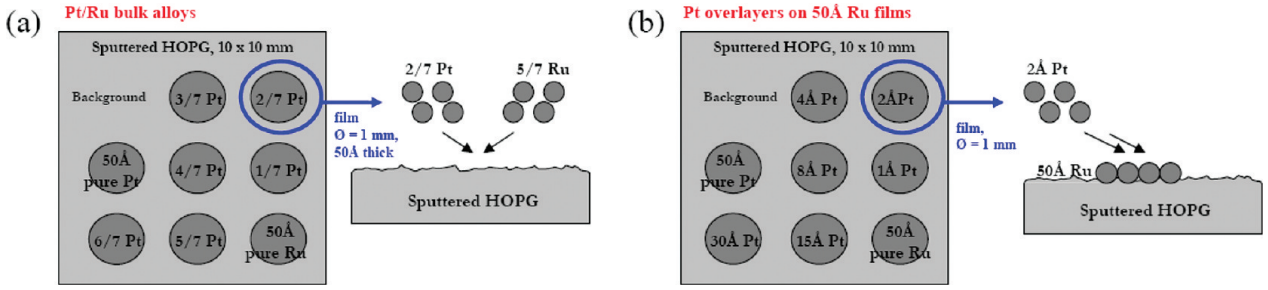


**Figure 1.** Sketch of the Pt/Ru bulk alloys (a) and of the Pt overlayers on Ru films (b) after deposition: the circular metal films (dark gray) are deposited on the sputtered HOPG substrate (light gray). The film composition is indicated on each film.

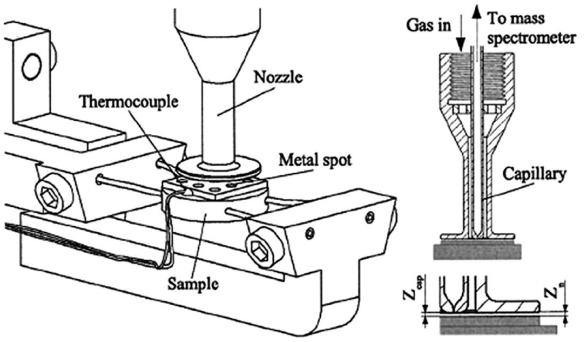


**Figure 2.** Principles of the high pressure experiment. Left: the gas sampling device positioned over a sample with circular metal films. Right: a section of the gas sampling device. The distance between the tip of the capillary, where the leak is situated, and the sample surface, $Z_{cap}$, is 0.2 mm, as is the distance between the nozzle and the sample surface, $Z_n$.

by calibrating the deposition rate with a quartz crystal microbalance. The Pt/Ru bulk alloys are prepared by coevaporation of Pt and Ru with different deposition rates, in order to have eight films of a total thickness of 50 Å, but with a different Pt−Ru bulk composition, as illustrated in Figure 1a. The Pt overlayers on Ru films are prepared by depositing first eight 50 Å thick Ru films and then on top of each film an amount of Pt which varies between 1 and 30 Å, as illustrated in Figure 1b. In a similar way, the Ru overlayers on Pt films are prepared. For the overlayers, the total thickness of each film varies, therefore, between 50 and 80 Å. For the three Pt−Ru systems, two of the eight films always consist of 50 Å of pure Ru and pure Pt, respectively, and an area of the HOPG far from any metal is used as background during measurements, as illustrated in Figure 1a,b. In a previous work on the H-D exchange reaction on Pt and Ru films,[27] it was found that the films consist of nanoparticles, and a relationship between film thickness and particle diameter was established by using STM. According to that, the Pt/Ru films produced in this study are expected to consist of particles with a diameter of around 5 nm.

After deposition, the catalysts are kept at 150 °C, and their cleanliness is checked by auger electron spectroscopy (AES), X-ray spectroscopy (XPS), and ion scattering spectroscopy (ISS) before and after experiments.

Experiments are carried out in the HPC, where the catalytic activity of the individual metal films is determined by measuring the local gas composition over the center of the circular metal films. Figure 2 shows the principles of the high pressure experiment. The gas is sampled with a quartz capillary leak and analyzed using mass spectrometry. The quartz tube is mounted concentrically in the gas inlet nozzle, and gas is blown toward the sample surface through the annulus between the capillary and the nozzle. The entire gas sampling device can be moved in three dimensions over the sample. When the sampling device is positioned over the center of one of the circular metal films, the gas flow will prevent products formed on the other films from influencing the measurement. Further details on the principles of the gas sampling device and on fluid dynamic calculations can be found in previous publications.[25,26] The HOPG substrate is glued onto a graphite disk, 10 mm in diameter and about 2 mm in thickness. The graphite disk is mounted on two tungsten wires, which are used for heating. The sample temperature is measured with a thermocouple glued at the edge of the HOPG substrate, as shown in Figure 2.

The gases used are N60 (99.9999%) $H_2$ and 99.8% $D_2$ (main contaminant HD), which are additionally purified by guard catalysts (Haldor Topsoe MK 121, activated in hydrogen at 240 °C). In order to avoid contamination by sulfur, the HPC is cleaned by flowing hydrogen through it at 1 bar for 48 h during bakeout at 150 °C. The HOPG sample is cleaned by Ar sputtering for several hours between experiments, followed by heating to 800 °C for 20 min to desorb any remaining Ar from the sample.

The high pressure measurements are carried out with a mixture of 1% $D_2$ in $H_2$ at 1 bar total pressure. The equilibrium $H_2$ exchange rate, which is equal to both the rates of dissociative $H_2$ adsorption and $H_2$ desorption at equilibrium, is determined by the progress of the H-D exchange reaction: $H_2 + D_2 \leftrightarrow 2HD$, in the temperature range of 40−200 °C. The sample is first kept in the HPC at 1 bar and 200 °C for at least 1 h, the time needed to align the gas sampling device. The measurements are then carried out for decreasing temperatures starting at 200 °C. To safeguard against changes in the reaction rate due to, e.g., contamination or structural changes of the surfaces, the first measurement is repeated at the end of the series. The total exposure time in the HPC varied between 4 h and 1 day, and no change in the reaction rate is observed during this time. The progress of the H-D exchange reactions is monitored by a mass spectrometer, by measuring the signals of 2 AMU for $H_2$, 3 AMU for HD, and 4 AMU for $D_2$.

## 3. DATA PROCESSING

A simple model, which is described in greater detail in an earlier publication,[28] is used to describe the kinetics of the HD exchange reaction. In the model, it is assumed that the equilibrium dissociative sticking probability, $S$, is the same for $H_2$, HD, or $D_2$ and that $S$ does not depend on the relative amount of H to

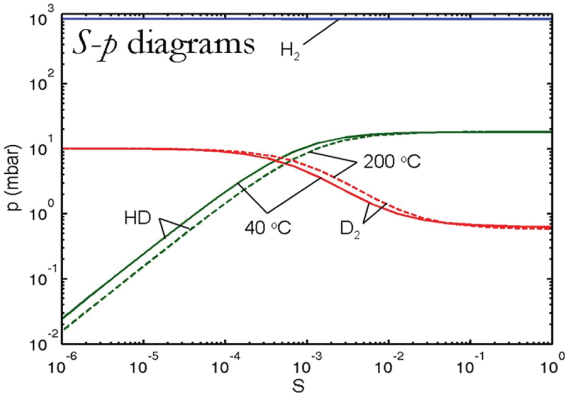


**Figure 3.** Calculated partial pressures of $H_2$, HD, and $D_2$ at the capillary leak as a function of the equilibrium sticking probability, $S$, at 40 °C (solid curves) and 200 °C (dashed curves). The gas mixture consists of 1% $D_2$ in $H_2$ at 1 bar, and the flow rate is 100 $(mL/min)_n$.

D on the surface but only on the total coverage. Since the experiments are made with only 1% $D_2$, the total coverage is assumed to equal that corresponding to 1 bar of pure $H_2$, which is close to one under the experimental conditions used in this investigation.[28−35]

In order to extract the dissociative $H_2$ sticking probability at equilibrium from the partial pressures of HD and $D_2$ measured over the catalytic metal surfaces, the gas composition at the point of measurement, i.e., the tip of the capillary as a function of $S$, is obtained from numerical calculations of the local gas velocity, temperature, and partial pressures inside the gas sampling device.[26,28] The results from these calculations are shown in Figure 3 where the partial pressures of $H_2$, HD, and $D_2$ are plotted as a function of the equilibrium $H_2$ sticking probability $S$. The equilibrium rate constant for $H_2$ desorption, $k_{des}$, can be obtained from $S$ since at equilibrium the adsorption rate, $R_{ads}$, is equal to de desorption rate, $r_{des}$

$$R_{ads} = r_{des} \leftrightarrow FS = k_{des}\,\theta_H{}^2 \approx k_{des} \quad (1)$$

where $F$ is the molecular flux of hydrogen, and $\theta_H$ is the equilibrium coverage of hydrogen, which is assumed to be very close to one. It is important to notice that $k_{des}$ is not the same desorption constant measured in a classical temperature programmed desorption (TPD) experiment, which is a nonequilibrium process.

In the low conversion region, the calculated partial pressure of HD is proportional to the desorption rate of HD that is proportional to $S$, which is clearly seen in Figure 3. Thus, it is easy to determine $S$ ($k_{des}$) from $p_{HD}$ at low conversion. At higher conversion, $p_{HD}$ gets limited by the equilibrium of the H-D exchange reaction, and $S$ is more accurately determined from the depletion in the minority reactant $D_2$. The partial pressure of $D_2$, $P_{D_2}$, is used to calculate $S$, if the lowering in $P_{D_2}$ relative to the $D_2$ pressure over the graphite surface (the partial pressure in the gas fed to the HPC) is more than 8%, otherwise the HD pressure is used to determine $S$. In the latter case, the calibration factor for the HD signal is obtained from a measurement where $P_{D_2}$ is also used to obtain $S$. The lower detection limit for the HD pressure is determined by the sensitivity limit of the mass spectrometer, which is only 0.1 mbar in this case, due to the background of $H^{3+}$ formed in the ion source. From Figure 3, it can be seen that 0.1 mbar HD corresponds to $S \approx 5 \times 10^{-6}$. For high values of $S$, the maximum sticking probability that can be measured reliably is $S \approx 3 \times 10^{-2}$. The signals for $H_2$ and $D_2$ are calibrated using the signals measured over the graphite substrate, where the gas composition is the same as in the gas fed to the HPC.[26] The relative uncertainty in the measured partial pressures of $H_2$ and $D_2$, $P_{H_2}$ and $P_{D_2}$, is approximately 1%. The dominating source of error, when determining the calibration factor for HD, is the uncertainty in the position of the capillary and the nozzle relative to the sample surface. This gives an uncertainty in the absolute value for the HD pressure, $p_{HD}$, of ±10%.[28]

## 4. RESULTS

**4.1. Measured Gas Compositions and Sticking Probability.** Figure 4a,c,d shows the measured partial pressure of HD, $p_{HD}$, plotted as a function of film composition for the Pt overlayers on Ru films, the Ru overlayers on Pt films, and the Pt/Ru bulk alloys, respectively, in the temperature range 40−200 °C, in a pure $H_2/D_2$ mixture. Figure 4b shows a 3-D map for $p_{HD}$ acquired at 200 °C on the Pt overlayers on Ru films by scanning the sniffer over the whole 10 × 10 mm sample for several hours.

The equilibrium dissociative sticking probability, $S$, is determined from the data in Figure 4, using the correlation in Figure 3. The results are shown in Figure 5a−c for the Pt overlayers on Ru films, the Ru overlayers on Pt films, and the Pt/Ru bulk alloys, respectively.

We find that pure Ru films are very active for the H-D exchange reaction, and $p_{HD}$ is weakly dependent on temperature. Pure Pt films show lower activity and a stronger temperature dependence. The results obtained for pure Ru and pure Pt are in agreement with a former investigation on 50 Å thick metal films,[27,36] where it was shown that Ru is the most active metal for the H-D exchange reaction and Pt is roughly half as active than Ru at 200 °C. Here, we measure an exchange rate and an equilibrium sticking probability, which exceed the ones measured on pure Ru films, when less than 10 Å of Pt are deposited on 50 Å Ru films, with a maximum corresponding to 4 Å of Pt, as shown in Figures 4a and 5a. We also measure a maximum of the exchange rate and $S$ on the Pt/Ru bulk alloys, corresponding to a bulk composition of 2/7 Pt and 5/7 Ru, as shown in Figures 4d and 5c. For the Ru overlayers on Pt films, $p_{HD}$ and $S$ increase with increasing Ru overlayer thickness on Pt films, as shown in Figures 4c and 5b. For this system, a stronger temperature dependence is observed for all the films, with the exception of pure Ru films.

When 10 ppm of CO are added to the $H_2/D_2$ mixture, the H-D exchange rate is inhibited significantly, also at 200 °C, and the temperature dependence in $p_{HD}$ becomes stronger, as shown in Figure 4e for the Pt/Ru bulk alloys. The exchange rate in the presence of CO is found to increase with an increasing amount of Ru in the bulk alloys and at 200 °C has a weak maximum corresponding to a bulk composition of 2/7 Pt and 5/7 Ru.

**4.2. Desorption Energies for $H_2$.** As described in eq 1, the $H_2$ desorption rate constant, $k_{des}$, can be determined from $S$ under the assumptions of hydrogen coverage close to one made in the kinetic model for the H-D exchange reaction. The apparent desorption energy for $H_2$ at the equilibrium coverage, $E_{app}$, can, therefore, be obtained from the data in Figure 5. Arrhenius plots of the desorption rate, $r_{H_2}$, for the Pt overlayers on Ru films, of the Ru overlayers on Pt films, and of the Pt/Ru bulk alloys are shown in Figure 6a−c, respectively. Straight lines are obtained from least-squares fits of the logarithm of the

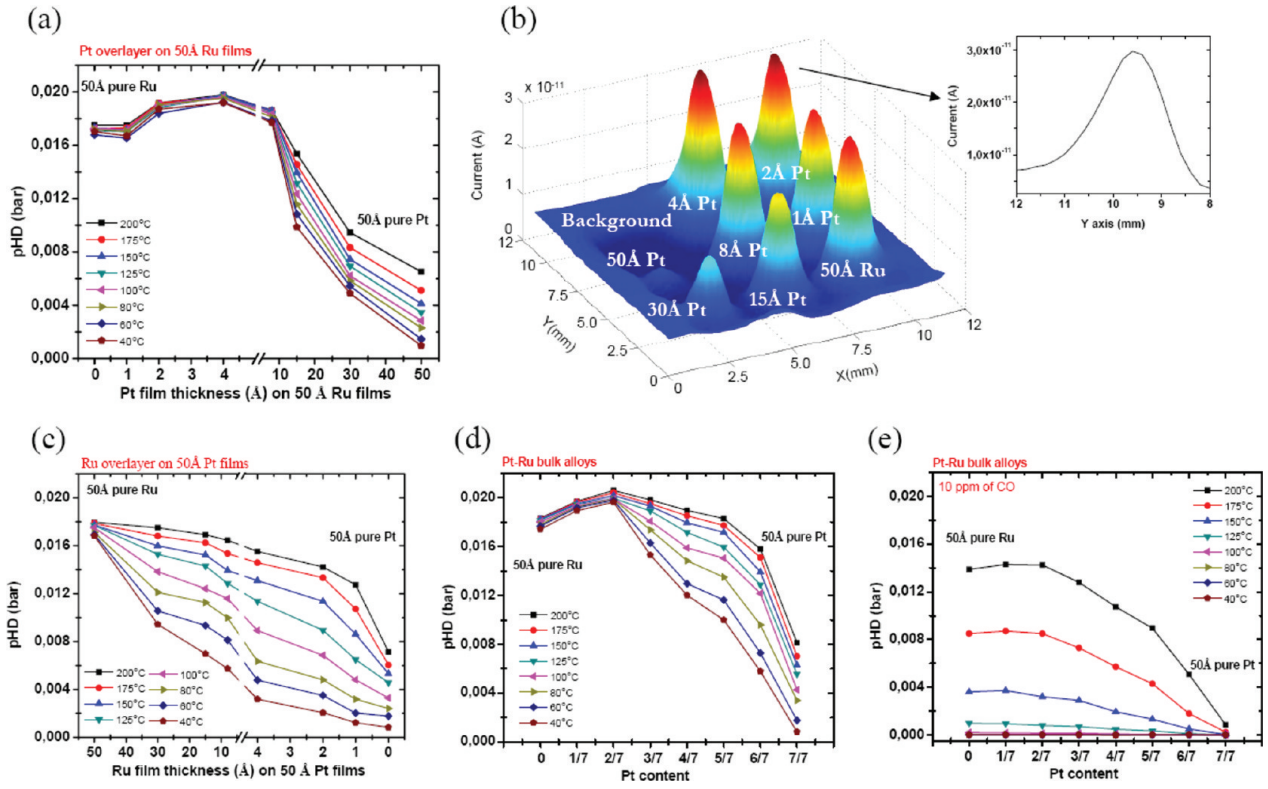


**Figure 4.** Measured values for $p_{HD}$ as a function of film composition over the center of the Pt overlayers on Ru films (a), of the Ru overlayers on Pt films (c) and of the Pt/Ru bulk alloys (d), in the temperature range 40−200 °C, in a pure $H_2/D_2$ mixture. (b) 3-D map for $p_{HD}$ acquired at 200 °C on the Pt overlayers on Ru films by scanning the sniffer over the whole 10 × 10 mm sample for several hours. A profile of one of the films is also shown. Notice that the width of the curve is larger than 1 mm, due to the gas diffusing from the sniffer. (e) Measured values for $p_{HD}$ as a function of film composition when 10 ppm CO is added to the gas mixture in the case of Pt/Ru bulk alloys.

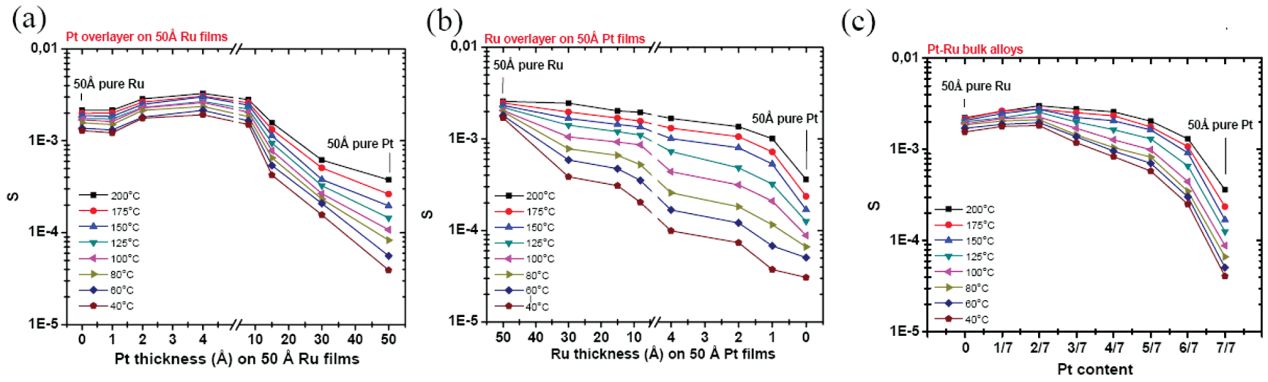


**Figure 5.** Equilibrium sticking probability for hydrogen at 1 bar, *S*, as a function of film composition for the Pt overlayers on Ru films (a), the Ru overlayers on Pt films (b), and the Pt/Ru bulk alloys (c), in the temperature range 40−200 °C.

desorption rate. Figure 7a−c shows $E_{app}$ as a function of the composition for the different films. $E_{app}$ shows a dramatic decrease with increasing Ru content for all the Pt/Ru systems, showing values that are 4 times lower when going from a pure Ru film to a pure Pt film.

**4.3. Surface Composition Analysis.** Ion scattering spectroscopy (ISS) is a very surface sensitive technique, and it provides the atomic composition of the outer layers of the Pt/Ru catalysts. Figure 8 shows ISS spectra for 1 keV $He^+$ ions scattered from the Pt/Ru surfaces after metal deposition and after the H-D exchange reactions in the HPC, with an $He^+$ current of 1.5 $\mu$A. The spectra are acquired at 150 °C and show no peaks at low energy, indicating that the surfaces are clean from any contaminations. In Figure 8, we only show the high energy region of the ISS spectra, which contains the Ru peak at 910 eV and the Pt peak at 977 eV. The 50 Å pure Ru and pure Pt films have a different peak height due to the difference in the cross-section of two metals, resulting in a higher peak for Pt with respect to Ru, for the same amount of deposited metal.[37,38] In order to get the correct surface composition on each film, the peaks

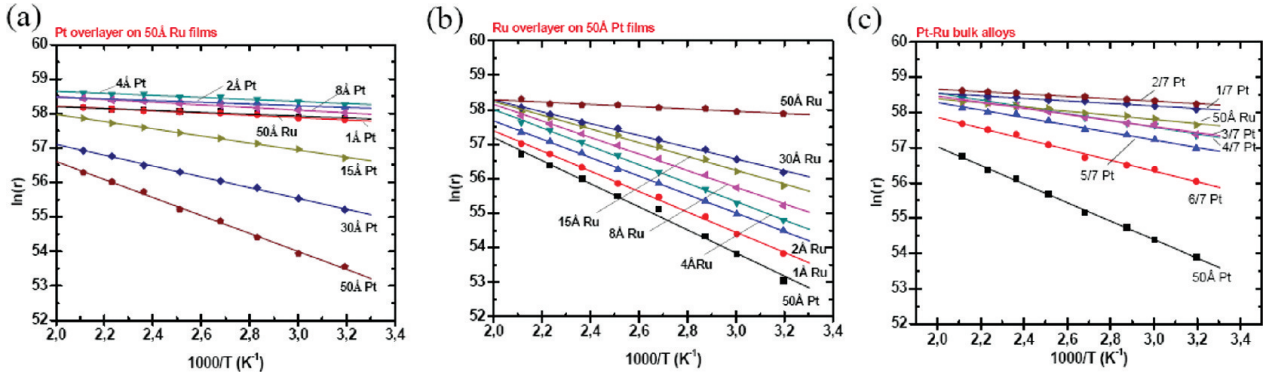


**Figure 6.** Arrhenius plots of the equilibrium hydrogen desorption rate for the Pt overlayers on Ru films (a), the Ru overlayers on Pt films (b), and the Pt/Ru bulk alloys (c). The data show a linear behavior in the plots.

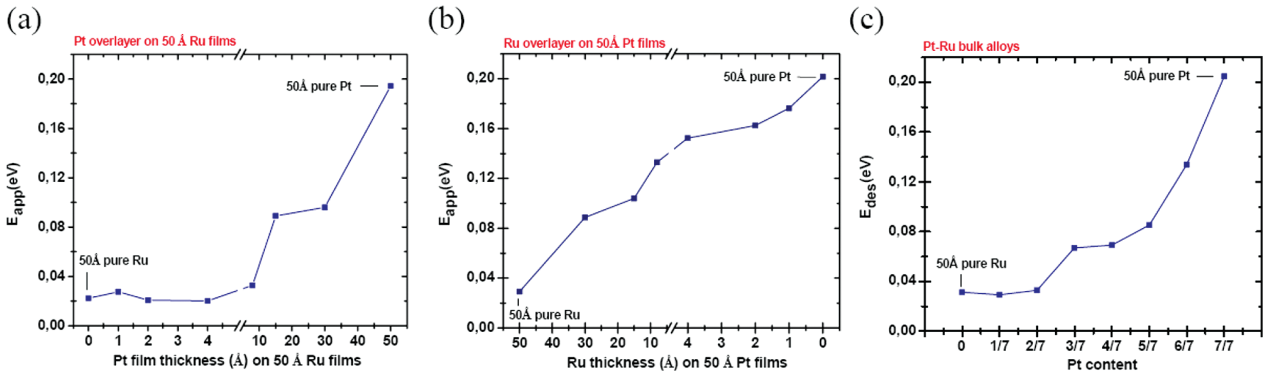


**Figure 7.** Desorption energy, $E_{app}$, as a function of the film composition for the Pt overlayers on Ru films (a), of the Ru overlayers on Pt films (b), and of the Pt/Ru bulk alloys (c). $E_{app}$ shows a dramatic increase with an increasing amount of Pt in the overlayers and bulk alloys.

are normalized to the peak generated by the pure metals according to the formula

$$x_a = 100\% \times \left( \frac{\frac{I_a}{I_A}}{\frac{I_a}{I_A} + \frac{I_b}{I_B}} \right) \quad (2)$$

where $x_a$ is the surface concentration of element $a$, $I_a$ and $I_b$ are the intensities of element $a$ and $b$ on the alloy, and $I_A$ and $I_B$ are the intensities on the pure metals.

Figure 8a,e,i shows the ISS spectra acquired from all the films after metal deposition. The corresponding surface concentrations, which are derived according to eq 2, are shown in Figure 8b,f,j. Figure 8c,g,k shows the ISS spectra acquired from all the films after the H-D exchange reaction, and Figure 8d,h,l, the corresponding surface concentrations.

We find that Ru and Pt are both present on the surface of the bulk alloys and the overlayer structures, also at the thickest overlayers, namely, the 30 Å of Pt deposited on 50 Å Ru films and the 30 Å of Ru on 50 Å Pt films. Figure 8d,h shows that for the Pt overlayers on Ru films and bulk alloys, there is an enrichment of Pt on the surface after experiments in the HPC, due to Pt surface segregation. A much stronger Pt segregation is observed for the Ru overlayers on Pt films, for which Pt dominates the surface of the catalysts after experiments, as seen when comparing Figure 8j,l.

## 5. DISCUSSION

Ru and Pt films show a different ability to dissociate $H_2$, with Ru being more active, as shown in Figure 4. This is in agreement with previous results, which have widely been explained in earlier works.[27,29] In this study, we screen over a range of different Pt/Ru compositions, and we find that for some ratio of the two metals, the exchange rate and the equilibrium sticking probability exceed the values measured on pure Ru, as seen in Figures 4 and 5. This happens when less than 10 Å of Pt are deposited on 50 Å Ru films, with a maximum corresponding to 4 Å of Pt, and when in the bulk alloys the two metals have a ratio of 2/7 Pt and 5/7 Ru. From the ISS spectra in Figure 8, we can see that both metals are present on the catalyst surfaces, also at the thickest overlayers, indicating that the two metals form a surface alloy already at 200 °C. Moreover, we find that the most active catalysts for hydrogen dissociation/desorption have a surface composition corresponding to a Pt/Ru ratio equal to 1:1. According to the literature, catalysts with a Pt/Ru ratio equal to 1:1 also give the highest activity for CO oxidation[38−41] and methanol oxidation.[42,43]

The explanation for the high activity of the Pt/Ru catalysts with respect to the individual metals is understood in terms of the d-band theory, according to which the modification of the chemical properties of the alloys, which include strain and ligand effects, are due to the changes in the d-band center of the surface alloy.[21,44−47] Compressive strain and ligand effects destabilize the Ru−H bond since the larger Pt atoms compress the neighboring Ru surface atoms and bring a lower hydrogen

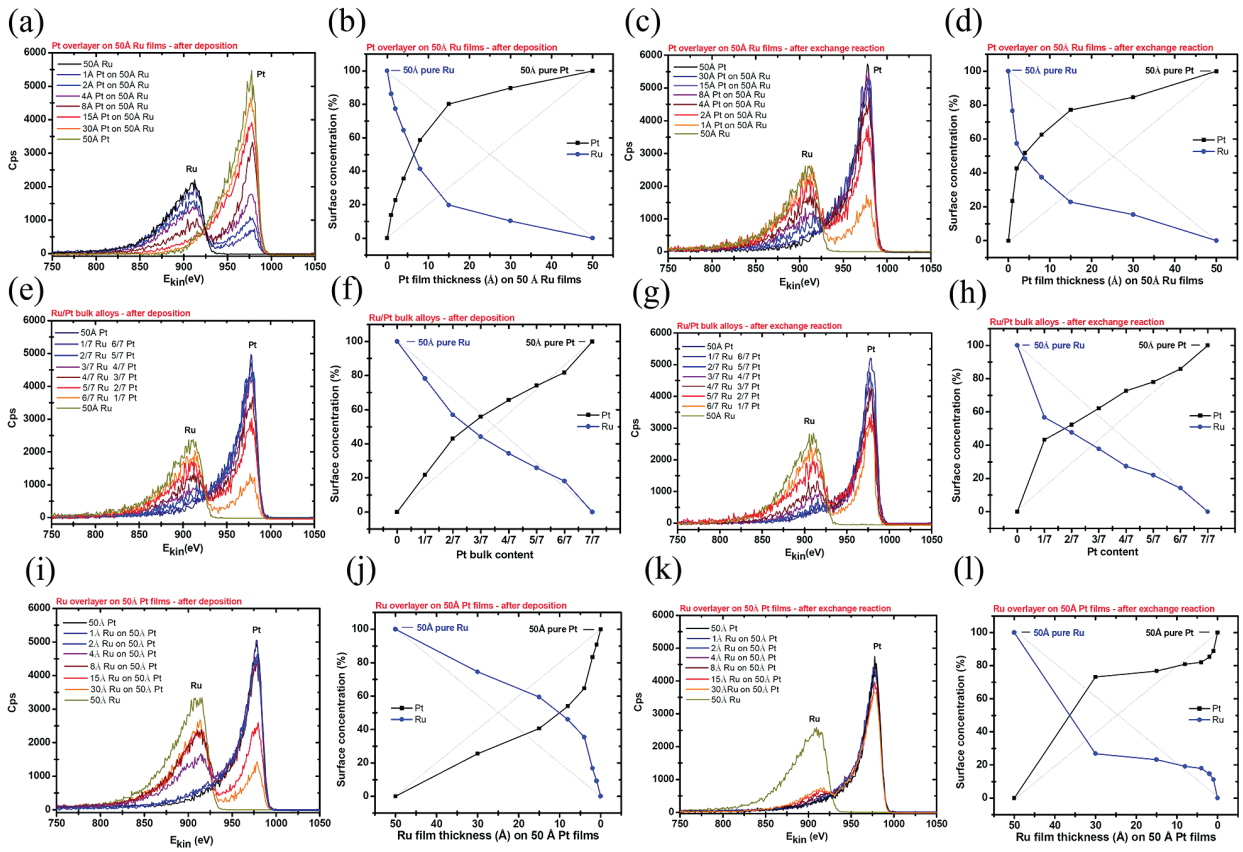


**Figure 8.** ISS spectra for 1 keV $He^+$ ions scattered from the Pt overlayers on Ru films, the Ru overlayers on Pt films, and the Pt/Ru bulk alloys after deposition (a, e, i) and after H-D exchange reaction (c, g, k). The corresponding surface concentrations after deposition (b, f, j) and after H-D exchange reaction (d, h, l) are also shown.

binding energy on the surface alloys compared to the pure metals. Indeed, when the dissociative adsorption energy for hydrogen is plotted as a function of the d-band center, a downshift is predicted for the Pt/Ru alloys with respect to the pure metals.[22,46,47] Moreover, experimental works on Pt/Ru alloys also show a downshift in temperature of the hydrogen (or deuterium) desorption peak with respect to the pure metals in TPD experiments and at saturation coverage, which is the coverage in our experiments, desorption starts already at the beginning of the temperature ramp.[48,49] The faster equilibrium hydrogen exchange rate that we measure with respect to the pure metals on the Pt/Ru alloys, which have a 1:1 ratio (see Figure 4), is then in agreement with these theoretical predictions and experimental works.

When 10 ppm of CO are added to the $H_2/D_2$ mixture, the H-D exchange rate on Pt decreases significantly, also at 200 °C, as shown in Figure 4e. The high sensitivity of Pt toward CO poisoning is discussed in previous studies.[27,36] In this study, we measure a higher tolerance toward CO poisoning of the Pt/Ru alloys with respect to pure Pt, which increases with an increasing amount of Ru in the bulk alloys. As shown in Figure 4e, the exchange rate maintains a high value on the alloys, which have a low content of Pt, with a weak maximum corresponding to 2/7 Pt in the alloy. Since we run the exchange reaction at 1 bar pressure with the addition of 10 ppm CO in the $H_2/D_2$ mixture and we do not have the overpotentials present in a PEM fuel cell, we are not able to measure any bifunctional effect. Therefore, we can state that strain and ligand effects with a consequential downshift of the d-band center are responsible for the higher CO tolerance that we measure in our experiments, which cause a reduction of the Pt−CO bond strength. This result is confirmed by a number of theoretical[21,22,50,51] and experimental works.[23,52−54]

The difference in activity between Ru and Pt gives an apparent desorption energy, $E_{des}$, which is much lower for Ru than for Pt, as shown in Figure 7. This result is in agreement with previous studies of the H-D exchange reaction on 50 Å transition metal films at 1 bar pressure.[27,29] Here, we find that the $E_{des}$ decreases dramatically with increasing Ru content in the three Pt/Ru systems, as we see in Figure 7a−c. Geometrical ensemble effects and the presence of mixed adsorption/desorption sites are found to be responsible for this behavior.[47] On close-packed metal surfaces, hydrogen is found to adsorb on the 3-fold sites of the surface,[55−58] which can be either monometallic or mixed sites on the Pt/Ru alloys. It has shown that desorption proceeds via recombination of two neighbor adatoms and involve five surface atoms, which have up to 20 different compositions.[48,59] This variety of compositions results in a desorption energy which vary almost continuously between the two cases of all Pt sites, which give the highest desorption energy, and all Ru sites, which give the lowest values, as shown in Figure 7.

From the ISS spectra shown in Figure 8, we can also see how the surface composition of the catalysts changes after the H-D exchange reaction, with respect to what it was after deposition. We find that Pt has a strong tendency to segregate to the surface

of the catalysts, when comparing the ISS spectra or the surface composition, before and after experiments. Since we do not anneal the catalysts before experiments (the sample is kept at 150 °C after deposition), the segregation occurs in the high pressure cell, and it can either be due to the increase in temperature from 150 to 200 °C during measurements or induced by the presence of 1 bar of hydrogen. The segregation of Pt to the surface is predicted by a number of theoretical works on bimetallic alloys,[60−63] and other experimental studies show that there is a barrier for Pt diffusion into the bulk of a Ru substrate, and Pt losses on the surface are negligible.[48,64]

In the case of Ru overlayers on Pt films, we find that the hydrogen exchange rate and the sticking probability increase with an increasing deposited amount of Ru, as shown in Figures 4c and 5b, respectively. From the ISS spectra in Figure 8i−l, we see that the Pt segregation results in a composition of more than 70% Pt on the surfaces of the catalysts, also at the thickest Ru overlayers on Pt films. According to these results, we can say that much more Ru is needed than the amount we have deposited on the Pt films in order to get the observed improvement in the activity as in the other two Pt/Ru systems since the surfaces do not reach the optimal composition of Ru/Pt equal to 1:1, but they are dominated by Pt. The abundance of Pt on the surface of the catalysts in this Pt/Ru system gives also a spread in temperature in the exchange rate and sticking probability, which is typical of the Pt films, as shown in Figures 4 and 5, respectively.

## 6. SUMMARY AND CONCLUSIONS

We measured the equilibrium hydrogen exchange rate between adsorbed and gas phase hydrogen at 1 bar on three different Pt/Ru systems: Pt overlayers on Ru films, Ru overlayers on Pt films, and Pt/Ru bulk alloys. The hydrogen exchange rate is measured in the temperature range 40−200 °C at 1 bar, by utilization of the H-D exchange reaction. We find that for Ru, the exchange rate, $r$, and the equilibrium dissociative sticking probability, $S$, are higher than those for Pt and have a maximum for a composition of 2/7 Pt in the bulk alloys. The Pt overlayers on Ru films give similar results for $r$ and $S$, and maximum activity is found when 4 Å of Pt are deposited on 50 Å Ru films. ISS spectra show that both Ru and Pt are on the surface, which indicates the formation of a surface alloy already at 200 °C. We also find that the maximum activity is given by the alloys with a surface composition of Pt/Ru equal to a 1:1 ratio. When 10 ppm CO are added to the $H_2/D_2$ mixture, we find that the hydrogen exchange rate decreases significantly on Pt, but alloying Pt with Ru significantly improves the resistance toward CO poisoning. The resistance increases with an increasing amount of Ru in the bulk alloys, with a weak maximum corresponding to 2/7 Pt in the alloy. The faster hydrogen exchange rate with respect to the pure metals and the higher CO tolerance of the alloys is attributed to strain and ligand effects, caused by the compression of the surface due to the presence of the larger Pt atoms in the neighboring Ru atoms. Finally, we measure an apparent energy of desorption at equilibrium, which decrease with an increasing amount of Ru in the three different Pt/Ru systems, and this is attributed to geometrical ensemble effects and mixed adsorption/desorption sites.

## AUTHOR INFORMATION

### Corresponding Author

*E-mail: e.fiordaliso@fysik.dtu.dk.

## ACKNOWLEDGMENT

Center for Individual Nanoparticle Functionality (CINF) is sponsored by The Danish National Research Foundation.

## REFERENCES

(1) Kitchin, J. R.; Nørskov, J. K.; Barteau, M. A.; Chen, J. G. *Phys. Rev. Lett.* **2004**, *93*, 156801.
(2) Holmblad, P. M.; Larsen, J. H.; Chorkendorff, I. *J. Chem. Phys.* **1996**, *104*, 7289.
(3) Sinfelt, J. H. *Bimetallic Catalysts: Discoveries, Concepts and Applications*; Wiley: New York, 1983.
(4) Stojíc, D. L.; Grozdić, T. D.; Kaninski, M. P. M.; Maksić, A. D.; Simić, N. D. *Int. J. Hydrogen Energy* **2006**, *31*, 841.
(5) Andersen, M.; Lytken, O.; Engbæk, J.; Nielsen, G.; Schumacher, N.; Johansson, M.; Chorkendorff, I. *Catal. Today* **2005**, *100*, 191.
(6) Stamenkovic, V. R.; Fowler, B.; Mun, B. S.; Wang, G.; Ross, P. N.; Lucas, C. A.; Marković, N. M. *Science* **2007**, *315*, 493.
(7) Baschuk, J. J.; Xianguo, L. *Int. J. Energy Res.* **2001**, *25*, 695.
(8) Hogarth, M. P.; Hards, G. A. *Platinum Met. Rev.* **1996**, *40*, 150.
(9) Ralph, T. R. *Platinum Met. Rev.* **1997**, *41*, 102.
(10) Maillard, F.; Gloaguen, F.; Hahn, F.; Léger, J.-M. *Fuel Cells* **2002**, *2*, 143.
(11) Buatier de Mongeot, F.; Scherer, M.; Gleich, B.; Kopatzki, E.; Behm, R. J. *Surf. Sci.* **1998**, *411*, 249.
(12) Markovic, M.; Ross, P. N. *Surf. Sci. Rep.* **2002**, *45*, 117.
(13) Conway, B. E.; Tilak, B. V. *Electrochim. Acta* **2002**, *47*, 3571.
(14) Gasteiger, H. A.; Markovic, N. M.; Ross, P. N. *J. Phys. Chem.* **1995**, *99*, 8290.
(15) Greeley, J.; Mavrikakis, M. *Nat. Mater.* **2004**, *3*, 810.
(16) Yoo, S. J.; Jeon, T. Y.; Kim, K. S.; Lim, T. H.; Sung, Y. E. *Phys. Chem. Chem. Phys.* **2010**, *12*, 15240.
(17) Wasmus, S.; Vielstich, W. *J. Appl. Electrochem.* **1993**, *23*, 120.
(18) Xiao-Juan, F.; Yan-Long, S.; Zhong-Ai, H. *Int. J. Electrochem. Sci.* **2010**, *5*, 489.
(19) Li, L.; Xing, Y. *J. Phys. Chem. B* **2007**, *111*, 2803.
(20) Markovic, N. M.; Gasteiger, H. A.; Ross, P. N., Jr; Jiang, X.; Villegas, I.; Weaver, M. J. *Electrochim. Acta* **1995**, *40*, 91.
(21) Ruban, A. V.; Skriver, H. L.; Nørskov, J. K. *Phys. Rev. B* **1999**, *59*, 15990.
(22) Bligaard, T.; Nørskov, J. K. *Electrochim. Acta* **2007**, *52*, 5512.
(23) Christoffersen, E.; Liu, P.; Ruban, A. V.; Skriver, H. L.; Nørskov, J. K. *J. Catal.* **2001**, *199*, 123.
(24) Roth, C.; Papworth, A. J.; Hussain, I.; Nichols, R. J.; Schiffrin, D. J. *J. Electroanal. Chem.* **2005**, *581*, 79.
(25) Johansson, M.; Hoffmann Jørgensen, J.; Chorkendorff, I. *Rev. Sci. Instrum.* **2004**, *75*, 2082.
(26) Johansson, M.; Johannesen, T.; Hoffman Jørgensen, J.; Chorkendorff, I. *Appl. Surf. Sci.* **2006**, *252*, 3673.
(27) Fiordaliso, E. M.; Murphy, S.; Nielsen, R. M.; Dahl, S.; Chorkendorff, I.; *Surf. Sci.* **2011**; DOI:10.1016/j.susc.2011.10.004.
(28) Johansson, M.; Lytken, O.; Chorkendorff, I. *Top. Catal.* **2007**, *46*, 175.
(29) Johansson, M.; Lytken, O.; Chorkendorff, I. *J. Chem. Phys.* **2008**, *128*, 034706.
(30) Conrad, H.; Ertl, G.; Latta, E. E. *Surf. Sci.* **1974**, *41*, 435.
(31) Behm, R. J.; Christmann, K.; Ertl, G. *Surf. Sci.* **1980**, *99*, 320.
(32) Christmann, K.; Ertl, G.; Pignet, T. *Surf. Sci.* **1976**, *54*, 365.
(33) Rendulic, K. D.; Winkler, A. *J. Chem. Phys.* **1983**, *79*, 5151.
(34) Christmann, K.; Schober, O.; Ertl, G.; Neumann, M. *J. Chem. Phys.* **1974**, *60*, 4528.
(35) Norton, P. R.; Davies, J. A.; Jackman, T. E. *Surf. Sci.* **1982**, *121*, 103.
(36) Johansson, M.; Lytken, O.; Chorkendorff, I. *Surf. Sci.* **2008**, *602*, 1863.
(37) Bouwman, R.; Sachtlers, W. M. H. *J. Catal.* **1972**, *26*, 63.
(38) Brongersma, H. H.; Draxler, M.; de Ridder, M.; Bauer, P. *Surf. Sci. Rep.* **2007**, *62*, 63.

(39) Iwasita, T.; Dalbeck, R.; Pastor, E.; Xia, X. *Electrochim. Acta* **1994**, *11/12*, 1817.
(40) Ianniello, R.; Schmidt, V. M.; Stimming, U.; Stumper, J.; Wallau, A. *Electrochim. Acta* **1994**, *39*, 1863.
(41) Alayoglu, S.; Nilekar, A. U.; Mavrikakis, M.; Eichhorn, B. *Nat. Mater.* **2008**, *7*, 333.
(42) Gasteiger, H. A.; Markovic, N.; Ross, P. N.; Cairns, E. J. *J. Electrochem. Soc.* **1994**, *141*, 1795.
(43) Li, L.; Xing, Y. *J. Phys. Chem. C* **2007**, *111*, 2803.
(44) Hammer, B.; Nørskov, J. K. *Adv. Catal.* **2000**, *45*, 71.
(45) Hammer, B.; Nørskov, J. K. In *Chemisorption and Reactivity on Supported Clusters and Thin Films*; Lambert, R.L., Pacchioni, G., Eds.; Kluwer Academic Publishers: Dordrecht, The Netherlands, 1997.
(46) Kitchin, J. R.; Nørskov, J. K.; Barteau, M. A.; Chen, J. G. *Phys. Rev. Lett.* **2004**, *93*, 156801.
(47) Ruban, A.; Hammer, B.; Stoltze, P.; Skriver, H. L.; Nørskov, J. K. *J. Mol. Catal. A: Chem.* **1997**, *115*, 421.
(48) Behm, R. J. *Z. Phys. Chem.* **2009**, *223*, 9.
(49) Diemant, T.; Hager, T.; Hoster, H. E.; Rauscher, H.; Behm, R. J. *Surf. Sci.* **2003**, *541*, 137.
(50) Davies, J. C.; Hayden, B. A.; Pegg, D. J. *Surf. Sci.* **2000**, *467*, 118.
(51) Behm, R. J. *Acta Phys. Pol., A* **1998**, *93*, 259.
(52) Koper, M. T. M.; Shubina, T. E.; van Santen, R. A. *J. Phys. Chem. B* **2002**, *106*, 686.
(53) Liu, P.; Logadottir, A.; Nørskov, J. K. *Electrochim. Acta* **2003**, *48*, 3731.
(54) Ge, Q.; Desai, S.; Neurock, M.; Kourtakis, K. *J. Phys. Chem. B* **2001**, *105*, 9533.
(55) Ishikawa, Y.; Liao, M. S.; Cabrera, C. R. *Surf. Sci.* **2002**, *513*, 98.
(56) Mitsui, T.; Rose, M. K.; Fomin, E.; Ogletree, D. F.; Salmeron, M. *Nature* **2003**, *422*, 705.
(57) Luo, M. F.; Hu, G. R.; Lee, M. H. *Surf. Sci.* **2007**, *601*, 1461.
(58) Tatarkhanov, M.; Rose, F.; Fomin, E.; Ogletree, D. F.; Salmeron, M. *Surf. Sci.* **2008**, *602*, 487.
(59) Pistonesi, C.; Pronsato, E.; Juan, A. *Appl. Surf. Sci.* **2008**, *254*, 5827.
(60) Diemant, T.; Rauscher, H.; Behm, R. J. *J. Phys. Chem. C* **2008**, *112*, 8321.
(61) Christensen, A.; Ruban, A. V.; Stoltze, P.; Jacobsen, K. W.; Skriver, H. L.; Nørskov, J. K. *Phys. Rev. B* **1997**, *56*, 5822.
(62) Ruban, A. V.; Skriver, H. L.; Nørskov, J. K. *Phys. Rev. B* **1999**, *59*, 15990.
(63) Ma, Y.; Balbuena, P. B. *Surf. Sci.* **2008**, *602*, 107.
(64) Hoster, H. E.; Bergbreiter, A.; Erne, P. M.; Hager, T.; Rauscherw, H.; Behm, R. J. *Phys. Chem. Chem. Phys.* **2008**, *10*, 3812.

Surface Science 606 (2012) 263–272

Contents lists available at SciVerse ScienceDirect

Surface Science

journal homepage: www.elsevier.com/locate/susc

# $H_2$ splitting on Pt, Ru and Rh nanoparticles supported on sputtered HOPG

E.M. Fiordaliso *, S. Murphy, R.M. Nielsen, S. Dahl, I. Chorkendorff

*Danish National Research Foundation's Center for Individual Nanoparticle Functionality (CINF) and Nano DTU, Department of Physics, Technical University of Denmark, DK-2800 Kgs. Lyngby, Denmark*

ARTICLE INFO

*Article history:*
Received 30 June 2011
Accepted 3 October 2011
Available online 8 October 2011

*Keywords:*
Hydrogen
H–D exchange
Platinum
Rhodium
Ruthenium
Nanoparticle
Sticking probability
Desorption energy

ABSTRACT

The equilibrium hydrogen exchange rate between adsorbed and gas phase hydrogen at 1 bar is measured for Pt, Ru and Rh nanoparticles supported on a sputtered HOPG substrate. The particles are prepared by Electron Beam Physical Vapor Deposition and the diameter of the particles varies between 2 and 5 nm. The rate of hydrogen exchange is measured in the temperature range 40–200 °C at 1 bar, by utilization of the H–D exchange reaction. We find that the rate of hydrogen exchange increases with the particle diameter for all the metals, and that the rate for Ru and Rh is higher than for Pt. In the case of Pt, the equilibrium dissociative sticking probability, $S$, is found to be nearly independent of particle diameter. For Ru and Rh, $S$ is found to depend strongly on particle diameter, with the larger particles being more active. The apparent energy of desorption at equilibrium, $E_{app}$, shows a dramatic increase with decreasing particle diameter for diameters below 5 nm for Ru and Rh, whereas $E_{app}$ is only weakly dependent on particle diameter for Pt. We suggest that the strong variation in the apparent desorption energy with particle diameter for Ru and Rh is due to the formation of compressed hydrogen adlayers on the terraces of the larger particles. Experiments are also carried out in the presence of 10 ppm CO. Pt is found to be very sensitive to CO poisoning and the H–D exchange rate drops below the detection limit when CO is added to the gas mixture. In the case of Ru and Rh nanoparticles, CO decreases the splitting rate significantly, also at 200 °C. The variation of the sensitivity to CO poisoning with particle diameter for Ru and Rh is found to be weak.



## 1. Introduction

The energy production of our society is based on fossil energy sources such as coal, oil and natural gas. Since the combustion of fossil fuels produces polluting compounds such as CO and $NO_x$ and greenhouse gases such as $CO_2$, alternative fuels are needed. An interesting alternative to oil as energy carrier is hydrogen, which can be used for generation of electricity in fuel cells. In the Proton Exchange Membrane (PEM) fuel cell, the hydrogen splitting occurs at the anode catalyst, which typically consists of Pt nanoparticles on a carbon support. The present interest in fuel cells and in hydrogen storage, along with the general interest in understanding the relationship between reactivity and structure of metal nanoparticles, has resulted in several fundamental studies of hydrogen dissociation on transition metal nanoparticles and alloys [1–6].

Presently, hydrogen is usually produced together with CO by steam reforming of natural gas, which results in a rest concentration of CO in hydrogen of at least 10 ppm. The splitting of hydrogen is poisoned by such low CO concentrations [7], which corresponds to a full monolayer of adsorbed CO on a polycrystalline Pt surface, at temperature relevant for PEM fuel cells [8]. The splitting of hydrogen in presence of CO has been studied under Ultra High Vacuum (UHV) conditions [9–12] and on thick metal films, typically 50 Å, at realistic hydrogen pressures [13–15].

This work is an investigation on how the nanoparticle diameter for Ru, Rh and Pt influences the hydrogen splitting rate and the apparent $H_2$ desorption energy at 1 bar hydrogen pressure. Experiments are also carried out in the presence of 10 ppm CO, aiming at investigating whether the resistance to CO poisoning may be improved by selecting a certain particle diameter.

## 2. Experimental details

The experiments are performed in a “Parallel Screening” apparatus, described in previous publications [16,17]. It combines an UHV chamber for sample preparation and surface analysis with a High Pressure Cell (HPC) for studies of catalytic reactions. The nanoparticles are produced by Electron Beam Physical Vapor Deposition (EBPVD), with typical deposition rates of 5–10 Å/min. A 10×10 mm Ar sputtered Highly Ordered Pyrolytic Graphite (HOPG) is used as substrate and deposition takes place at room temperature. The film thickness is determined by calibrating the deposition rate with a quartz crystal microbalance. Catalytic circular metal films of 1 mm diameter are deposited and the films have an average metal thickness from 0.2 to 30 Å, see Fig. 1. A Scanning Electron Microscope (SEM) image of a sputtered HOPG area far from any deposited metal is

* Corresponding author. Tel.: +45 45253196; fax: +45 45932399.
*E-mail addresses:* e.fiordaliso@fysik.dtu.dk, elisafiordaliso@hotmail.com (E.M. Fiordaliso).

0039-6028/$ – see front matter © 2011 Elsevier B.V. All rights reserved.
doi:10.1016/j.susc.2011.10.004

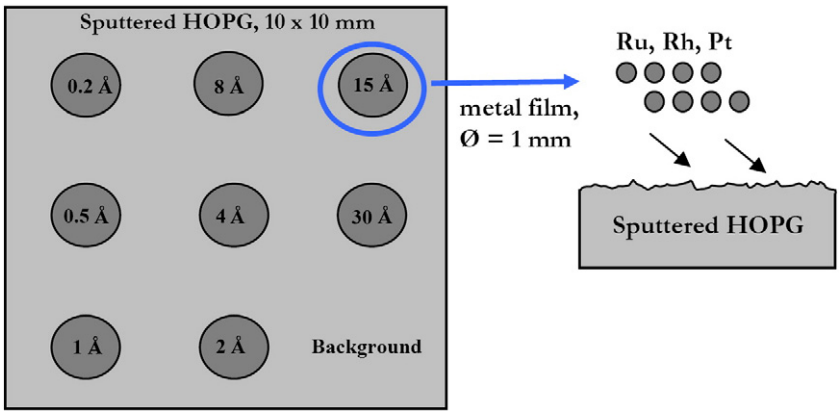


**Fig. 1.** A sketch of the sample after deposition: the circular metal films (dark gray) are the nanoparticles of Ru, Rh and Pt deposited on the sputtered HOPG substrate (light gray). The average thickness is indicated on each film.

shown in Fig. 2. The roughness of the surface is due to the Ar sputtering, performed for several hours between experiments, followed by heating to 800 °C for 20 min to desorb any remaining Ar from the substrate. After deposition, the sample is kept at 150 °C. The model catalysts are characterized by Auger Electron Spectroscopy (AES), X-ray Photoelectron Spectroscopy (XPS) and Ion Scattering Spectroscopy (ISS) before and after experiments. In order to obtain information on the size distribution of the nanoparticles, the sample is transferred in air to an apparatus equipped with a Scanning Tunneling Microscope (STM). STM was performed at room temperature in constant current mode, using a W tip. Further details on the techniques used and on the programs used for image analysis can be found in Ref. [18].

Experiments are carried out in the HPC, where the catalytic activity of the individual metal films is determined by measuring the local gas composition over the center of the circular metal films. Fig. 3 shows the principles of the high pressure experiment. The gas is sampled with a quartz capillary leak and analyzed using mass spectrometry. The quartz tube is mounted concentrically in the gas inlet nozzle and gas is blown toward the sample surface through the annulus between the capillary and the nozzle. The entire gas sampling device can be moved in three dimensions over the sample. When the sampling device is positioned over the center of one of the circular metal films, the gas flow will prevent products formed on the other films from influencing the measurement [17]. The sputtered HOPG substrate is glued onto a graphite disk, 10 mm in diameter and about 2 mm in thickness. The graphite disk is mounted on two tungsten wires, which are used for heating. The sample temperature is measured with a thermocouple glued at the edge of the HOPG substrate, see Fig. 3. The gases used are N60 (99.9999%) $H_2$ and 99.8% $D_2$ (main contaminant HD) which are additionally purified by guard catalysts (Haldor Topsoe MK 121, activated in hydrogen at 240 °C). In order to avoid contamination by sulfur, the HPC is cleaned by flowing hydrogen through it at 1 bar for 48 h during bakeout at 150 °C.

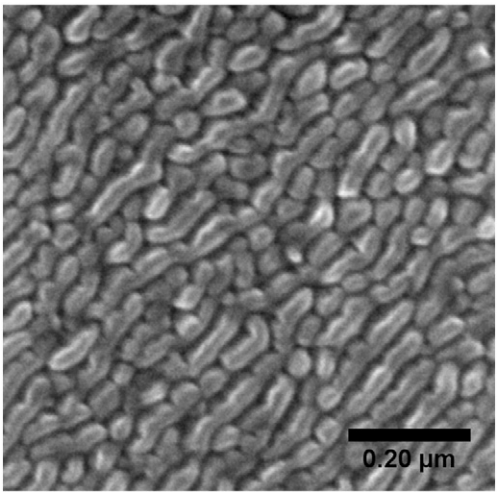


**Fig. 2.** A SEM image of a sample area with no deposited metal. The roughness of the surface is due to the Ar sputtering, performed for hours in order to clean the surface between experiments.

The high pressure measurements are carried out with a mixture of 1% $D_2$ in $H_2$ at 1 bar total pressure. The equilibrium $H_2$ exchange rate, which is equal to both the rates of dissociative $H_2$ adsorption and $H_2$ desorption at equilibrium, is determined by the progress of the H–D exchange reaction: $H_2 + D_2 \leftrightarrow 2HD$, in the temperature range of 40–200 °C. The sample is first kept in the HPC at 1 bar and 200 °C for at least 1 h, the time needed to align the gas sampling device. The measurements are then carried out for decreasing temperatures with start at 200 °C. To safeguard against changes in the reaction rate due to, e.g., contamination or structural changes of the surfaces, the first measurement is repeated at the end of the series. The total exposure time in the HPC varied between 4 h and 1 day, and no change in the reaction rate is observed during this time. The progress of the H–D exchange reactions is monitored by a mass spectrometer, by measuring the signals of 2 AMU for $H_2$, 3 AMU for HD and 4 AMU for $D_2$.

## 3. Data processing

A simple model, which is described in greater detail in an earlier publication [13], is used to describe the kinetics of the HD exchange reaction. In the model it is assumed that the equilibrium dissociative sticking probability, $S$, is the same for $H_2$, HD or $D_2$ and that $S$ does not depend on the relative amount of H to D on the surface, but only on the total coverage. Since the experiments are made with only 1% $D_2$, the total coverage is assumed to equal that corresponding to 1 bar of pure $H_2$, which is close to one under the experimental conditions used in this investigation [13,14,19–24].

In order to extract the dissociative $H_2$ sticking probability at equilibrium from the partial pressures of HD and $D_2$ measured over the catalytic metal surfaces, the gas composition at the point of measurement, i.e. the tip of the capillary as a function of $S$, is obtained from numerical calculations of the local gas velocity, temperature, and partial pressures inside the gas sampling device [13,17]. The results from these calculations are shown Fig. 4 where the partial pressure of $H_2$, HD and $D_2$ is plotted as function of the equilibrium $H_2$ sticking probability $S$. The equilibrium rate constant for $H_2$ desorption, $k_{des}$, can be obtained from $S$ since at equilibrium the adsorption rate, $R_{ads}$, is equal to de desorption rate, $r_{des}$:

$$R_{ads} = r_{des} \Leftrightarrow FS = k_{des}\theta_H^2 \approx k_{des} \quad (1)$$

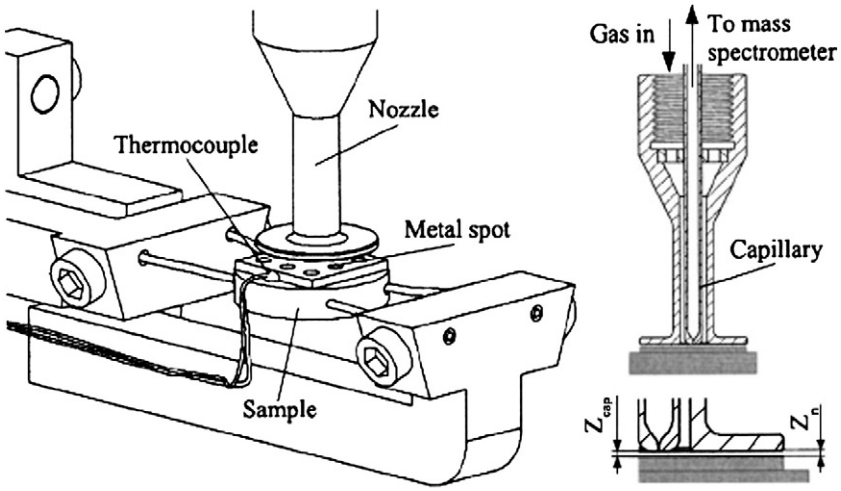


**Fig. 3.** The principles of the high pressure experiment. Left: the gas sampling device positioned over a sample with circular metal films. Right: a section of the gas sampling device. The distance between the tip of the capillary, where the leak is situated, and the sample surface, $Z_{cap}$, is 0.2 mm, as is the distance between the nozzle and the sample surface, $Z_n$. Published with kind permission from Springer Science and Business Media B.V.

where $F$ is the molecular flux of hydrogen and $\theta_H$ is the equilibrium coverage of hydrogen, which is assumed to be very close to one.

In the low conversion region, the calculated partial pressure of HD is proportional to the desorption rate of HD that is proportional to $S$, which is clearly seen in Fig. 4. Thus it is easy to determine $S$ ($k_{des}$) from $p_{HD}$ at low conversion. At higher conversion, $p_{HD}$ gets limited by equilibrium of the H–D exchange reaction and $S$ is more accurately determined from the depletion in the minority reactant $D_2$. The partial pressure of $D_2$, $p_{D_2}$, is used to calculate $S$, if the lowering in $p_{D_2}$ relative to the $D_2$ pressure over the graphite surface (the partial pressure in the gas fed to the HPC) is more than 8%, otherwise the HD pressure is used to determine $S$. In the latter case, the calibration factor for the HD signal is obtained from a measurement where $p_{D_2}$ is also used to obtain $S$. The lower detection limit for the HD pressure is determined by the sensitivity limit of the mass spectrometer, which is only 0.1 mbar in this case, due to the background of $H^{3+}$ formed in the ion source. From Fig. 4 it can be seen that 0.1 mbar HD corresponds to $S \approx 5 \cdot 10^{-6}$. For high values of $S$ the maximum sticking probability which can be measured reliably is, $S \approx 3 \cdot 10^{-2}$. The signals for $H_2$ and $D_2$ are calibrated using the signals measured over the graphite substrate, where the gas composition is the same as in the gas fed to the HPC [17]. The relative uncertainty in the measured partial pressures of $H_2$ and $D_2$, $p_{H_2}$ and $p_{D_2}$ is approximately 1%. The dominating source of error, when determining the calibration factor for HD, is the uncertainty in the position of the capillary and the nozzle relative to the sample surface. This gives an uncertainty in the absolute value for the HD pressure, $p_{HD}$, of ±10% [13].

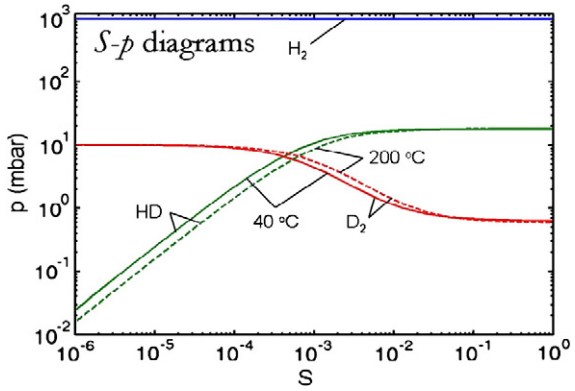


**Fig. 4.** The calculated partial pressures of $H_2$, HD and $D_2$ at the capillary leak as a function of the equilibrium sticking probability, $S$, at 40 (solid curves) and 200 °C (dashed curves). The gas mixture consists of 1% $D_2$ in $H_2$ at 1 bar and the flow rate is 100 $(ml/min)_n$.
Published with kind permission from Springer Science and Business Media B.V.

## 4. Results

### 4.1. STM analysis

STM images acquired on Pt and Ru films are shown in Fig. 5. Rather than forming a continuous film, each circular metal film consists of nanoparticles decorating the rough structure of the HOPG surface, even at a deposition thickness of 30 Å. This is the reason why the carbon peak is still visible when acquiring AES spectra on thin films and even on thick films [14,15].

Fig. 5(a) and (b) shows STM images acquired on 2 Å and 8 Å Pt films, respectively, whereas Fig. 5(c) and (d) shows STM images

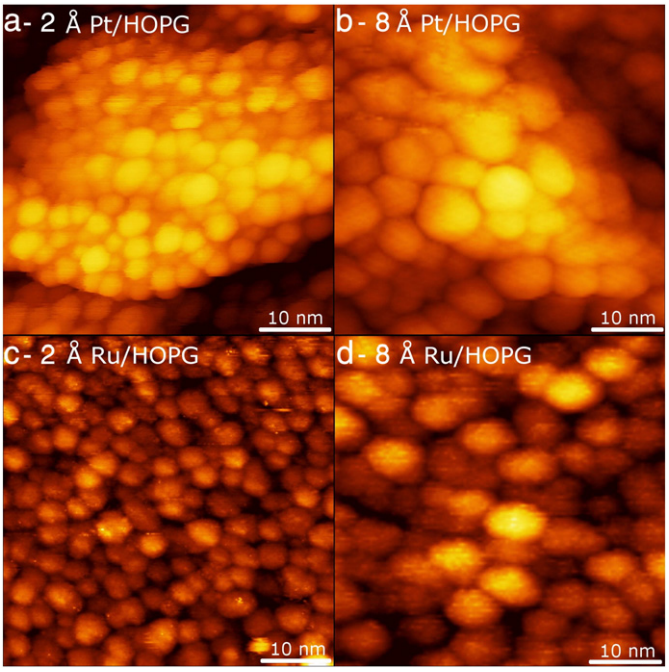


**Fig. 5.** STM images of Pt nanoparticles corresponding to 2 Å (a) and 8 Å Pt films (b). STM images of Ru nanoparticles corresponding to 2 Å (c) and 8 Å Ru films (d). The diameter of the nanoparticles varies between 2 and 5 nm.

acquired on 2 Å and 8 Å Ru films. The particles appear round in the STM and indicate insignificant sintering below 200 °C. This is in agreement with previous results on the morphology of Ru nanoparticles deposited on HOPG, obtained with STM and TEM techniques [18,25], where it was found that Ru nanoparticles with diameter below 6 nm are round and they start to exhibit hexagonal symmetry only above this diameter.

The particle diameter as a function of the film thickness for Pt and Ru nanoparticles is plotted in Fig. 6. Each point represents the average diameter of the nanoparticles corresponding to a certain film thickness, derived by size distribution analysis. We find that the Ru and the Pt films of the same thickness are made of nanoparticles with similar sizes and that the particle diameter varies between 2 and 5 nm. A relationship between film thickness and nanoparticle diameter can be established, as shown in the inset in Fig. 6. It is not surprising that for a 30 Å film we get 5 nm diameter particles, since the films are not flat and continuous and particles taller than the nominal film thickness can form.

The particle size is determined by two main factors: (a) the thickness of the deposited film, i.e. the density of particles, and (b) the presence of the substrate defect sites, which are created by $Ar^+$ sputtering and are randomly distributed on the HOPG, preventing particle diffusion and aggregation. This is shown in a study on size-selected silver clusters deposited on graphite [26]. The Rh metal films have not been characterized by STM, but based on what determines the particle size, we can assume that the diameter of the Rh nanoparticles falls in the same range as for Ru and Pt, within the error bar.

### 4.2. Metal surface area

The active surface area of the catalytic films formed by EBPVD depends on the film thickness. The relative surface area, $A_r$, for the metal film $i$, is equal to the ratio between the active surface area and the total planar surface area, which is the same for all the films, since they are they are deposited in a circular area of 1 mm diameter. $A_r$ can be calculated as:

$$A_r = N_i \cdot A_n = \frac{t_i}{V_n} A_n \tag{2}$$

where $N_i$ is the number of particles per area in the film $i$, equal to the ratio between the thickness of the metal film, $t_i$, and the average volume $V_n$ of the nanoparticles in the film. $A_n$ is the surface of the nanoparticles. Assuming semi spherical nanoparticles of radius $r_i$, which is estimated by STM analysis (see Fig. 6), both $V_n$ and $A_n$ can be calculated from $r_i$, which results in the relative surface area, $A_r$, as a function of film thickness plotted in Fig. 7. In this model the relative area of the thickest film is overestimated, since more than one monolayer of nanoparticles are formed. By looking at the STM images in Fig. 5, we are not able to find a good way to describe the arrangement of the particles on the substrate, which is needed in order to get a reasonable value for the relative area of the thickest film. However, assuming that the nanoparticles have a honeycomb-like arrangement, we estimate that the relative surface area of the thickest film is around 2, represented by the black dots in Fig. 7.

### 4.3. Measured gas compositions

Fig. 8 shows the measured partial pressure of HD, $p_{HD}$, over the center of Ru, Rh and Pt circular metal films in the temperature range 40–200 °C, as a function of the film thickness. We choose the film thickness as x-axis since this is the actual parameter that we control during deposition. The nanoparticle size derived by STM analysis is indicated in each plot. Fig. 8(A), (B), and (C) shows $p_{HD}$ in the pure $H_2/D_2$ mixture and we find that Ru and Rh nanoparticles are very active for the H–D exchange reaction. $p_{HD}$ is weakly dependent on temperature for those two metals and increases with film thickness. Pt nanoparticles show lower activity and a strong temperature dependence. The results displayed in Fig. 8 are in agreement with a former investigation on 50 Å thick transition metal films [14]. It was found that Ru is the most active metal for the H–D exchange reaction, immediately followed by Rh, whereas Pt is less active, roughly half of the activity for Ru and Rh at 200 °C. The addition of 10 ppm CO inhibits the reaction significantly, also at 200 °C, as shown in Fig. 8(D) and (E). We also find that the temperature dependence in $p_{HD}$ becomes stronger in the presence of CO. For Pt films with thickness up to 30 Å, $p_{HD}$ in the presence of CO is below the detection limit. The H–D exchange reaction on 50 Å Pt films in the presence of 10 ppm CO was previously investigated and it was shown that Pt is very sensitive to CO and that $p_{HD}$ for 50 Å Pt films decreases roughly of a factor of 20 at 200 °C relative to the value in pure $H_2/D_2$ mixture [15].

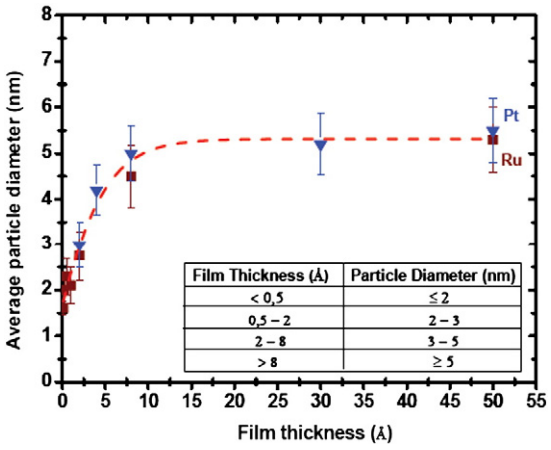


**Fig. 6.** The nanoparticle diameter as a function of the film thickness for Pt and Ru particles. The dots are the average values for the diameter of Pt nanoparticles (blue dots) and Ru nanoparticles (brown dots) and the error bar is the standard deviation. The red dashed line is a sigmoidal fit to the data and is supplied as a guide to the eye. The inset is a table representing the relation between the film thickness and nanoparticle size.

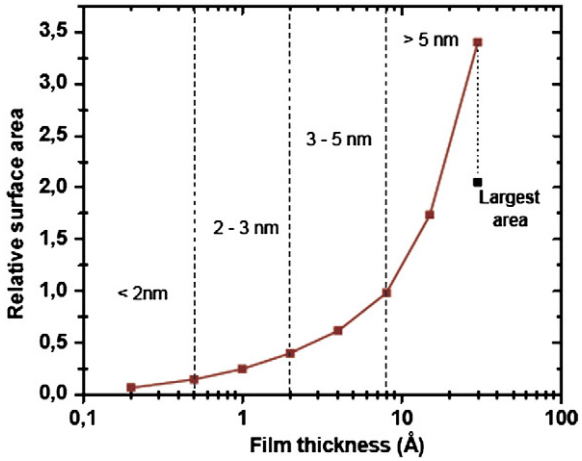


**Fig. 7.** The relative surface area of the metal films as a function of film thickness. The relative surface is equal to the ratio between the active metal surface area and the geometrical area, which is a constant value for all the films. The black dot represents an estimate of the largest area obtainable when more than one layer of close packed nanoparticles is formed, which holds for the thickest film. The diameter in nm of the nanoparticles is also indicated in the figure.

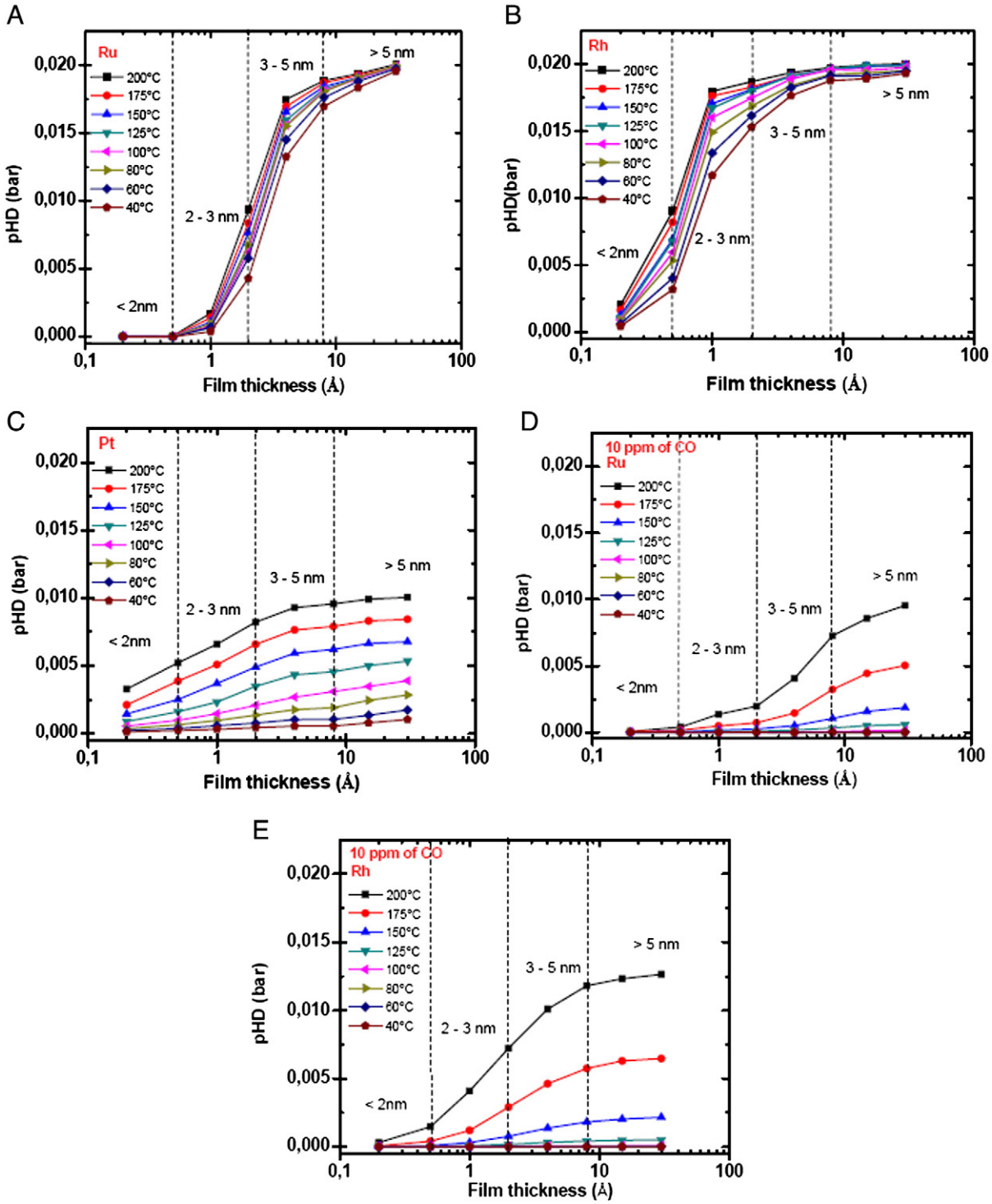


**Fig. 8.** Measured values for $p_{HD}$ over the centers of circular metal films of Ru, Rh and Pt nanoparticles in the temperature range 40–200 °C as a function of the film thickness. The diameter in nm of the nanoparticles is also indicated in the figure. Panels (A), (B) and (C) show $p_{HD}$ obtained in experiments in pure $H_2/D_2$ mixture, whereas panels (D) and (E) show $p_{HD}$ when 10 ppm CO is added to the gas.

### 4.4. The sticking probability

The equilibrium dissociative sticking probability for $H_2$ on the surface of the different nanoparticles is determined from the results in Fig. 8 using the correlation in Fig. 4. and dividing by the relative surface area shown in Fig. 7. The resulting sticking probabilities are shown in Fig. 9(A), (B), and (C). The oscillatory behavior of some of the results is an artifact that mainly stems from the uncertainty in determining the relative surface area of the nanoparticle films. It is therefore only the overall trends of the results that will be discussed here. We find that $S$ in the pure $H_2/D_2$ mixture for Ru and Rh is weakly dependent on temperature and decrease for nanoparticle diameters below 3 nm. For Pt nanoparticles $S$ does not change significantly with the nanoparticle diameter and shows lower values compared to Ru and Rh nanoparticles. Moreover, $S$ for Pt nanoparticles shows a strong temperature dependence and increases significantly with increasing temperature.

In the presence of 10 ppm CO, $S$ can only be determined above 100 °C in the case of Ru and Rh nanoparticles, as shown in Fig. 9(D)

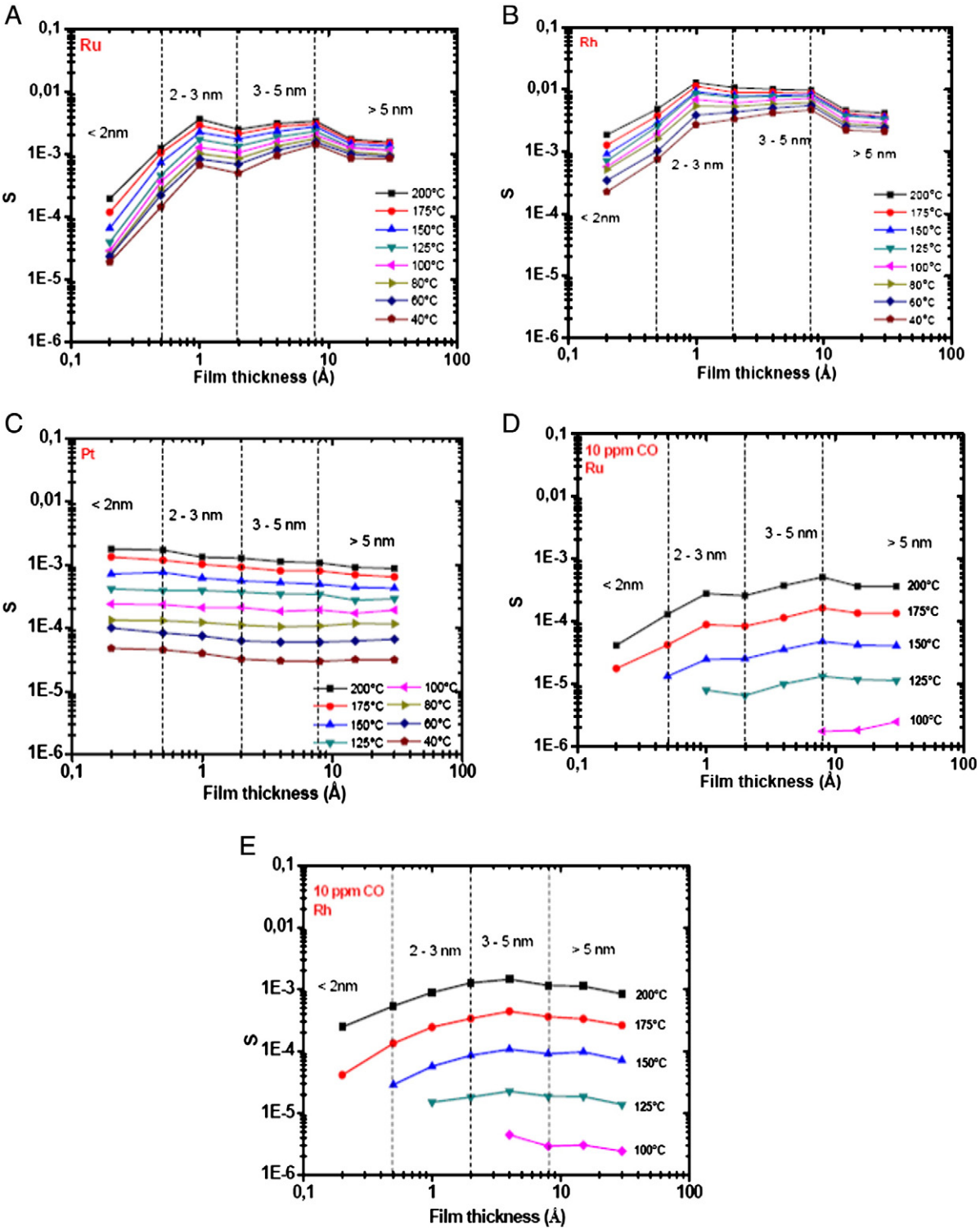


**Fig. 9.** The equilibrium sticking probability for hydrogen at 1 bar, *S*, for Ru, Rh and Pt nanoparticles in the temperature range 40–200 °C as a function of the film thickness. The diameter in nm of the nanoparticles is also indicated in the figure. Panels (A), (B) and (C) show *S* obtained in experiments in pure $H_2/D_2$ mixture, whereas panels (D) and (E) show *S* when 10 ppm CO is added to the gas.

and (E). Moreover, *S* does not change significantly with nanoparticle diameter for Ru and Rh in the presence of CO. For Pt films with thickness up to 30 Å, *S* in the presence of CO cannot be determined because the HD signal is below the detection limit. A previous investigation showed that *S* in the presence of 10 ppm CO can only be measured above 200 °C for a 50 Å Pt film, giving a value which is roughly a factor of 30 lower compared to the value obtained in the pure $H_2/D_2$ mixture [15]. The high sensitivity to CO has been explained by the fact that the difference in binding energy for hydrogen and CO is particularly large for Pt [15].

### 4.5. Desorption energies for $H_2$

As described in Eq. (1), the $H_2$ desorption rate constant, $k_{des}$, can be determined from *S* under the assumptions of hydrogen coverage close to one. The apparent desorption energy for $H_2$ at the

equilibrium coverage, $E_{app}$, can therefore be obtained from the data in Fig. 9. If the assumption of hydrogen coverage close to one is wrong, it is the apparent desorption energy, which includes a temperature dependence of the hydrogen coverage, which can be determined. Arrhenius plots of the desorption rate,$r_{H_2}$, for Ru, Rh and Pt nanoparticles, calculated from Eq. (1) are shown in Fig. 10(A), (B) and (C). Generally the data show a linear behavior in the plots, even though small deviations are observed for nanoparticles smaller than 2 nm in diameter, due to a low signal. $E_{app}$ for Ru, Rh and Pt nanoparticles as a function of the film thickness is shown in Fig. 11. $E_{app}$ shows a decrease with the nanoparticle diameter in the case of Ru and Rh nanoparticles: for 5 nm particles $E_{app}$ is roughly 3–4 times lower than for 2 nm particles. In the case of Pt nanoparticles $E_{app}$ decreases slightly with nanoparticle diameter and the values are higher compared to those for Ru and Rh.

## 5. Discussion

For all the metals, there is an increase in $p_{HD}$, and thus in the rate of the H–D exchange as a function of the film thickness, as shown in Fig. 8. The increase in the rate is due to a combination of two effects: an increase of the active surface area, as shown in Fig. 7, and a change in reactivity with nanoparticle diameter, which is significant for Ru and Rh. This is evident when the sticking probability per metal area, $S$, is calculated from the measured $p_{HD}$, as shown in Fig. 9. Thus $S$ obtained in the experiments with the pure $H_2/D_2$ mixture decreases for nanoparticle diameters below 3 nm for Ru and Rh. The temperature dependence of the rate varies strongly with particle diameter, which manifests itself as an apparent desorption energy at equilibrium, $E_{app}$, which decreases nearly to zero over the range of particle diameters studied, as shown in Fig. 11.

For all the nanoparticle diameters investigated, Ru and Rh show higher $H_2$ equilibrium exchange rates than Pt at 1 bar pressure. This is similar to the observations made for 50 Å metal films, where it was found that Ru and Rh give much higher values for $S$ than Pt, despite the fact that the heat of adsorption for H on Ru and Rh is much higher than for Pt at low coverage [14]. So far, the unexpectedly high activity of these two metals has been attributed to the presence of special adsorption states with low heat of adsorption that are populated at the high hydrogen coverage at equilibrium [14]. One possibility is that such adsorption states are located at steps, defects, corners or edges on the nanoparticle surfaces. The ratio of the undercoordinated sites to terrace sites on equilibrium shaped nanoparticles increases as the nanoparticles get smaller and, for some reactions, these sites give reaction rates which are orders of magnitude higher than on terraces [27,28]. In such cases, the reaction rate is expected to increase with decreasing particle size, which, however, is the opposite effect of what we observe in this study. We think that the formation of a compressed hydrogen adlayer, where the heat of adsorption is lowered with coverage as a consequence of H–H repulsion, is the reason for the strong change in the exchange rate and in the apparent desorption energy with particle diameter for Ru and Rh, due to quantization of the hydrogen binding energy.

The principle of a compressed adlayer is illustrated in the following simplified model, where it is assumed that the heat of adsorption on a single facet of a nanoparticle, $\Delta H_{ads}$, can be expressed as

$$\Delta H_{ads} = \Delta H_{ads,0} + \theta_H \varepsilon = \Delta H_{ads,0} + \frac{n}{N_s}\varepsilon. \quad (3)$$

Here $\theta_H$is the coverage of hydogen, $n$ is the number of hydrogen atoms adsorbed on the surface and $N_s$ the number of available sites on the facet. $\Delta H_{ads,\,0}$ is the low coverage limit of $\Delta H_{ads}$ and must be a negative number if any adsorption should occur. For simplicity we assume a linear coverage dependence which is naturally not valid at low coverage, where there will be little or no repulsion, but that is not the case in our experiments, since the hydrogen coverage is close to one. The Gibbs free energy of adsorption, $\Delta G_{ads}$, is given by

$$\Delta G_{ads} = \Delta H_{ads} - T\Delta S_{ads} \quad (4)$$

where $\Delta S_{ads}$ is the change in entropy by adsorption. The equilibrium is characterized by $\Delta G_{ads} = 0$ and since $\Delta S_{ads}$ is always negative due

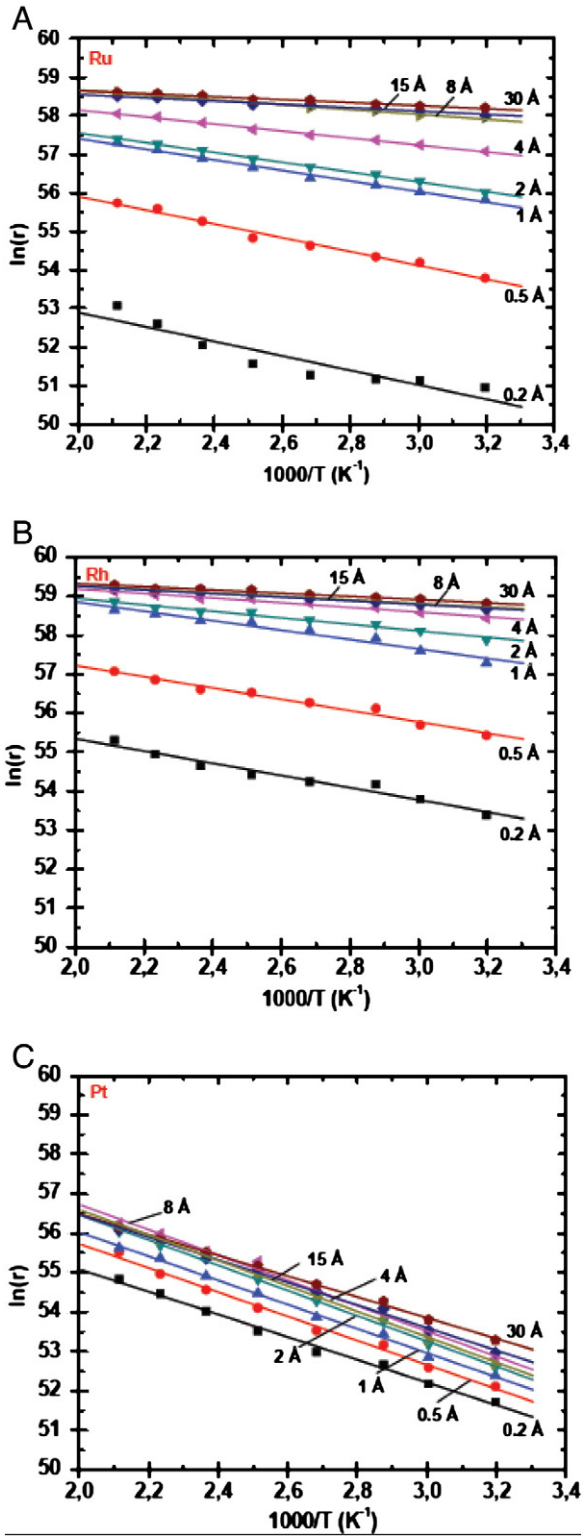


**Fig. 10.** Arrhenius plots of the equilibrium hydrogen desorption rate on for Ru (A), Rh (B) and Pt (C) nanoparticles. Straight lines are obtained from a least squares fits of the logarithm of the desorption rate $r_{H_2}$.

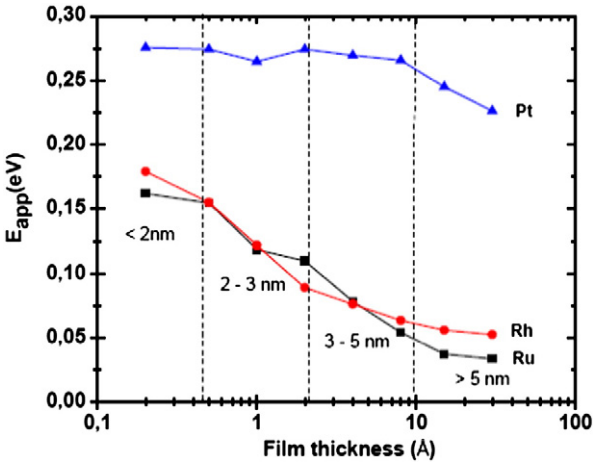


**Fig. 11.** The apparent desorption energy, $E_{app}$, for Ru, Rh and Pt nanoparticles as a function of the film thickness. The diameter in nm of the nanoparticles is also indicated in the figure. $E_{app}$ shows a dramatic decrease with the nanoparticle diameter for Ru and Rh nanoparticles. For Pt nanoparticles $E_{app}$ decreases slightly with nanoparticle diameter and it shows higher values with respect to Ru and Rh.

to the loss of entropy when going from the gas phase to the more localized adsorption, $\Delta H_{ads}$ will have to be negative at equilibrium. The change in $\Delta H_{ads}$ when one adsorbed atom is added into the facet is $\varepsilon/N_s$. This number will be small for large $N_s$ and appear continuous, however, for small values of $N_s$ , i.e. small terraces, there will be a gap in $\Delta H_{ads}$ of at most $\varepsilon/N_s$ when $\Delta G = 0$, as illustrated in Fig. 12. For instance, adding a hydrogen atom to a terrace with 25 sites for which $\varepsilon = 100$ kJ/mol will give a gap of 4 kJ/mol. In this simple illustration we have neglected that the adsorption sites close to edges and corners may have a different heat of adsorption than the sites on the terraces and that the heat of adsorption may change with particle size.

In the following we show how this may result in an apparent desorption energy close to zero, as measured in Fig. 11. Normally the desorption energy is associated with the numerical value of the adsorption enthalpy i.e. $E_{des} = -\Delta H_{ads}$ when there is no barrier for adsorption, which is the quantity measured in a temperature programmed desorption (TPD) experiment. But TPD is not an equilibrium measurement as the exchange experiments in this manuscript. At equilibrium $-\Delta H_{ads}$ has to be significant and equal to $T\Delta S_{ads}$. The net rate of adsorption at equilibrium is

$$r = 0 = r_{ads} - r_{des}. \tag{5}$$

In the mean field approximation the desorption rate is described as

$$r_{des}(\theta_H) = A(\theta_H, T)\cdot e^{-\frac{E_{des}(\theta_H)}{RT}}\cdot \theta_H \theta_D \tag{6}$$

and this is the rate measured in our exchange experiments. In the following analysis we assume for simplicity that the hydrogen and deuterium behave in the same way, that the total coverage is close to one and the ratio is given by the gas composition, i.e. the coverages show little or no temperature dependence for the interval studied here. The definition of the apparent activation energy, $E_{des}^{app}$, for a desorption reaction with desorption rate, $r_{des}$, is given by

$$E_{des}^{app} \equiv RT^2 \frac{d\ln(r_{des})}{dT}. \tag{7}$$

If it is assumed that the pre-exponential factor is only very weakly dependent on temperature and coverage, i.e. $A(\theta_H, T) \cong A$, the apparent desorption energy, $E_{des}^{app}$, from a compressed hydrogen adlayer is given by

$$E_{des}^{app}(\theta_H) = RT^2 \frac{d\ln(r_{des}(\theta_H))}{dT} = RT^2 \frac{d\left(-\frac{E_{des}(\theta_H)}{RT}\right)}{dT} = -T\frac{dE_{des}(\theta_H)}{dT} + E_{des}(\theta_H). \tag{8}$$

In the case of exchange reaction at the equilibrium conditions, the hydrogen coverage will be the one for which the free energy of adsorbed hydrogen, $G_{H_{ads}}(\theta_H^{eq})$, is equal to the free energy of gas phase hydrogen, $G_{H_2(g)}$:

$$G_{H_{ads}}(\theta_H^{eq}) - G_{H_2(g)} = \left(H_{H_{ads}} - TS_{H_{ads}}\right) - \left(H_{H_2(g)} - TS_{H_2(g)}\right) = \Delta H_{H_{ads}}(\theta_H^{eq}) - T\Delta S_{H_{ads}} = \Delta G_{ads}(\theta_H^{eq}) = 0. \tag{9}$$

Since $E_{des}$ is equal to $-H_{H_{ads}}$ when there is no barrier for adsorption we get

$$0 = G_{ads}(\theta_H^{eq}) = H_{H_{ads}}(\theta_H^{eq}) - TS_{H_{ads}} = -E_{des}(\theta_H^{eq}) - TS_{H_{ads}}. \tag{10}$$

So if the adsorption energy can be tuned continuously, due to compression of the hydrogen adlayer, the last two terms in Eq. (10)

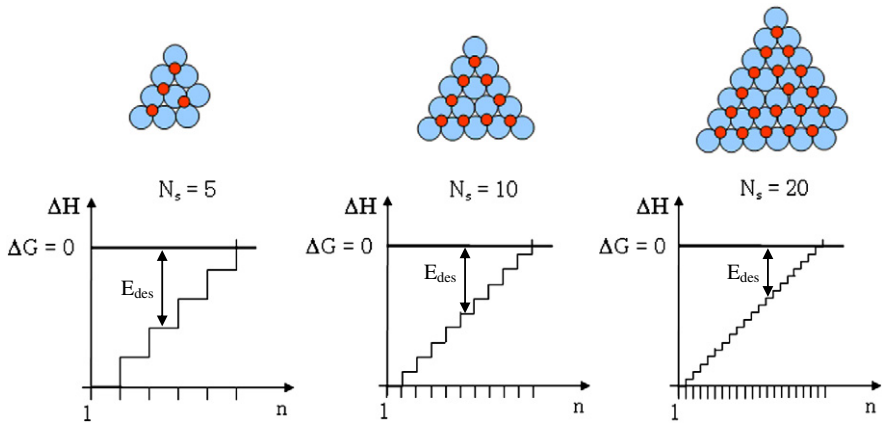


**Fig. 12.** The principles of a quantized adsorption energy in a compressed overlayer. The upper panels show a schematic picture of a facet at maximum coverage. The lower panels show schematic energy diagrams for adsorbed H as a function of the number of adsorbed H, $n$, for a various number of available sites, $N_s$. The hydrogen bond to the surface must be strong enough to keep below the $\Delta G = 0$ line. The diagrams show how at maximum coverage small facets will lead to an increasingly larger apparent desorption energy the smaller the facet gets.

will be exactly equal. Hence if we assume that the entropy only changes slowly with temperature we get that

$$E_{des}\left(\theta_H^{eq}\right) = -TS_{H_{ads}} \rightarrow \frac{dE_{des}\left(\theta_H^{eq}\right)}{dT} = -S_{H_{ads}} - T\frac{dS_{H_{ads}}}{dT} \cong -S_{H_{ads}}. \quad (11)$$

The apparent desorption energy can therefore by written as

$$E_{des}^{app}\left(\theta_H^{eq}\right) = -T\frac{dE_{des}\left(\theta_H^{eq}\right)}{dT} + E_{des}\left(\theta_H^{eq}\right) = TS_{H_{ads}} + E_{des}\left(\theta_H^{eq}\right) = 0 \quad (12)$$

according to the equilibrium conditions in Eqs. (10) and (11).

However if $E_{des}\left(\theta_H^{eq}\right) = -H_{ads}$ is a step function as illustrated in Fig. 12, it may not be able to match the continuous function $TS_{H_2}$ but be slightly larger, resulting in an apparent desorption energy. This will naturally be most evident when the steps in $H_{H_{ads}}$ are large, i.e. for small terraces. For the largest Ru and Rh nanoparticles the majority of the terraces are large enough to allow free tuning of the adsorption energy by compression of the adlayer, so that $E_{des}(\theta_H^{eq}) = TS_{H_2}$. For the smallest nanoparticles this is not possible for most of the terraces, which means that the apparent desorption energy will be higher than zero.

The catalysts produced in our experiments contain a range of nanoparticle sizes with different facets and $E_{app}$ is a measure of an ensemble average. If there is no barrier for adsorption for Ru and Rh, this explains why $E_{app}$ increases as the particles (and thus the terraces) become smaller. The formation of a compressed adlayer would also explain why the measured $E_{app}$ is so much lower than the heat of adsorption for H on clean Ru and Rh, which is about 100 kJ/mol $H_2$ [14].

The argument of a compressed adlayer formation on large terraces has been used previously in TPD experiments of isotopic exchange of CO on Pt and Ru single crystals and nanoparticles as the explanation for a faster exchange rate observed on the single crystal surface compared to the surface of the nanoparticles, due to size effects [29,30].

In the case of Pt, we measure a much slower exchange rate as a function of nanoparticle diameter and a larger but nearly constant apparent activation energy for desorption with respect to Ru and Rh, as shown in Figs. 9(C) and 11. The small variation in rate with particle diameter indicates that the surface structure for Pt is not very important for hydrogen splitting and desorption, or possibly that the local surface structure and defect density in these experiments are similar for all particle diameters. The high values measured for the apparent desorption energy could find an explanation in the hydrogen adsorption being slightly activated on the terraces of Pt nanoparticles in the range of size investigated, while not activated on undercoordinated sites. This is consistent with the observed increase in the hydrogen splitting rate with increasing temperature, as shown in Figs. 8(C) and 9(C). Adsorption of $H_2$ is activated on Cu [31] and Ni [32–35] and there are also indications of activation energies on the terraces of Pt single crystals and Pt alloys [36–38]. Moreover, if steps and defects are relevant sites in the hydrogen splitting on Pt nanoparticles, the HD exchange rate on small particles may be enhanced by the presence of these sites, which will annihilate the compressed adlayer effect observed for Ru and Rh nanoparticles. The existence of a barrier on the terraces of Pt nanoparticles would also be one of the reasons for the high sensitivity of Pt toward CO poisoning, besides the large difference in binding energy between hydrogen and CO on Pt [15], since it binds to step sites more strongly than to terraces [39]. The value for $E_{app}$ for the largest Pt particle diameters agrees well with the value of 0.21 eV reported for 50 Å thick deposited films on graphite. This value was found to be in good agreement with values for the heat of adsorption measured at high coverage on Pt(111) under vacuum conditions [13].

When 10 ppm of CO is added to the $H_2/D_2$ mixture, $p_{HD}$ drops for all the metals, as shown in Fig. 8(D) and (E), indicating a lower HD exchange rate. As a consequence, $S$ is inhibited significantly for all the metals, even at 200 °C, as shown in Fig. 9(D) and (E). Even if there is a slight decrease in $S$ for particle diameters below 3 nm in those cases where $S$ is measurable, there is no evidence of special nanoparticle diameters that are more resistent to CO poisoning than others.

## 6. Summary and conclusions

The equilibrium hydrogen exchange rate between adsorbed and gas phase hydrogen is investigated as a function of the nanoparticle diameter for Pt, Ru and Rh supported on a sputtered HOPG substrate by measuring the rate of the H–D exchange reaction at a hydrogen pressure of 1 bar, in the temperature range 40–200 °C. We find that Ru and Rh nanoparticles show higher ability than Pt in splitting hydrogen at 1 bar. The partial pressure of HD increases with the nanoparticle diameter for all the metals, as a consequence of a combination of a change in active surface area and in reactivity. In the case of Ru and Rh nanoparticles the equilibrium sticking probability per surface area, $S$, decreases for nanoparticle diameter below 3 nm, indicating that the hydrogen splitting is size sensitive at very small diameters and that it is faster on larger surfaces. The apparent energy of desorption, $E_{app}$, shows an increase for nanoparticle diameters below 5 nm. This is explained by the formation of a compressed hydrogen adlayer on Ru and Rh nanoparticles, where the heat of adsorption is lowered with coverage as a consequence of H–H repulsion. For Pt nanoparticles $S$ does not change significantly with the nanoparticle diameter, indicating that the hydrogen splitting is not size sensitive. The higher values of $E_{app}$ for Pt with respect to Ru and Rh are attributed to a possible activation energy for hydrogen dissociation on the terraces of the Pt nanoparticles at high coverage, which is consistent with the observed increase in the hydrogen splitting rate with increasing temperature.

Experiments are also carried out in the presence of 10 ppm CO. Pt is found to be very sensitive to CO poisoning and the hydrogen splitting rate in the presence of CO on Pt nanoparticles is below detection limit. In the case of Ru and Rh nanoparticles, CO decreases the splitting rate significantly, also at 200 °C. There is no evidence for Ru and Rh of special nanoparticle diameters that in the splitting of hydrogen improve the resistence to CO poisoning.

## Acknowledgment

Center for Individual Nanoparticle Functionality (CINF) is sponsored by The Danish National Research Foundation. Assistant Professor Thomas Jaramillo is kindly acknowledged for the useful and stimulating discussions.

## References

[1] S. Chen, B.D. Adams, A. Chen, Electrochim. Acta 56 (2010) 61.
[2] I. Pino, G.J. Kroes, M.C. van Hemert, J. Chem. Phys. 133 (2010) 184304.
[3] L. Wang, R.T. Yang, J. Phys. Chem. C 112 (2008) 12486.
[4] M. Yamauchi, H. Kobayashi, H. Kitagawa, ChemPhysChem 10 (2009) 2566.
[5] H. Kobayashi, M. Yamauchi, H. Kitagawa, Y. Kubota, K. Kato, M. Takata, J. Am. Chem. Soc. 132 (2010) 5576.
[6] R. Campesi, F. Cuevas, E. Leroy, M. Hirscher, R. Gadiou, C. Vix-Guterl, M. Latroche, Microporous Mesoporous Mater. 117 (2009) 511.
[7] J.J. Baschuk, Li Xianguo, Int. J. Energy Res. 25 (2001) 695.
[8] H. Igarashi, T. Fujino, M. Watanabe, J. Electroanal. Chem. 391 (1995) 119.
[9] T. Engel, G. Ertl, The Chemical Physics of Solid Surfaces and Heterogeneous Catalysis, Fundamental Studies of Heterogeneous Catalysis, Vol. 4, Elsevier, Amst., 1982, 0-444-41987-x.
[10] J.M. White, S. Akhter, CRC Crit. Rev. Solid State Mater. Sci. 14 (1988) 131.
[11] B. Riedmüller, D.C. Papageorgopoulos, B. Berenbak, R.A. van Santen, A.W. Kleyn, Surf. Sci. 515 (2002) 323.
[12] I.M. Ciobica, A.W. Kleyn, R.A. van Santen, J. Phys. Chem. B 107 (2003) 164.
[13] M. Johansson, O. Lytken, I. Chorkendorff, Top. Catal. 46 (2007) 175.
[14] M. Johansson, O. Lytken, I. Chorkendorff, J. Chem. Phys. 128 (2008) 034706.
[15] M. Johansson, O. Lytken, I. Chorkendorff, Surf. Sci. 602 (2008) 1863.
[16] M. Johansson, J. Hoffmann Jørgensen, I. Chorkendorff, Rev. Sci. Instrum. 75 (2004) 2082.

[17] M. Johansson, T. Johannesen, J. Hoffman Jørgensen, I. Chorkendorff, Appl. Surf. Sci. 252 (2006) 3673.
[18] R.M. Nielsen, S. Murphy, C. Strebel, M. Johansson, J.H. Nielsen, I. Chorkendorff, Surf. Sci. 603 (2009) 3420.
[19] H. Conrad, G. Ertl, E.E. Latta, Surf. Sci. 41 (1974) 435.
[20] R.J. Behm, K. Christmann, G. Ertl, Surf. Sci. 99 (1980) 320.
[21] K. Christmann, G. Ertl, T. Pignet, Surf. Sci. 54 (1976) 365.
[22] K.D. Rendulic, A. Winkler, J. Chem. Phys. 79 (1983) 5151.
[23] K. Christmann, O. Schober, G. Ertl, M. Neumann, J. Chem. Phys. 60 (1974) 4528.
[24] P.R. Norton, J.A. Davies, T.E. Jackman, Surf. Sci. 121 (1982) 103.
[25] R.M. Nielsen, S. Murphy, C. Strebel, M. Johansson, I. Chorkendorff, J.H. Nielsen, J. Nanopart. Res. 12 (2010) 1249.
[26] F. Claeyssens, S. Pratontep, C. Xirouchaki, R.E. Palmer, Nanotechnology 17 (2006) 805.
[27] S. Dahl, A. Logadottir, R.C. Egeberg, J.H. Larsen, I. Chorkendorff, E. Törnqvist, J.K. Nørskov, Phys. Rev. Lett. 83 (1999) 1814.
[28] M.P. Andersson, F. Abild-Pedersen, I.N. Remediakis, T. Bligaard, G. Jones, J. Engbæk, O. Lytken, S. Horch, J.H. Nielsen, J. Sehested, J.R. Rostrup-Nielsen, J.K. Nørskov, I. Chorkendorff, J. Catal. 255 (2008) 6.
[29] M. Andersen, M. Johansson, I. Chorkendorff, J. Phys. Chem. B 109 (2005) 10285.
[30] S. Murphy, C. Strebel, S.B. Vendelbo, C. Conradsen, Y. Tison, K. Nielsen, L. Bech, R.M. Nielsen, M. Johansson, I. Chorkendorff, J.H. Nielsen, Phys. Chem. Chem. Phys. 13 (2011) 10333.
[31] P.B. Rasmussen, P.M. Holmblad, H. Christoffersen, P.A. Taylor, I. Chorkendorff, Surf. Sci. 287 (288) (1993) 79.
[32] J.N. Russel Jr., S.M. Gates, J.T. Yates Jr., J. Chem. Phys. 85 (1986) 6792.
[33] J.T. Yates Jr., J.N. Russel Jr., I. Chorkendorff, S.M. Gates, in: M. Grunze, H.J. Kreuzer (Eds.), Springer Series in Surface Science 8, Springer-Verlag, Heidelberg, 1987.
[34] D.O. Hayward, A.O. Taylor, Chem. Phys. Lett. 124 (1986) 264.
[35] H. Karner, M. Luger, H.P. Steinrück, A. Winkler, K.D. Rendulic, Surf. Sci. Lett. 163 (1985) 641.
[36] I.M.N. Groot, A.W. Kleyn, L.B.F. Juurlink, Angew. Chem. Int. Ed. 50 (2011) 5174.
[37] A.C. Luntz, J.K. Brown, M.D. Williams, J. Chem. Phys. 93 (1990) 5240.
[38] P. Sanson, A. Nesbitt, B.A. Koel, A. Hodgson, J. Chem. Phys. 109 (1998) 3255.
[39] H.R. Siddiqui, X. Guo, I. Chorkendorff, J.T. Yates Jr., Surf. Sci. 191 (1987) L813.

# Strong metal support interaction of Pt and Ru nanoparticles deposited on HOPG probed by the H-D exchange reaction

*Elisabetta. M. Fiordaliso*, Søren Dahl, Ib Chorkendorff*

Danish National Research Foundation's Center for Individual Nanoparticle Functionality (CINF) and Nano DTU, Department of Physics, Technical University of Denmark, DK-2800 Kgs. Lyngby, Denmark

*E-mail address: e.fiordaliso@fysik.dtu.dk

**ABSTRACT:** The interaction between metals and support is investigated in the case of 50 Å Pt and 50 Å Ru films deposited on a HOPG substrate. The films are prepared by Electron Beam Physical Vapor Deposition and annealed in UHV to temperatures up to 700°C. The equilibrium hydrogen exchange rate between adsorbed and gas phase at 1 bar is measured before and after annealing. The rate is measured in the temperature range 40 – 200 °C at 1 bar, by utilization of the H-D exchange reaction. Experiments are performed on fresh cleaved and sputtered HOPG, which give similar results. We find that annealing the films from 150 °C up to 700 °C increases the amount of carbon present in the films up to 95%, as derived by surface analysis, indicating the formation of a carbon layer on top of the metal films. The exchange rate decreases dramatically with increasing carbon content on the films for both metals, pointing to a decrease in the hydrogen adsorption on the films, due to the strong metal support interaction (SMSI). We show how to reverse the SMSI by performing $He^+$ sputtering, which enables to remove the carbon layer and regenerate the Pt catalysts. ISS spectra show that the Pt signal increases to

around 95% of its initial value and we measure an exchange rate at 200 °C comparable to the value measured before annealing.

**KEYWORDS:** Support interaction, Platinum, Ruthenium, Carbon, Annealing, Ion Scattering Spectroscopy.

## 1. INTRODUCTION

In heterogeneous catalysis, reactions are often carried out on supported catalysts, which are dispersed on the substrate in order to obtain and maintain a large surface area, where the catalytic reactions take place. Supports are generally metal oxides or different forms of carbon, able to provide a stable high surface area. The efficiency of the catalysts is often also dependent on the metal-support interactions, which can affect significantly the catalytic properties of the metals. Strong metal-support interactions (SMSI) have been intensively studied in the last decades in the case of the group VIII-X metals supported on reducible oxides such as $TiO_2$, for which it is found that $H_2$ and CO chemisorption is drastically decreased after reduction at high temperature,[1,2] whereas methanation of CO or $CO_2$ and $H_2$ is significantly increased.[3] It has been shown that the modification of the catalytic activity is related to an encapsulation of the deposited metal by a reduced thin oxide layer migrating from the support during annealing, which causes the strong decrease on the metals ability to adsorb $H_2$ and CO.[4-10] It has also been shown that re-oxidation and reduction cycles, steam treatments at different conditions and sputtering can reverse the SMSI state, leading to a full recovery of the metallic states of the catalysts and of their catalytic properties.[11-13]

In this work we investigate the interaction between 50 Å Pt and Ru films and a carbon support, namely Highly Ordered Pyrolytic Graphite (HOPG), when the metals are annealed in UHV to high temperatures, as in the case of metals supported on $TiO_2$. The hydrogen exchange rate of the Pt and Ru films is measured before and after annealing and a SMSI is observed, causing a significant decrease in the ability of dissociating hydrogen for Pt and Ru. We also show that it is possible to reverse the SMSI state by performing $He^+$ sputtering, which enables the regeneration of the catalytic performance of the

metal films. Finally we try to quantify the thickness of the carbon layer covering the metals upon annealing.

## 2. EXPERIMENTAL DETAILS

The experiments are performed in a Parallel Screening apparatus described in previous publications.[14,15] It combines an UHV chamber for sample preparation and surface analysis with a High Pressure Cell (HPC) for catalytic reactions. Circular metal films of 1 mm diameter are produced by Electron Beam Physical Vapor Deposition (EBPVD), with typical deposition rates of 5 – 10 Å/min and a 10×10 mm HOPG is used as substrate. Deposition takes place at room temperature and the thickness of the films is determined by calibrating the deposition rate with a quartz crystal microbalance. In a previous work on the H-D exchange reaction on Pt and Ru films, it was found that the films consist of nanoparticles and a relationship between film thickness and particle diameter was established by using STM.[16] According to that, the 50Å Pt and Ru films analyzed in this study are expected to consist of close packed particles with a diameter of around 5 nm.

After deposition, cleanliness of the Pt and Ru films is checked by Auger Electron Spectroscopy (AES), X-Ray Photoelectron Spectroscopy (XPS) and Ion Scattering Spectroscopy (ISS) at 150 °C, in order to keep the films clean from CO. Afterwards, the catalysts are annealed from 300 °C to 700 °C in steps of 100 °C, with a temperature ramp of 1 K/s, in the UHV chamber, which has a basal pressure of $1.0 \cdot 10^{-10}$ Torr. The sample is kept at each annealing temperature for two minutes and it is cooled down to 150 °C. AES, XPS and ISS are used to investigate the surface of the Pt and Ru films after each annealing temperature. All the spectra shown in this document are acquired at 150 °C.

The H-D exchange reaction is carried out in the HPC, where the activity is determined by measuring the local gas composition over the center of the circular metal films. The gas is sampled with a quartz capillary leak and analyzed using mass spectrometry. The HOPG substrate is glued onto a graphite disk, 10 mm in diameter and about 1 mm in thickness. The graphite disk is mounted on two tungsten wires,

which are used for heating. The sample temperature is measured with a thermocouple glued at the edge of the HOPG substrate, as shown in Figure 1.[17]

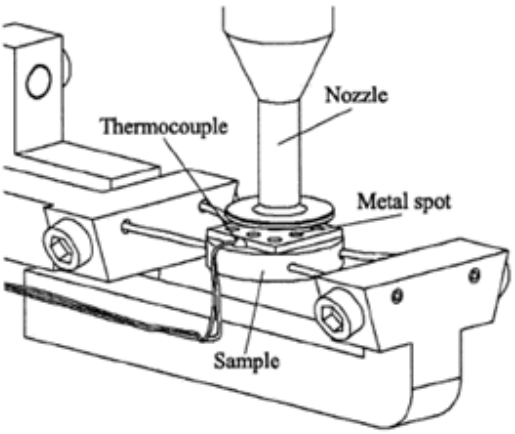


**Figure 1**. A sketch of the gas sampling device positioned over a sample with circular metal films.[17] *Published with kind permission from Springer Science and Business Media B.V.*

The gases used are N60 (99.9999%) $H_2$ and 99.8% $D_2$ (main contaminant HD) which are additionally purified by guard catalysts (Haldor Topsoe MK 121, activated in hydrogen at 240 °C). In order to avoid contamination by sulfur, the HPC is cleaned by flowing hydrogen through it at 1 bar for 48 h during bakeout at 150 °C. The HOPG sample is cleaned by Ar sputtering for several hours between experiments, followed by heating to 800 °C for 20 min to desorb any remaining Ar from the surface of the HOPG. In this study a fresh cleaved HOPG is also used as substrate, in order to see if any significant difference occurs upon annealing with respect to the films deposited on sputtered HOPG.

The high pressure measurements are carried out with a mixture of 1% $D_2$ in $H_2$ at 1 bar total pressure. The equilibrium $H_2$ exchange rate, which is equal to both the rates of dissociative $H_2$ adsorption and $H_2$ desorption at equilibrium, is determined by the progress of H–D exchange reaction: $H_2 + D_2 \leftrightarrow 2HD$, in the temperature range of 40 – 200 °C. The sample is first kept in the HPC at 1 bar and 200 °C for at least 1 h, the time needed to align the gas sampling device. The measurements are then carried out for decreasing temperatures with start at 200 °C. To safeguard against changes in the reaction rate due to,

e.g., contamination or structural changes of the surfaces, the measurement at 200 °C is repeated at the end of the series. The progress of the H-D exchange reactions is monitored by a mass spectrometer, by measuring the signals of 2 AMU for $H_2$, 3 AMU for HD and 4 AMU for $D_2$.

## 3. DATA PROCESSING

A simple model, which is described in detail in earlier publications,[15,17] is used to describe the kinetics of the HD exchange reaction. The model provides information on the equilibrium dissociative sticking probabilities, *S*, for $H_2$, $D_2$ and HD, which are numerically calculated from the partial pressures measured by the gas sampling device placed on top of the centers of the circular metal films and from the local gas velocity and temperature inside the gas sampling device.[15,17] The equilibrium rate constant for $H_2$ desorption, $k_{des}$, can be obtained from *S* since at equilibrium the adsorption rate, $R_{ads}$, is equal to the desorption rate, $r_{des}$:

$$R_{ads} = r_{des} \Leftrightarrow FS = k_{des}\theta_H^2 \approx k_{des} \quad (1)$$

where F is the molecular flux of hydrogen and $\theta_H$ is the equilibrium coverage of hydrogen, which is assumed to be very close to one, under experimental conditions in this investigation.[17-21]

## 4. RESULTS

### 4.1. Surface composition analysis on 50 Å Pt films deposited on sputtered HOPG

ISS with 1 keV $He^+$ ions is performed at 150 °C on the 50 Å Pt films deposited on sputtered HOPG, to investigate the composition of the outer layer of the films after deposition. The films are eventually annealed in UHV at temperatures up to 700 °C and they are cool down to 150 °C before performing ISS. The ISS spectra are shown in Figure 2 and the wide energy range is reported. The Pt film generates a peak located at 977 eV, whereas for C we are not able to measure any signal in this energy range. This is in agreement with results of a previous work, where it was shown that a graphitic carbon signal is

detectable only at primary energies of 3.5 keV or higher.[22] We find that with increasing temperature the Pt signal drops significantly and no other peaks are appearing. Since the Pt is not simply disappearing, our interpretation is that carbon, likely in a graphitic form, is segregating to the surface of the Pt films upon annealing. This is also similar to the observations made in a work on a carbon doped Re sample, where it was found that by increasing the temperature a full layer of graphitic carbon was formed and the Re ISS signal dropped to the noise level.[22]

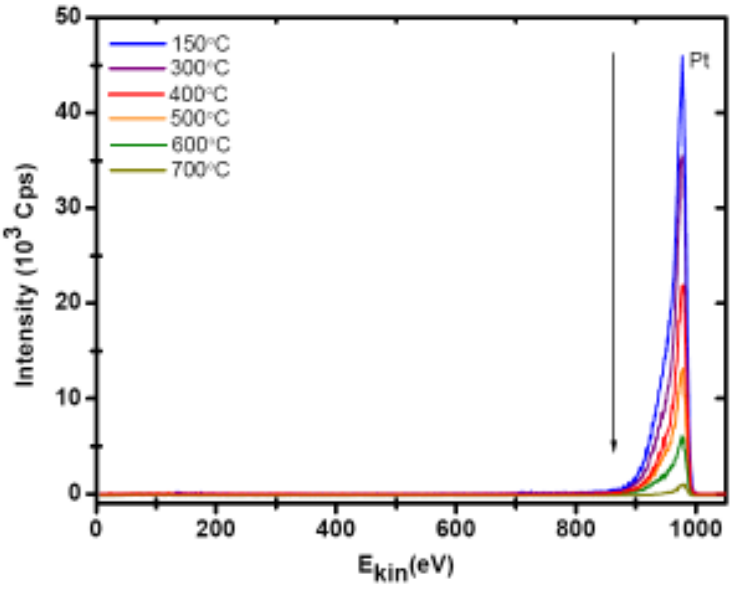


Figure 2. ISS spectra for 1keV $He^+$ ions scattered from the 50 Å Pt films deposited on sputtered HOPG after annealing to temperatures up to 700 °C.

AES is also performed on the 50 Å Pt films, since with this technique the Pt and the C signals are both detectable. AES spectra with 3 keV electrons are acquired on the films at 150 °C after metal deposition and after annealing in UHV to temperatures up to 700 °C. The AES spectra are acquired in a wide energy range but since no contaminations are observed, only narrow energy windows are shown in Figure 3 (a-g), where the main Pt and C AES lines are located at 64 eV and 272 eV, respectively. The low kinetic energy of these auger electrons indicates that the sampling depth for this technique is ~ 0.5 nm for Pt and 0.7 nm for C,[23] corresponding roughly to the first few layers of the Pt film. For

comparison, an AES spectrum of the HOPG at 150 °C far from the metal films is shown in Figure 3 (h), in a narrow energy window around the C peak. We find that with increasing annealing temperature the Pt signal decreases and the C signal increases significantly, confirming that the surface of the Pt films get covered by C upon annealing.

Finally, XPS with 1253.6 eV photons coming from a $Mg_{Ka}$ anode is also used to characterize the 50 Å Pt films deposited on sputtered HOPG. Figure 4 shows the XPS spectra acquired at 150 °C after annealing the films in UHV to 400 °C, 600 °C and 700 °C. A narrow range of energy from 100 eV to 0 eV, where the Pt $4f_{7/2}$ and Pt $4f_{5/2}$ peaks are located at 74 eV and 71 eV, respectively, is reported. The insert of Figure 4 shows a narrow energy window around the C peak, located at 284 eV. For comparison, a spectra of the HOPG far from the metal films is also shown. The kinetic energy of the emitted photoelectrons for Pt and C is higher compared to the Auger electrons, meaning that XPS has a larger sampling depth than AES, of around 1.8 nm for Pt and 1.6 nm for C.[23] We find that with increasing temperature the Pt signal decreases and the C signal increases.

The changes in the C and Pt signals as a function of the temperature are reported in Figure 5 (a) and (b), respectively, which show a dramatic increase of C upon annealing. In Figure 5 (b) the decrease of the Pt signal as a function of the temperature measured by ISS is also plotted, where the initial value for the Pt signal is normalized to the initial value given by AES, which is reasonable due to the high surface sensitivity for Pt of both ISS and AES techniques, resulting in a similar trend in the drop of the Pt signal. With XPS a larger C signal is measured compared to AES. This is due to the large sampling depth of XPS combined to a large sampling area, which causes a signal from the carbon underneath the Pt film (the support) and from the Pt free areas of the HOPG (the surrounding areas) to reach the analyzer. According to that, the XPS signals are not considered for further analysis in this document. Considering this increased complexity and the decreased surface sensitivity we are not using the XPS signals for further analysis in this work.

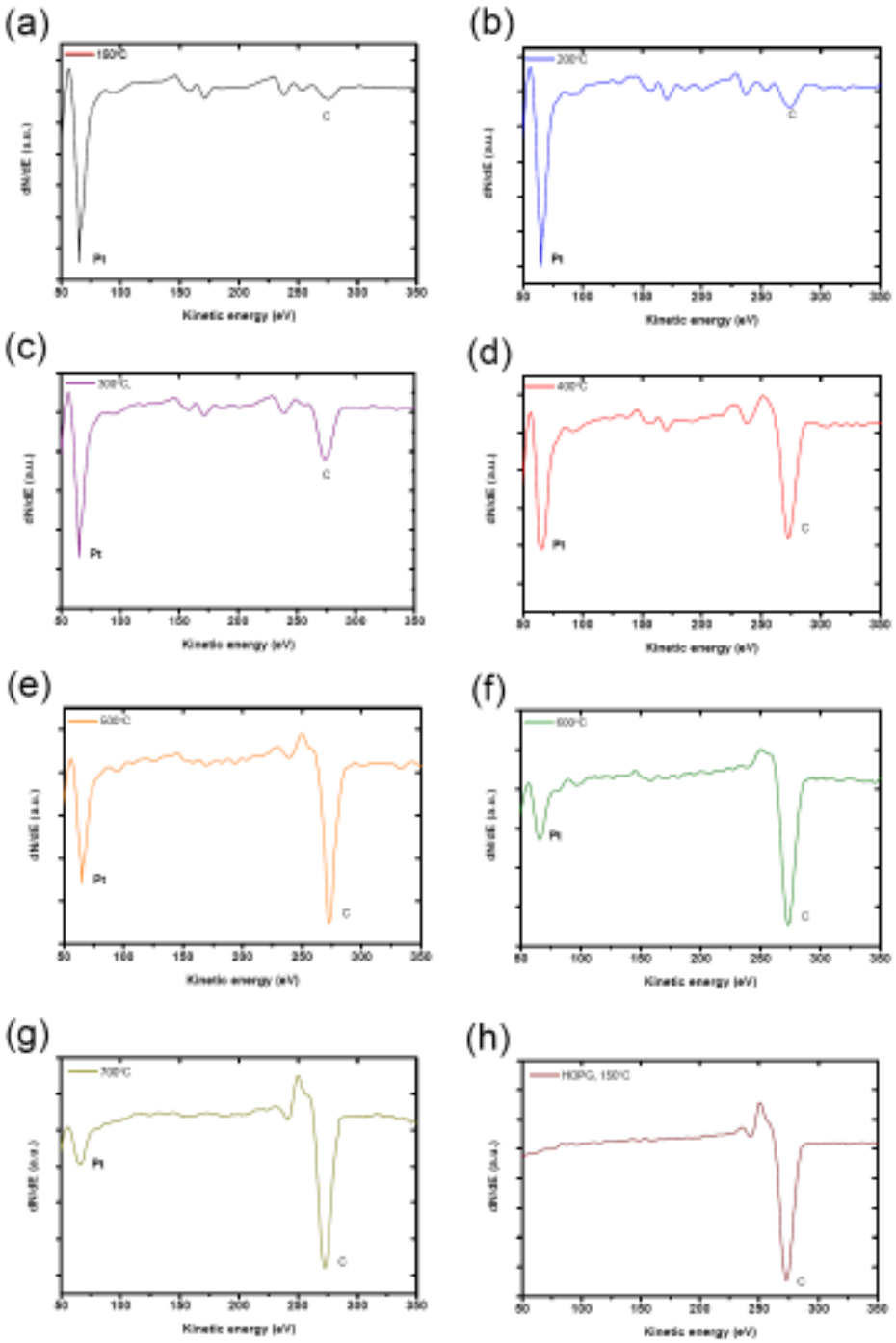


Figure 3. (a-g) AES spectra for 3 keV electrons of a 50 Å Pt film deposited on sputtered HOPG, after annealing to temperatures up to 700 °C. (h) AES spectrum of the HOPG.

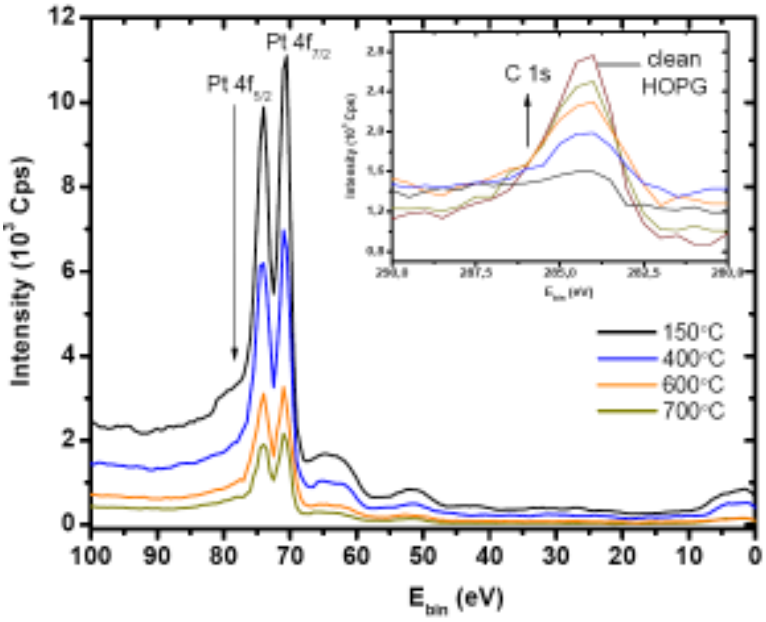


Figure 4. XPS spectra of a 50 Å Pt film deposited on sputtered HOPG, after annealing to temperatures up to 700 °C. The insert shows the C signal.

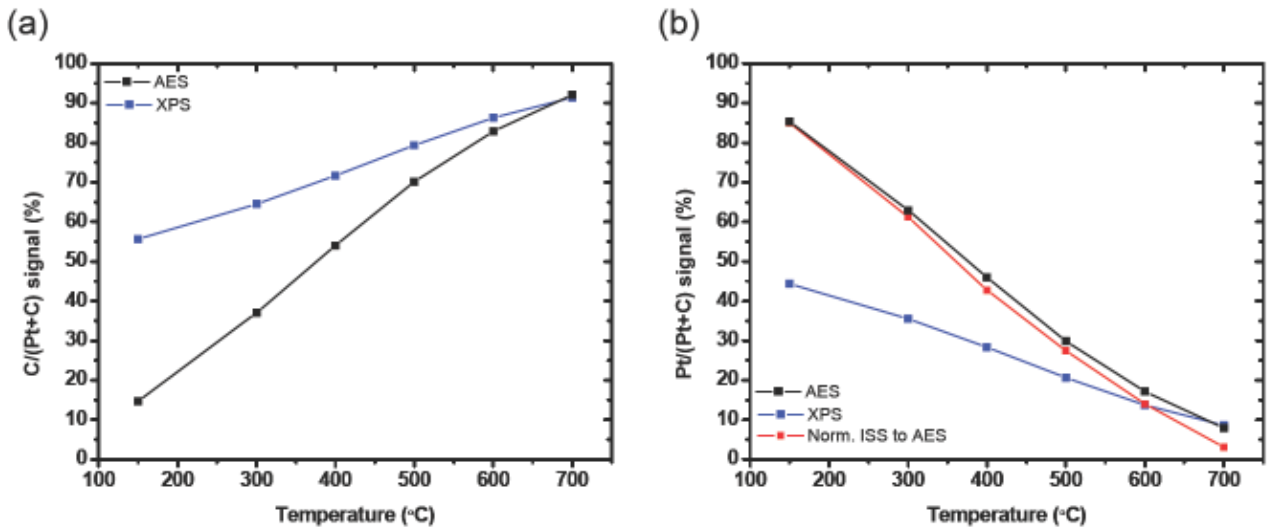


Figure 5. (a) C/(Pt+C) signal as a function of annealing temperature, as derived by AES amd XPS analysis. (b) Pt/(Pt+C) signal as a function of annealing temperature, as derived by AES, XPS and ISS analysis, where the initial Pt signal given by ISS is normalized to the initial signal given by AES.

### 4.2. H-D exchange rate for 50 Å Pt films deposited on sputtered HOPG

Figure 6 shows the results of the H-D exchange reaction measured on the 50 Å Pt films after annealing to temperatures up to 700°C. $p_{HD}$ is plotted as a function of the reaction temperature, in the range 40 – 200 °C. We find that $p_{HD}$ increases as a function of temperature and decreases dramatically with annealing temperature, due to the increase of the carbon content in the Pt films upon annealing, as shown in Figure 5 (b), as a consequence of the SMSI.

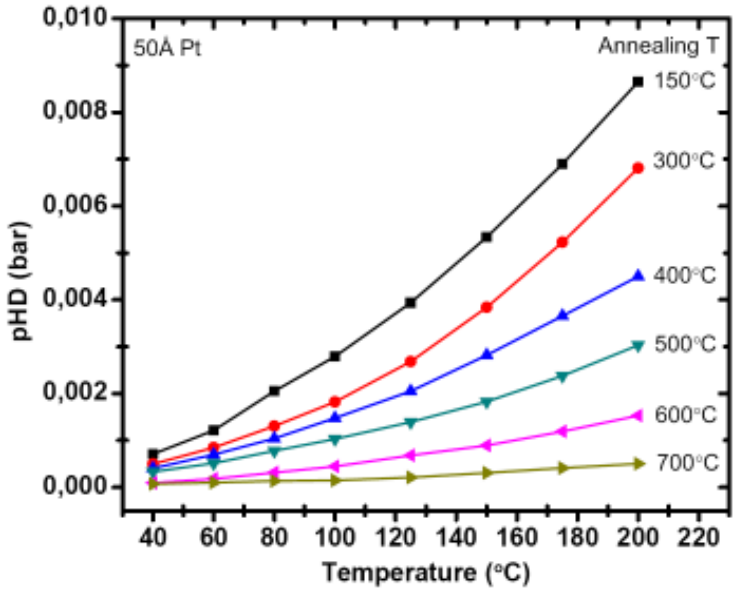


**Figure 6.** Measured values for $p_{HD}$ as a function of the reaction temperature over the center of the Pt films deposited on sputtered HOPG. The annealing temperatures are indicated for each curve.

In Figure 7 $p_{HD}$ measured at 200°C is plotted as a function of the Pt signal, given by ISS, after annealing the 50 Å Pt films to temperatures up to 700 °C, which are indicated in the plot. A linear decrease of $p_{HD}$ is observed with decreasing Pt signal, indicating that the hydrogen exchange reaction on Pt is not structure sensitive. This result is in agreement to a previous study of the $H_2$ splitting on Pt nanoparticles, which showed that the exchange rate on Pt is nearly constant with particle size.[16]

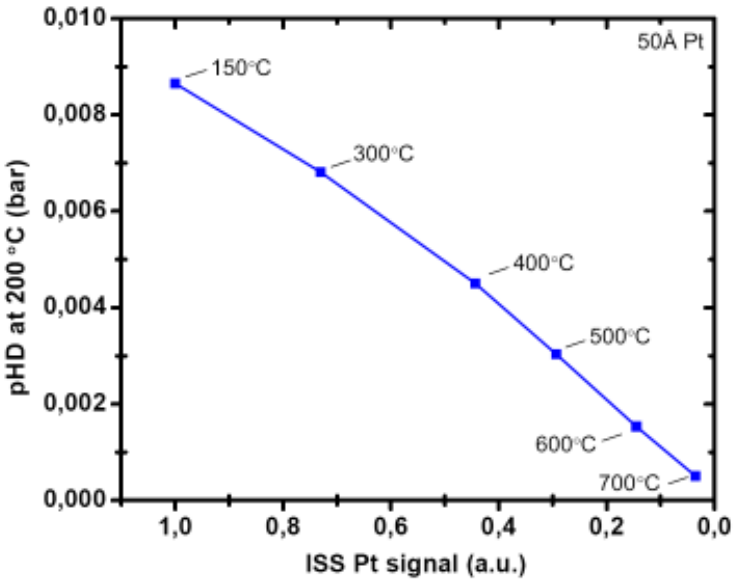


**Figure 7.** Measured values for $p_{HD}$ at 200 °C over the center of the Pt films deposited on sputtered HOPG, as a function of the Pt signal, given by ISS. The annealing temperatures are indicated besides the data points.

### 4.3. Surface composition analysis and H-D exchange rate for 50 Å Ru films deposited on sputtered HOPG

Similar experiments are performed on 50 Å Ru films deposited on sputtered HOPG, since Ru was found to be the most active catalyst for the hydrogen exchange reaction among different metals.[18] AES spectra with 3 keV electrons are acquired on the films at 150 °C after deposition. Afterwards, the films are annealed in UHV to temperatures up to 700 °C and the temperature is decreased to 150 °C before performing AES. Figure 8 (a) and (b) shows AES spectra of 50 Å Ru films acquired at 150 °C after deposition and after annealing to 700 °C, in a narrow energy window around the Ru AES lines. Since the main AES line for Ru is located at 273 eV and overlaps with the C line, located at 272 eV, quantification of the surface composition is difficult with this technique. However we can definitely observe a dramatic decrease in the amplitude of the secondary lines for Ru after the films are annealed to 700 °C, indicating that largest contribution to the main peak in Figure 8 (b) is given by C. ISS is also

performed on the 50 Å Ru films at 150 °C, with 1 keV $He^+$ ions, after annealing the films up to 700 °C. ISS spectra are shown in Figure 8 (c) in a narrow energy window around the Ru peak, which is located at 934 eV. We find that with increasing temperature the Ru signal decreases down to around 5 % of the initial value, as in case of the Pt films, indicating that the SMSI occurs also between Ru and HOPG causing the surface of the Ru films to get covered by C upon annealing. Finally we also perform the H-D exchange experiment on the Ru films, after deposition and after annealing to 700 °C. The results are shown in Figure 8 (d), where $p_{HD}$ is plotted as a function of the reaction temperature, in the range 40 – 200 °C. We find that $p_{HD}$ decreases significantly when the Ru films are annealed to 700 °C, due to the SMSI which causes a suppression of the catalytic activity of Ru, as for Pt.

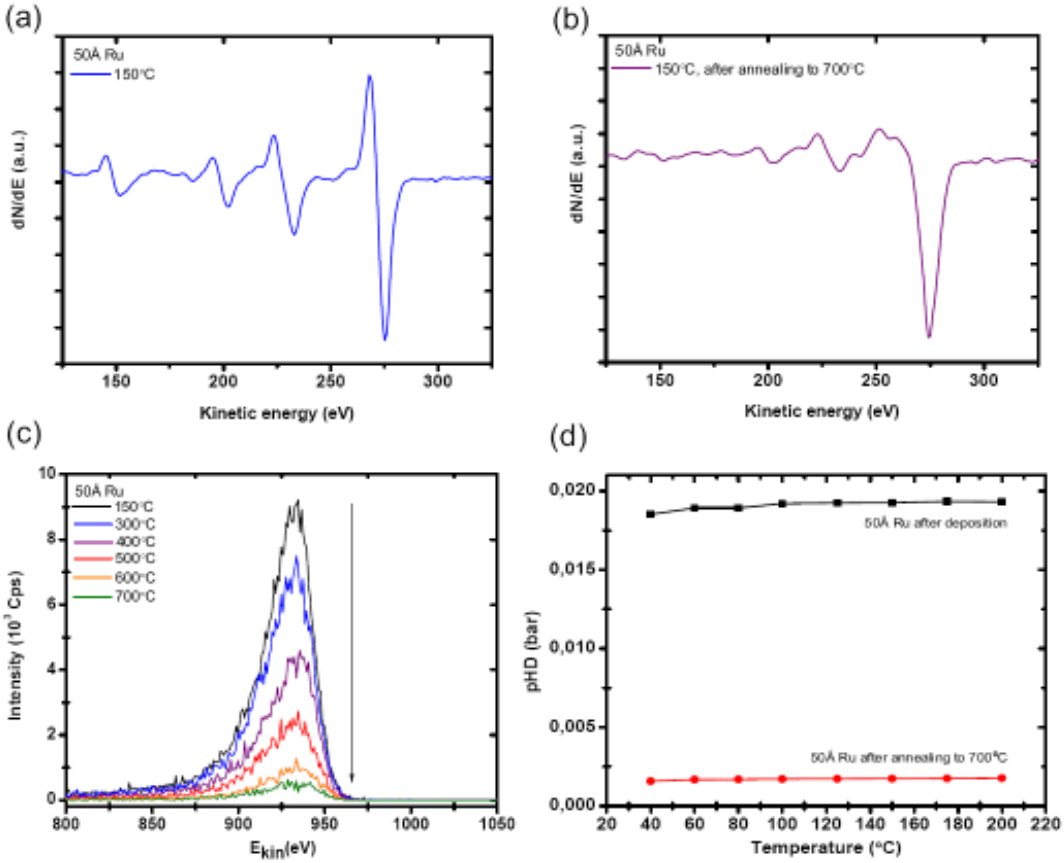


**Figure 8.** (a) and (b) AES spectra for 3 keV electrons of a 50 Å Ru film deposited on sputtered HOPG acquired at 150 °C, after deposition and after annealing to 700 °C, respectively. (c) ISS spectra at 150 °C for 1keV $He^+$ ions scattered from the 50 Å Ru film at different annealing temperatures. (d) Measured

values for $p_{HD}$ as a function of the reaction temperature over the center of the Ru films after deposition and after annealing to 700 °C.

### 4.4. Surface composition analysis and H-D exchange rate on 50 Å Pt and Ru films deposited on fresh cleaved HOPG

The $Ar^+$ sputtered HOPG is a highly defective substrate which could contain loose carbon and strongly fragmented graphite sheets. In order to investigate if the sputtering process is responsible for the SMSI, 50Å Ru and Pt films are deposited on a fresh cleaved HOPG.

First, the H-D exchange rate is measured on the films after deposition and the results are reported in Figure 9 (a), where they are compared to the values measured on the films deposited on sputtered HOPG. We find that the values for $p_{HD}$ on the films deposited on unsputtered HOPG are lower than the ones measured on sputtered HOPG at any temperature, for both metals. The loss in activity is a consequence of a decrease of the nanoparticles surface area within the films, caused by sintering effects due to a poorer adhesion to the substrate, which has a low density of nucleation sites when it is not sputtered. The effect of the substrate conditions on the particle size formation has been shown in previous works on Ru and Ag particles deposited on carbon substrates.[24,25] Moreover the decrease in activity is larger for Pt than for Ru, which is likely due to Ru being more reactive and having a higher melting point with respect to Pt, making the Pt nanoparticles more inclined to sintering on a unsputtered substrate.

Eventually, the films are annealed in UHV to 700 °C. Figure 9 (b) shows an AES spectrum for 3 keV electrons of the Pt films, in a narrow energy window around the Pt and the C peaks. The insert shows the AES spectrum acquired after deposition. We find that the C signal on the Pt films after annealing is around 90% and is comparable to the value found on the films deposited on sputtered HOPG, shown in Figure 5. Depositing the metals on unsputtered HOPG therefore does not prevent that the metals upon annealing get covered by C.

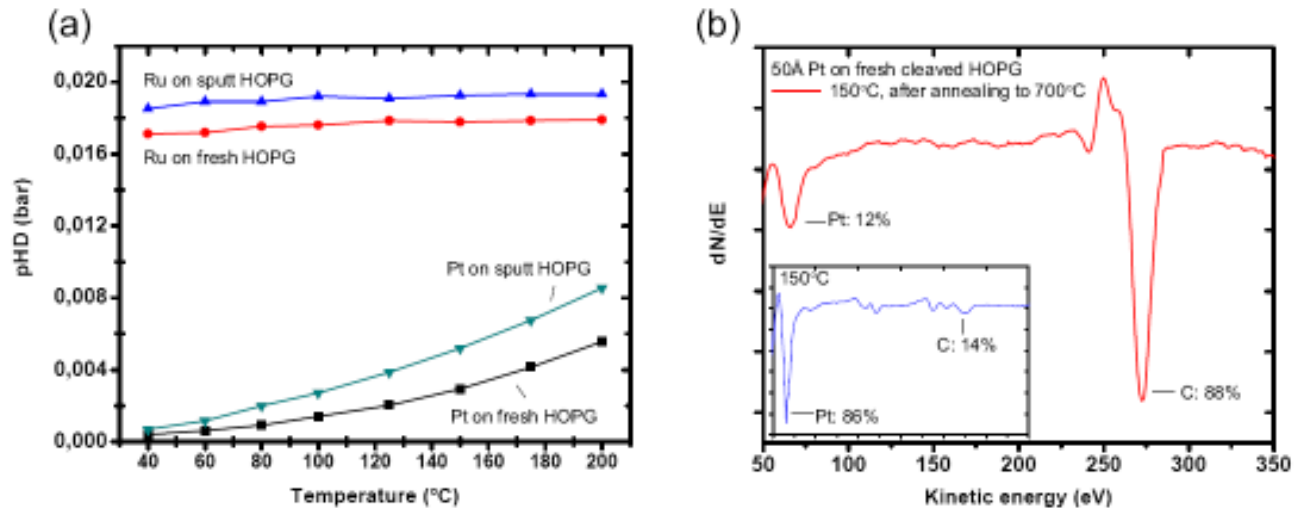


**Figure 9.** (a) Measured values for $p_{HD}$ as a function of the reaction temperature over the center of the Pt and Ru films after deposition on a fresh cleaved HOPG, compared to the values measured on sputtered HOPG. (b) AES spectra for 3 keV electrons of a 50 Å Pt film deposited on a fresh cleaved HOPG after annealing to 700 °C. The insert is a AES spectrum of the Pt films, as deposited.

### 4.5. Reversing the SMSI with $He^+$ sputtering

The ISS Pt signal of the Pt film deposited on sputtered HOPG after annealing to 700 °C drops to less than 5% of its initial value, as shown in Figure 5. The 1 keV $He^+$ ion beam is used as soft sputter beam, which is focused on the Pt film. The current through the sample is around 20 nA and the beam is rastered on an area of 1 $mm^2$, to cover the whole Pt film. The temperature of the sample is 150°C. Under these conditions an ISS spectrum is acquired every 5 minutes for 1 h and the results are reported in Figure 10. We find that the Pt signal increases with sputtering time and it reaches around 95% of its initial value after around 45 minutes of sputtering, leveling out after this time.

Eventually the catalytic activity of the Pt films is tested and the measured partial pressure of HD, $p_{HD}$, is plotted in Figure 11, as a function of the reaction temperature, in the range 40 – 200 °C. In the figure, $p_{HD}$ is compared to the values measured on the Pt film after deposition and we find that the activity of the Pt films after sputtering is roughly 95% of what it was after deposition, which is consistent with the ISS results.

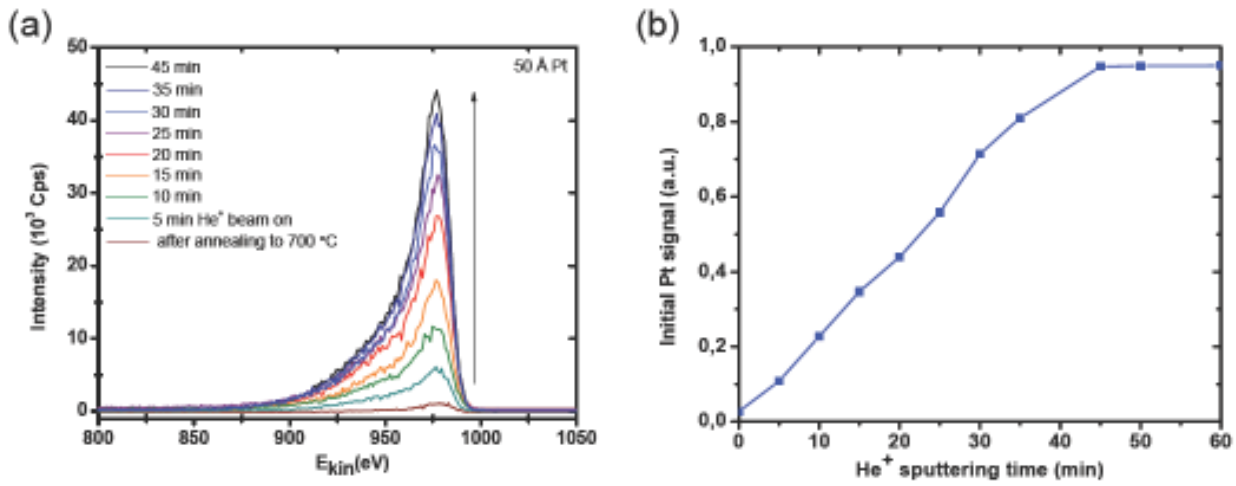


**Figure 10.** (a) ISS spectra at 150 °C for 1keV $He^+$ ions scattered from a 50 Å Pt film which was annealed to 700 °C, acquired within 45 minutes. (b) Pt signal as a function of the sputtering time.

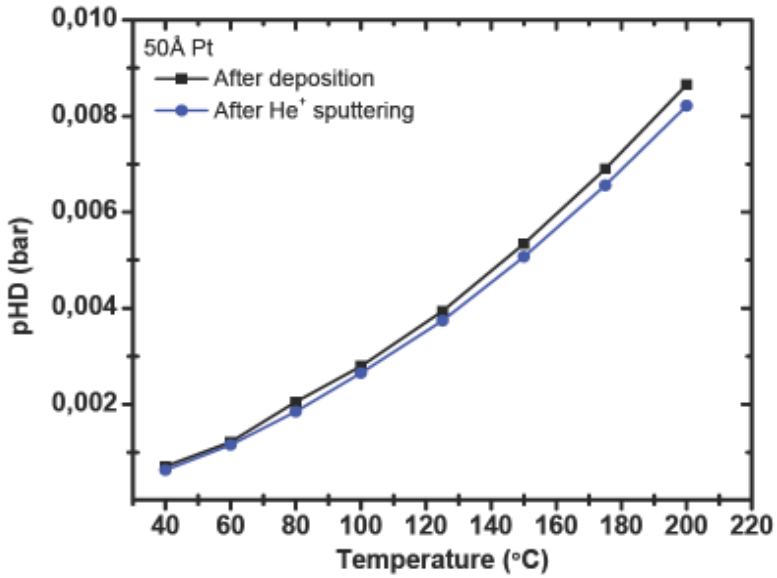


**Figure 11.** Measured values for $p_{HD}$ as a function of the reaction temperature over the center of the 50 Å Pt film after deposition and after 60 minutes $He^+$ sputtering.

## 5. DISCUSSION

In the previous section we show that annealing 50 Å Pt and Ru metal films supported on sputtered or unsputtered HOPG to high temperature in UHV, causes a significant increase of C on the metal films, with a consequent suppression of their catalytic activity. We think that a SMSI is responsible for this effect, which consists in the formation of a carbon layer on the surface of the films, rather than loss of surface area due to particle sintering upon annealing. This conclusion is based on the high roughness of the support surface, especially on the sputtered HOPG, which prevents sintering to happen, and on the fact that we are able to regenerate the catalytic activity of the Pt films by performing $He^+$ sputtering, indicating that the SMSI state can be reversed. Our results are similar to what is found in the case of metals annealed on reducible oxides, for which it has been shown that the modification of the activity is caused by a reduced thin oxide layer migrating from the support onto the metals during annealing, causing the suppression of the metals ability to adsorb $H_2$ and CO.[4-10]

In the follow we try to quantify the thickness of the carbon layer covering the Pt films upon annealing. In order to do that, we calculate how many layers of carbon are removed while sputtering the films with the 1 KeV $He^+$ beam, which is able to regenerate the Pt signal, as shown in Figure 10. The sputtering rate per hour, $S_r$, is given by:

$$S_r = \frac{J}{M} Y_\theta \,, \tag{2}$$

where $J$ is the beam current density on the sample, given by

$$J = \frac{I}{A} = \frac{0.02\mu A}{0.01 cm^2} = 12.5 \cdot 10^{12} \frac{q}{s \cdot cm^2} \,. \tag{3}$$

$M$ is the density of graphene per monolayer, equal to $2.05 \cdot 10^{15}$ atoms/($cm^2$·ML). $Y_\theta$ is the angular sputter yield, equal to $Y \cdot \cos(\theta)^{-1}$,[26,27] where $\theta$ is the angle between the $He^+$ beam and the sample, which is 50° in our experiments. A sputter yield of 0.07[28] results in $Y_\theta \approx 0.1$.

According to these values, we find that $S_r$ is 1.7 ML/h, indicating that upon annealing the Pt films get covered by between one and two carbon layers. $S_r$ is only an indicative number, which is strongly

dependent on the values used while calculating it, especially since *Y* and its angular dependence are not exactly defined. However, a sputtering rate of 1.7 ML/h is a reasonable number.

Another way to estimate the thickness of the carbon layer is to use the AES signals from Pt and C to calculate the damping in the Pt signal due to the formation of the C overlayer. The probability to escape from the sample of electrons which are emitted from a depth of z, can be calculated as:

$$\frac{P_{Pt}(z)}{P_C(z)} = \frac{S_{Pt}}{S_C} \frac{\int_a^\infty N_{Pt}(z) \cdot e^{-\frac{z}{\lambda_{Pt}}} dz}{\int_0^a N_C(z) \cdot e^{-\frac{z}{\lambda_C}} dz}, \tag{4}$$

where $P_{x,} S_x$ and $N_x$ are the AES signal of the element *X*, its AES sensitivity and its density, *a* is the thickness of the carbon layer that we want to estimate and $\lambda_x$ is the elastic mean path for the emitted electron. Eq. (4) can be simplified by considering the film homogeneous and using the same density for Pt and C. Moreover the inelastic mean path can also be approximated to be the same for Pt and C, roughly equal to 0.5 nm. With these assumptions we get:

$$\frac{P_{Pt}(z)}{P_C(z)} = A \frac{\int_a^\infty e^{-\frac{z}{\lambda_{Pt}}} dz}{\int_0^a e^{-\frac{z}{\lambda_C}} dz} = A \frac{e^{-\frac{a}{\lambda_{Pt}}}}{(1 - e^{-\frac{a}{\lambda_C}})} = \frac{A}{e^{\frac{a}{\lambda}} - 1}, \tag{5}$$

where *A* is the ratio of the AES sensitivity for Pt and C and $\lambda$ is the inelastic mean path, which we assume it the same for both elements. Solving Eq. 5 for *a* and using the AES signals as a function of the temperature, we find that the thickness of the carbon layer increases with temperature and reaches roughly 0.54 nm after annealing to 700°C, as shown in Figure 12. Since the C-C distance between graphene layers is 0.33 nm, we find that with this calculation the Pt films get covered by almost two carbon layers, which is in agreement with the result provided by the sputtering rate. However, since the sputtered HOPG surface is highly defected, with a roughness factor around 2,[16] it is reasonable that the actual amount of carbon covering the Pt films is roughly just a single monolayer.

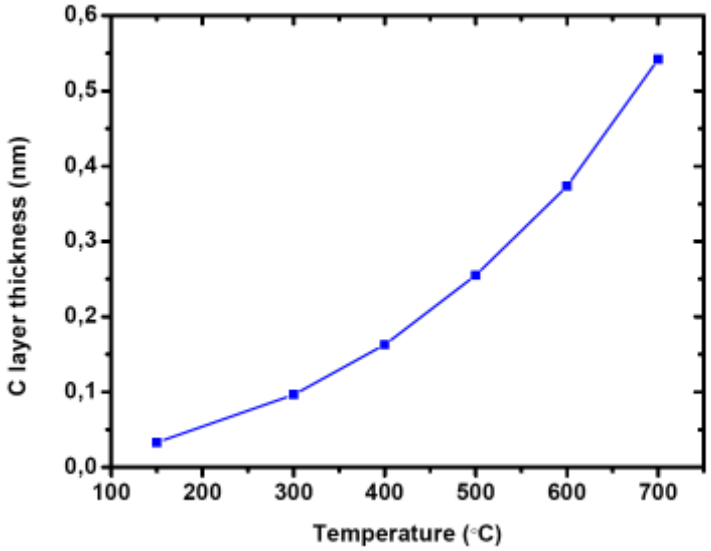


**Figure 12.** The thickness of the C layer which covers the surface of the Pt films upon annealing to high temperature in UHV, as calculated according to Eq. 5.

## 6. SUMMARY AND CONCLUSIONS

We have shown a strong metal-support interaction between Pt and Ru films and HOPG, other sputtered or fresh cleaved, when the films are annealed to high temperatures in UHV. We find that the surface of the Pt and Ru films get covered by carbon upon annealing, which causes a suppression of the hydrogen exchange rate for both metals. We also show, in the case of the Pt films, that the SMSI state can be reverse by performing $He^+$ sputtering for 45 minutes, which is able to remove the carbon from the metal´s surface and regenerate the activity. We also try to quantify the thickness of the carbon layer forming on the metal films upon annealing, by calculating the sputtering rate and the damping of the AES Pt signal through the carbon layer as a function of temperature. Due to the roughness of the HOPG surface, it is reasonable that the actual amount of carbon covering the Pt films is roughly a single monolayer.

**ACKNOWLEDGMENT**

Center for Individual Nanoparticle Functionality (CINF) is sponsored by The Danish National Research Foundation.

**REFERENCES**

(1) Tauster, S. J.; Fung, S. C.; and Garten, R. L. *J. Amer. Chem. Soc.* **1978**, *100*, 170.

(2) Vannice, M. A.; Hasselbring, L. C.; and Sen, B. *J. Phys. Chem.* **1985**, *89*, 2972.

(3) Haller G. L.; and Resasco, D. E. *Adv. Catal.* **1989**, *36*, 173.

(4) Sadeghi, H. R.; Henrich, V. E. *Appl. Surf. Sci.* **1984**, *19*, 330.

(5) Bowker, M.; Stone, P.; Morrall, P.; Smith, R.; Bennett, R.; Perkins, N.; Kvon, R.; Pang, C.; Fourre, E.; Hall, M. *J. Catal.* **2005**, *234*, 172.

(6) Bowker, M.; Stone, P.; Bennett, R.; Perkins, N. *Surf. Sci.* **2002**, *497*, 155.

(7) Bowker, M.; Fourré, E. *Appl. Surf. Sci.* **2008**, *254*, 4225.

(8) Bowker, M. *Phys. Chem. Chem. Phys.* **2007**, *9*, 3514.

(9) Qin, Z.-H.; Lewandowski, M.; Sun, Y.-N.; Shaikhutdinov, S.;Freund, H.-J. *J. Phys.: Condens. Matter* **2009**, *21*, 134019.

(10) Zhou, Y.; Perket, J. M.; Zhou, J. *J. Phys. Chem. C* **2010**, *114*, 11853.

(11) Anderson, J. B. F.; Burch, R.; Cairns, J. A. *Appl. Catal.* **1986**, *25*, 173.

(12) Tauster, S.J.; Fung, S.C.; Baker R.T.K.; Horsley, J.A. *Science* **1981,** *211*, 1121.

(13) Sadeghi, H. F.; Henrich, V. E. *J. Catal.* **1984**, *87*, 279.

(14) Johansson, M.; Hoffmann Jørgensen, J.; Chorkendorff, I. *Rev. Sci. Instrum*. **2004**, *75*, 2082.

(15) Johansson, M.; Johannesen, T.; Hoffman Jørgensen, J.; Chorkendorff, I. *Appl. Surf. Sci.* **2006**, *252*, 3673.

(16) Fiordaliso, E. M.; Murphy, S.; Nielsen, R. M.; Dahl, S.; Chorkendorff, I. accepted *Surf. Sci.* doi:10.1016/j.susc.2011.10.004.

(17) Johansson, M.; Lytken, O.; Chorkendorff, I. *Top. Catal.* **2007**, *46*, 175.

(18) Johansson, M.; Lytken, O.; Chorkendorff, I. *J. Chem. Phys.* **2008**, *128*, 034706.

(19) Behm, R. J.; Christmann, K.; Ertl, G. *Surf. Sci.* **1980**, *99*, 320.

(20) Rendulic K.D.; Winkler, A. *J. Chem. Phys.* **1983**, *79*, 5151.

(21) Norton, P.R.; Davies J. A.; Jackman, T. E. *Surf. Sci.* **1982**, *121*, 103.

(22) Mikhailov, S.N.; Elfrink, R.J.M.; Jacobs, J.-P.; van den Oetelaar, L.C.A.; Scanlon, P.J.; Brongersma, H.H. *Nucl. Instrum. Methods Phys. Res.B* **1994**, *93*, 210.

(23) Gabor A. Somorjai, Cornell University Press, Ithaca, **1981**.

(24) Claeyssens, F.; Pratontep, S.; Xirouchaki C.; Palmer, R. E. *Nanotechnology* **2006**, *17*, 805.

(25) Nielsen, R. M.; Murphy, S.; Strebel, C.; Johansson, M.; Nielsen, J. H.; Chorkendorff, I. *Surf. Sci*. **2009**, *603*, 3420.

(26) Wei, Q.; Li, K. D.; Lian, J.; Wang, L. *J. Phys. D: Appl. Phys*. **2008**, *41*, 172002.

(27) Sigmund P. *Phys. rev.* **1969**, *184*, 383.

(28) Behrisch, R.; Eckstein, W. *Top. Appl. Phys.* **2007**, *110*, 33.